Nonlinear Adaptive Filtering with Application to Acoustic Echo Control

submitted by

A. Neil Birkett, B. Eng/M. Eng.

A thesis submitted to
the Faculty of Graduate Studies and Research
in partial fulfillment of
the requirements for the degree of

Doctor of Philosophy

Ottawa-Carleton Institute for Electrical Engineering
Faculty of Engineering
Department of Systems and Computer Engineering

Carleton University
Ottawa, Ontario, Canada K1S 5B6
April, 1997

The undersigned recommend to

the Faculty of Graduate Studies and Research

acceptance of the thesis

Nonlinear Adaptive Filtering with Application to Acoustic Echo Control

submitted by

Neil Birkett, B.Eng/M. Eng.

in partial fulfillment of the requirements for

the degree of Doctor of Philosophy

Thesis Supervisor

Chair, Department of Systems and Computer Engineering

External Examiner

Carleton University

April 15, 1997

Abstract

This thesis deals with nonlinear adaptive filtering for identification of systems comprised of weakly nonlinear systems convolved with large order linear systems. The intended use is for acoustic echo cancellers (AEC's) operating in handsfree telephones (HFT's) where a microphone and nonlinear loudspeaker share a common enclosure.

Limitations of AEC's are first determined using analytical models verified with simple computer simulations and real-world experimental data. It is shown that enclosure resonances and vibrations, loudspeaker nonlinearity, system undermodelling and audio transducer quality all affect the achievable Echo Return Loss Enhancement (ERLE) performance.

A third-order Volterra filter achieves 6.2dB of improved ERLE over a linear Finite Impulse Response (FIR) filter, however with a training complexity almost 20 times that of the simple Normalized Least Mean Square (NLMS) algorithm.

Simple feedforward neural based filters are shown to achieve the best performance/complexity trade-off for compensating nonlinear loudspeaker effects in AEC's, compared to Volterra and recursive Infinite Impulse Response (IIR) structures. Using a mixed linear/sigmoidal activation function in the neural based filters, several dB's of ERLE improvement can be achieved depending on the range of the linear section and the severity of nonlinearity.

A simple two-stage neural filter is proposed. It achieves an 11 dB improvement over the NLMS-FIR structure with only a 2% increase in complexity. The activation function is then modified to be adaptive, with a resulting ERLE improvement of between 1 and 5 dB over the fixed activation function architecture.

A nonlinear fast conjugate gradient (NFCG) backpropagation algorithm is developed next for improving the convergence rate for coloured signals like speech. The algorithm has a simple gradient-based update and provides a complexity/performance trade-off determined by the size of a gradient window n_w. When applied to the two stage neural filter using real speech signals, a 5 dB improvement in ERLE is achieved compared to the Stabilized Fast Transversal Filter (SFTF) with the same initial convergence rate as the SFTF algorithm.

A linear version of the NFCG is also developed using a line search based on a variable step size technique.

Acknowledgements

This thesis was completed with the help of many people who contributed both directly and indirectly in many ways.

First and foremost, it is my pleasure to acknowledge my supervisor Dr. Rafik Goubran for his constant support, motivation, patience and reassurance during some trying times. I am indebted to you.

I am grateful to Jeff Lariviere, Trevor Moat, Tim Webster, and Nong Li, people who shared the DSPLAB with me for several years, and also who provided invaluable discussions, diversions, and entertainment. Thanks also to Rajeev Bector for helping design and develop the experimental setup. To Danny Lemay for always attending to the DSPLAB network when required, and keeping the PCs operational.

Thanks to Dr. Jack Kelly for allowing unlimited access to the anechoic chamber in the Loeb Building.

To the Nortel staff, special thanks go to Dr. Andre Van Shyndel for providing speech files, several loudspeakers handsfree telephone sets and vital information on audio transducers. Thanks also to Scot McLennan for providing valuable feedback on industrial concerns, and especially Dr. Heping Ding who provided constructive comments on Chapter 6 of this thesis.

To the Department of Systems and Computer Engineering at Carleton University, I thank you for financial support that was provided through scholarship and teaching employment. Thanks are also due to NSERC, OGS, TRIO and Nortel for additional financial assistance.

To my mother and father and sister I would like to express a deep thanks for the encouragement and love that have always been there.

I would like to thank Darlene, my wife, for being loving, patient and understanding during the completion of this thesis, and finally my sons Colin, Byron and Sheldon for always providing me with a daily reminder of the really important studies in life.

Table of Contents

List of Figures

List of Tables

List of Symbols

Rules Regarding Boldface Symbols

A boldface uppercase letter generally refers to a matrix of numbers or variables. A boldface lowercase letter generally refers to a vector of numbers or variables. An unbolded uppercase or lowercase letter is a scalar quantity.

Arabic Symbols

a	Sigmoid slope parameter.
a,b,c	Magnitude of linear, quadratic and cubic distortion coefficients.
a_i	i^{th} feedback coefficient value for a recursive IIR filter.
$A(z)$	Linear model polynomial coefficients associated with $d(n)$ regressors.
b_i	i^{th} feedforward coefficient value for an FIR filter.
b	Bias potential.
B	Magnetic flux density in the air gap.
B_c	Number of binary quantization levels for DSP coefficient representation.
B_d	Number of binary quantization levels for DSP data representation.
$B(z)$	Linear model polynomial coefficients associated with $x(n)$ regressors.
C	Compliance of the suspension system.
ΔC	Change in electret microphone capacitance.
$d(n)$	Sample of desired response at time n.
$\mathbf{d}_k$	Conjugate direction vector at iteration k.
$\mathbf{d}(n)$	Desired signal sample vector at time n.
$e(n)$	Adaptive filter prediction error at time n.
$e(t)$	Applied voice coil voltage.
E_b	Voltage induced in the voice coil by the mechanical circuit.
$E(\ )$	Expected value of a function.

f_{M}	Force deflection characteristic of the loudspeaker cone suspension system.
$\mathbf{F}(\,)$	Hessian of an m x m matrix.
$\mathbf{g}_k$	Conjugate gradient estimate at iteration k.
h_p	p^{th} order Volterra kernel.
$\mathbf{h}_e$	Extended Volterra weight vector.
$\mathbf{h}_p$	p^{th} order Volterra coefficient vector.
$H(z)$	Transfer function in the z domain
H_1, H_2	Linear dispersive system transfer functions.
$i(t)$	Amplitude of the current in the voice coil.
J	General cost function.
$J_{\min}$	Minimum mean square error
J_{tot}	Total mean square error
l	MLP layer index.
l	Length of the voice coil inductor.
L	Inductance of the voice coil.
m	(i) Square matrix size (ii) Total mass of coil, cone and air load.
m_p	Number of inputs in the p^{th} order section of a polynomial filter.
M	Order of a “supervector”.
n_a	Number of pole coefficients.
n_b	Number of zero coefficients.
n_{w}	CG averaging window length.
$p(n)$	Sample of primary signal at time n.
p	Size of linear region in variable activation function.
$p_j(n)$	p value for the j^{th} node at the n^{th} iteration.
$\Delta p_j(n)$	Correction value for $p_j(n)$ at the n^{th} iteration.
$\mathbf{p}(n)$	Vector of p parameters.
$\mathbf{p}_k$	Conjugate gradient estimate at $\mathbf{y}_k$ at iteration k.

$\mathbf{P}(n)$	Matrix derived from input $x(n)$ used to improve convergence rate.
P	Conjugate gradient reuse rate.
$q(n)$	Measure of the input signal power.
$\mathbf{Q}$	General $m \times m$ matrix.
$r(n)$	Sample of reference signal at time n.
r_M	Total mechanical resistance due dissipation in the air load and suspension system.
R	(*i*) Conjugate direction reuse rate (*ii*) Total electrical resistance of the generator and voice coil.
$\mathbf{R}(n)$	Autocorrelation matrix of an input vector $\mathbf{x}(n)$.
s	Activation potential
$s_j^{(l)}(n)$	Input activation to node j in layer l.
$\mathbf{u}(n)$	Input regression vector.
ΔV	Change in microphone output voltage.
$v_j^{(l)}(n)$	Backward error activation for the j^{th} node in layer l at time n.
$w_{i,j}^{(l)}(n)$	Weight connecting the i^{th} node in layer l to the j^{th} node in layer l+1 at time n.
$\mathbf{w}_{i,j}^{(l)}(n)$	Synaptic FIR weight vector connecting the i^{th} node in layer l to the j^{th} node in layer l+1 at time n.
$\overline{\mathbf{w}}_{i,j}^{(l)}(n)$	Accumulated synaptic FIR weight vector connecting the i^{th} node in layer l to the j^{th} node in layer l+1 at time n, of length n_w.
w_{bias}	Bias weight.
$\mathbf{w}(n)$	Weight vector at time n.
$\mathbf{w}_{opt}$	Optimum weiner filter coefficient vector.
$x(n)$	Current input sample at time n.
$\mathbf{x}(n)$	Input sample vector at time n.
$x_j^{(l)}(n)$	Output of node j in layer l.
$\mathbf{x}_j^{(l)}(n)$	Output vector of node j in layer l.
$\mathbf{x}_e$	Extended Volterra regression vector.
$y(n)$	Adaptive filter output sample at time n.

$\mathbf{y}(n)$	Output sample vector at time n.
$\mathbf{y}_k$	Estimate of the new conjugate weight vector.

Greek Symbols

α, β, γ	Nonlinear compliance modelling coefficients.
α	Momentum constant.
$\tilde{\alpha}$	Normalized step size parameter
α_k	Direction vector constants.
β_k	Coefficient for generating $\mathbf{d}_{k+1}$ from $\mathbf{d}_k$.
γ	MVSS convergence rate parameter.
Γ	MVSS filtered error averaging time constant.
Γ_H	Hankel matrix of an all zero impulse response.
$\delta_j^{(l)}(n)$	Local gradient delta for node j in layer l at time n.
$\overline{\Delta}_j^{(l)}(n)$	Accumulated local gradient delta vector for node j in layer l at time n of length n_w.
ε	Small positive constant.
$\theta_j^{(l)}$	Bias potential added to node j in layer l.
Σ	Diagonal matrix of Hankel singular values.
φ	(i) General nonlinear operator (ii) Sigmoid operator.
$\varphi'_s(s, p)$	Derivative of a sigmoid operator with respect to the s parameter.
λ	forgetting factor (RLS, FTF, SFTF)
λ_i	i^{th} eigenvalue of the input correlation matrix.
λ_{max}	Maximum eigenvalue of the input correlation matrix.
μ	Step size parameter.
μ_{TDNN}	Step size parameter for the TDNN portion of the two layer neural filter.
μ_2, μ_3	Step size parameters for quadratic and cubic sections of a third order Volterra filter.
$\nabla_{\mathbf{w}}$	Multidimensional gradient with respect to vector **w.**
σ_i	i^{th} Hankel singular value.

σ^2_c	Coefficient quantization noise.
σ^2_d	Data quantization noise.
σ^2_p	Variance of the primary signal.
σ^2_e	Variance of the error signal.
σ^2_R	Room noise.
σ^2_M	Microphone noise.
ω	Angular frequency.
$\xi_j(n)$	Local gradient for the parameter $p_j(n)$.
ζ	MVSS step size averaging parameter.

List of Abbreviations

AEC	Acoustic Echo Canceller
AF	Adaptive Filter
AIR	Acoustic Impulse Response
AR	Auto Regressive
ARMA	Auto Regressive Moving Average
ARMAX	Auto Regressive Moving Average with Exogenous inputs
ARX	Auto Regressive with Exogenous Input
BP	Backpropagation
BPF	Bandpass Filter
CES	Composite Error Surface
CG	Conjugate Gradient
CGR	Conjugate Gradient Reuse
CRA	Composite Regressor Algorithm
DAT	Digital Audio Tape
DSP	Digital Signal Processing
DT	Double Talk
DVM	Digital Voltmeter
EBP	Enhanced Backpropagation
EE	Equation Error
EKA	Extended Kalman Algorithm
ELR	Early-to-Late Ratio
ERLE	Error Return Loss Enhancement
FAP	Fast Affine Projection
FCG	Fast Conjugate Gradient
FIR	Finite Impulse Response
FFT	Fast Fourier Transform
FNTF	Fast Newton Transversal Filter
FTF	Fast Transversal Filter
GF	Generalized Feedforward

GMDF	Generalized Multi-Delay Filter
HFT	Handsfree Telephone
HQL	High Quality Loudspeaker
HQM	High Quality Microphone
IC	Instantaneous Cost
ICVA	Instantaneous Cost Variable Activation
IEEE	Institute for Electric and Electronic Engineers
IIR	Infinite Impulse Response
LMS	Least Mean Squares algorithm
LPF	Lowpass Filter
LQL	Low Quality Loudspeaker
LQM	Low Quality Microphone
LREM	Loudspeaker-Room-Enclosure-Microphone
LRGF	Locally Recurrent Globally Feedforward
MA	Moving Average
MLP	Multilayer Perceptron
MMSE	Minimum Mean Squared Error
MSE	Mean Squared Error
MVSS	Modified Variable Step Size
NARMAX	Nonlinear ARMAX
NARX	Nonlinear ARX
NCG	Nonlinear Conjugate Gradient
NFIR	Nonlinear FIR
NOE	Nonlinear Output Error
NLMS	Normalized Least Mean Square
NSS	Nonlinear State Space
OE	Output Error
PSD	Power Spectral Density
QAM	Quadrature Amplitude Modulation
RLS	Recursive Least Squares
RMS	Root Mean Square
ROM	Read Only Memory
RPE	Recursive Prediction Error

SCG	Scaled Conjugate Gradient
SFTF	Stabilized Fast Transversal Filter
SDR	Signal to Distortion Ratio
SMM	Steiglitz McBride Method
SNR	Signal to Noise Ratio
SPL	Sound Pressure Level
SS	State Space
TC	Total Cost
TDL	Tapped Delay Line
TDNN	Tapped Delay line Neural Network
TIP	Total Impulse Response Power
TP	Tail Power
TWT	Travelling Wave Tube
USASI	United States of America Standards Institute
VA	Variable Activation
VCG	Variable Stepsize Conjugate Gradient
VCGR	VCG with Gradient Reuse
VSS	Variable Step Size

Chapter 1
Introduction

1.1 Motivation for the Research

Real-time system identification, filtering and/or tracking of signals produced in nonstationary environments requires the use of an adaptive filter. Much of the literature available on adaptive filter theory deals only with linear structures which have difficulty in accurately identifying systems that include nonlinearities. In the real world, examples of such nonlinear systems include the production of human speech signals, audio transducers such as loudspeakers and channel nonlinearities in high-speed data communications channels, usually caused by amplifier circuits operating near saturation.

A *handsfree telephone* (HFT) is one such system that contains a nonlinear component, the loudspeaker. An *acoustic echo canceller* (AEC) designed for use in an HFT attempts to remove the acoustic echos by modelling the *loudspeaker-room-enclosure-microphone* (LREM) system and subtracting an echo replica from the microphone signal. However, in this case, the system to be

identified includes a reverberant room as well as the loudspeaker and therefore is a cascade of both linear and nonlinear sections that have memory associated with the process. The acoustic echoes associated with reverberant rooms can be modelled effectively by linear filters consisting of all-zero adaptive *Finite Impulse Response* (FIR) structures or in some cases *Infinite Impulse Response* (IIR) structures consisting of one or more poles. A loudspeaker is a nonlinear device that exhibits hysteresis, hence a structure that can process *nonlinear temporal* information is required to achieve significant modelling accuracy. Existing linear algorithms in the AEC domain are therefore unable to achieve high *echo return loss enhancement* (ERLE) when the loudspeaker is operating in the nonlinear region. This idea was originally suggested by Knappe and Goubran [1] as a steady state performance limitation in acoustic echo cancellers and was a primary motivating factor for the work presented here.

This thesis is primarily about the study of nonlinear algorithms aimed at identifying cascaded linear and nonlinear systems with specific application to the reduction of nonlinear loudspeaker distortion effects encountered in the domain of acoustic echo cancellation.

Four basic questions are answered in this thesis:

1. *What sort of limitations do typical nonlinear loudspeakers present to achieving high ERLE values in typical HFT's ?* Small inexpensive loudspeakers generate several percent nonlinear distortion at volumes typically used in the handsfree mode, and thus limit the ERLE to values less than 30 dB in most cases.

2. *What kind of filters are best suited for nonlinear AEC applications and how can we arrive at that conclusion?* Feedforward structures offer simplicity of design compared to recursive structures, especially in the nonlinear domain. Structures proposed also need to be robust in noisy

environments.

3. *How can an efficient nonlinear structure and training algorithm be designed that is not overly complicated yet provide reasonable improvements in performance?* Low complexity is of utmost importance in AEC's, hence the nonlinear training algorithm should provide a trade-off between complexity and performance. Structures and algorithms based on a combination of neural networks and linear adaptive filtering theory provide encouraging results.

4. *Can the new structures/algorithms be successfully applied in real-world applications?* The nonlinear AEC's are applied to experimental data collected on several commercially available HFT's in conference environments with positive results using both noise and speech signals.

Throughout the thesis, the handsfree telephony AEC is used to demonstrate the effectiveness of the proposed algorithms and structures, with verification using field data collected using a number of commercially available HFT's in different anechoic and conference room environments. However it should be stressed that in general these algorithms can be applied to many fields, for example, public address (PA) systems, active noise control using remotely placed loudspeakers to cancel unwanted signals, and identification of channel nonlinearities in high speed data communications channels.

1.2 Contributions of the Thesis

The primary contribution of this thesis is the development of a set of new nonlinear adaptive filter structures and algorithms to compensate for nonlinear loudspeaker distortion effects in AEC's intended for handsfree telephony. The procedure consists of the following steps

- Determination of the limitations in AEC's due to nonlinear transducers.
- Evaluation of existing nonlinear structures for compensating nonlinearity in AEC's.
- Construction of new architectures for compensating for transducer nonlinearity.
- Development of an efficient training algorithms for the proposed structures.
- Application and testing of the new nonlinear structures using speech and noise signals recorded in HFT's in audio conference environments.

The main contributions to the field of nonlinear adaptive filtering are as follows:

1. Development of a two stage neural filter consisting of an FIR filter and tapped delay line neural network (TDNN) structure, which successfully models loudspeaker nonlinearity convolved with an echo path.
2. Development and use of a mixed linear sigmoidal activation (squashing) function to replace the hyperbolic tangent function which is commonly used in neural networks.
3. Extension of the mixed linear sigmoidal activation function to the fully adaptive case.
4. Development of a new temporal adaptation mechanism to adapt the variable activation function which is sandwiched between FIR synaptic filters.
5. A fast nonlinear conjugate gradient algorithm for improved convergence speed is developed and then applied to the nonlinear structures above to improve performance, which is verified using real speech signals.
6. A linear algorithm based on the fast conjugate gradient algorithm and the concept of variable step size line search is constructed. A simplified version using *gradient reuse* is also developed.

A full test setup for performing experimental testing is constructed, consisting of various amplifiers, filters and interface circuits. Experimental determination of the performance limitations of the

test setup using real equipment in anechoic and conference rooms conditions is made. During this phase, it was determined that enclosure vibration, resonances and rattling effects also place a limit on the achievable steady state acoustic echo cancellation[1]. Subsequently the following statements can be made which represent a secondary contribution, specifically to the design and development of HFT's:

1. Enclosure vibration can be a more serious problem than nonlinear distortion at high loudspeaker volumes for typical desktop HFT's in a low noise conference room.

2. Effective design of the acoustic enclosure is necessary to enable the nonlinear algorithms to work properly. Otherwise, the vibration and resonances within the enclosure mask the loudspeaker nonlinearity.

3. A microphone with a low mechanical vibration sensitivity is necessary to mitigate vibration effects.

4. The steady state performance limitations of AEC's for HFT's in a typical low noise conference room environment are *in order of severity* for the cases studied (i) undermodelling[2] (ii) loudspeaker nonlinearity[3] (iii) vibration and resonances (iv) room noise (v) DSP and algorithmic noise.

---

1. No mention of the performance limitation caused by vibration and resonances has yet been found in the literature on AEC's.

2. Undermodelling is a more serious limitation than other factors when the order of the AEC is much less than the LREM.

3. Only if vibration and resonances are controlled through appropriate enclosure design.

1.3 Thesis Outline and Scope

This thesis has four central chapters: Chapter 4 discusses the acoustic echo cancellation problem with subsections on the experimental setup and performance limitations, including important new results on the effects of vibration and resonances within the HFT enclosure, and nonlinear loudspeaker distortion. Several new nonlinear adaptive structures and algorithms are developed and tested in Chapters 5, and 6. Supporting Chapters 2,3 and 7 review loudspeaker dynamics, provide the necessary background theory in nonlinear adaptive filtering, and summarize and draw conclusions.

Chapter Two presents a quick review of loudspeaker basics, including the lumped parameter equivalent model and an analysis of low frequency nonlinear distortion.

Chapter Three discusses the principles of nonlinear adaptive filtering and corresponding adaptation algorithms. It briefly introduces linear FIR and IIR filters, Volterra filters, and neural networks. This chapter furnishes the reader with the necessary background theory and lays the foundation for the following chapters.

Chapter Four discusses the handsfree telephone problem, presents a description of the experimental setup and discusses the steady state performance limitations of AEC's such as undermodelling of the acoustic transfer function, room noise and DSP/algorithmic noise. A subsection on IIR structures for AEC is presented. Subsections studying the effect of enclosure vibration and resonances within the HFT enclosure, as well as effects of nonlinear transducers are also provided. Simulation and experimental results are presented throughout to provide a measure of the relative severity of the performance limitations.

Chapter Five first presents a comparison of Volterra and neural filters for nonlinear loudspeaker compensation. Subsequently a two stage neural filter is developed to identify a nonlinear LREM and provide measurable improvements in performance. A mixed linear-sigmoidal activation function is proposed and a training algorithm is derived. A new architecture and temporal training algorithm for adaptive activation functions sandwiched between temporal FIR synapses is also derived. The behavior of the proposed models is demonstrated using both simulated and experimental HFT data.

Chapter Six outlines a new fast version of the conjugate gradient algorithm for enhancing the convergence rate of neural filters. The performance of the algorithm is subsequently tested using computer simulations and field data consisting of both noise and speech signals. A linear variation of of the fast conjugate gradient algorithm using the concept of variable step size line search and *gradient reuse* is also presented.

Chapter Seven summarizes the results and draws conclusions arising from the research work. Significant contributions are highlighted and finally, future research directions are suggested.

Chapter 2
The Electrodynamical Loudspeaker

As mentioned in the first chapter, one focus of this thesis is in applying nonlinear filtering techniques to compensate for loudspeaker nonlinearity in AEC's for handsfree telephony. Before proceeding, a review of loudspeaker dynamics and an analysis of loudspeaker distortion at low frequencies is necessary.

2.1 Loudspeaker Model

In an electrodynamic loudspeaker, sound waves are produced by a *diaphragm* which moves in response to an alternating current passing through a *voice coil* which is positioned in a permanent magnetic field. Figure 2.1 illustrates a typical loudspeaker transducer, and equivalent lumped parameter model [2]. The diaphragm can be plane, cone or dome-shaped. The diaphragm is suspended at the outer edge by means of a flexible *surround* or rim, and at the inner edge by a *spider.* The spider is rotationally symmetrical and centers the voice coil. It has a large stiffness for radial motion and a smaller but finite stiffness for axial motion. The simplified model of a loudspeaker behaves like a mass-spring system. The spring part is formed by the suspension and spider and the

mass is formed by the diaphragm, the voice coil, the mass of the cone/suspension system and the air load [3].

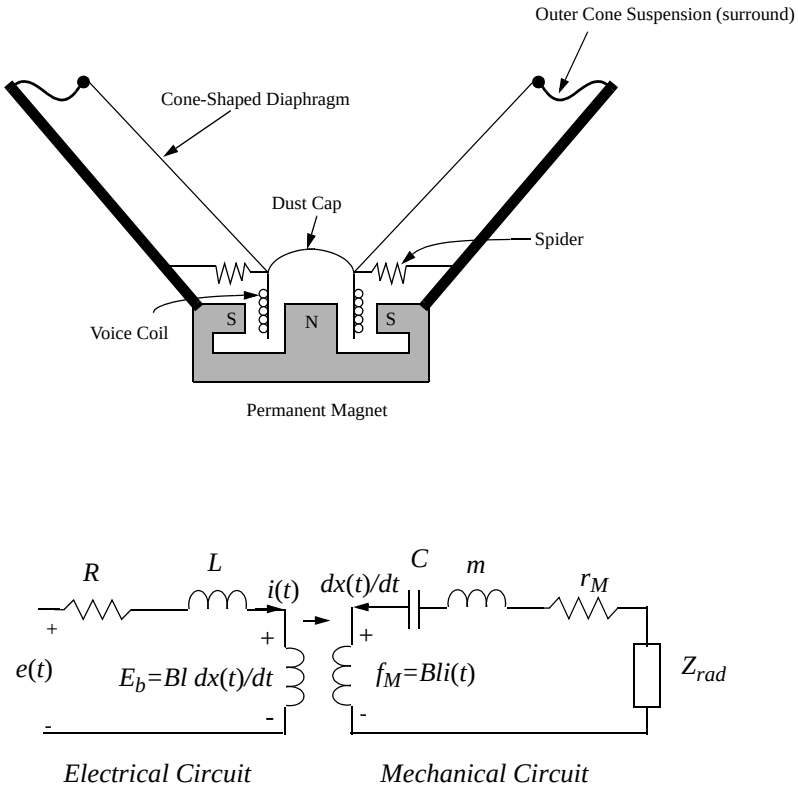

FIGURE 2.1 Loudspeaker electro-mechanical model.

In model of Figure 2.1, the parameter $e(t)$ indicates the internal voltage of the generator, R is the total electrical resistance of the generator and voice coil, L is the inductance of the voice coil, $i(t)$ is the amplitude of the current in the voice coil, E_b is the voltage induced in the electrical circuit by the mechanical circuit, which equals $Bl\ dx(t)/dt$. B is the magnetic flux density in the air gap, l is the length of the voice coil conductor, and x is the cone displacement. In the mechanical circuit m is the total mass of the coil, cone and air load. r_M is the total mechanical resistance due to dissipation in the air load and the suspension system. C is the compliance of the suspension and f_M is the force generated in the voice coil and equals Bli. The mechanical radiation resistance Z_{rad} has a real

and imaginary part.

As shown in Figure 2.1 the electrical and mechanical part are connected through the magnetic field. The resulting equations of motion can be described by two coupled nonlinear differential equations [4]:

$$e(t) = i(t)R + L(x(t))\frac{di(t)}{dt} + B(x(t))l\frac{dx(t)}{dt} \quad (2.1)$$

$$B(x(t))li(t) = m\frac{d^2}{dt}x(t) + r_M\frac{d}{dt}x(t) + \frac{x(t)}{C(x(t))} \quad (2.2)$$

where the displacement dependent parameters $L(x(t))$, $B(x(t))$ and $C(x(t))$ have been modelled by a Taylor series expansion, which can be truncated after an arbitrary number of terms:

$$L(x(t)) = L_0 + L_1x(t) + L_2(x(t))^2 \quad (2.3)$$

$$B(x(t)) = B_0 + B_1x(t) + B_2(x(t))^2 \quad (2.4)$$

$$C(x(t)) = C_0 + C_1x(t) + C_2(x(t))^2 \quad (2.5)$$

In these expressions, L_i, B_i and C_i are modelling constants up to the i-th order and $x(t)$ is the time dependent displacement of the voice coil. If we assume for the moment that B and C are linear such that the higher order coefficients in (2.4) and (2.5) are equal to zero, and that in the low frequency range, the inductance is negligible so that the approximation $L(x(t))=0$ is valid, then asecond order linear transfer function in the Laplace domain can be obtained as [5];

$$\frac{X(s)}{E(s)} = \frac{B_0l/R}{s^2m + s[r_M + (B_0l)^2/R] + 1/C_0} \quad (2.6)$$

A loudspeaker has several sources of nonlinearity which occur in the motor part (i.e. the magnet

system and voice coil), in the mechanical part, and due to nonlinear sound radiation. These components have a frequency dependency, however, if we restrict our discussion to the lower frequencies, we only have to take into account those nonlinearities that depend closely on the voice coil excursion [2]. The most prominent nonlinearities corresponding to $L(x(t))$, $B(x(t))$ and $C(x(t))$ are [4]:

- The *electric self inductance* $L(x(t))$ which depends on the voice-coil excursion. This is because the voice coil protrudes from the central position, yielding a *reluctance force* F_x (or *back electromotive force*) proportional to $i(t)^2$.
- The *force factor* $B(x(t))l$, which depends on the voice-coil excursion. In the case of constant current drive, the force on the voice coil depends on the position of the coil, since $\int B\ dl$ is a function of the voice coil displacement. A typical force factor vs. displacement curve is shown in Figure 2.2 a).
- Suspension system nonlinearity. The force vs. displacement curves of the spider and surround are not straight lines and show *hysteresis*. A typical curve is shown in Figure 2.2 b).

Generally, the mechanomotive force in the voice coil is a nonlinear function of the displacement *x*. The compliance of the suspension system can be obtained by;

$$C(x(t)) = \frac{x(t)}{f_M(x(t))} = \frac{1}{\alpha + \beta x(t) + \gamma x(t)^2} = \frac{1}{k(x(t))} \tag{2.7}$$

where $f_M(x(t))$ represents the force deflection characteristic of the loudspeaker cone suspension system and $k(x(t))$ is the nonlinear suspension *stiffness* factor.

Substituting (2.7) into (2.2), we obtain;

$$B(x(t))li(t) = m\frac{d^2}{dt}x(t) + r_M\frac{d}{dt}x(t) + \alpha x(t) + \beta x(t)^2 + \gamma x(t)^3 \tag{2.8}$$

Suspension system nonlinearity manifests itself as *soft clipping* at the loudspeaker output and results in odd-order harmonics under large signal conditions. As well, there is a frequency dependence. Equations (2.1) and (2.2) show that at high frequencies, the derivatives are large, so that the effect of the nonlinearities is small, i.e. the system is *weakly nonlinear.* However, at low frequencies, the converse is true and the effect of the nonlinearities is more pronounced. It should also be noted that distortion does not only occur at large signal levels. Significant distortion also occurs at extremely *low levels* due to unbalanced 2-point suspension, i.e., the surround and the spider [2],[3].

In the HFT domain, it is necessary to use small (i.e. inexpensive) loudspeakers. To obtain reasonably comfortable listening levels in the lower frequencies, excessive diaphragm excursions are needed, which will generate significant distortion products which can be 5% to 10% of the signal amplitude.

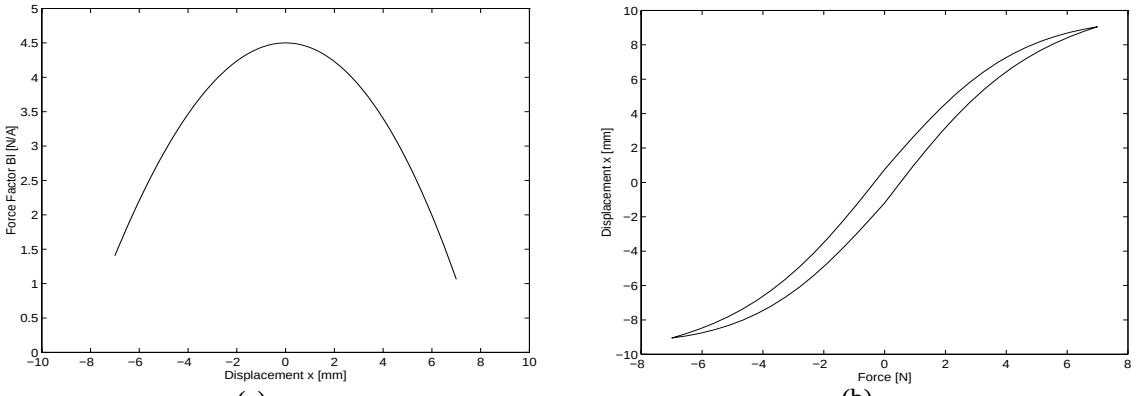

(a) (b)

FIGURE 2.2 (a) Typical force vs. displacement curve of a loudspeaker. (b) Typical force vs. displacement curve of the spider.

2.2 Nonlinear Modelling

An equation determining the excursion of the voice coil x may be constructed by forming a higher order differential equation by substituting (2.3), (2.4), and (2.5) into (2.1) and (2.2) and eliminating the parameter i. The solution to this equation may be attempted by the use of a Volterra series expansion (See [4]), however hysteresis effects cannot be modelled by this method. As well, a loudspeaker response cannot be written as an ordinary power series as is possible for a memoryless (dispersion-free) system, like a network with resistors. For the memoryless case, the Volterra series degenerates into a power series. When dispersive effects are included, the size of the Volterra model can become large.

Alternatively, we may cast the difference equations in state space form [6]. In the equations that follow, $L(x) = L_0$ is assumed to be linear. Let the state variables $x_1 = i$, $x_2 = x$ and $x_3 = dx_2/dt$. From the equivalent electrical/mechanical circuits, one can obtain the following state-space dynamical equations;

$$\frac{dx_1}{dt} = \frac{1}{L_0}(-Rx_1 - B_0 l x_3 + e - B_1 l x_2 x_3 - B_2 l x_2^2 x_3) \tag{2.9}$$

$$\frac{dx_2}{dt} = x_3 \tag{2.10}$$

$$\frac{dx_3}{dt} = \frac{1}{m}(B_0 l x_1 - \alpha x_2 - r_M x_3 - \beta x_2^2 - \gamma x_2^3 + l B_1 x_1 x_2 + l B_2 x_1 x_2^2) \tag{2.11}$$

$$y(t) = x_2(t) \tag{2.12}$$

The above equations can be discretized using the Euler approximation,

$$\left.\frac{dx}{dt}\right|_{t=nT} = \frac{x(n+1)-x(n)}{T} \tag{2.13}$$

where T is the sampling period and $x(n)$ is used to denote $x(nT)$ for convenience. Thus, the following difference equations are formed,

$$\begin{aligned}\mathbf{x}(n+1) &= \begin{bmatrix} a_{11} & 0 & a_{13} \\ 0 & 1 & a_{23} \\ a_{31} & a_{32} & a_{33} \end{bmatrix}\mathbf{x}(n) + \begin{bmatrix} b_1 \\ 0 \\ 0 \end{bmatrix}u(n) \\ &+ \begin{bmatrix} p_{11}x_2(n)x_3(n) + p_{12}x_2^2(n)x_3(n) \\ 0 \\ p_{31}x_2^2(n) + p_{32}x_2^3(n) + p_{33}x_1(n)x_2(n) + p_{34}x_1(n)x_2^2(n) \end{bmatrix}\end{aligned} \tag{2.14}$$

$$y(n) = (0,1,0)^T\mathbf{x}(n) \tag{2.15}$$

where $u(n)$ is the system input and a_{11}=1-TR/L_0, a_{13}=-$T/B_0/L_0$, a_{23}=T, a_{31}=TB_0l/m, a_{32}=-$T\alpha/m$, a_{33}=1-Tr_M/m, b_1=T/L_0, p_{11}=-TB_1/L_0, p_{12}=-TB_2l/L_0, p_{31}=-$T\beta/m$, p_{32}=-$T\gamma/m$, p_{33}=TB_1l/m, and p_{34}=TB_2/m. Knowledge of the associated loudspeaker parameters (suggested in [6]) yield for the simulation:

$$\begin{aligned}\mathbf{x}(n+1) &= \begin{bmatrix} -0.1 & 0 & -0.2 \\ 0 & 1 & 1 \\ 0.6 & -0.5 & -0.15 \end{bmatrix}\mathbf{x}(n) + \begin{bmatrix} 0.4 \\ 0 \\ 0 \end{bmatrix}u(n) \\ &+ \begin{bmatrix} -0.04x_2(n)x_3(n) + -0.05x_2^2(n)x_3(n) \\ 0 \\ -0.08x_2^3(n) + 0.01x_1(n)x_2(n) + 0.02x_1(n)x_2^2(n) \end{bmatrix}\end{aligned} \tag{2.16}$$

$$y(n) = (0,1,0)^T\mathbf{x}(n) \tag{2.17}$$

The sample period T is set to unity and β is set to zero since it is small in practice. Figure 2.3 illustrates the input and output signals obtained from the linear and nonlinear models using an input test signal $x(t) = 3.5\sin(0.6\omega t) + 5.0(1.0)\cos(1.6\omega t)$ where $\omega = 100\pi$. It is shown that the nonlinear model exhibits soft-clipping at high excursion peaks. The corresponding impulse response is illustrated in Figure 2.4..

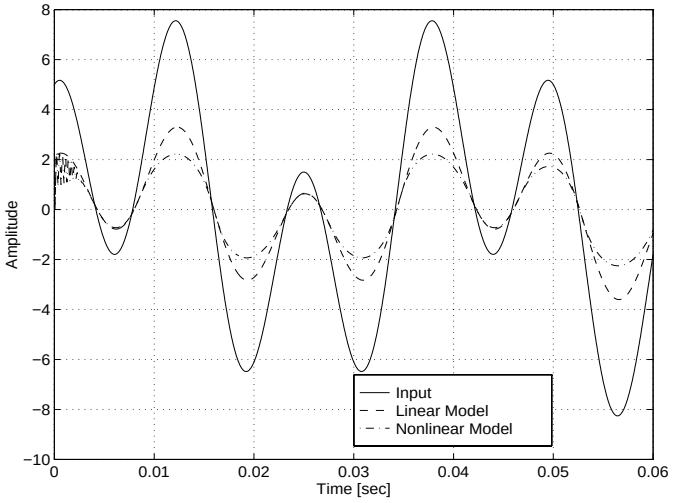

FIGURE 2.3 Comparison of the input signal e(t) with the linear model and nonlinear model outputs. The nonlinear model exhibits soft-clipping during amplitude peaks.

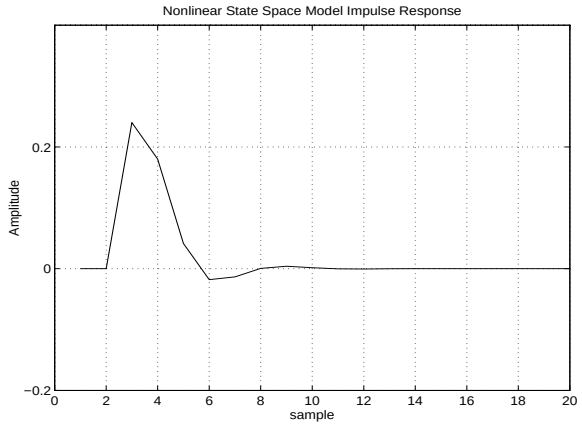

FIGURE 2.4 Nonlinear state-space model impulse response.

2.3 Measurement of Nonlinear Parameters

Accurate determination of the nonlinear parameters usually requires that the cone displacement be measured in synchronization with the applied coil voltages or currents. Laser displacement systems are typically required to achieve the accuracy. Once the displacement data is obtained, it may then be applied to a general linear (see for example Ljung [5]) or nonlinear system identification techniques [7] . The simplest method is to measure the lumped parameters as the voice coil is displaced *statically* and then fit the coefficients of a power series via least squares curve fitting [8]. However, to determine stiffness and hysteresis, a *dynamic* method is required, where the applied signal is a combination of continuous wave or swept-tone sinusoids. This method is sometimes referred to as the *harmonic input excitation* method. An alternate method in [9] uses several gaussian noise inputs with different root-mean-square (RMS) amplitudes. The advantage of dynamic methods like harmonic excitation is that a simple microphone can be used to obtain frequencies and relative amplitudes of the harmonic and distortion products. The coefficients of a power series may then be obtained by a set of equations (See for example [8],[9],or [10]) for estimating the nonlinear parameters. Care must be taken however in removing any echo associated with the loudspeaker-microphone measurement system, as discussed in [11].

2.4 Methods for Reducing Nonlinear Distortion

The reduction of loudspeaker distortion may be done using *open-loop* or *closed-loop* systems. An open-loop system obtains the nonlinear parameters using one-time measurement techniques described in Section 2.3 and then applies these values in a *pre-distortion* circuit. Examples of such systems based on the Volterra series can be found in [12][13] and [14], however the later does not compensate for loudspeaker hysteresis effects. A pre-distortion open-loop technique using the *mir-*

ror filter is described in [15]. An open-loop compensation system using a Matlab® model developed from measured parameters is described in [16]. In [17] an inverse loudspeaker/room model is developed using a Time Delay Neural Network to provide single point room equalization, but no experimental measurements were presented.

A closed-loop system based on the correction of the displacement dependent force factor is described in [18], however, this requires the use of a displacement transducer. Sometimes the loudspeaker itself is used as the sensor for reasons of cost and the cone velocity is detected by a bridge arrangement [19]. The method in [20] uses three operational amplifiers to detect voice coil current to provide negative feedback. Another method based on providing *acceleration feedback* is described in [21].

2.5 Summary

In this chapter, the nonlinear loudspeaker model is reviewed. A brief description of the electromechanical model is presented and the corresponding differential equations describing the dynamics of motion were introduced. A linear system block diagram shows that the loudspeaker is basically a mass spring system. Next, a review of the primary sources of nonlinear distortion is presented, concluding that the loudspeaker exhibits both temporal distortion (hysteresis) as well as amplitude distortion generated mainly due to nonuniform flux density and suspension system nonlinearity. Simulations based on linear/nonlinear state-space models show that at high signal levels, the loudspeaker exhibits soft-clipping distortion. Finally, a brief literature summary of some techniques available for measuring nonlinear loudspeaker parameters and reducing distortion is presented.

Chapter 3
Review of Nonlinear Adaptive Filtering Techniques

This chapter furnishes the reader with the necessary background theory, techniques, algorithms and structures related to this thesis. It starts with a brief survey of some nonlinear system identification techniques and applications followed by a definition of terms and a quick review of linear models. Subsequently, sections on the *stochastic gradient, recursive least squares*, and the *conjugate gradient* search techniques are presented. The chapter concludes with a discussion of the adaptive nonlinear *Volterra* filter and the multilayer perceptron *neural network*.

3.1 Applications and a Survey

Linear adaptive filtering techniques are unable to benefit from higher order statistics of a nonlinear process and therefore are limited in scope. For example, conventional linear adaptive filtering algorithms are usually phase blind (Li, [22]) in the sense that they do not respond to phase information contained in a signal in excess of a minimum phase characteristic. Linear models will also fail miserably when trying to correlate two signals with non-overlapping spectral components (Mathews [23]). In order to exploit the full information context of a signal, it is necessary to

invoke nonlinear signal processing techniques. The process of identifying a signal can be viewed as an “understanding” process or as a “learning” process. Understanding a process involves being able to construct a relatively accurate model based on *a-priori* information, and state-space models are generally of this class (Gershenfeld [24]). Learning a process on the other hand is more effective when there is little a-priori information about the underlying dynamics of a system, but the available input/output information is plentiful. Thus, we can construct an ordered system from a relatively unstructured initial model. Volterra filters and neural networks are two such “learning” structures.

The Volterra series expansion (Schetzen [25]) can model a large class of nonlinear systems and is attractive in adaptive filtering applications because the expansion is a linear combination of nonlinear functions of the input signal. However, the Volterra filter belongs to a class of *polynomial filters* which have a *superlinear* increase in the number of parameters for both increasing filter order and polynomial order, and are therefore restricted to applications where the system order is low. In the literature, Volterra filters have been applied to general nonlinear system identification [26],[27],[28],[29], nonlinear echo cancellation for data hybrids [30],[31],[32], nonlinear noise cancellation [33],[34], and estimation and compensation of loudspeaker distortion [13],[14],[35],[36]. However, rarely does the discussion go beyond a 2nd order system.

For compensation of loudspeaker nonlinearity, most distortion products are 3rd order and higher, thus filter polynomial orders greater than three are required to effectively model the speaker transfer function. However, when the loudspeaker output is convolved with a dispersive echo channel, it very quickly leads to an unmanageably huge model. As a result, structures which are “less general” are proposed in the literature. An example of a “weakened” Volterra filter is the cascaded linear-nonlinear-linear system described by Cowan and Adams [37], which consists of memoryless

non-linearity sandwiched between two linear filters (See Figure 3.1). In [37], the nonlinearity

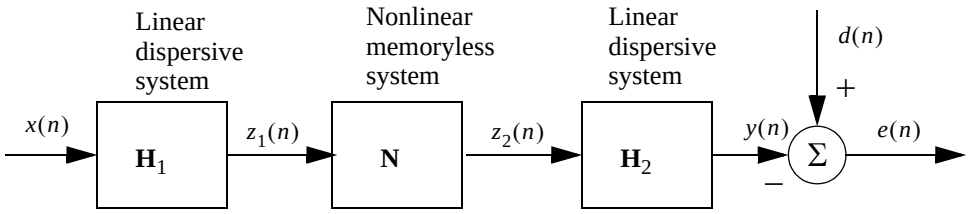

FIGURE 3.1 A weakened Volterra filter that consists of cascaded linear-nonlinear-linear subsystems.

takes the form of a Taylor series expansion. Most signal processing problems can be reduced to similar forms by isolating the known nonlinear component and then compensating for its nonlinearity by using a finite number of terms in the expansion. For example, one such system that can be represented by Figure 3.1 is a general satellite communications channel with a nonlinearity introduced by a TWT in the transponder (Namiki [38]).

Neural networks offer an alternative method of dealing with high order system nonlinearities without the “curse of dimensionality” associated with polynomial filters. One of the attractive features of a neural network is its ability to adaptively learn subtle relationships from the data without knowing the underlying process. As well, the network has the ability to generalize, i.e. being able to respond correctly to input patterns not contained in the original training sequence. This is useful in real-world applications where the data is often distorted and incomplete. In the literature, neural networks filters have been used for general nonlinear system identification (Chen [39],[40]) prediction of nonstationary nonlinear speech signals (Haykin [41]), equalization of high power amplifiers in communications systems (Paolo *et al.* [42],[43]), speech enhancement and noise reduction

in hearing aid systems (Knecht [44],[45]), and inverse filtering of loudspeaker-room acoustics (Chang et al. [17]). *Neural filters* can be constructed by arranging the input into a tapped delay line, an architecture first proposed by Waibel *et al.* [46]. It is possible to construct similar architectures as shown in Figure 3.1 using a neuron as the memoryless nonlinearity. This form of neural network is called a *synaptic* FIR neural network and requires the use of a *temporal* training algorithm if the output error is used to train the network. The first temporal training algorithm for neural networks can be traced back to Wan [47].

FIR synaptic neural networks belong to a class of *generalized feedforward* (GF) structures, which by definition can have either FIR or IIR filters between nonlinear nodes. GF structures employing IIR synapses are called *locally recurrent globally feedforward* (*LRGF*) structures (Tsoi [48]). Back and Tsoi [49] have shown that models based on local feedback have better convergence and stability behavior than those based on global feedback. In addition to this, if the outputs are obtained after the sigmoid activation function, the usual stability monitoring devices used in the linear IIR case are not necessary due to the bounded outputs from the sigmoids.

3.2 Regressors, Mappings and Definitions

The basic adaptive filter structure, be it linear or nonlinear, is illustrated in Figure 3.2 The adaptive filter is assumed to be discrete in nature. In Figure 3.2 the output $y(n)$ of the adaptive filter is an estimate of the desired signal $d(n)$ when applied with the input $x(n)$. A *feedforward* structure ensures that the output $y(n)$ is a function of the input data $x(n)$ only. A well known example of a feedforward structure is the *finite impulse response* (FIR) filter. A *recurrent* structure on the other hand will generate an output which is dependent on the input data as well as past values of the output $y(n)$. *Infinite impulse response* (IIR) structures are recurrent.

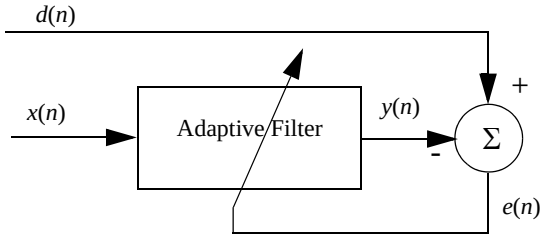

FIGURE 3.2 An adaptive filter.

If we have observation inputs $x(n)$ and outputs $d(n)$ from a dynamical system;

$$\mathbf{x}(n) = [x(n), x(n-1), \ldots, x(1)]^T \quad (3.1)$$

$$\mathbf{d}(n) = [d(n), d(n-1), \ldots, d(1)]^T \quad (3.2)$$

we can state the general nonlinear relationship between past observations $[\mathbf{x}(n-1), \mathbf{d}(n-1)]$ and future system outputs $d(n)$;

$$d(n) = \varphi[\mathbf{x}(n-1), \mathbf{d}(n-1)] + e(n) \quad (3.3)$$

where φ is a general *nonlinear operator.* The additive term $e(n)$ accounts for the fact that the next output $d(n)$ will not be an exact function of the past data. If $e(n)$ is small, we may think of $\varphi[\mathbf{x}(n-1), \mathbf{d}(n-1)]$ as a good *prediction* of $d(n)$, given past data.

The model structure of (3.3) has been found to be too general. It is more useful to construct the nonlinear operator φ as a concatenation of two mappings: one that takes the increasing number of past observations $\mathbf{x}(n-1), \mathbf{d}(n-1)$ and past outputs $\mathbf{y}(n-1)$ and maps them to a finite dimensional vector $\mathbf{u}(n)$, and one that takes this vector to the output space via a nonlinearity. Hence, the output *estimate* at time *n* is simply;

$$y(n) = \varphi[\mathbf{u}(n), \mathbf{w}(n)] \quad (3.4)$$

where,

$$\mathbf{u}(n) = \mathbf{u}(\mathbf{x}(n-1), \mathbf{d}(n-1), \mathbf{y}(n-1)) \quad (3.5)$$

is called the *regression vector*, and its components are referred to as *regressors*, and the vector $\mathbf{w}(n)$ can be thought of as a *weight vector* operating on regression vector $\mathbf{u}(n)$ with a length equal to the choice of regression vector. The choice of nonlinear mapping in (3.4) is thus decomposed into two partial problems for dynamical systems:

1. Selection of the regression vector $\mathbf{u}(n)$ from a finite value of past inputs and outputs.
2. Selection of the nonlinear mapping φ from the regressor space to the output space.

Nonlinear mappings come in a variety of flavors including tensor products, radial basis functions, fuzzy networks, sigmoidal neural networks and wavelets. The ones that are considered in this thesis are;

- *Tensor Product*: The regression vector is put into a *state-expander*, which maps the inputs to a large number of outputs, depending on the size and order of nonlinearity desired. The Volterra and Taylor series expansions are well known examples.
- *Sigmoid Functions*: For the neural networks, a number of possible nonlinear mappings exist, commonly referred to as *activation functions*. A well known mapping is the unit step function.

An alternative to the sigmoid function is the *hyperbolic tangent* activation function, which can output *bipolar* values between 1 and -1;

$$\varphi(v) = \tanh(av) \quad (3.6)$$

where a is a slope parameter, usually set to one. Various combinations of linear and nonlinear functions can also be constructed to obtain tailor-made activation functions (see for example [50] and [51]).

3.3 Linear Models

Multi-input single-output linear structures used in practice can all be summarized by the general family (Ljung [7]);

$$A(z)d(n) = \frac{B_1(z)}{F_1(z)}x(n-k_1) + \ldots + \frac{B_m(z)}{F_m(z)}x(n-k_m) + \frac{C(z)}{G(z)}e(n) \qquad (3.7)$$

where,

$$A(z) = 1 + a_1 z^{-1} + \ldots + a_{n_a} z^{-n_a} \qquad (3.8)$$

$$B_j(z) = b_{0,j} + b_{1,j} z^{-1} + \ldots + b_{n_b,j} z^{-n_b} \qquad (3.9)$$

$$F_j(z) = 1 + f_{1,j} z^{-1} + \ldots + f_{n_f,j} z^{-n_f} \qquad (3.10)$$

m is the number of *exogenous* inputs, *z* is the unit shift operator, and $C(z)$, $G(z)$ have similar forms to $A(z)$. The simplest linear dynamical model is the *FIR* model, sometimes referred to the *moving average* (*MA*) model;

$$\begin{aligned} d(n) &= y(n) + e(n) \\ &= B(z)x(n-1) + e(n) \\ &= b_0 x(n-1) + b_1 x(n-2) + \ldots + b_{n_b} x(n-n_b-1) + e(n) \end{aligned} \qquad (3.11)$$

The various models associated with (3.7) are basically variants of (3.11) using different ways of picking up “poles” of the system and different ways of describing the noise characteristics. A list

of the special cases of the general family is illustrated in Table 3.1.

TABLE 3.1 Special cases of the general linear model.

Name	Acronym	Polynomials
Moving Average	MA	A = C = G= F = 1
AutoRegressive	AR	F=C=G=1, B=0
AutoRegressive with eXogenous input.	ARX	F=C=G=1
Autoregressive Moving Average	ARMA	G = F = 1, B=0
Autoregressive Moving Average with eXogenous input	ARMAX	G = F = 1
AutoRegressive ARX	ARARX	C = F = 1
AutoRegressive ARMAX	ARARMAX	F=1
Output Error	OE	A = C = G= 1
Box-Jenkins	BJ	A=1

The predictor associated with linear models can be given in *pseudo-linear regression* form as;

$$y(n) = \mathbf{w}^T(n)\mathbf{u}(n) \tag{3.12}$$

The regressors typically associated with $\mathbf{u}(n)$ for the systems studied in this thesis are;

- $x(n-k)$ (associated with the *B*-polynomial)
- $d(n-k)$ (associated with the *A*-polynomial)

Linear *State-Space* (*SS*) models can be described as a pseudo-linear regression by constructing a transfer function from the state variables. For more details see Johns *et al.*[52].

The *multi-input ARX* model with two inputs is equivalent to the *Equation-Error* (*EE*) IIR formulation. The *ARMAX* is a one of a family of more sophisticated *EE* model structures including *ARARX* and *ARARMAX* which utilize additional filters for the error signal, however, since they involve a greater number of coefficients they are not considered further.

3.4 Search Methods and Algorithms

The weights in an adaptive filter are adjusted by an algorithm that minimizes some function of the error $e(n)$ between the desired signal $d(n)$ and the filter output $y(n)$. A general form for filter parameter adaptation, for minimization of the *cost function J* is stated below [53];

$$\mathbf{w}(n+1) = \mathbf{w}(n) - \mu(n)\mathbf{P}(n)\nabla_{\mathbf{w}}(J) \quad (3.13)$$

where:

$\mathbf{w}(n)$ and $\mathbf{w}(n+1)$ are the weight vector parameter estimates at time n and $n+1$

$\mu(n)$ is a bounded step size

$\mathbf{P}(n)$ is a matrix obtained from input values that is used to improve the *convergence rate*[1].

J is a function of the prediction error.

$\nabla_{\mathbf{w}}(J)$ is the gradient of the cost function J with respect to the parameter **w,** defined as:

$$\nabla_{\mathbf{w}}(J) = \frac{\partial J}{\partial \mathbf{w}} \quad (3.14)$$

Gradient Search Method. In the gradient search method J is the *mean square error* (MSE) *cost function* defined as:

$$J = E\{e^2(n)\} \quad (3.15)$$

where E is the statistical expectation operator and $e(n) = d(n) - y(n)$. It can be shown (see Widrow [54]) that the optimum weight vector $\mathbf{w}_{opt}$ minimizes J and can be obtained by solving the Wiener-Hopf equation,

1. Convergence rate is defined as the rate at which the MSE approaches the minimum value during the training phase of adaptation.

$$E[\mathbf{u}(n)\mathbf{u}^T(n)]\mathbf{w}_{opt} = E[d(n)\mathbf{u}(n)] \quad (3.16)$$

The corresponding *minimum mean square error* (MMSE) at $\mathbf{w}_{opt}$ equals,

$$\varepsilon_{min} = E[d^2(n)] - E[d(n)\mathbf{u}(n)]^T E[\mathbf{u}(n)\mathbf{u}^T(n)]^{-1} E[d(n)\mathbf{u}(n)] \quad (3.17)$$

Gradient based learning algorithms for FIR and IIR structures are presented in Section 3.4.1 and Section 3.4.2.

Least Squares Search Method. The least squares search method minimizes the sum-squared error (SSE) cost function;

$$J(n) = \sum_{i=t_1}^{t_2} \lambda^{n-i} e^2(n) \quad (3.18)$$

where t_1 and t_2 refer to the index limits over which the cost function is obtained and λ is a forgetting factor, between 0 and 1. *Recursive Least Squares* (RLS) learning algorithms applicable to AEC's are presented in Section 3.4.3.

Conjugate Gradient Search Method. The conjugate gradient (CG) algorithm updates the tap weights of a filter structure with new directions that are "non-interfering", in other words, conjugate to each other. More importantly, the CG algorithm can be applied to both linear *and* nonlinear systems as a method of obtaining improved convergence. The CG learning method is covered in Section 3.4.4.

3.4.1 Gradient Learning Algorithms for FIR Structures

The regression vector $\mathbf{u}(n)$ of an FIR structure contains only *x* inputs, hence we define;

$$\mathbf{u}(n) = \mathbf{x}(n) = [x(n), x(n-1), \ldots, x(n-n_b)]^T \quad (3.19)$$

$$\mathbf{w}(n) = [b_0(n), b_1(n) \ldots b_{n_b}(n)]^T \quad (3.20)$$

By replacing the expectation operator in the true gradient expression in (3.14) with an approximation based on the *instantaneous error*, the gradient now becomes;

$$\begin{aligned} \nabla_{\mathbf{w}}(J) &= \frac{\partial}{\partial \mathbf{w}}(e^2(n)) = 2e(n)\frac{\partial}{\partial \mathbf{w}}[d(n) - y(n)] \\ &= -2e(n)\frac{\partial}{\partial \mathbf{w}}[\mathbf{w}^T(n)\mathbf{x}(n)] = -2e(n)\mathbf{x}(n) \end{aligned} \quad (3.21)$$

Substitution of (3.21) into (3.13) we obtain the general form of the *accelerated steepest descent algorithm* [53].

$$\begin{aligned} y(n) &= \mathbf{w}^T(n)\mathbf{x}(n) \\ e(n) &= d(n) - y(n) \\ \mathbf{w}(n+1) &= \mathbf{w}(n) + \mu(n)e(n)\mathbf{P}(n)\mathbf{x}(n) \end{aligned} \quad (3.22)$$

The factor of 2 in (3.21) has been absorbed into the step size value $\mu(n)$. The matrix $\mathbf{P}(n)$ is chosen based on some *a priori* knowledge to improve the convergence.

LMS Algorithm . If $\mathbf{P}(n)$ is selected as the *identity matrix*, and the step size is fixed in the general formula given in (3.22), then we obtain the *least-mean-square* (LMS) *algorithm*. The LMS filter is stochastic in that it provides an approximation to the Weiner filter as it converges [54]. The tap weight update formula for the LMS algorithm is;

$$\mathbf{w}(n+1) = \mathbf{w}(n) + \mu e(n)\mathbf{x}(n) \quad (3.23)$$

The complete algorithm is described in Appendix D.1.

Normalized LMS (NLMS) algorithm. In the NLMS algorithm, the step size is normalized by the Euclidean norm of the input vector $\mathbf{x}(n)$. This algorithm is appropriate when the input power is unknown or highly variable and is a benchmark standard for AEC applications. The complete algorithm is described in Appendix D.2.

Variable Step Size (VSS) algorithm. Variable step size (VSS) LMS-based algorithms use a large step size when the filter parameters are far from the optimum to achieve fast convergence, and a small step size when the weights are close to the optimum. The VSS algorithm used in this thesis is the Modified VSS algorithm (MVSS) as described by Mayyas [55]. The advantage of the MVSS algorithm over the standard VSS algorithm described in [56] is its relative insensitivity to noisy signals due to the time average autocorrelation process. The complete algorithm is listed in Appendix D.3.

3.4.2 Gradient Learning Algorithms for IIR Structures

There is a rich body of literature on IIR structures that includes direct form [53],[57],[58], lattice form [59], parallel [60], and cascaded [61] structures. Fundamentally there have been two approaches to adaptive IIR filtering that correspond to different formulations of the prediction error. The two forms are *equation error* (*EE*) and *output error* (*OE*) methods.

The difference between the *OE* and *EE* IIR structures in a system identification context is illustrated in Figure 3.3. Each method has its own advantages and disadvantages. The *EE* model gives rise to a *unimodal error surface* with easy stability monitoring, but when the plant signal is con-

taminated with noise σ_n^2, the resulting parameter estimates are biased away from the optimum values which give the MMSE [62]. The *OE* has no such bias, however the error surface is *multimodal* and stability monitoring is non-trivial. As a result, the parameter estimates may converge to a *local minimum* and not necessarily the *global minimum*. Various methods exist which combine the ben-

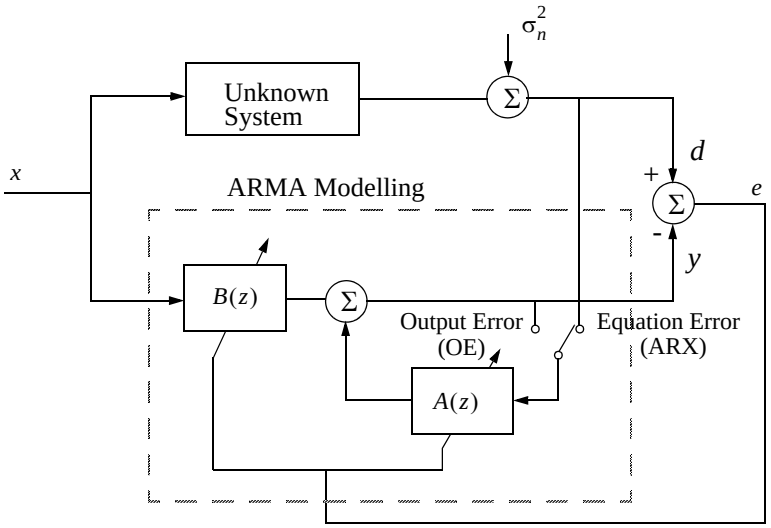

FIGURE 3.3 *EE* and *OE* model structures in system identification.

eficial properties of the *OE* and *EE* methods to provide composite algorithms. These methods are generally referred to *composite error surface* (*CES*) methods. A good example of a CES is the *Steiglitz-McBride Method* (*SMM*) [63]. Other examples of CES methods include the *composite regressor algorithm* (*CRA*) [64] and the *composite gradient algorithm* [65]. Still other methods exist for removing the bias associated with the *EE* method altogether [66], however, these are considered beyond the scope of this thesis.

Equation Error Formulation . The *EE* formulation is characterized by the multi-input *nonrecursive ARX* difference equation with two inputs:

$$y(n) = \sum_{i=1}^{n_a} a_i(n)d(n-i) + \sum_{i=0}^{n_b} b_i(n)x(n-i) \quad (3.24)$$

Note that the output $y(n)$ depends only on the two inputs $x(n)$ and $d(n)$, consequently the weights can be updated using well understood LMS type algorithms. The complete algorithm for the *EE-IIR* structure is listed in Appendix D.6.

Output Error Formulation: The *OE* formulation can be described using the *recursive* difference equation:

$$y(n) = \sum_{i=1}^{n_a} a_i(n)y(n-i) + \sum_{i=0}^{n_b} b_i(n)x(n-i) \quad (3.25)$$

Notice that the output is now dependent on previous outputs $y(n-i)$. The *OE-IIR* algorithm and derivation of the update equations using the simplified gradient is listed in Appendix D.7.

3.4.3 Recursive Least Squares Learning Algorithms

Exponential Recursive Least-Square (RLS) Algorithm . In the general parameter update equation (3.13), if **P** approximates $\mathbf{R}^{-1}$, where **R** is the true *autocorrelation matrix* of the input vector $\mathbf{x}(n)$, defined by;

$$\mathbf{R} = E[\mathbf{x}(n)\mathbf{x}^T(n)] \quad (3.26)$$

and the step size parameter $\mu(n)$ is replaced by;

$$\mu(n) = \frac{1}{1+q(n)} \quad (3.27)$$

where

$$q(n) = \lambda^{-1}\mathbf{x}^T(n)\mathbf{P}(n-1)\mathbf{x}(n) \quad (3.28)$$

is a measure of the signal input power, with a normalization introduced by $\mathbf{P}(n\text{-}1)$, then the convergence time of the algorithm can be reduced substantially even in cases of high eigenvalue spread. This is the basis for the RLS algorithm (λ=1) which is a special case of the *Kalman filter.* The forgetting factor λ reduces the effects of past data over time and therefore improves the ability of the algorithm to track variations in the statistics of the input data. However, this imposes a stability limit on the minimum value of λ. The RLS algorithm for an FIR structure is described further in Appendix D.3. Note that the RLS update may also be applied to the OE-IIR structure as is described in Appendix D.4.

The important property of the RLS algorithm is its *fast convergence*. When the input is time-invariant, the MSE in the RLS algorithm converges in about 2*M* iterations where *M* is the filter order. The RLS algorithm demands a high computational load compared to the LMS algorithm, requiring $O(M^2)$ multiply-adds for each update, and therefore "fast" versions of the RLS (i.e. computationally efficient) have been implemented, as discussed below.

Fast Transversal Filter (FTF) algorithm. The FTF algorithm takes advantage of the redundancies in the standard RLS algorithm to bring the computational load down to $O(7M)$ operations per iteration update. The FTF algorithm suffers from numerical precision problems and is generally viewed as unstable. A method of stabilizing the algorithm, known as the *Stabilized Fast Transversal Filter* (SFTF) mitigates the problem but increases the complexity from $O(7M)$ to $O(8M)$ operations per iteration. A method of improving the tracking capability of the SFTF is by the use of a time varying acceleration factor $\eta(n)$ which effectively modifies the time constants of the algorithm such that the *effective* forgetting factor λ_{eff} varies between λ (when ρ=0) and 0 (when ρ =1).

The accelerated SFTF algorithm used in this thesis was proposed in [67] and [68] and is described further in Appendix D.5.

3.4.4 Conjugate Gradient Learning Algorithms

The conjugate gradient algorithm is obtained by iteratively constructing successive direction vectors that are mutually conjugate and linearly independent as the method progresses (Hestenes [69]). Thus, the directions are determined sequentially at each step of the iteration. At step *k*, one evaluates the current negative gradient vector and adds to it a linear combination of the previous direction vectors to obtain a new conjugate direction vector along which to move.

The CG algorithm has convergence properties that will minimize a quadratic function $f(\mathbf{x})$ of m variables (i.e weights) in no more than m iterations and provide fast convergence. The function $f(\mathbf{x})$ is defined as

$$f(\mathbf{x}) = \frac{1}{2}\mathbf{x}^T\mathbf{Q}\mathbf{x} - \mathbf{b}^T\mathbf{x} \tag{3.29}$$

where $\mathbf{x}$ is of size m and $\mathbf{Q}$ is of size $m \times m$. The approach in the conjugate direction method is to obtain a set of linearly independent direction vectors $\mathbf{d}_0, \mathbf{d}_1, \ldots, \mathbf{d}_{m-1}$ which are conjugate with respect to $\mathbf{Q}$ such that equation (3.29) is minimized. The solution is obtained when $\mathbf{g} = \mathbf{Q}\mathbf{x} - \mathbf{b} = 0$, i.e.,

$$\mathbf{Q}\mathbf{x}_{opt} = \mathbf{b} \tag{3.30}$$

The vectors $\mathbf{d}_0, \mathbf{d}_1, \ldots, \mathbf{d}_{m-1}$ are said to be $\mathbf{Q}$-conjugate if

$$\mathbf{d}_i^T\mathbf{Q}\mathbf{d}_j = 0, \qquad i \neq j \tag{3.31}$$

Conjugate Direction Coefficients α_k**.** The optimum solution vector $\mathbf{x}_{opt}$ minimizes (3.30) where $\mathbf{x}_{opt}$ can be expressed as;

$$\mathbf{x}_{opt} = \alpha_0\mathbf{d}_0 + \alpha_1\mathbf{d}_1 + \ldots + \alpha_{m-1}\mathbf{d}_{m-1} \tag{3.32}$$

and the constants are given by (Luenberger [70]);

$$\alpha_k = -\frac{\mathbf{g}_k^{\mathrm{T}}\mathbf{d}_k}{\mathbf{d}_k^{\mathrm{T}}\mathbf{Q}\mathbf{d}_k} \tag{3.33}$$

where $\mathbf{g}_k = \mathbf{Q}\mathbf{x}_k - \mathbf{b}$. The conjugate gradient algorithm determines the appropriate orthogonal set of direction vectors and constants α_k iteratively and generates a new $\mathbf{x}_k$ according to;

$$\mathbf{x}_{k+1} = \mathbf{x}_k + \alpha_k\mathbf{d}_k \tag{3.34}$$

If the direction vectors $\mathbf{d}_k$ are mutually conjugate and linearly independent, then the initial guess $\mathbf{x}$ will converge to the optimum $\mathbf{x}_{opt}$ after m steps, that is $\mathbf{x}_m = \mathbf{x}_{opt}$.

Conjugate Direction Vectors $\mathbf{d}_k$**.** The initial direction vector is chosen as the negative gradient at the initial point: $\mathbf{d}_0 = -\mathbf{g}_0$. Successive directions are obtained from a linear combination of the current gradient and the previous direction;

$$\mathbf{d}_{k+1} = -\mathbf{g}_{k+1} + \beta_k\mathbf{d}_k \tag{3.35}$$

Given that successive directions must be $\mathbf{Q}$ conjugate, i.e.;

$$\mathbf{d}_{k+1}^{T}\mathbf{Q}\mathbf{d}_k = [-\mathbf{g}_{k+1} + \beta_k\mathbf{d}_k]^{T}\mathbf{Q}\mathbf{d}_k = 0 \tag{3.36}$$

gives the update equation for β_k as

$$\beta_k = \frac{\mathbf{g}_{k+1}^T \mathbf{Q}\mathbf{d}_k}{\mathbf{d}_k^T \mathbf{Q}\mathbf{d}_k} \tag{3.37}$$

Extension to Nonquadratic Problems. The *quadratic approximation* method extends the CG algorithm to general *nonlinear* functions by interpreting (3.29) as a second order Taylor series expansion of the objective function. For details the reader is referred to papers by Johansson *et al.* [71], Charalambous [72], and Boray and Srinath [73]. Essentially, the following associations are made at $\mathbf{x}$;

$$\mathbf{g}_k \leftrightarrow \nabla f(\mathbf{x}_k) \qquad \mathbf{Q} \leftrightarrow \mathbf{F}(\mathbf{x}_k) \tag{3.38}$$

$\mathbf{F}_k(\mathbf{x}_k) = \nabla^2 f(\mathbf{w}_k(n))$ is the $m \times m$ Hessian matrix of the function at $\mathbf{x}_k$, and $\mathbf{g}_k$ is the $m \times 1$ gradient of the function at $\mathbf{x}_k$.

Since the calculation of the hessian $\mathbf{F}$ of a matrix is $O(m^3)$ complexity [74], avoiding the calculation of $\mathbf{F}$ would be advantageous for large order systems. It can be shown (see [73] and p. 138 [69]) that $\mathbf{Q}\mathbf{d}_k = -\mathbf{Q}\mathbf{g}_k = \mathbf{p}_k - \mathbf{g}_k$ where $\mathbf{p}_k = \nabla f(\mathbf{y}_k)^T$ is the gradient at $\mathbf{y}_k = \mathbf{x}_k - \mathbf{g}_k$. Hence, the update equation for the direction constants can be given by

$$\alpha_k = -\frac{\mathbf{g}_k^T \mathbf{d}_k}{\mathbf{d}_k^T \mathbf{Q}\mathbf{d}_k} = -\frac{\mathbf{g}_k^T \mathbf{d}_k}{\mathbf{d}_k^T (\mathbf{p}_k - \mathbf{g}_k)} = \frac{\mathbf{g}_k^T \mathbf{d}_k}{\mathbf{d}_k^T (\mathbf{g}_k - \mathbf{p}_k)} \tag{3.39}$$

In addition, $\mathbf{Q}$ may be eliminated from the expression for β_k to yield [71];

$$\beta_k = \frac{\mathbf{g}_{k+1}^T [\mathbf{g}_{k+1} - \mathbf{g}_k]}{\mathbf{d}_k^T [\mathbf{g}_{k+1} - \mathbf{g}_k]} = \frac{\mathbf{g}_{k+1}^T [\mathbf{g}_{k+1} - \mathbf{g}_k]}{\mathbf{g}_k^T \mathbf{g}_k} = \frac{\mathbf{g}_{k+1}^T \mathbf{g}_{k+1}}{\mathbf{g}_k^T \mathbf{g}_k} \tag{3.40}$$

The first expression is the Hestenes-Stiefel formula for β_k and the second and third expressions are

referred to as the Polak-Ribiere and Fletcher-Reeves formulas respectively.

Using the above expressions, we may obtain a recursive formulae for computing successive α_k and β_k that do not require the computation of **F**. However, the method is based on the Taylor approximation of a general nonlinear function and the **Q**-conjugacy of the direction vectors will deteriorate as the method proceeds. Hence, it is common practise to reinitialize $\mathbf{d}_k$ to $\mathbf{g}_k$ at every *nth* iteration.

Partial Conjugate Gradient Method. The partial conjugate gradient method carries out the conjugate gradient procedure for $k<m-1$ steps [70]. The special case of $k=0$ corresponds to the standard method of steepest descent, while $k=m-1$ corresponds to the full conjugate gradient method. Thus, choosing $k<m$ results in reduced complexity. If equations (3.39) and (3.40) are used to compute the optimum direction and step size, we do not need to compute the Hessian **F.** The penalty is that *two* gradient calculations must be performed per iteration, one at the current value of the vector $\mathbf{x}_k$ and one at $\mathbf{y}_k$. However, since the computation of the Hessian matrix is of order $O(m^3)$ and the calculation of a single gradient is of order $O(m^2)$, the savings are substantial if the filter order m is large and if $k<m$.

We now replace the dependent variable $\mathbf{x}_k$ given above with a set of weights $\mathbf{w}_k(n)$ we obtain the following algorithm, which is based on the method of Partial CG, that does not require the use of a line search or the calculation of the Hessian matrix. Given an initial weight estimate $\mathbf{w}_0$ of length m, the CG algorithm generates the sequence of new weights $\mathbf{w}_1, \mathbf{w}_2, \ldots$ for the network $\varphi(\mathbf{u}(n), \mathbf{w}(n))$ using the following scheme. Note that n refers to the time index and k refers to the conjugate direction count in the sequel.

Conjugate Gradient Algorithm:

Initialization: $\mathbf{w}_0(0)=\mathbf{0}$

For each iteration n, do steps 1,2 and 3.

Step 1. a) Starting with an initial weight vector $\mathbf{w}_0(n)$ compute the following;

$$\mathbf{g}_0(n) = [\nabla f(\mathbf{w}_0(n))]^T \quad (3.41)$$

$$\mathbf{y}_0(n) = \mathbf{w}_0(n) - \mathbf{g}_0(n) \quad (3.42)$$

$$\mathbf{p}_0(n) = [\nabla f(\mathbf{y}_0(n))]^T \quad (3.43)$$

b) set $\mathbf{d}_0(n) = \mathbf{g}_0(n)$

Step 2. Repeat for k=0,1,. . . ,m-1

a) set $\mathbf{w}_{k+1}(n) = \mathbf{w}_k(n) + \alpha_k \mathbf{d}_k(n)$ where α_k is the optimum step size;

$$\alpha_k = \frac{\mathbf{g}_k^T(n)\mathbf{d}_k(n)}{\mathbf{d}_k^T(n)(\mathbf{g}_k(n) - \mathbf{p}_k(n))} \quad (3.44)$$

b) Compute the gradients at the new weight vector $\mathbf{w}_{k+1}$

$$\mathbf{g}_{k+1}(n) = [\nabla f(\mathbf{w}_{k+1}(n))]^T \quad (3.45)$$

$$\mathbf{y}_{k+1}(n) = \mathbf{w}_{k+1}(n) - \mathbf{g}_{k+1}(n) \quad (3.46)$$

$$\mathbf{p}_{k+1}(n) = [\nabla f(\mathbf{y}_{k+1}(n))]^T \quad (3.47)$$

(*c*) Unless k=m-1, obtain the new direction vector

$$\mathbf{d}_{k+1}(n) = -\mathbf{g}_{k+1}(n) + \beta_k \mathbf{d}_k(n) \quad ; \quad (3.48)$$

$$\text{where} \quad \beta_k = \frac{\mathbf{g}_{k+1}^T(n)\mathbf{g}_{k+1}(n)}{\mathbf{g}_k^T(n)\mathbf{g}_k(n)} \tag{3.49}$$

and repeat *Step 2 (a)*.

Step 3. Replace $\mathbf{w}_0(n)$ by $\mathbf{w}_m(n)$ and go back to *Step 1*

β_k gives a measure of the rate of change of successive gradients. If $\beta_k > 1$, then the magnitude of a successive gradient vector is not decreasing, meaning that the minimum has been reached. $\beta_k > 1$ is a termination condition for conjugate direction k in Step 2). The calculation of β_k is done according to the Fletcher-Reeves method rather than the Polak-Ribiere method [70] since it tends to give a smoother convergence.

The CG algorithm can be computationally expensive if real time processing is required, thus simplification techniques exist which can reduce the complexity substantially. This is covered in more detail in Chapter 6.

3.5 Nonlinear Models

In the nonlinear domain, $\varphi \neq 1$. Following the nomenclature for the linear models, it is natural to coin similar names for nonlinear models, for example [75];

- *NFIR*-models, which use only $x(n-k)$ as regressors. Examples include Volterra filters and feedforward neural networks. These are covered in Section 3.6 and Section 3.7.
- *NARX*-models, which use $x(n-k)$ and $d(n-k)$ as regressors. Narendra and Parthasarathy [76] present a *NARX* neural network which they refer to as a series-*parallel* model. A method of selecting the parameters in a neural network NARX model is given by Urbani [77] .

- *NOE*-models. For example, Narendra and Parthasarathy [76] present a *NOE* neural network which they refer to as a *parallel* model.
- *NARMAX*-models. For example Chen and Billings [78] present a general paper on nonlinear identification using the *NARMAX* model. Jang and Kim [9] present a *NARMAX* specifically for identifying a nonlinear loudspeaker.
- *Nonlinear State-Space* (*NSS*) models, that use past components of virtual outputs, i.e. signal values at internal nodes of the network that do not correspond to the output variable. For examples see Gao, [79] and [80].

The adaptive *bilinear* structure [23] [81] can be considered as an NOE or NARX model depending on whether the inputs include $y(n)$ or $d(n)$. Despite its simplicity, the bilinear model is an important nonlinear model since it can be shown (Mohler [82]) that a large class of nonlinear systems can be approximated with arbitrary precision using truncated bilinear system models. However, like the *EE* method, it produces a biased MMSE if $d(n)$ is noisy.

Next, a brief review of the Volterra filter and neural network filter structures is presented.

3.6 The Volterra Filter

The Volterra filter is a general nonlinear feedforward structure that has been successfully applied to identifying low order nonlinear systems. The Volterra filter is a *polynomial* structure with an output that results from a summation of homogenous systems each with consecutive degrees. A homogenous system of degree k yields an output $a^k y_k(n)$ for an input $ax(n)$ where $y_k(n)$ is the response to $x(n)$. The output $y(n)$ of a nonlinear process can be approximated by a truncated Volterra series;

$$y(n) = h_0 + \sum_{m_1=0}^{N_1} h_1(m_1)x(n-m_1) + \sum_{m_1=0}^{N_1}\sum_{m_2=0}^{N_2} h_2(m_1, m_2)x(n-m_1)x(n-m_2) + \ldots + \sum_{m_1=0}^{N_1} \ldots \sum_{m_k=0}^{N_p} h_p(m_1, m_2, \ldots, m_p)x(n-m_1)x(n-m_2)\ldots x(n-m_p) \quad (3.50)$$

where $h_p(m_1, m_2, \ldots, m_p)$ denote the so called *p-th* order *Volterra kernels* of the system and $N_1, \ldots, N_p$ represent the orders of the nonlinear sections. For the purposes of this discussion, we have dropped the time dependence on *n*. We will also assume that the kernels $h_2(m_1, m_2), h_3(m_1, m_2, m_3), \ldots, h_k(m_1, m_2, \ldots, m_k)$ are symmetric, i.e. that the indexes are exchangeable. Define the *p-th* order Volterra kernel vectors and *p-th* order input space regression vectors at time *n*;

$$\mathbf{h}_p(n) = [h_p(m_1, m_1, \ldots, m_1), h_p(m_1, m_1, \ldots, m_2), \ldots, h_p(m_p, m_p, \ldots, m_p)]^T \quad (3.51)$$

$$\mathbf{x}_p(n) = \mathbf{x}_1(n) \otimes \mathbf{x}_{p-1}(n) \quad (3.52)$$

where $\otimes$ is the Kronecker product of vectors and it is assumed that the duplicate terms have been removed. We may rewrite (3.50) as a vector product of an *extended* weight vector and regressor;

$$y(n) = h_0 + \mathbf{h}_1^T(n)\mathbf{x}_1(n) + \ldots + \mathbf{h}_p^T(n)\mathbf{x}_p(n) = \mathbf{h}_e{}^T(n)\mathbf{x}_e(n) \quad (3.53)$$

where

$$\mathbf{h}_e{}^T(n) = [h_0, \mathbf{h}^T{}_1(n), \ldots, \mathbf{h}_p^T] \quad (3.54)$$

$$\mathbf{x}_e{}^T(n) = [1, \mathbf{x}^T{}_1(n), \ldots, \mathbf{x}_p^T] \quad (3.55)$$

We can see from (3.53) that the first term is the DC component of the output, and the subsequent terms are the linear, quadratic, cubic, up to the *p-th* order polynomial components of the output respectively, and that for *p=1*, we obtain the linear FIR filter. The structure is illustrated in Figure 3.4.

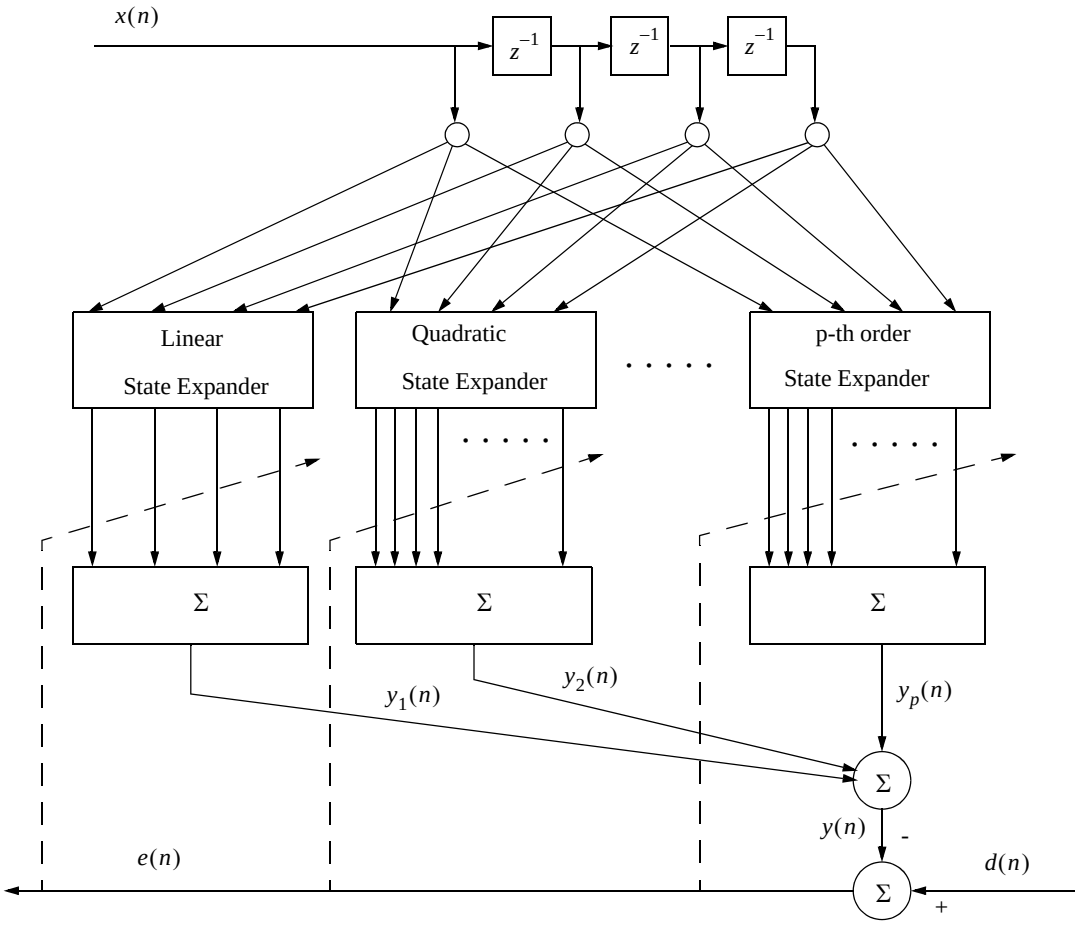

FIGURE 3.4 An adaptive Volterra filter structure consists of a number of homogenous systems operating on extended input vectors. The extended inputs are calculated using the tensor product nonlinear mapping strategy.

3.6.1 Performance Surfaces

There is a super-linear increase in the eigenvalue spread of the performance surface for nonlinear models, which limits the convergence when gradient search techniques are used to update the tap weights. RLS versions of the Volterra algorithm can be used to mitigate this problem (See for example Mathews [23]), however, for large filter orders the complexity is prohibitive. Figure 3.5 (a) and (b) show the structure of a linear and nonlinear filter, each consisting of two taps. The performance surfaces for the two models are plotted in Figure 3.6.

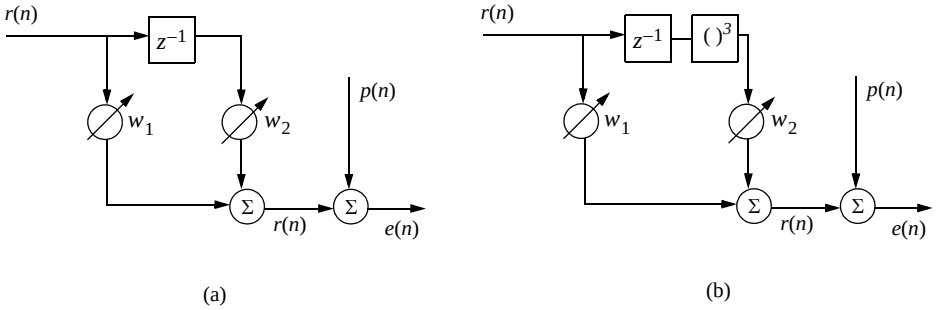

FIGURE 3.5 (a) Linear filter with two weights. (b) Nonlinear filter with two weights.

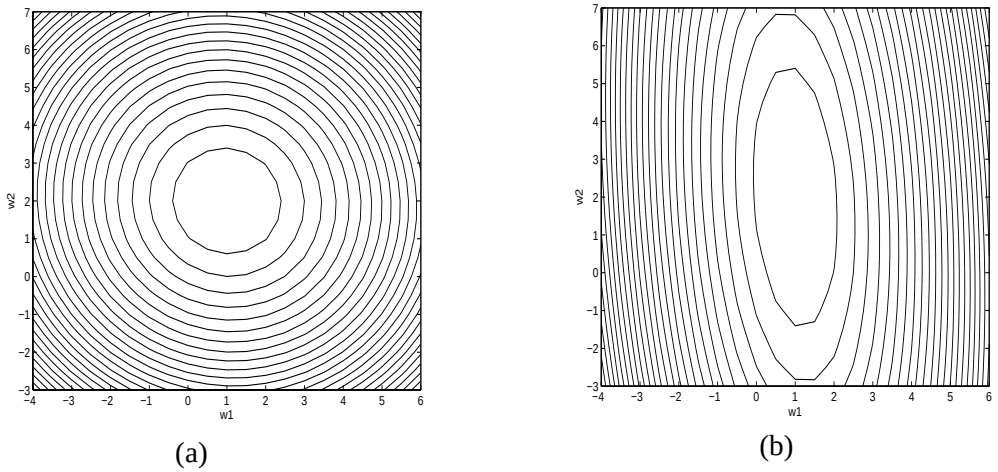

FIGURE 3.6 Error performance surface (a) Linear model. (b) Nonlinear model has elliptical performance surface.

The unknown system to be identified has the same structure, with optimum weights chosen as w_1=1, w_2=2. It can be seen from the results that the performance surface for the nonlinear model has an elongated bowl shape, which will result in an increased eigenvalue spread. For filtered or coloured inputs, this elongation of the performance surface becomes more acute.

3.6.2 Adaptive Learning Algorithm

Analogous to linear filter theory, the optimum coefficients solve the *extended* Wiener-Hopf equations:

$$E[\mathbf{x}_e(n)\mathbf{x}_e^T(n)]\mathbf{h}_e(n) = E[d(n)\mathbf{x}_e(n)] \quad (3.56)$$

The corresponding LMS adaptive updating of the *p-th* order coefficients is performed according to the following equations;

$$\mathbf{h}_p(n+1) = \mathbf{h}_p(n) + \mu_p e(n)\mathbf{x}_p(n) \quad (3.57)$$

where μ_p is the step size for the *p-th* power term. The corresponding Volterra minimum MSE can be computed from;

$$\varepsilon_{min} = E[d^2(n)] - E[d(n)\mathbf{x}_e(n)]^T E[\mathbf{x}_e(n)\mathbf{x}_e^T(n)]^{-1} E[d(n)\mathbf{x}_e(n)] \quad (3.58)$$

which includes the linear MMSE in the case *p*=1. A summary of the LMS-Volterra algorithm is given in Appendix D.8.

The advantages of using the Volterra filter is that linear adaptive filter theory can be applied to the extended vectors for on-line adaptation. As well, the MSE surface space does not contain any local minima, because the filter output depends linearly on the extended coefficients. However, the disadvantages are that the dimension of the extended input vector $\mathbf{x}_e(n)$ becomes very large for larger

filter orders, and thus slows the convergence time. The dimension of the extended vector $\mathbf{x}_e(n)$ can be calculated from the following formula;

$$dim(\mathbf{x}_e) = dim(\mathbf{h}_e) = \sum_{l=0}^{p} \binom{N_l + l - 1}{l} \quad (3.59)$$

For example, a 3rd order Volterra system with $N_1 = N_2 = N_3 = 50$ will have 23,425 elements in $\mathbf{h}_e(n)$, and this assumes that combinations such as $h_2(2,3)$ and $h_2(3,2)$ are counted as one value! With this in mind, it is important to weed out as many non-essential terms as possible, in order to simplify the structure.

IIR and higher order systems. Several new methods have recently been proposed to model general higher order systems using lower order subsystems. For example, a parallel cascaded truncated Volterra system has been proposed in [83] as a method to combine lower order systems to approximate a much higher order Volterra system. Also, a recent paper [84] presents a second order Volterra infinite impulse response (IIR) structure for modelling sinusoidal harmonics, however, when applied to real-world data consisting of engine and vibration signals, the net gains were marginal compared to the second order Volterra finite impulse response (FIR) structure.

Stability and Convergence. It can be shown in linear adaptive theory that the values of the coefficients converge if the step sizes μ_p are chosen such that $0 < \mu_p < 2/\lambda_{max}$ where λ_{max} is the maximum eigenvalue of the autocorrelation matrix of the extended input vector $\mathbf{x}_e(n)$. The problem for nonlinear filtering is that the eigenvalues spreads are in general very large. *Even when the input signal is white, the presence of nonlinearities in the input vector will cause the eigenvalue spread to be more than one*. Consequently, algorithms and structures that have convergence behaviors that are independent of (or less dependent on) the statistics of the input signal are often used. It is pos-

sible to apply the RLS update operator to the extended weights (Mathews [23]), however there is a corresponding increase in complexity. An alternate method for improving the convergence rate using the LMS update is the *variable step size* algorithm for Volterra filters, proposed by Sicuranza [85].

3.7 Multilayer Perceptron Neural Networks

A multilayer perceptron (MLP) neural network can solve certain complex problems more accurately than linear techniques if the underlying physical mechanism responsible for the process output is inherently nonlinear. Neural networks may also be more applicable than polynomial filters to real-life systems since rarely in nature does the output of a nonlinear system increase without bound for increasing inputs. Most physical systems will exhibit some form of clipping or limiting before this happens.

The neuron constructs a nonlinear mapping from the regression space to the output space via a nonlinear activation function. There are an infinite number of possible candidate activation functions, however, the most widely used are the *linear model*, the *McCullough-Pitts model* characterized by a threshold function, the *piece-wise linear model*, characterized by a linear function which is clipped beyond a defined linear range, and the *sigmoid* function.

Consider a multilayer feedforward neural network filter as shown in Figure 3.7. The activation level at the input to the sigmoidal nonlinearity of neuron j in layer l+1 is;

$$s_j^{(l+1)}(n) = \sum_{i=0}^{N_l} w_{ij}^{(l)}(n) x_i^{(l)}(n) \qquad (3.60)$$

where $x_i^{(l)}(n)$ represents the output from the previous layer and is the input to weight elements

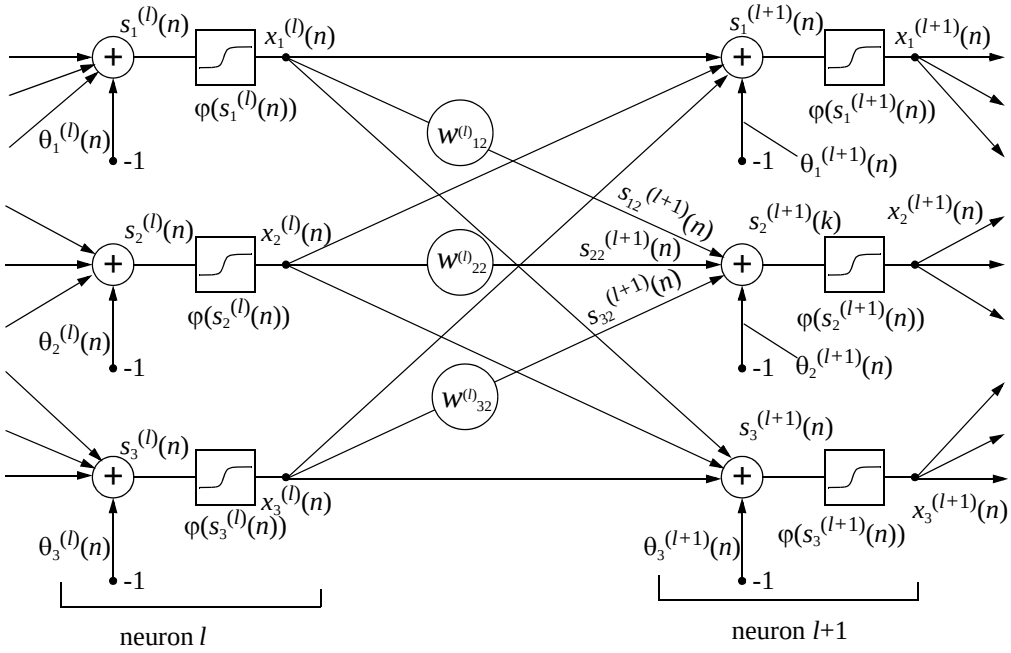

FIGURE 3.7 Forward signal propagation in a neural network. The single weight values θ are the bias weights.

$w_{ij}^{(l)}(n)$ at time n and N_l is the number of nodes in layer l. The output of node j in layer l is;

$$x_j^{(l)}(n) = \varphi(s_j^{(l)}(n)) \tag{3.61}$$

where φ represents the nonlinear activation function. The MLP output for node j in the output layer is

$$y_j(n) = x_j^{(L)}(n) \tag{3.62}$$

3.7.1 Backpropagation Learning Algorithm

The basic mechanism behind *supervised* learning rules is to update the network weights and bias terms until the MSE between the network output y and desired target signal d is minimized to below a predetermined level. The *backpropagation* (*BP*) *algorithm* [86] is a supervised learning algorithm based on propagating errors through to hidden nodes using an instantaneous gradient

estimate. For the on-line training mode, the instantaneous cost function J_{inst} at time n is defined as;

$$J(n) = J_{inst}(n) = \frac{1}{2}e^2(n) = \frac{1}{2}\sum_{i=1}^{N_L} e_i^2(n) \quad (3.63)$$

where;

$$e_i(n) = d_i(n) - y_i(n) \quad (3.64)$$

is the error signal at time n and $y_i(n)$ and $d_i(n)$ represent the output and desired signals respectively for the output of a neuron *i.* $N_L = 1$ for a network with a single output. The backpropagation algorithm attempts to minimize the J by the delta rule [87]for the vector $\mathbf{w}$ by incrementing at each step toward the optimum vector using the negative gradient at that point;

$$\mathbf{w}(n+1) = \mathbf{w}(n) - \mu\frac{\partial J}{\partial \mathbf{w}} \quad (3.65)$$

where μ is a fixed step size and $\mathbf{w}$ is a vector consisting of all the weights in the network

$$\mathbf{w}(n) = [w_{11}^{(1)}(n), w_{12}(n), \ldots, w_{m_1 n_1}^{(1)}(n), \ldots w_{m_L n_L}^{(L)}(n)] \quad (3.66)$$

Details of the derivation of the BP algorithm can be found in Pao [88] or Haykin [87]. The complete update algorithm can be expressed as follows;

$$w_{ij}^{(l)}(n+1) = w_{ij}^{(l)}(n) - \mu\delta_j^{(l+1)}(\dot{n}) \cdot x_i^{(l)}(n) \quad (3.67)$$

$$\delta_j^{(l)}(n) = \begin{cases} -2e(n)\varphi'(s_j^{(L)}(n)) & \ldots l = L \\ \varphi'(s_j^{(l)}(n)) \cdot \sum_{k=1}^{N_{L+1}} \delta_k^{(l+1)}(n) \cdot w_{jk}^{(l)}(n) & \ldots 1 \le l \le L-1 \end{cases} \quad (3.68)$$

where;

$x_i^{(l)}(n)$ represents the output from node *i* in layer *l*,

$w_{jk}^{(l)}(n)$ represents the weight connecting node *i* in layer *l* to node *j* in layer *l+1*

$s_j^{(l)}(n)$ represents the input activation to node *j* in layer *l*

φ'( ) represents the derivative of the sigmoid function

$\delta_j^{(l)}(n)$ represents the local gradient "delta" term of node *k* in layer *l*.

L is the total number of layers in the network

n is the time index

μ is the step size parameter

The backpropagation terms are illustrated in Figure 3.8.

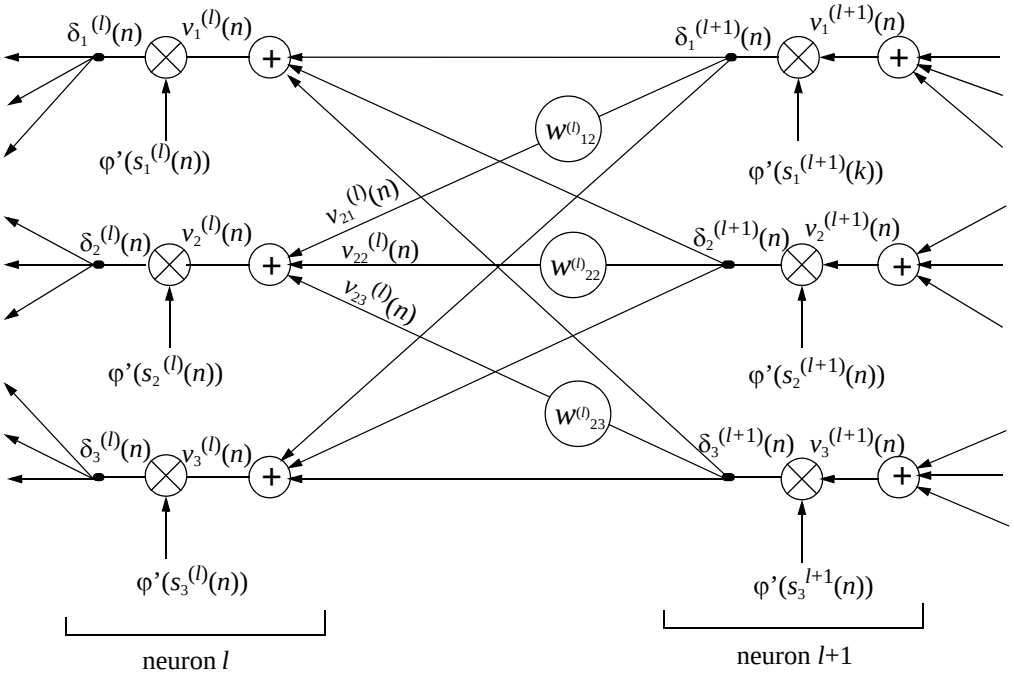

FIGURE 3.8 Backward error propagation.

3.7.2 Enhanced Backpropagation Methods

One of the simplest and most popular methods for enhancing the speed of convergence of the BP method is to apply momentum [86] to the weight updates according to,

$$w_{ij}^{(l)}(n+1) = w_{ij}^{(l)}(n) + \alpha[w_{ij}^{(l)}(n) - w_{ij}^{(l)}(n-1)] - \mu\delta_j^{(l+1)}(\dot{n}) \cdot x_i^{(l)}(n) \qquad (3.69)$$

where $0 < \alpha < 1$ is called the momentum constant. Essentially, a small amount of the previous weight value is added to the current weight update. This has the effect of stabilizing oscillating weight updates and accelerating weight updates which have the same sign [89].

The Kalman algorithm may be applied to neural networks to improve convergence rates in the same way that the RLS can speed up convergence rates for FIR based structures. The *Enhanced Backpropagation* (EBP) method [90][91] divides the MLP into a number of linear subsystems for each layer and invokes the RLS (or linear Kalman filter algorithm) to update the weights so as to minimize the error in each layer with respect to the activation potential into each neuron. All neurons in the same layer have the same input vector **x**(*n*) and only one **P** matrix per layer is required.

The *Extended Kalman Algorithm* (EKA) on the other hand divides the MLP into a number of nonlinear subsystems and minimizes the error at the neuron output [91][92][93]. The activation function output is linearized by using a Taylor series expansion about the current weight estimate. Each neuron perceives its own “linearized” input and therefore must also maintain its own copy of **P** even if the input **x**(*n*) is shared with other neurons. This leads to higher computational and storage cost [94] compared to the EBP algorithm, but also provides superior performance [91].

Enhanced BP methods are attractive for enhancing convergence in certain classification problems and for inputs that have a large eigenvalue spread. In the linear domain, RLS algorithms have

poorer tracking ability than algorithms based on instantaneous gradient estimates (for example LMS), when operating in low SNR conditions [95]. The fact that the RLS algorithm is used to train the weights may cause poorer tracking ability than the conventional BP algorithm, however, the author could find no results presented in the literature to confirm this hypothesis. It may also be possible to enhance EKA based algorithms with an acceleration factor similar to the one used in the accelerated SFTF algorithm used on linear FIR structures.

3.8 Summary

In this chapter, the principles and adaptation techniques of linear and nonlinear adaptive filters were reviewed. A brief survey of the research work in this area and some applications were presented. Following a discussion of the adaptive FIR and IIR filter, the gradient based search technique was presented including the LMS, NLMS, MVSS algorithms, as well as the EE-IIR and OE-IIR LMS variations for IIR filters. The least squares search techniques presented included the exponential RLS and SFTF algorithms, including the RLS update as applied to the OE-IIR filter. The third search technique presented was the conjugate gradient algorithm. The theory of Volterra filters and the LMS based training technique were next covered, followed by neural network filters and the celebrated gradient backpropagation algorithm.

Chapter 4
Acoustic Echo Cancellation

This chapter contains six major subsections. Section 4.1 introduces the acoustic echo control problem in HFT's and presents performance requirements. Section 4.2 presents the physical test system used to obtain the field data, including precautions taken to prevent impaired measurements. Section 4.3 investigates the use of IIR for AEC's. Section 4.4 investigates the performance limitations of AEC's including both physical and algorithmic factors, with supporting analysis, simulations and experimental test results. Section 4.5 presents results on the effects of enclosure vibrations and rattling with a typical HFT. Section 4.6 determines how transducer nonlinearities affect the performance of linear algorithms, and finally a summary is presented in Section 4.7.

4.1 The Handsfree Telephone Problem

The basic objective of a handsfree AEC is to provide ease of communications for conversational purposes by allowing the user to move about freely in his or her environment without any loss in speech quality. However, acoustical feedback and echoes are major sources of annoyance in conversations using HFT's, hence a method of controlling echo is needed. Figure 4.1 shows a hands-

free telephone set intended for *full-duplex* operation. The microphone or *primary* signal, is a summation of the received echo, room noise and *near end speech* signal. The HFT contains two echo control devices. The first is a *hybrid echo canceller* which removes echoes that leak through the imperfect 2-to-4 wire hybrid coupler, as well as reflections from the line. The second is an *acoustic echo canceller* which removes part or all of the acoustic signal coming from the loudspeaker, including echoes from the environment. Hybrid echo characteristics can change from call to call, and acoustic echo characteristics are affected by any movements within the immediate surroundings, hence it is necessary to implement *adaptive filter* to cancel the echoes. However, the task of acoustic echo cancellation is a far more difficult task than hybrid echo cancellation for the following reasons:

- The hybrid echo characteristics are typically *stationary* on a per-call basis, whereas the acoustic echo path is affected by any movements within its surroundings. This means that dynamic tracking is extremely important in AEC's.
- The acoustic echo duration is far greater than the hybrid echo duration, typically by an order of magnitude, possibly up to a few hundred milliseconds in large rooms. This means that filter structures with a long memory (i.e. filter order) are required in AEC applications.
- The hybrid is well modelled by a *linear* system whereas the acoustic path has at least one *non-linear* component (the loudspeaker), as well as other components that are difficult to model, for example air turbulence in the vicinity of the microphone and vibration and resonances within the HFT enclosure.
- The magnitude of the coupling between the loudspeaker and microphone is significant and results from a direct path through the air and the enclosure itself. The desired speaker signal is usually much smaller in magnitude than the signal to be cancelled. In hybrid echo cancellation, this large acoustical coupling is absent.
- The magnitude of the background noise in a room can be significant, whereas in hybrid systems, the noise level is usually much less severe.

The effects of the above differences limit the performance of acoustic echo cancellers compared to hybrid echo cancellers. Typically, 70 dB of echo cancellation can be achieved in practice for hybrids [96] whereas 25 dB seems to be the current practical limit to the achievable acoustic echo cancellation [1][95][97][98]. To be commercially attractive and audibly nonintrusive, HFT's should achieve echo cancellation levels of at least 30 dB in times of less than 100 ms [1] with voice signals using reasonably priced *digital signal processors* (DSPs). The state-of-the-art in AEC's for handsfree terminals cannot yet reach this goal and as a result it has been a hotbed of on-going research for many years. A complete background survey in this area is beyond the scope of this chapter, however, references [99], [100] and [101] provide an exhaustive summary of over 100 technical papers.

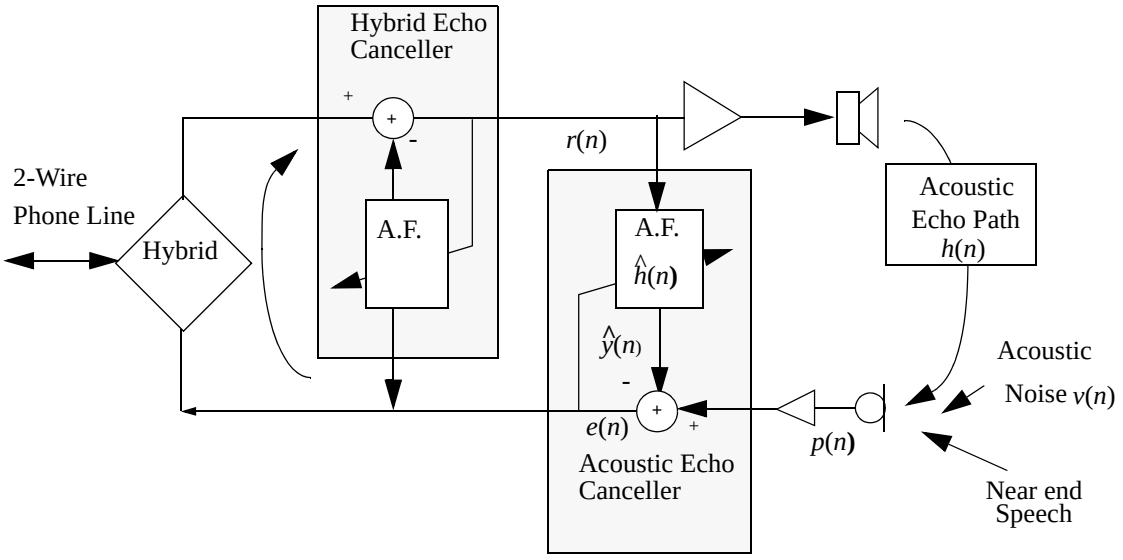

FIGURE 4.1 Echo cancellation in the handsfree environment. The hybrid echo canceller is shown on the left and the acoustic echo canceller is shown on the right. The echo replica $\hat{y}(n)$ is subtracted from primary signal $p(n)$ to give the error signal $e(n)$.

1. Internal correspondence with Nortel.

4.1.1 Performance Requirements

Objective Requirements. A commonly used AEC performance metric is the steady-state *Echo Return Loss Enhancement* (ERLE) during *single talk mode,* i.e. when the near end speech is absent, and is defined by [102];

$$ERLE(dB) = \lim_{N \to \infty}\left[10\log\frac{E[p^2(n)]}{E[e^2(n)]}\right] \approx 10\log\left[\frac{\sigma^2_p}{\sigma^2_e}\right] \approx 10\log\left(\frac{\sum_{r=0}^{n_w}[d(n-r)]^2}{\sum_{r=0}^{n_w}[e(n-r)]^2}\right) \quad (4.1)$$

where σ^2_p and σ^2_e refer to the variances of the primary and error signals respectively and E is the statistical expectation operator. For on-line measurements, the later expression in (4.1) is used to compute the ERLE at time n where n_w is the size of the window average, nominally set to 500.

The ERLE value provides a measure of how much the echo is attenuated in the absence of measurement noise, however, the value obtained from (4.1) includes the effects of both the *acoustical isolation* between the loudspeaker and microphone, and the electrical modelling accuracy. For example, an infinite ERLE can be obtained with *either* a perfect electrical model in the AEC portion or 100% acoustic isolation between the loudspeaker and microphone. Generally, the physical ERLE value recorded is a combination of the two mechanisms. In addition, a large uncorrelated noise component in the primary signal will also affect the ERLE value so some caution should used when using ERLE as the primary objective measure of modelling performance. Objective performance standards may be found in [103] through [108] which are summarized as follows;

TABLE 4.1 Objective performance requirements for handsfree telephones.

Quantity	Description	Value
TIC	Initial convergence time	1 sec, 20 dB
TRDT	Recovery time after double talk	1 sec, 20 dB
TCLWPV	Echo loss during echo path variation	>10 dB
TRPV	Recovery time after echo path variation	1 sec, 20 dB
TCLWST	Echo loss in single talk	>45 dB
TCLWDT	Echo loss in double talk mode	>25 dB
ARDT	Received speech attenuation in double talk mode	>6 dB
ARST	Transmitted speech attenuation in double talk mode	>6 dB
DRST	Received speech distortion in double talk mode	currently under study
DRDT	Transmitted speech distortion in double talk mode	currently under study
TONST	Break-in time in single talk mode	20 ms, 3 dB
TONDT	Break-in time in double talk mode	20 ms, 6 dB

The attainable *early-to-late ratio*[1] (ELR) is another objective performance measure which is defined as the ratio of energy received before 40 ms to that received after. A high ELR is subjectively more pleasing than a low ELR.

Subjective Requirements. Very little work has been done to correlate objective criteria and subjective test results with regard to acoustic echo control [109]. Quantities such as naturalness of transmitted speech and quality of conversation with regard to ease of speaking and interruption are not well defined in the literature, although these are most important to the user. The echo cancellation level *subjectively* required for HFT's depends highly on the environment. For example, in [110] an assessment is performed in audio teleconferencing environments, where for an overall round trip delay time of 100 ms and a reverberation time of 400 ms, 40 dB of acoustic echo cancellation is considered necessary. Experiments on the minimum detectable delay of speech (assuming a single

1. Performance metric at Nortel.

echo) confirm that 23 ms seems to be the detectable limit [111] and that human sensitivity to the echo signal *increases* as the delay between the original and echo signal increases. Mean opinion scores on speech signals also degrade with increased echo delay (i.e. lower ELR). Experimental results in [109] show that the annoyance due to acoustic echo level is strongly dependent of the background noise level, and that the annoyance of the background noise subjectively *masks* the echo. Additional results presented in [112] for automobile interiors show that echoes are attenuated approximately 1 dB for every 1 ms of delay which means that by the time the echo is perceivable, it has already become attenuated by at least 20 dB. It would appear that given this information, the AEC problem (in automobiles) is of secondary importance with respect to noise cancellation. In the context of improving the subjective quality of HFT's, both speech enhancement (i.e. noise and distortion reduction) and echo cancellation should therefore be taken into account for obtaining an overall quality enhancement. However, where noise reduction can be achieved with linear systems, distortion reduction usually requires a nonlinear architecture.

Implications for HFT Design. High figures of ERLE up to 45 dB are often proposed in the case of large transmission delays (See Table 4.1) however, since current technology/algorithms are generally unable to provide such high attenuation, additional *variable losses* in the receive and/or transmit path are frequently used. *More importantly, there seems to be no mention of how physical limitations such as loudspeaker nonlinearity will affect the practical achievement of such high ERLE values without the inclusion of additional losses.* In terms of achieving both a subjectively pleasing speech quality and the specifications listed in Table 4.1 it would appear necessary to accommodate the nonlinearity of the loudspeaker model into the AEC design.

4.1.2 Acoustic Reverberation in Rooms

In this section we investigate the characteristics of acoustic reverberation in rooms, and how it impacts on the architecture of AEC's.

Reverberation Time. The reverberation time T_{60} is defined as the length of time necessary for all reflections in a room to decay by 60 dB [113];

$$T_{60} = \frac{6.91}{\delta} = \frac{-13.8}{c\left(\frac{1}{L_x} + \frac{1}{L_y} + \frac{1}{L_z}\right)\ln\beta} \quad (4.1)$$

where δ is the average damping constant of all surfaces in the room, $c \approx 340$ ms is the speed of sound in air and L_x, L_y, L_z are the *x,y,z* room dimensions[1]. β is the reflection coefficient varying between 0-1. More importantly, β has a *frequency dependence*; generally low frequencies have a higher reflection coefficient than higher frequencies for most reflecting surfaces. Values of T_{60} can range from 0.3s (living rooms and furnished conference rooms) up to 10s (large churches). For an AEC in a typical conference room operating with a sample rate of 8kHz, this means that (in the absence of other limitations) up to *several thousand* taps are required to obtain 40-60 dB echo cancellation.

Vibrational Modes. In a rectangular room, the number of vibrational modes N in the frequency range from 0 to f is given by [113];

$$N = \frac{4\pi}{3}V\left(\frac{f}{c}\right)^3 + \frac{\pi}{4}S\left(\frac{f}{c}\right)^2 + \frac{L}{8}\left(\frac{f}{c}\right) \quad (4.2)$$

where V is the volume of the room, S is the area of all walls, L the sum of all edge lengths of the walls of the rectangular room. For example: for a room with dimensions L_x=3m, L_y=4m and

1. Equation (4.1) is intended for regularly shaped rooms free of furniture and people.

L_z=5m, the number of *eigenfrequencies*[1] in the range [0, 3.4 kHz] is 247787. Since this number represents *half* the number of poles necessary to *completely* model the physical phenomenon exactly, it is obvious that exact cancellation would require an extremely complicated architecture. *Acoustic reverberation is so complicated that it can only be investigated under statistical considerations.* The number of acoustic modes in the audiofrequency range is much greater than the coefficients available to obtain a 40-60 dB ERLE typically demanded of an AEC. Fortunately, the eigenfrequencies are highly overlapped and therefore they can be reduced to statistical averages to provide a much more parsimonious number of modes [114]. It has been observed that the frequency response of typical rooms are composed of a sequence of maxima and minima spaced roughly 5 Hz apart. The average frequency spacing of adjacent maxima can be calculated using Rice's formula $(\Delta f_{max}) = \delta/(\sqrt{3})$ [115]. If we model each maximum/minimum pair by a 2nd order IIR filter section consisting of 5 free parameters each, the total number of parameters to model the range [0-3.4 kHz] assuming a 5 Hz spacing is approximately 3400. This is far less than described by (4.2) however, it is still quite large.

Temporal Distribution of Reflections. The temporal nature of a reverberant signal in a room can be obtained by using the method of room images [113]. The resulting temporal density of reflections N_R arriving at time t is;

$$\frac{dN_R}{dt} = 4\pi\frac{c^3t^2}{V} \tag{4.3}$$

T_{60} and N_R can be used to generate realistic simulated room impulse responses and is one of the methods used in simulations presented in this thesis.

1. Eigenfrequencies are the solutions to the room wave equation and can be thought of as vibrational modes (or frequencies) for which a standing wave will exist in a rectangular room with rigid boundaries.

4.2 Experimental Set-up

The measurement setup used in this thesis is shown in Figure 4.2. A modified speakerphone[1] is positioned in either an anechoic chamber or a conference room and excited with either bandlimited white noise or speech depending on the conditions desired. Noise was generated using a General Radio Company 1390-B Random Noise Generator. Artificial speech recordings were provided by Bell Northern Research and reproduced using a Sony TC-D7 Digital Audio Tape (DAT) recorder. The source signal selected was then filtered to the telephony bandwidth (200Hz to 3400Hz) with a cascade of two National Semiconductor TP3040 switched capacitor filters to provide greater than 60dB of stopband attenuation. The loudspeaker of the modified phone was driven with an amplified version of this filtered excitation signal. The amplification was accomplished with a 75W dual-channel Samson Servo-150 studio-quality power amplifier. The output level of the amplifier can be varied to provide a *sound pressure level* (SPL) anywhere from 60 dB to 100 dB as measured 0.5m directly above the loudspeaker, depending on the HFT used. Conference room dimensions and layouts may be found in Appendix A. A listing of the equipment used and relevant parameters may be found in Appendix B.

A set of pre-conditioning circuits were used to attenuate the reference signal, and amplify the primary microphone signal to equate their levels at the DAT's inputs. Both circuits are based on the Analog Devices AD524 instrumentation amplifier. A separate high quality microphone was sometimes used to bypass the electret microphone in order to remove enclosure vibration and coupling effects. The primary and reference signals were recorded to DAT using a Teac DA-P20 DAT recorder at a level of approximately -6 dB with noise, and a peak level of -6dB with speech. The data was later downloaded to a personal computer workstation (PC) for off-line processing by res-

1. Each phone is modified to allow access to the internal loudspeaker and microphone terminals.

ampling the data at 16kHz with an Ariel DSP-96 card. The data vectors were then issued to a variety of adaptive filtering programs written specifically for this thesis in Matlab and C. Schematics of various circuits used in the experimental setup can be found in Appendix C.

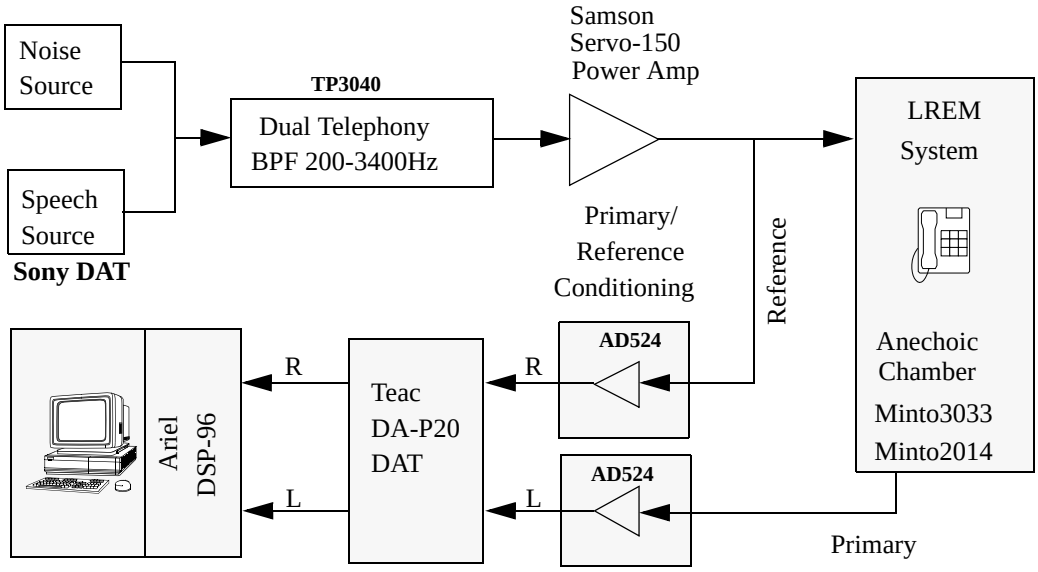

FIGURE 4.2 Block diagram of the experimental setup

Several commercially available HFT's are used in the experiments (refer to Appendix B for a list of HFT and transducer parameters). The HFT under test is placed either on top of a conference table (conference room recording) or on a 1m square board on the floor of an anechoic chamber (anechoic recording). Measurements were made with a number of modified handsfree terminals and separate microphone and loudspeaker components. By separating the loudspeaker and microphone, different quality loudspeakers can be tested for linearity, and in addition, the coupling between the loudspeaker and microphone due to the enclosure effects can be removed.

Loudspeakers tested outside of a handsfree terminal enclosure in this way were mounted in a standard baffle made of 3/4 inch plywood with the loudspeakers placed as indicated in Appendix A,

Figure A.3. For quick recordings in the lab, a noise shielding box was constructed consisting of two boxes, one inside the other to provide noise immunity from the external environment. It was constructed with 0.25 inch thick cardboard with corrugated foam glued to both the inside and outside surfaces. The box provided 21.9 dB of sound attenuation, however, some reverberation was still observed at 100 ms.

Impulse response measurements are obtained experimentally by averaging the weight values over the last few thousand samples of a 4 second data file. The reference excitation in this case is filtered noise, with amplitudes varying between 55 dB and 100 dB sound pressure level (depending on HFT used and measurement desired) as measured 0.5 m from the loudspeaker. Results obtained using HFT #1 in anechoic and conference room environments are shown in Figure 4.3.

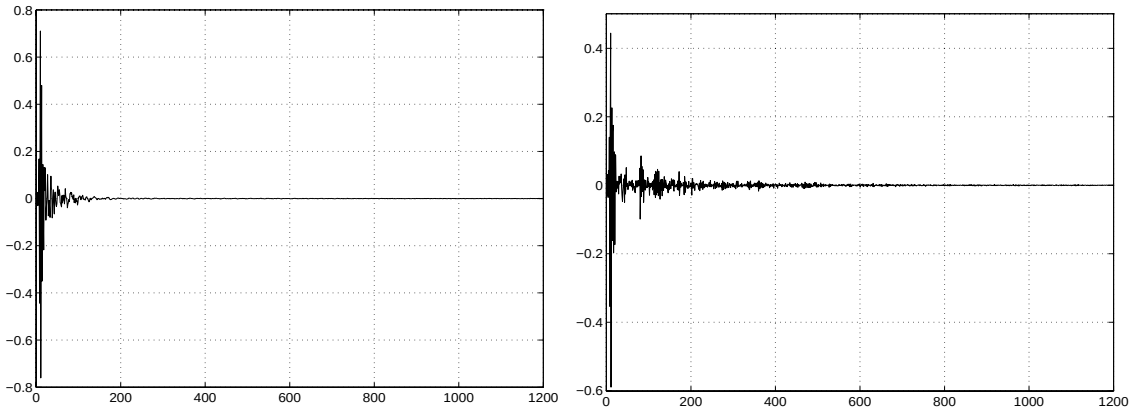

(a) (b)

FIGURE 4.3 HFT#1 impulse responses. (a) as measured in the anechoic chamber (b) as measured in conference room #2 .

4.2.1 Considerations for Practical Problems

There were many practical problems associated with obtaining good measurements with the experimental setup. These problems included obtaining correct dynamic range for the DAT both during

recording, and during playback to the ARIEL board, common mode voltages caused by 60 Hz AC power lines and fluorescent lighting, DC bias effects and linearity settings on the ARIEL card itself.

- Particular attention to circuit layout and ground loops was necessary. Initial problems were caused by high gain amplifiers and balanced-to-single ended conversion circuits, and lack of a single point ground.
- In initial amplifier designs, harmonics from the 60 Hz AC power lines and 33 KHz electric fields generated by fluorescent lights were picked up by the microphone amplifier. A number of circuit revisions were necessary to obtain decent rejection of these interfering signals.
- Physical separation of the signal conditioning amplifiers was necessary to prevent electrical crosstalk from correlating the reference and primary signals.
- Solid grounding and installation of small decoupling capacitors on the inputs and outputs of the switched capacitor filter circuits were necessary to reduce noise generated by a 2.048 MHz TTL level master clock inside the BPF box.
- Any unshielded cables tended to pick up noise in the audio band, primarily 60Hz harmonics, due to the close proximity of the test equipment to the circuits. It was necessary to use a shielded[1] twin-axial cable to obtain small (microphone) signals, as well as prevent crosstalk between the high level reference and low level primary cable inputs.
- Linearity and gain settings to avoid clipping in the ARIEL board had to be adjusted to optimal settings. Early measurements revealed that the linearity of the ARIEL card was not adjusted correctly.

DC bias compensation. In any physical circuit, DC bias voltages will be present. Temperature and loading fluctuations will vary the DC bias at the amplifier outputs up to 10mV or more. Offsets in the Ariel card were found to be approximately -15 mV and -30 mV for the left and right channels respectively. Algorithms that do not compensate for DC bias will not converge to the optimum

1. The shield is grounded to chassis ground at the AD524 end, an is ungrounded at the microphone end.

weights. Rather than modifying the data files, each of the algorithms was modified to include an adaptive DC bias term. The compensated NLMS algorithm (for example) is the same as previously described except an additional tap weight is added to insert a DC bias value;

$$y(n) = \mathbf{w}^T(n)\mathbf{x}(n) + w_{bias}(n)b \quad (4.4)$$

$$\mathbf{w}(n+1) = \mathbf{w}(n) + \mu e(n)\mathbf{x}(n) \quad (4.5)$$

$$\mathbf{w}_{bias}(n+1) = \mathbf{w}_{bias}(n) + \mu e(n)b \quad (4.6)$$

where b is a fixed bias weight, in most cases set to 0.01 and μ is the step size which must be chosen so that:

$$\mu = \frac{\alpha}{\varepsilon + \|\mathbf{x}(n)\|^2 + b^2} \quad (4.7)$$

The effect of this additional parameter is to slow convergence slightly and reduce the achievable ERLE from approximately 127 dB to approximately 70 dB, however, this value is still far below where most physical ERLE values were located (20-40 dB).

4.2.2 Maximum Achievable ERLE of the Experimental Set-up

The maximum achievable ERLE of the experimental setup was found by replacing the *Loud-speaker-Room-Enclosure-Microphone* (LREM) system (see Figure 4.2) with a passive attenuator network. The modified setup was excited with bandlimited white noise. The achievable ERLE was calculated using a 10 tap NLMS adaptive filter with a step size of 0.5. The resulting curve is shown in Figure 4.4. Also plotted is an asymptotic curve which represents an estimate of the maximum achievable ERLE of the experimental setup based on an estimate of the primary signal's

SNR. The maximum achievable ERLE of the measurement setup was found to be approximately 56dB.

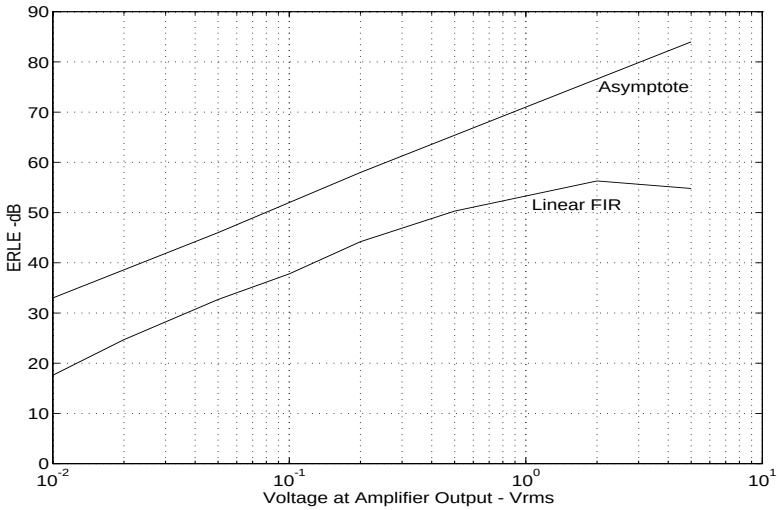

FIGURE 4.4 Optimum steady-state ERLE performance of the experimental setup based on the converged ERLE of a 10 tap NLMS adaptive filter with a step size of 0.5 (Linear FIR curve), and an estimate of the SNR of the primary signal (Asymptote curve).

Further experiments were conducted to evaluate the experimental setup more completely and provide an explanation for the limitation in performance. The results are displayed in Figure 4.5. The line labelled *Ariel* corresponds to converged ERLE values for a variety of equivalent DAT record levels[1] obtained by injecting bandlimited white noise directly into the analog input ports of the Ariel board. An achievable ERLE in excess of 70dB was obtained for record levels greater than -13dB. The additional quantization noise added by first sampling the data to DAT degraded the achievable ERLE by approximately 8dB as shown in the curve labelled *DAT + Ariel*. Finally, the performance of the complete setup is illustrated by the line labelled *Full Setup*. This curve is similar to that shown in Figure 4.4 except that the reference signal voltage is held constant at 1Vrms

1. For the *Ariel* curve the input voltage is converted to an *equivalent* DAT record level with knowledge of the DAT's input/output transfer characteristics to support comparison between the curves.

while the record level at the DAT is adjusted. These results suggest that the current limitation of 56dB is caused by noise added by the primary (microphone) amplifier. Improving the noise performance of this amplifier is unnecessary, however, because as demonstrated in the remainder of this chapter a variety of physical limitations act to limit ERLE to a level below 56dB.

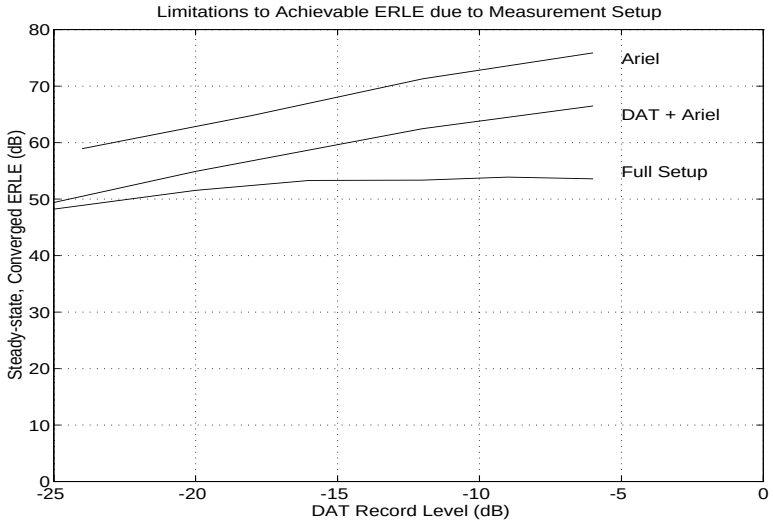

FIGURE 4.5 Comparison of optimum steady-state ERLE of the Ariel, the DAT and Ariel, and the full setup based on a 10 tap NLMS adaptive filter with a step size of 0.5.

4.2.3 Speakerphone Test Results

The six HFT's listed in Appendix B were tested in an anechoic chamber to determine the magnitude of the limitations to ERLE caused by design variation. The purpose here is to provide some measure of the spread in ERLE due to HFT designs, and not to isolate each of the factors which contribute to this error. The steady-state ERLE performance for each HFT, at each SPL level was obtained by averaging the instantaneous ERLE over the last 4000 samples of 4 seconds of adaptation (sampled at 16 kHz) using the NLMS algorithm with a step size α=0.5. The results are plotted in Figure 4.6. The steady-state ERLE varies over a very large range, with HFT#1 and #6 having

the best performance characteristics and HFT#5 having the worst. At high volumes, all HFT's are limited by strong nonlinear distortion and vibration effects[1] introduced by low-quality loudspeakers and poor acoustic design. Based on these results, HFT #1 and #6 are used for subsequent experimental baseline measurements.

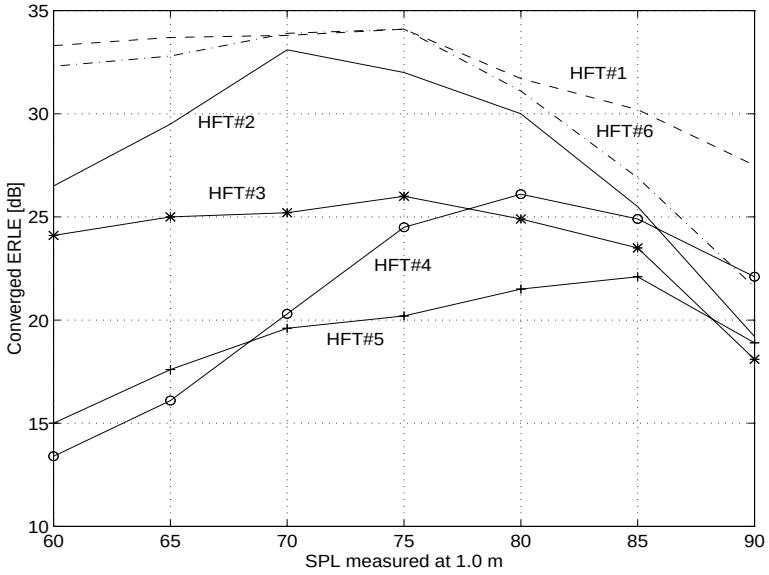

FIGURE 4.6 Converged ERLE for six HFT's at various sound pressure levels (measured 1m from the loudspeaker) in an anechoic chamber. 1000 tap FIR trained with NLMS, all cases.

4.3 Evaluation of Linear IIR Structures for Acoustic Echo Control

In the literature on this subject, Tahernezhadi and Liu [116] propose a real-time implementation of an IIR AEC using the LATIN (*Lat*tice and *In*verse Lattice) structure originally proposed by Chao and Tsujii [117]-[118]. Experimental ERLE values in [116] of 25 dB are reported using only 30 zeros and 30 poles on speech signals, however no simulations were provided to verify these findings and the characteristics of the LREM are not presented. Chao and Tsujii [117] use a simplified LREM consisting of one pole and 9 zeros. It has been found (see Section 4.2) that small amounts

1. To be shown in Section 4.6 and Section 4.5.

of crosstalk in physical circuits can correlate the primary and reference signals and provide overly optimistic results, which might explain how 25 dB ERLE is obtained with so few variables assuming that a real LREM was used. In [119] Fan and Jenkins show that an IIR echo canceller for a data hybrid performs better than an FIR filter *after* convergence, and that convergence is quite slow if the order of the filter is greater than two. However, it is not clear if the same conclusions can be extended to the AEC case.

4.3.1 Hankel Error Bound for Approximating an FIR Filter with an IIR Filter

In [114] the fundamental question of whether poor performance stems from a sub-optimality of the updating procedure or from an irrelevancy of the pole-zero structure itself is investigated. Is it possible to approximate with a small error bound an all-zero transfer function by a pole-zero transfer function[1] with fewer parameters, and does it make sense to fit a pole-zero model to the phenomenon underlying the LREM? The Hankel-norm approximation of a known all-zero transfer function $H(z)$ of order M can be used to obtain an error bound on the use of a reduced order IIR filter [120][121]. If $H(z)$ is defined as the useful part of an all zero transfer function to be identified;

$$H(z) = h_1 + h_2 z^{-1} + \ldots + h_M z^{-(M-1)} \quad (4.8)$$

Then the Hankel matrix Γ_H is defined as a symmetric matrix formed out of the coefficients $h_1 ... h_M$ of the room impulse function $H(z)$;

1. Although an actual room impulse response theoretically consists of poles only, because all frequencies are reflected to some degree, it is convenient to model the impulse response with an all-zero structure

$$\Gamma_H = \begin{bmatrix} h_1 & h_2 & \dots & h_M \\ h_2 & \dots & h_M & 0 \\ \dots & h_M & 0 & 0 \\ : & : & : & : \\ h_M & 0 & \dots & 0 \end{bmatrix} \qquad (4.9)$$

The maximum error bound on approximating the M^{th} order FIR response with an N^{th} order IIR response can be obtained by the following equation;

$$error\ bound \le 2[\sigma_{K+1} + \sigma_{K+2} + \dots + \sigma_M] \qquad where\ \sigma_1 \ge \sigma_2 \ge \dots \ge \sigma_M > 0 \qquad (4.10)$$

where $\sigma_1, \sigma_2, \dots, \sigma_M$ are the Hankel singular values of Γ_H, K=M-N, where M is the number of coefficients in $H(z)$ and N is the order of the approximating IIR filter. The diagonal matrix Σ may be obtained by finding a nonsingular transformation matrix **T** such that

$$\mathbf{T}^T\mathbf{W}\mathbf{T} = \Sigma = diag[\sigma_1, \sigma_2, \dots, \sigma_M] \qquad (4.11)$$

$$\text{where } \mathbf{W} = \Gamma_H{}^T\Gamma_H \qquad (4.12)$$

Simulations results in [114] showed that a radio-mobile echo path consisting of 512 all-zero coefficients could efficiently be modelled with a -30 dB error using a pole-zero structure with 128 parameters, however, a -28.8 dB error could be obtained with an FIR structure with the same number of coefficients!

Hankel Bound Experimental Results. Two room impulse responses (slowly decaying and quickly decaying) were generated using the techniques described in Section 4.1.2. The results showing the approximation error bounds are shown in Figure 4.7. The low error bound near O(IIR)=256 is artifactual and comes about as perfect modelling is achieved when O(FIR)=O(IIR). However, the

results do provide a rough estimate of the achievable error bound for lower IIR filter orders up to approximately 200.

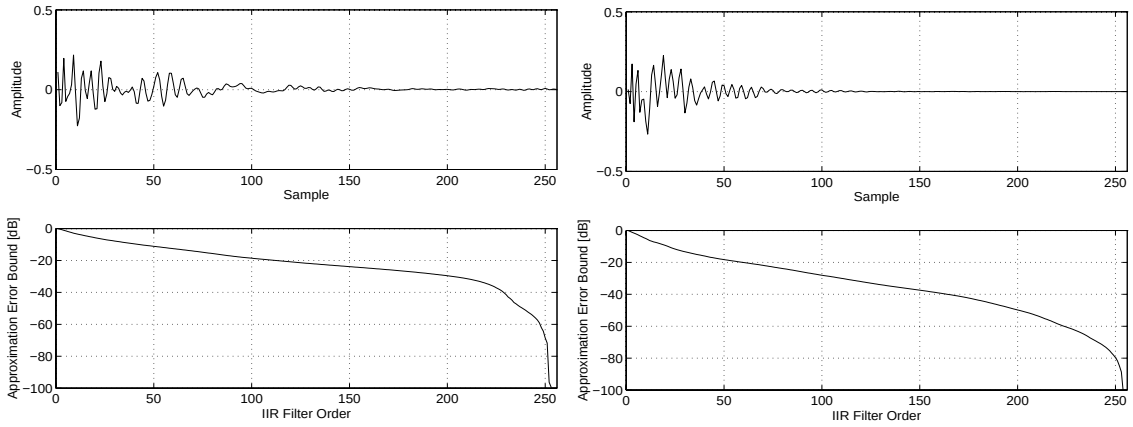

FIGURE 4.7 Approximation error bound [dB] for identifying LREM's with different reverberation times. Impulse responses are obtained from measured LREM's truncated to 256 points. (a) Slowly decaying LREM needs an IIR filter order of 200 to achieve a -30 dB error bound. (b) Quickly decaying LREM needs an IIR order of 110 to achieve the same error bound.

For a slowly decaying LREM impulse response, the number of IIR parameters required to model the impulse is almost the same as the FIR case, however, for faster decaying impulses, the number of IIR parameters is correspondingly less. This analysis suggests that for environments that posses small reverberation times, like automobiles, IIR structures might be suitable filter candidates, however, for environments that have long reverberation times, the advantages of IIR compared to FIR structures are marginal.

4.3.2 Comparison of MA, ARX and OE-IIR Modelling

In the literature, Gundvangen and Flockton [122] [123] made a comparison between pole-zero and all-zero modelling of acoustic transfer functions. Three different identification structures were used, one FIR and two IIR structures based on output error (OE) and equation error[1] (EE) formulations. In the IIR models there is another parameter in addition to the total number of coefficients,

namely the *ratio* of zeros to poles. The ratio that gave the best ERLE for the OE model was approximately 5:2, although the exact ratio was not at all critical. They found that the OE consistently gave marginally better performance than the FIR and that the EE model performed a few dB worse than the FIR due to the bias of this particular model. They also reported that to achieve a particular ERLE, the number of coefficients for both the FIR and IIR models was found to increase substantially with increased reverberation time.

Experimental Results using OE and EE-IIR Modelling. In order to investigate the pole/zero ratio question as applied to transducer components only (which was not covered in [123]) an OE-IIR model was fitted to measured data obtained in an anechoic chamber with results shown in Figure 4.8 (a). For comparison, results using the EE-IIR algorithm on data collected using HFT#6 are shown in Figure 4.8 (b).

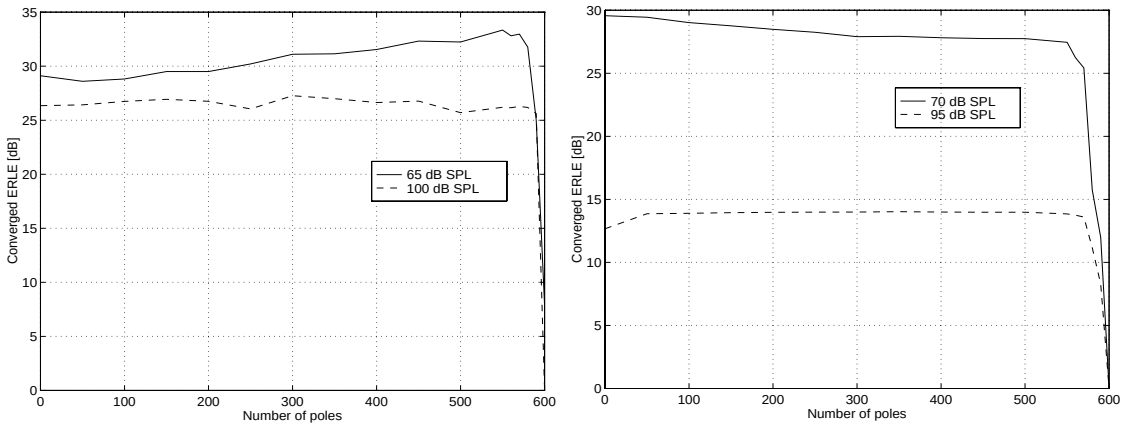

(a) (b)

FIGURE 4.8 Experimental results of IIR modelling showing ERLE vs. ratio of poles to zeros for IIR models fitted to experimental LREM data. (a) ARX modelling for SPK#1 and MIC#2 in an anechoic chamber. (b) OE-IIR model for HFT#6 in conference room #2.

1. The EE formulation can be obtained through a two input ARX fitting.

For both experiments, the total number of parameters was fixed at 600, with the number of poles varying between 0 (i.e. all-zeros) to 600 (all-pole). The parameters used are shown in Table 4.2.

TABLE 4.2 Parameters for experimental results presented in Figures 4.8(a) and (b).

Figure	Algorithm	Parameters	Location	Comments
(a)	EE LMS IIR, Appendix D.6	$\mu_a=\mu_b=0.001$.	Anechoic	Transducers
(b)	OE LMS IIR, Appendix D.7	$\mu_a=\mu_b=0.001$.	Conf. Rm. #2	HFT#6

The EE-IIR algorithm obtains a slight improvement in performance with an increasing number of poles, for low volumes. Almost no change in ERLE is observed at high volumes by changing the pole/zero ratio. The results verify conclusions made in [123] about the ratio of pole/zero ratio (being not critical) and also suggest, as in [123] that *in the HFT context, the advantages of IIR modelling are minimal*. Results using the OE-IIR algorithm shown in Figure 4.8 (b) indicate again that there seems to be no overall gain in ERLE by swapping poles for zeros.

Conclusions. It does not appear possible to obtain the same ERLE with *significantly* less parameters using IIR filters (compared to an FIR filters) to model a reverberant echo path. This seems to be confirmed by the Hankel-norm error bound of Figure 4.7. *Based on the above analysis, literature survey, and DSP processing limitations, it would appear that all-zero FIR structures have an advantage over IIR methods.* Considering that a typical LREM impulse may be thousands of milliseconds duration, we must be satisfied to model the physical phenomenon with an undermodelled system and try to obtain the best fit possible according to the reverberation characteristics.

4.4 AEC Performance Limitations

The limitations of AEC's include the following:

1. ***Noise, Finite Precision and Quantization***: Acoustic noise from fans and air conditioning in the room as well as thermal and impulsive circuit noise from amplifiers, and DSP related noise such as truncation, quantization and finite word lengths place a limit on the achievable steady-state ERLE [124] [97].
2. ***Undermodelling of the Acoustic Transfer Function***: When the number of taps or variables in the AEC adaptive filter is less than the acoustic impulse response of the room, the uncancelled tail portion of the LREM manifests itself as a finite error at the output of the AEC [1][125].
3. ***Enclosure Vibration Effects***: An important new finding[1] is that vibration and resonances within the enclosure can significantly limit achievable ERLE if proper *acoustic* design of the enclosure is not realized. In addition, the early reflections in the impulse response are due to LREM coupling effects which are generally much larger in amplitude than the delayed echoes [126].
4. ***Transducer Nonlinearities***:[2] Generated mainly in the loudspeaker, nonlinear distortion effectively puts a limit on the achievable ERLE of algorithms based on linear mechanics [127].
5. ***Algorithmic Performance:*** Initial convergence rate, dynamic tracking ability in nonstationary conditions, behavior with correlated (speech) inputs [95] and the ability to detect and handle double talk situations [128].

All of the above mentioned limitations will serve to reduce the achievable ERLE and will be discussed in greater detail subsequently. The model used in the analysis includes the above limitations is shown in Figure 4.9.

4.4.1 Noise, Finite Precision and Quantization

Noise components in the primary signal include room noise, microphone circuit noise and quanti-

1. No mention of this important physical limitation has been mentioned in the literature.
2. First mentioned by Knappe and Goubran [1] as a limitation in AEC's.

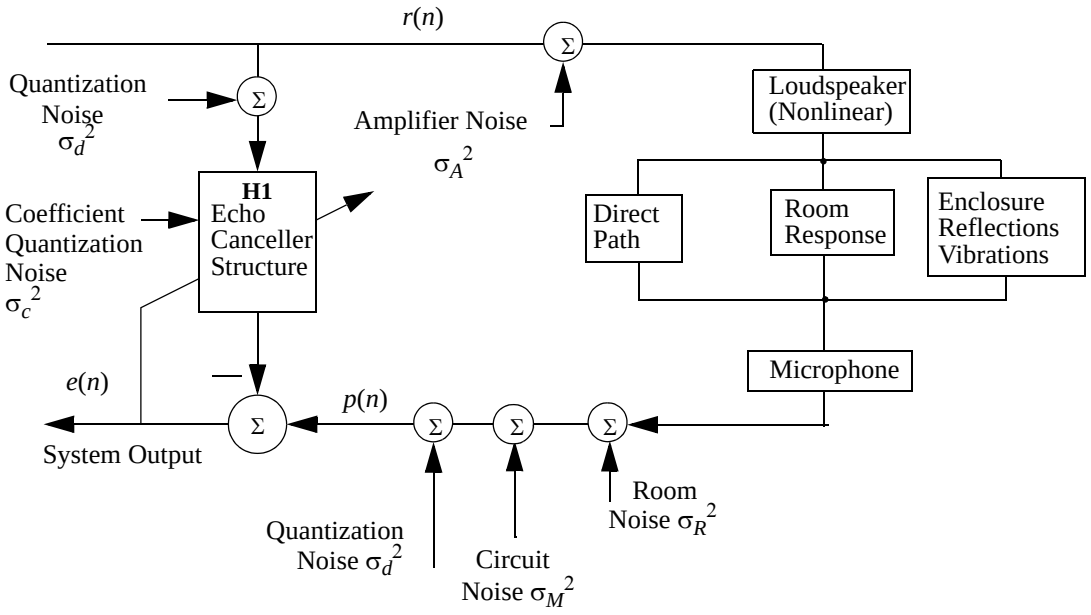

FIGURE 4.9 Complete LREM model includes enclosure reflections and vibration as well as transducer nonlinear responses. The model should also include room, quantization and circuit noise.

zation noise. These can be modelled as white noise sources with variances σ_R^2,σ_M^2 and σ_d^2. The effect of these noise components is to reduce the achievable steady-state ERLE to a level approximately equal to equation (4.1) where σ^2_e is replaced by σ^2_T and $\sigma^2_T = \sigma^2_R + \sigma^2_M + \sigma^2_d$. Uncorrelated room noise is usually the largest contributor to the overall noise introduced into the primary path. In the absence of other effects, room noise contribution becomes the asymptote for the achievable converged ERLE [1].

Microphone/Circuit Noise. This is generated mainly in the sensing electronics for the microphone element. A typical electret microphone will be biased through a dropping resistor of a few kΩ to provide a bias voltage for the microphone element. The output voltage change ΔV from such a microphone is defined by $\Delta V = \alpha V_b \Delta C$ where α is a constant, V_b is the bias voltage across the electret capacitive element and ΔC is the change in capacitance due to the impinging sound wave.

Thermal noise from the bias resistor will be added to the microphone which itself has a noise level in the vicinity of -100 dBV. The microphone output signal is amplified to line levels of approximately 100 mVrms which also amplifies the noise. However, except for anechoic conditions at very low volume levels, this noise has been found to be generally far below typical room noise. This conclusion is also verified by the results shown in Figure 4.5.

Quantization and Fixed Point Internal Arithmetic in DSPs. A full analysis of fixed point arithmetic for the LMS algorithm can be found in [125] which states that the total output mean square error for the LMS algorithm can be expressed as:

$$J = J_{min} + \frac{1}{2}\mu J_{min} tr(\mathbf{R}) + \frac{N\sigma_c^{\,2}}{2a^2\mu} + \frac{1}{a^2}(|\mathbf{w}_o| + c)\sigma_d^{\,2} \qquad (4.13)$$

where J is the MSE at the output, J_{min} is the minimum MSE of the optimal (Weiner) filter $\mathbf{w}_o$, a is a scaling factor used to bring the maximum levels to +/- 1.0, N is the number of taps in the FIR structure, μ is the step size parameter, and c is a constant. The coefficient quantization noise $\sigma_c^2 = 2^{-2B_c}/12$ is the variance introduced by the coefficient quantization where B_c is the number of binary quantization levels (i.e. bits) in the coefficient representation. Similarly, $\sigma_d 2$ is the variance introduced by the data (sampling) quantization introduced by B_d quantization levels.

Although one may be tempted to reduce the step size μ to reduce the excess mean square error (i.e. the second term), it may result in a large quantization error generated in the third term due to the *stalling phenomenon* in fixed point processors. There exists an optimum value of μ which minimizes the total output MSE, however, it is too small to allow the algorithm to converge completely. Figure 4.10(a) illustrates the MSE as a function of the adaptation step size μ where the number of bits B_d in the data representation and B_c in the coefficient representation are the same.

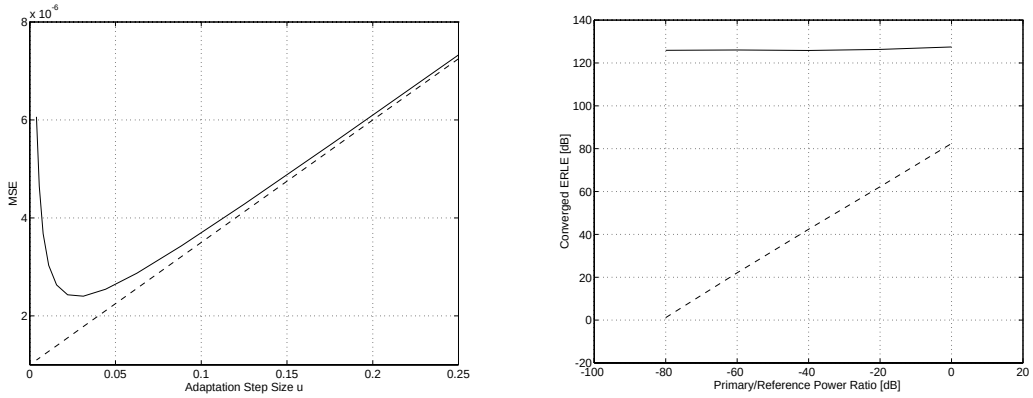

(a) **(b)**

FIGURE 4.10 (a) Total MSE as a function of μ where B_d=B_c=16 bits, MMSE=1e-6, *M*=500 taps, reference input variance σ_r^2=0.1. The dashed line shows the equivalent infinite precision case. (b) ERLE for a variable primary signal power when *p*(*n*) is quantized to 16 bits (dotted line) and for *p*(*n*) unquantized(solid line).

In the LREM model of Figure 4.9, quantization noise is uncorrelated with the primary signal so appears at the output essentially unchanged. Reference signal quantization noise on the other hand is modified by the adaptive filter transfer function as it adapts. The effect of A/D quantization noise on ERLE is illustrated in Figure 4.10(b). The converged ERLE is *independent* of the signal level of the primary or reference signal levels when floating point is used. However, when the *primary* signal is quantized, the maximum level of converged ERLE will be determined by the *ratio* of the primary signal power to the quantization noise at the location of A/D converter.

In practice an ERLE of 25 to 35 dB seems to be the physical limit to the achievable ERLE in real systems. *The results presented in this section have shown that the limitations due to algorithmic noise and truncation effects are far below this limit, and therefore should not have a significant impact on the final ERLE value.*

4.4.2 Undermodelling of the LREM

In this section we investigate the effect of using an FIR structure to model a transfer function where the number of parameters in the candidate system will be less than that required to exactly identify the system. This gives the undermodelled system: $deg(\hat{H}) < deg(H)$. An analysis of the finite length AEC by Kuo and Chen [129] shows that *a finite filter length will have a better ERLE performance using speech than white noise*. Poltmann [130] showed that the achievable ERLE is a function of both the step size and magnitude of the modelled and undermodelled LREM coefficients. For a system modelled by an FIR transfer function the achievable steady state ERLE assuming a white noise input can be calculated from;

$$ERLE = 10\log\left[\frac{2-\mu}{2}\left(\frac{\|h\|^2}{\|\Delta h\|^2}+1\right)\right] \approx TIP/TP \qquad (4.14)$$

where $\|h\|^2$ represents the power in the modelled coefficients up to order *M*-1 and $\|\Delta h\|^2$ represents the power in the tail portion of the LREM from *M* to infinity. If μ is set to 0, (4.14) is equal to the *Total Impulse response Power to the uncancelled Tail Power* (TIP/TP) ratio originally proposed by Knappe and Goubran [1], who demonstrated that the TIP/TP ratio defines the achievable ERLE up to approximately 20 dB. Beyond this point, other effects dominate. Experimental measurements in [1] show that even at ratios of (S+N)/N of greater that 40 dB, the ERLE did not go beyond 25 dB, with the most likely suggested cause of this ERLE limitation being loudspeaker nonlinearities.

The TIP/TP ratio is invaluable for determining the optimum number of AEC filter taps to use given a certain loudspeaker, microphone and enclosure. For example, the impulse response of HFT #6 measured inside conference room #2 at 85 dB SPL is shown in Figure 4.11 (a). Figure 4.11 (b) shows the calculated TIP/TP vs. ERLE ratio compared to the measured ERLE by using (4.14) and

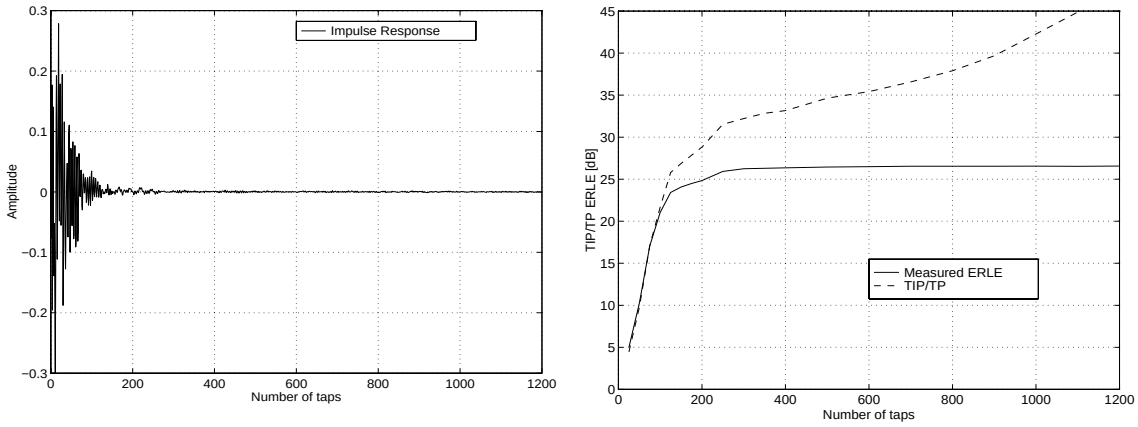

(a) (b)

FIGURE 4.11 Undermodelling of the LREM. Measured results of HFT #6 at 85 dB SPL. (a) Impulse response measured in a conference room #2. (b) calculated TIP/TP and measured ERLE using NLMS algorithm.

the NLMS algorithm. The ERLE will follow the TIP/TP ratio very closely up to a certain number of taps according to (4.14), however, in experimental recordings, nonlinearities and vibration effects will limit the achievable ERLE.

Comparison with Hankel Norm Error Bound. A plot showing the comparison of the logarithmic "inverse" of the TIP/TP ratio and Hankel norm error bound for HFT#6 is shown in Figure 4.12. The results show that the Hankel error bound closely follows (but is lower than) the TIP/TP ratio and verifies earlier conclusions that the performance gains of IIR structures over FIR structures are not substantial, and that given the added complexity, FIR based structures are preferable.

4.4.3 Algorithmic Limitations

Dynamic Tracking in Nonstationary Conditions. As objects move and the input signal characteristics become nonstationary, the tracking ability of the algorithm becomes important. For example, although RLS based algorithms have fast convergence and have been shown theoretically to have

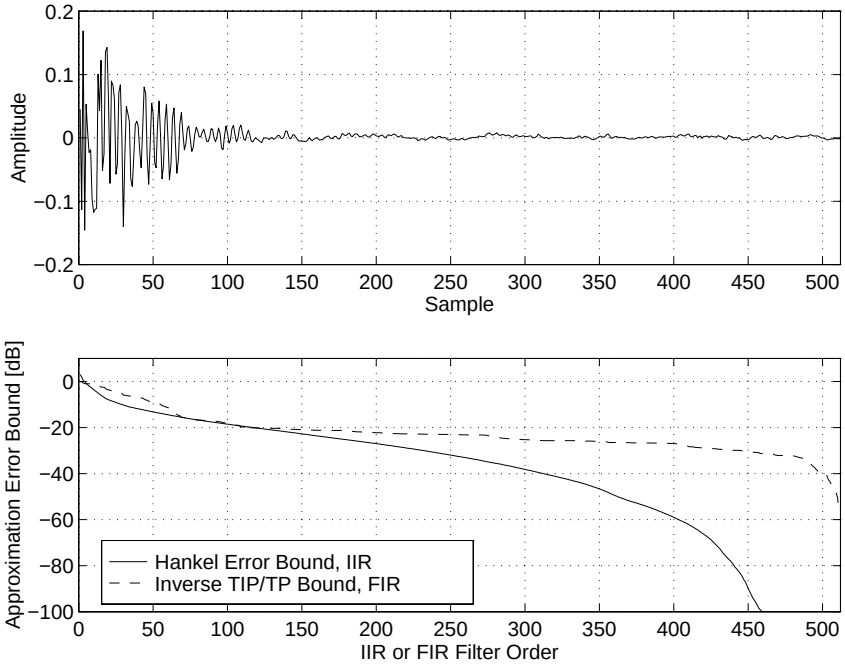

FIGURE 4.12 Comparison of TIP/TP ratio with Hankel error bound for data measured in conference room #2 using HFT #6 at 65 dB SPL.

tracking capability equivalent or better than the LMS algorithm in low noise [131], it has been found in [95] that algorithms based on instantaneous gradient estimates like the LMS family outperform RLS algorithms in conference room conditions using real speech where the SNR of the primary signal is often quite low.

Colour Insensitive Algorithms. LMS based algorithms suffer from poor convergence when trained by quasi-periodic signals with highly coloured spectra, like speech. The most mature scheme for mitigating this problem is subband filtering [132] [133], however, RLS based algorithms [134] and block frequency domain methods [135] are also popular. Often, a combination of architectures and algorithms is necessary to obtain satisfactory performance. A brief summary is presented in [112]. A comparative analysis of eight different algorithms is presented in [136] showing measured performance metrics (See Table 4.1) for the single talk mode only using both

USASI noise signals and speech signals. Of eight algorithms/structures tested, the *generalized multi-delay filter* (GMDF) [137], which is based on [138] obtains the best performance metrics. The *unconstrained fast LMS* [139] and *wavelet decomposition* technique [140] also produce good results. An algorithm presented in [141] uses a fast Newton training scheme to obtain performance enhancement with speech signals. However, measurements were obtained using a short impulse response (for use in automobile environments). No results were presented for an HFT in a highly reverberant venue. Recently, the *Fast Affine Projection* (FAP) algorithm [143] [144] has been proposed as an alternative to RLS type algorithms. The FAP can be considered a generalization of the NLMS algorithm with weight updates based on an affine projection in multiple dimensions.

Double Talk. Double talk (DT) occurs during periods when the far end speaker and near end speaker are simultaneously talking. The effect of DT is to increase the noise in the primary signal (similar to additive room noise described in Section 4.4.1) causing a temporary *decrease* in the ERLE and a slowing of the convergence and tracking ability. In a full-duplex system, it is often necessary to freeze the adaptive filter coefficients such that divergence of the tap weights does not occur. The most drastic form of DT control is push-to-talk (half-duplex or single-talk mode) which was the “defacto” standard until the advent of adaptive filters for removing echo. The literature is full of techniques for performing DT, for example [137] describes a method of detecting local speaker activity by comparing the spectral shapes of the primary and reference signals, using an appropriate distance. A large Euclidean distance is an indicator of the presence of a local talker. The method described in [145] proposes a short term cross correlation between the error output $e(n)$ and the canceller output $y(n)$ for controlling the step size. The correlation is used to obtain fast convergence during single-talk periods and low sensitivity during double-talk periods. Other methods are outlined in [128] and [130].

4.4.4 Complexity Issues

The choice of algorithm has an impact on the type of hardware resources needed to implement a real-time system. For a review of the impact of specific algorithm architectures on available DSP platforms see [142]. In terms of complexity, Table 4.3 summarizes the comparison between various algorithms previously introduced.

TABLE 4.3 Comparison of Algorithm Complexities

Algorithm	Type	Convergence Speed	Multiplications per sample	Comment
LMS	LMS	slow	$2M$	simple
NLMS	LMS	slow	$2M$+1	
VSS	LMS	slow	2M	
MVSS	LMS	slow	2M	
RLS	RLS	fast	$2M^2$+6M	Complex
FTF	RLS	fast	7M	unstable
SFTF	RLS	fast	8M	
LMS-IIR	OE	slow	$4(n_a+n_b)$	local minima
LMS-IIR	EE	slow	$2(n_a+n_b)$	biased minimum
FCG	CG	selectable	LMS to RLS	complexity/performance tradeoff
FNTF	RLS	selectable	2M+12P	complexity/performance tradeoff
FAP	RLS	selectable	2M+30N	complexity/performance tradeoff

Note: M refers to the order of the filter, and N refers to the projection window size and P refers to the size of the predictor variables. n_a and n_b refer to the number of poles and zeros in an IIR structure.

4.5 Effect of Enclosure Vibration and Resonance

An important new discovery is that vibration and resonances within the enclosure can significantly limit achievable ERLE if proper acoustic design of the enclosure is not realized. In addition, rattling of the handset and keys has been observed. Recent measurements have shown that in HFT's with plastic enclosures, rattling and vibration cause a significant increase in the uncorrelated noise

signal introduced into the primary path, depending on the volume of the loudspeaker signal.

4.5.1 Experimental Results

Experimental Results: Converged ERLE. Figure 4.13 shows the effects that rattling and vibration have on the achievable ERLE of HFT #1. The basic loudspeaker and microphone configuration

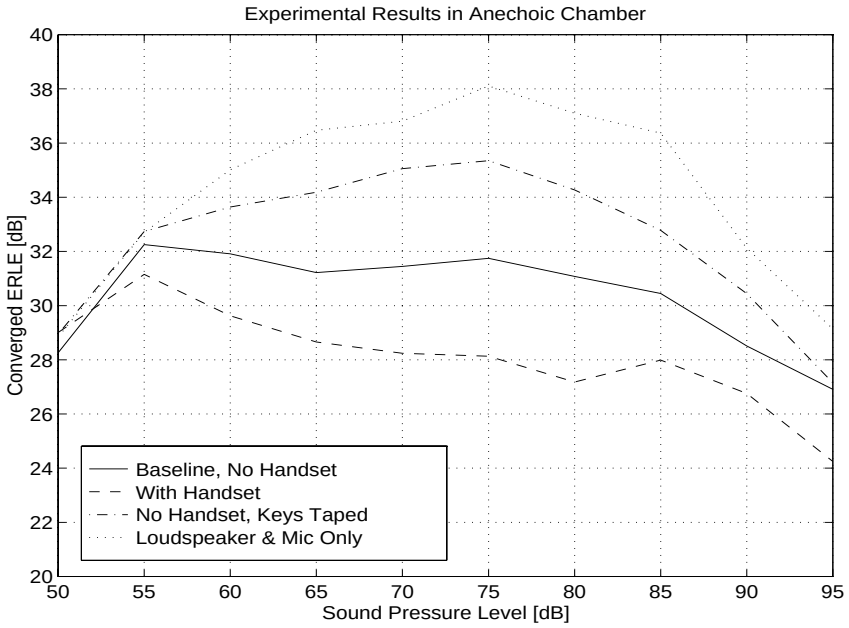

FIGURE 4.13 Effects on achievable ERLE due to vibration and rattling. HFT #1. Converged ERLE as volume in increased from 60 dB SPL to 100 dB SPL with various handset configurations. 600 tap FIR trained with the NLMS algorithm, all cases.

obtains the highest ERLE. The performance drops when the components are added into the enclosure. When the keys are allowed to rattle, the ERLE drops even further and finally, when the handset is placed on the set, a 10 dB reduction in ERLE is observed at 75dB SPL as compared to the case with microphone and loudspeaker only. At the low volume levels near 50 dB SPL, the ERLE is limited primarily by the SNR of the primary signal and unbalanced two point suspension system nonlinearities within the loudspeaker.

Primary Power Spectral Density . The primary *power spectral density* (PSD) of HFT #1 is illustrated in Figure 4.14(a). It is clear that when the components are mounted inside the enclosure, the level of the out-of-band (distortion) signal increases substantially with an increase in the reference signal level. Figure 4.14(b) shows the PSD of the loudspeaker and microphone components when they are removed from the plastic enclosure (this removes the effect of vibration, noise and echo). *Notice that the distortion in the frequency range 4-8 kHz is significantly reduced*. However, there is still an increase in the out-of-band signal level which is essentially the nonlinear components of the original bandlimited (reference) signal. However, the level of distortion is much less than that due to vibration (shown in 4.14 (b)).

This is an important result which tells us that vibration can be a more serious problem than loudspeaker distortion in the HFT domain.

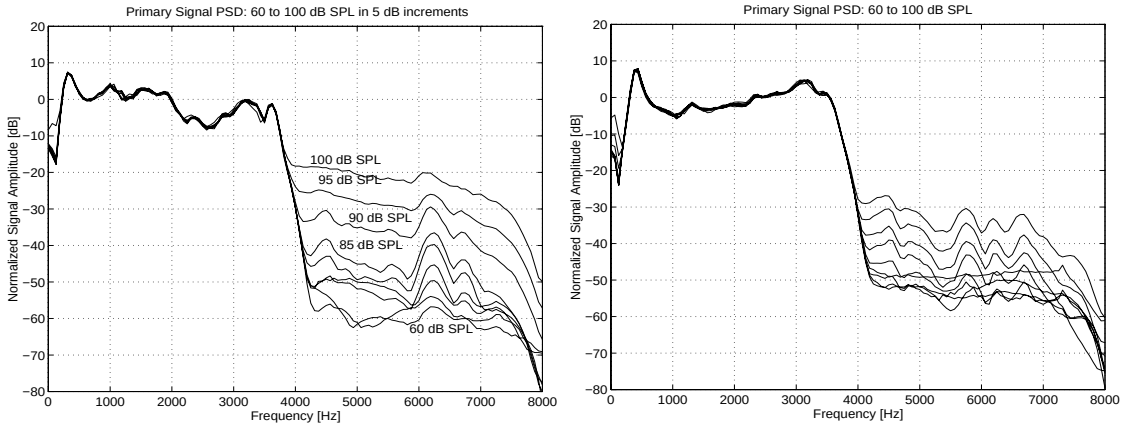

(a) (b)

FIGURE 4.14 Effect of enclosure vibration and nonlinearity. (a) HFT #1. Primary signal PSD with loudspeaker and microphone inside the HFT enclosure. Out-of-band components increase in level as the volume is increased from 60 dB SPL to 100 dB SPL. (b) same as (a) but with components removed from enclosure and mounted inside a standard baffle.

Enclosure Effects on Impulse Response. The early reflections in the impulse response are in part due to LREM coupling effects which are generally much larger in amplitude than the delayed ech-

oes. Some of this coupling comes from the air path between the loudspeaker and microphone, however, *a substantial part is due to vibrational coupling in the HFT enclosure itself*. Results shown in Figure 4.15(a) illustrate the large early reflections when the transducers are mounted inside the HFT enclosure. The measurements were performed using the setup of Figure 4.2 in the anechoic chamber. Also shown in Figure 4.15 (b) is the recovered impulse response when the transducers have been *removed* from the HFT enclosure. The loudspeaker is placed in a standard baffle with the microphone placed 8" directly in front. The large tap values at the beginning of the LREM impulse response, which correspond to the enclosure vibration coupling are totally absent.

Direct coupling can be modelled with fixed parameters (if the parameters are known) or using the adaptive filter with a small step size for the early part of the reflection. This technique is called *Beta-grading* and is described further in [112] and [146].

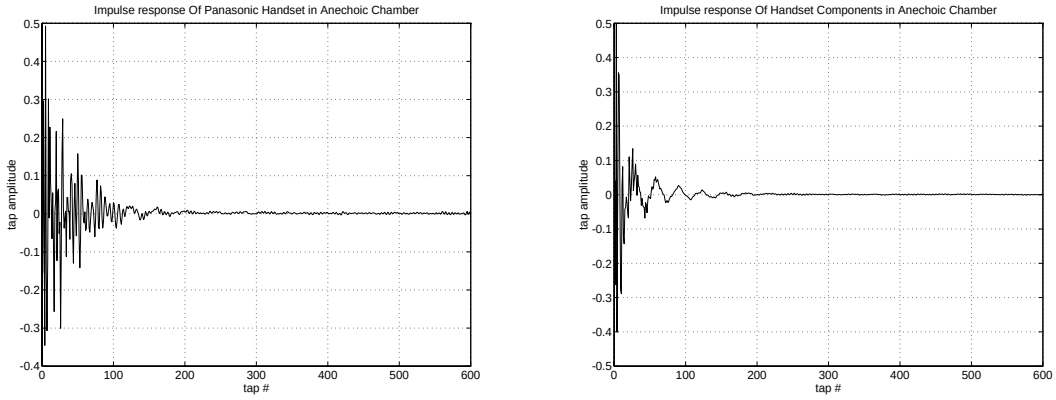

(a) (b)

FIGURE 4.15 Experimental Results inside the anechoic chamber. (a) Impulse response of HFT#5 measured at medium volume. (b) Impulse response of the microphone and loudspeaker removed removed from HFT #5 and placed in a standard baffle is significantly different. Parameters: NLMS algorithm, α=0.5, 32000 samples @ 16kHz, averaged over last 2000.

4.5.2 Microphone vibrational sensitivity

Given that enclosure vibration is a problem, a microphone element with low mechanical vibration sensitivity will reduce the vibration effect mentioned previously and minimize the magnitude of the early reflections. The mechanical sensitivity of a microphones will depend on the orientation of the microphone element with respect to the axis of vibration and also displays a frequency dependence with the lower frequencies being more sensitive than higher frequencies. A typical electret microphone will exhibit a peak vibration response in the low frequency ranges in the vicinity of 300 Hz. Table 4.4 lists some typical measured audio sensitivities of electret microphones and Table 4.5 lists the corresponding mechanical vibrational sensitivities in dbV/G.

TABLE 4.4 Electret microphone acoustic sensitivity

Orientation	Microphone Sensitivity	Nominal Acoustic Level	Output Voltage
Parallel	-30 (to -40) dBV/Pa	-30 dBPa	-64 dBV

TABLE 4.5 Mechanical vibrational sensitivity

Orientation	Frequency	Sensitivity	Acceleration	Output Voltage
Parallel	300 Hz	-32 dBV/G	1 G	-32dBV
Parallel	1KHz	-36 dBV/G	1 G	-36dBV
Perpendicular	1KHz	-65 dBV/G	1 G	-65 dBV

If we model the vibrational acceleration using a one dimensional harmonic motion $x = r\cos\omega t$, the acceleration a acting on the microphone element is $a = -\omega^2 r\cos\omega t$. Thus, a microphone element must travel a radius of 2.8 μm to generate 1G acceleration (9.8m/s^2) at 300 Hz. It is reasonable to assume[1] that the microphone output due to vibrational coupling is not negligible when compared to the acoustical coupling. The measurements presented here (See Figure 4.14) seem to confirm this hypothesis.

1. Based on correspondence with [147].

4.6 Effect of Transducer Nonlinearities

In this section transducer nonlinearities are investigated. Generated mainly in the loudspeaker, nonlinear distortion effectively puts a limit on the achievable ERLE when using algorithms based on linear mechanics.

4.6.1 Computer Simulation Setup

A computer simulation setup to determine the effects of distortion products on an FIR filter trained with the NLMS is described. The setup for the identification of a nonlinear system is illustrated in Figure 4.16.

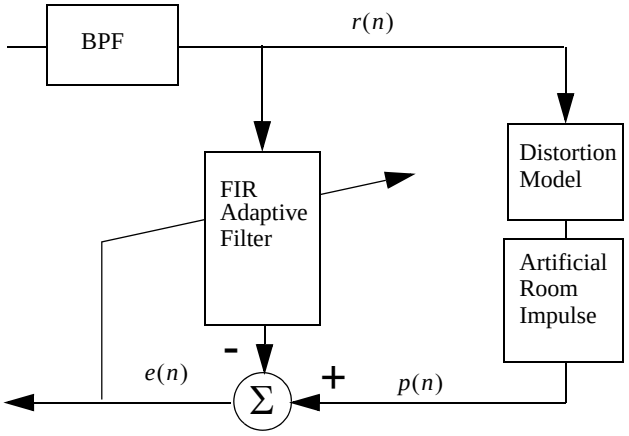

FIGURE 4.16 Nonlinear system identification model. The system to be identified consists of a fixed or variable memoryless nonlinearity followed by an exponentially decaying impulse transfer function.

The reference training signal is white gaussian noise with a unit variance which is subsequently bandlimited by a 10^{th} order elliptical bandpass or lowpass filter with a frequency response that closely corresponds to the characteristics of the switched capacitor transmit filters used in the experimental setup. The frequency responses are shown in Figure 4.17.

The implied sampling rate is 16 kHz, even though the filter cutoff is 3.4 kHz. The justification for

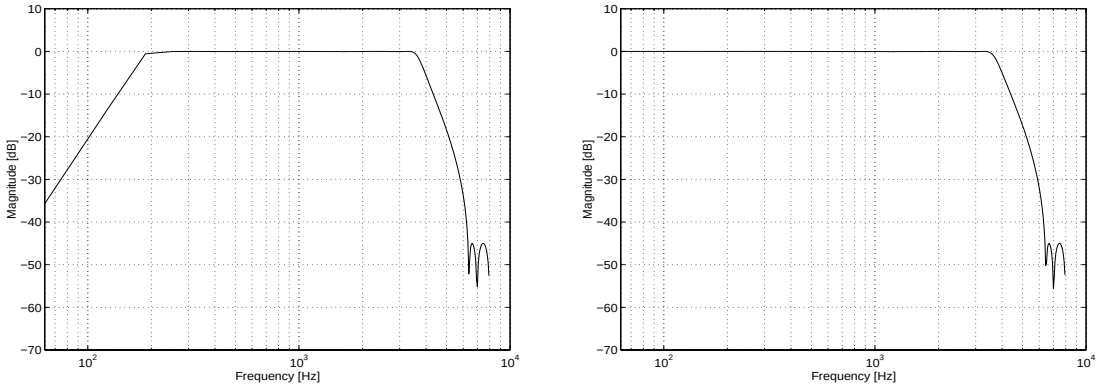

(a) (b)

FIGURE 4.17 Telephony Filter Characteristics. (a) Bandpass (b) Lowpass.

this oversampling is that significant distortion products are generated “outside” the bandwidth of the filter allowing one to obtain a rough estimate of the severity of the distortion by observing the increase in out-of-band distortion products. In the model of Figure 4.16, The distortion is generated by one of three methods given below.

Distortion Method #1. The first distortion model generates an output which is defined by;

$$d(n) = \frac{ax(n) + bx^2(n) + cx^3(n)}{|a| + |b| + |c|} \qquad (5.1)$$

where a, b and c refer to the magnitudes of the linear, quadratic and cubic products respectively.

Distortion Method #2. The second distortion model generates an output defined by;

$$d(n) = \frac{1}{a}\tanh(ax(n)), \qquad 0 < a < \infty \qquad (5.2)$$

where a is a parameter which regulates the amount of squashing. For high values of a, the squashing distortion becomes more severe as shown in Figure 4.18.

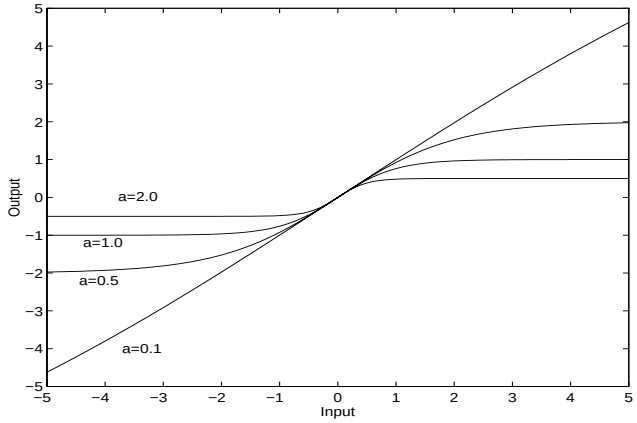

FIGURE 4.18 Variable hyperbolic tangent squashing function for different values of the parameter *a*.

Distortion Method #3. The third method of generating distortion is by using the nonlinear state-space equations (2.9) through (2.12) as listed in Section 2.2. In this case, the amplitude of the reference signal is amplified before being applied to the distortion model.

4.6.2 Computer Simulation Results

Table 4.6 lists the distortion parameters used for the three distortion methods.The artificial room

TABLE 4.6 Distortion Parameters.

Distortion Method	Figure	Distortion Parameters
1	Figure 4.19(a)	a=1, b varied 1e-3,3e-3,1,e2,3e-2,1e-1,3e-1,1 c=0
1	Figure 4.19(a)	a=1, b=0, c varied: 1e-3,3e-3,1,e2,3e-2,1e-1,3e-1,1
1	Figure 4.19(a)	a=1, b=c=1e-3,3e-3,1,e2,3e-2,1e-1,3e-1,1
2	Figure 4.19(b)	Squashing function a=0.1,0.3,0.5,1,1.5,2.0
3	Figure 4.19(c)	Reference signal amplification factor a=0.1,0.3,0.5,1,1.5,2.0

impulse is obtained from the methods outlined in Section 4.1.2 and is truncated to a length of 10 for simulation purposes. A 15th order DC-compensated NLMS algorithm with a normalized step

size parameter α=0.5 is used in all the following simulations. The converged ERLE values averaged over the last 4000 iterations of a 48000 sample data file are plotted.

For distortion method #1 the coefficients *b* and *c* produce a *signal-to-distortion ratio* (SDR) which is computed based on the method presented in Appendix E. The simulation results for distortion methods 1,2 and 3 are shown in Figure 4.19(a),(b) and (c). .

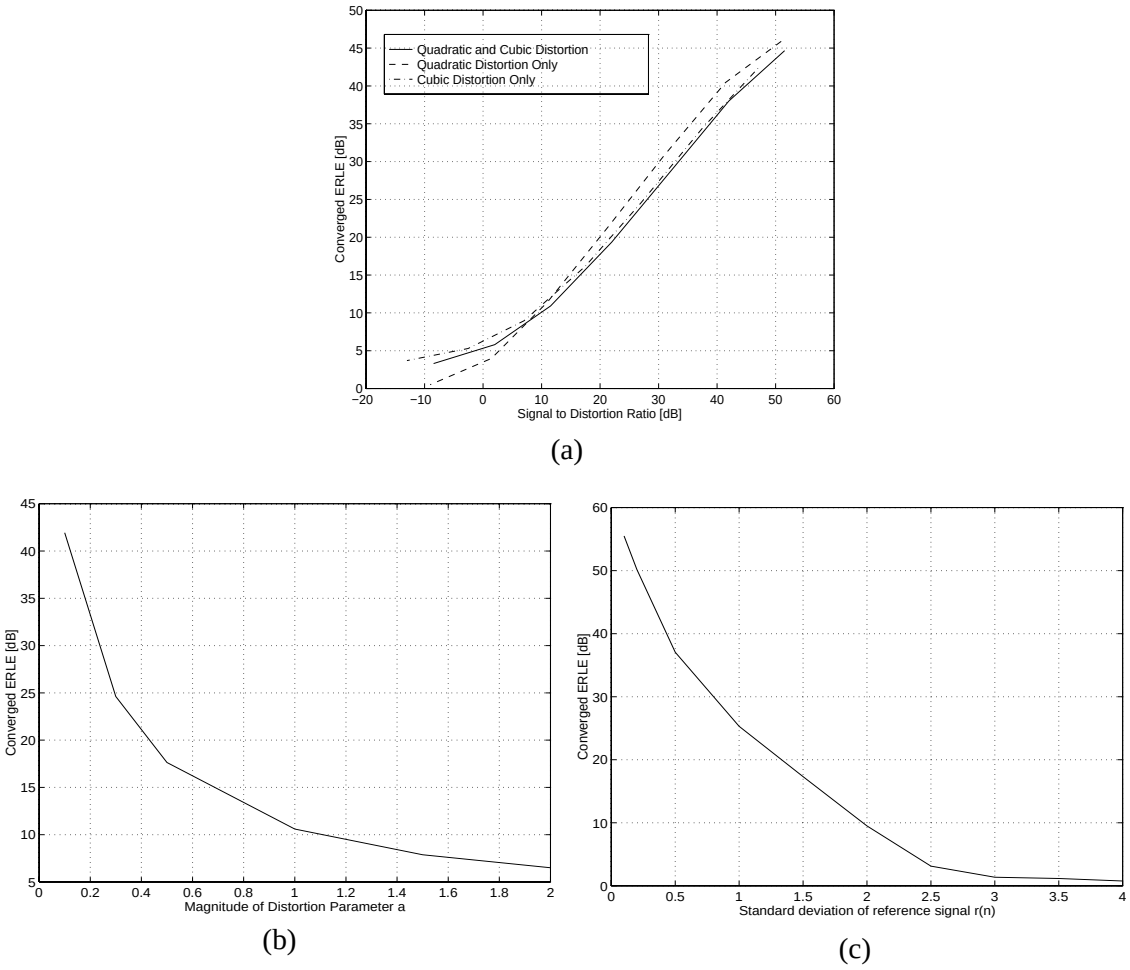

FIGURE 4.19 Simulation results showing ERLE performance of an adaptive FIR filter trained with the DC-compensated NLMS algorithm. (a) Distortion model #1. (b) Distortion model #2. (c) Distortion Model #3.

Effect of Bandlimited Primary Signal for Distortion Method #3. The primary, reference and error signal PSD's are plotted in Figure 4.20 for the case where a=1.5. In Figure 4.20 (a), the primary signal is not bandlimited. The error signal closely approximates the primary signal out-of-band, suggesting that the nonlinearity has produced out-of-band distortion products that cannot be removed by the linear adaptive filter. The converged ERLE is 18.14 dB. In Figure 4.20 (b), the primary signal is bandlimited to remove the out-of-band distortion products. However, in-band distortion products still limit the converged ERLE to 18.94 dB.

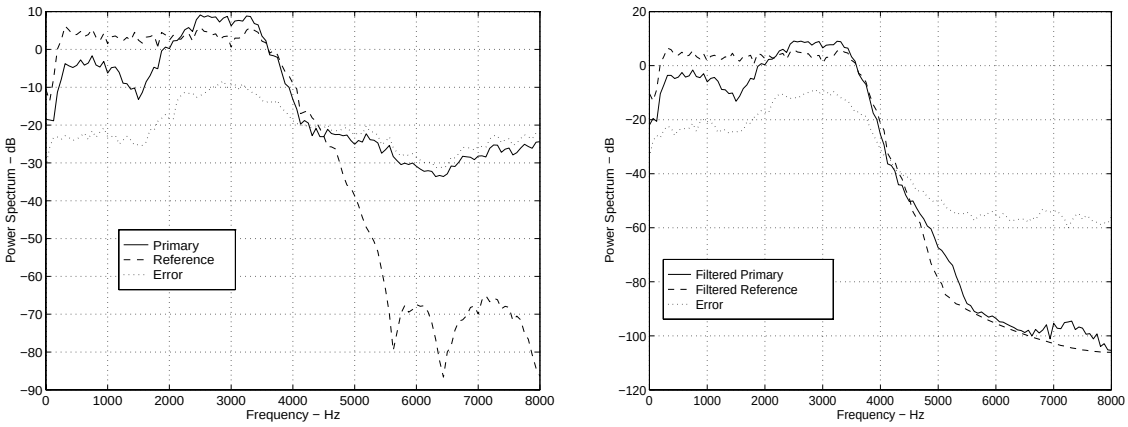

(a) (b)

FIGURE 4.20 Simulation results showing the PSD of the primary, reference and error signals for distortion model #3, a=1.5. (a) Unfiltered primary signal. PSD of error signal closely approximates the primary signals at the frequencies beyond the filter cutoff resulting in a converged ERLE of 18.14 dB. (b) Filtered primary signal. PSD of error signal is attenuated due to filter, however, in-band distortion products still limit ERLE to 18.94 dB.

4.6.3 Experimental Results

Figure 4.21 illustrates the PSD of the primary, reference and error signals of the transducer components of HFT #1 (mounted using the standard baffle) inside an anechoic chamber. The volume is 100 dB SPL, as measured 0.5 m from the loudspeaker. The error signal is obtained at the output of an adaptive FIR filter trained with the NLMS algorithm, a=0.5 and N=600 taps. Similar to the

computer simulation results shown in Figure 4.20, it can be seen that the error signal closely approximates the out-of-band primary distortion components in the 4-8 kHz frequency range. The converged ERLE for this SPL averaged over the last 4000 samples of a 32000 length training vector is 18.69 dB. These results are very similar to the simulated case.

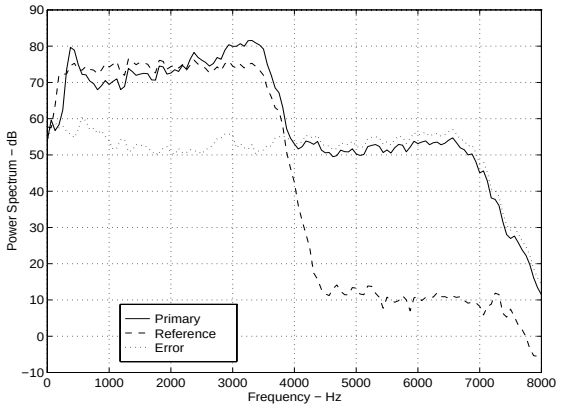

FIGURE 4.21 Experimental results showing the PSD of the primary, reference and error signals for HFT #1 transducer components as measured inside the anechoic chamber. The error signal closely approximates the primary signals at the frequencies beyond the filter cutoff.

4.6.4 Effect of Transducer Quality

A simple test showing the effect of a combination of high and low quality loudspeakers and microphones is illustrated in Figure 4.22. The relevant parameters are listed in Table 4.7.

TABLE 4.7 Transducer Parameters

Name	Definition	Model	Rating	Notes
HQL	High quality Loudspeaker	AD4061/W8	8Ω, 10W	4” dia. round. Large magnet, high quality.
LQL	Low quality loudspeaker		8Ω, 0.25W, 2”round spkr.	Removed from HFT#4
HQM	High quality microphone	Audio Technica AT831b and power module	Cardioid sens. -44 dBm 200Ω.	“High quality” microphone element.
LQM	Low quality microphone	Archer 270-090	4.5VDC thru ext. 1kΩ. S/N >40 dB, Sens.=-6.5 dB	Electret Microphone (low cost).

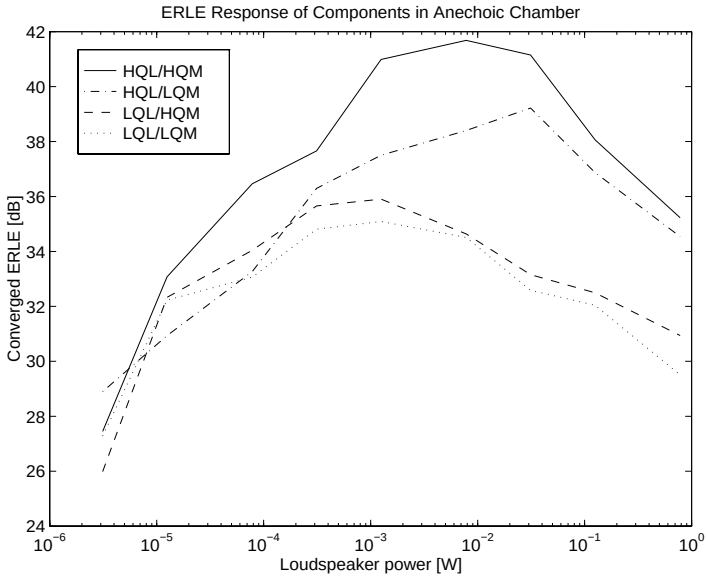

FIGURE 4.22 Combination of high or low quality loudspeaker (HQL or LQL) and a high or low quality microphone (HQM or LQM) on the ERLE performance as a function of loudspeaker power. The loudspeaker quality is the major component affecting achievable ERLE and the microphone quality is secondary. Parameters: 1000 tap dc compensated NLMS, α=0.5.

The ERLE averaged over the last 4000 iterations of a 48000 sample data file are plotted. The results show that the loudspeaker has the major effect on the achievable steady ERLE performance. The microphone has some effect on achievable ERLE but this is secondary with respect to the loudspeaker. These measurements were made in an anechoic chamber with the loudspeaker mounted in a standard baffle and the microphone placed 30 cm directly in front of the loudspeaker using a microphone boom. This measurement technique removes the effects of room noise, enclosure vibration, echoes and direct coupling. *The important observation is that the converged ERLE is low at both the high volume end (where nonlinearity is significant), and the low volume end, where circuit noise and two point suspension effects become significant*. The minimum modelling error occurs in the middle volume ranges

4.7 Summary and Discussion

The chapter has addressed the acoustic echo cancellation problem in HFT's. A review of the performance requirements has determined the following:

- Both speech enhancement and noise reduction techniques need to be employed to obtain an overall subjective improvement.
- Transducer nonlinearities need to be addressed to obtain the high ERLE values cited in the performance recommendations.
- Acoustic reverberation is shown to be an extremely complicated process that can only be modelled under statistical considerations.

Section 4.2 presents the measurement setup and illustrates that potential problems such as circuit noise, grounding, and cross-talk must be treated before making measurements to ensure that the minimum MSE obtained using a particular algorithm is due to the algorithm itself and *not* limitations in the test setup. Experiments have confirmed the maximum converged ERLE of the basic setup is approximately 56 dB.

In Section 4.3, the study of the application of IIR structures to the AEC problem concludes as follows:

- IIR model approximations do not lead to significant decreases in the number of parameters (compared to FIR models) necessary to obtain the same ERLE values.
- The Hankel norm approximation error bound for IIR filters has similar characteristics to the TIP/TP ratio, and suggest that IIR structures are not well suited to modelling typical LREM's.

In Section 4.4, various performance limitations are studied, with conclusions as follows:

- An analysis of noise, finite precision effects and quantization shows that these limitations are generally far below the typical ERLE levels encountered in real world AEC's.

- There seems to be a close correlation between the ERLE limits predicted by the TIP/TP ratio and the Hankel error bound.

In Section 4.5, the effects of enclosure vibration and resonances are studied, with the following conclusions:

- Rattling keys and handsets on the terminal have a measurable effect on the achievable ERLE. Limiting the movement of keys and handsets generally improves the achievable ERLE.
- Results have been presented which illustrate that direct coupling between the microphone and loudspeaker due to the enclosure radically changes the impulse response.
- Enclosure vibration can be a more serious problem than loudspeaker distortion as measured in a number of commercially available HFT's. However, it is highly dependent on the type of HFT enclosure.

In Section 4.6, the effects of transducer nonlinearity are studied. The conclusions are summarized as follows:

- In the absence of other limitations, loudspeaker nonlinearity will limit the achievable steady state ERLE in linear structures. The ERLE value will be determined approximately as the ratio of the powers of the nonlinear distortion products to the linear products within the primary signal.
- Distortion products manifest themselves as harmonics which will be generated both within and outside the bandwidth of interest.
- There is a high degree of correlation between the uncancelled error signal and the out-of-band distortion products in both simulated and experimental results using linear structures.
- Given that the vibration and resonances can be removed through proper acoustic design, improvements in transducer quality will also improve the achievable ERLE.

Summary of Steady-State Performance Limitations.

- Undermodelling of the acoustic transfer function is directly related to the number of taps in the adaptive filter, and will be the major limitation when the number of taps is insufficient to cover the LREM impulse response.
- Given a sufficient number of taps, the limitations to the steady-state ERLE are *in order of importance*; (1) enclosure vibration and/or nonlinear distortion, (2) room noise (in a typical conference room) and (3) DSP and circuit noise.
- The effect that vibration and loudspeaker nonlinearity have on the achievable ERLE is highly dependent on the frequency and volume of the reference signal as well as the type of HFT being used.

An illustration showing the relative contributions is illustrated in Figure 4.23.

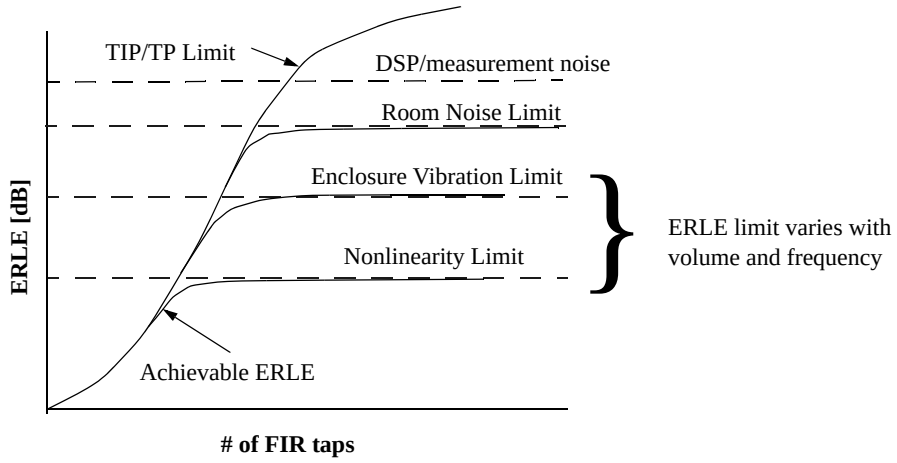

FIGURE 4.23 Achievable ERLE as a function of physical limitations.

Chapter 5
Nonlinear Structures For Acoustic Echo Control

This chapter presents several new architectures consisting of cascaded nonlinear and linear sections for the identification of nonlinear systems with memory and dispersion. The specific application is for improved ERLE performance for nonlinear echo cancellation in the HFT domain.

In the first two subsections the Volterra and multi-layer neural network filter models are applied to the identification of both simulated and experimental data. The results presented form a *baseline* for comparison to the new architectures presented in subsequent sections. Next, the following new structures are developed; (1) A parallel cascaded neural network-FIR structure with a *mixed linear-sigmoid* activation function; (2) A TDNN structure that uses *fully adaptive* activation functions in addition to the variable weights in the hidden layers; (3) A cascaded *synaptic FIR* neural network including the *adaptive activation* functions described previously. The learning rules are derived by modifying the gradient backpropagation algorithm for the specific architecture.

5.1 The Adaptive Volterra Filter

Adaptive Volterra filters have been applied to compensation of low frequency loudspeaker nonlin-

earities [4][13], however, all the loudspeakers tested in the literature are “woofer” designs and the author could find no literature on the application of Volterra filters to small loudspeakers, such as those encountered in the HFT domain. To this end, data obtained from an HFT inside a typical conference room, as well as HFT audio transducers (as measured inside an anechoic chamber) are applied to a nonlinear adaptive Volterra filter to determine how well it is suited for this application. Simulation results comparing the LMS-Volterra and NLMS-FIR filters on the distortion models from Section 4.6.1 are first examined.

5.1.1 Simulation Examples

A 3rd order adaptive LMS-Volterra filter is constructed to study how it behaves while attempting to model nonlinearity as generated using the artificial distortion methods of Section 4.6.1. Tap updates are based on the Volterra algorithm in Appendix D.8. Results are compared to the NLMS-FIR filter. For each of the simulation results, the filters are allowed to train for 64,000 samples and the converged ERLE results are obtained from the average of the last 4000 points.

Distortion Model #1, combined quadratic and cubic distortion. In this test the following parameters are used: $m_1 = m_2 = m_3 = 10$, $\alpha = 0.5$, $\mu_1 = 0.1$, $\mu_2 = 0.01$, $a = 1$, $b = c = 0.2$. The results are shown in Figure 5.1 with a performance summary given in Table 5.1. The reference signal $r(n)$ in this test case is a uniformly distributed white noise source with unit variance, which is either filtered first or applied directly to the distortion generator and dispersive LREM, similar to the method in Figure 4.16.

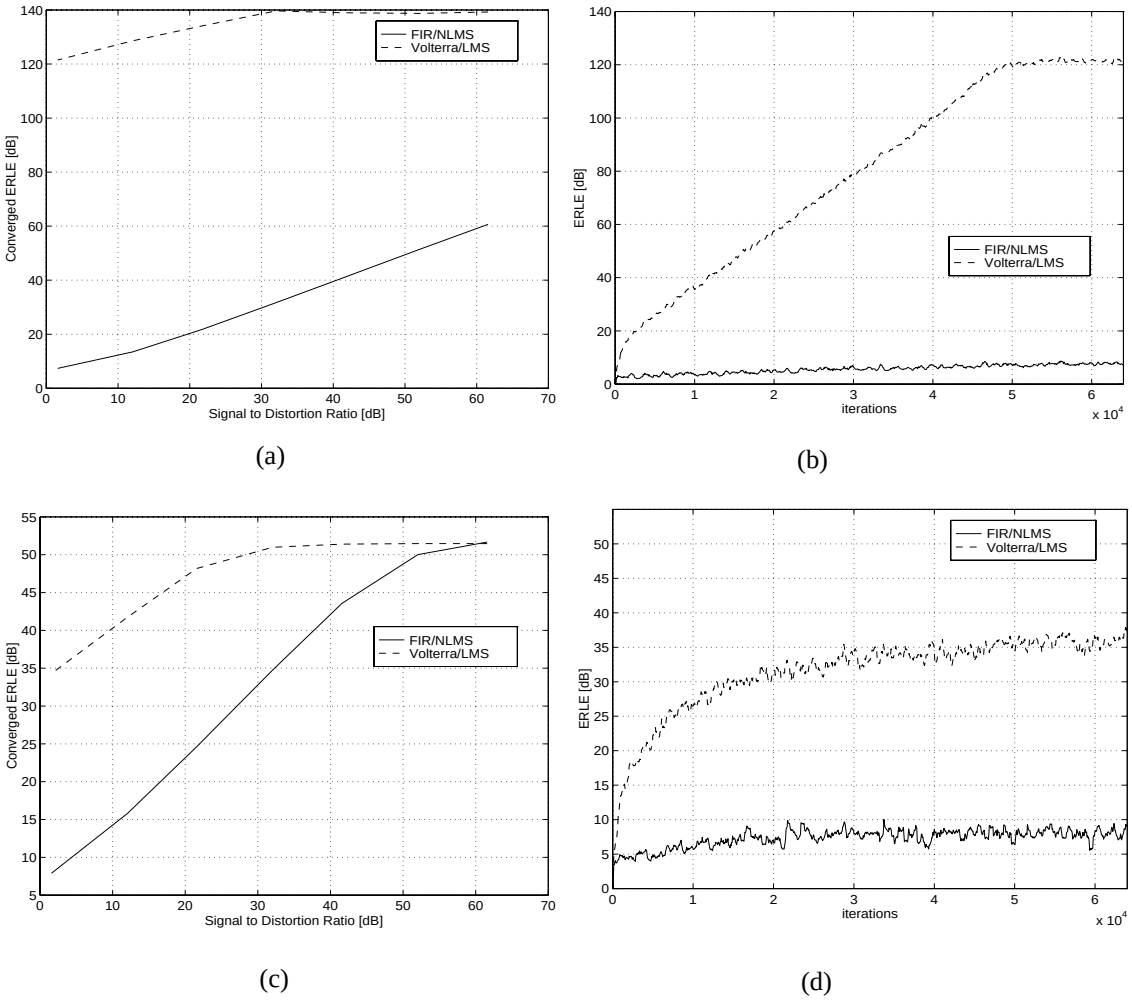

FIGURE 5.1 Simulation results. Volterra identification of a nonlinear system generated using distortion model #1 (a) converged ERLE vs. SDR, unfiltered *r*(*n*). (b) convergence curve for highest distortion level, unfiltered *r*(*n*). (c) converged ERLE vs. SDR, filtered *r*(*n*). (d) convergence curve for highest distortion level, filtered *r*(*n*).

TABLE 5.1 Summary of simulation results shown in Figure 5.1.

Reference Filtering	**Figure**	**Converged ERLE**	
		NLMS-FIR	**LMS-Volterra**
Unfiltered	Figure 5.1(a), (b)	17.9 dB	132.9 dB
BPF filtered	Figure 5.1(c), (d)	15.3 dB	44.2 dB

The results shown in Figure 5.1 (a) and (b) illustrate the convergence curves for the unfiltered case

for different distortion parameters, where *b=c* are varied. The Volterra filter can easily identify the unknown system. However, the results in Figure 5.1 (c) and (d) also indicate that when the signal is filtered, the performance of the LMS-Volterrafilter is degraded.

Distortion Model #2 and #3. The simulation results for distortion model #2 and #3 are shown in Figure 5.2(a) and (b). For distortion model #2, $m_1=m_2=m_3=10$. For distortion model #3, $m_1=m_2=m_3=20$. For both cases, $\alpha_1=0.5$, μ_2=1e-1 and μ_3=1e-2.

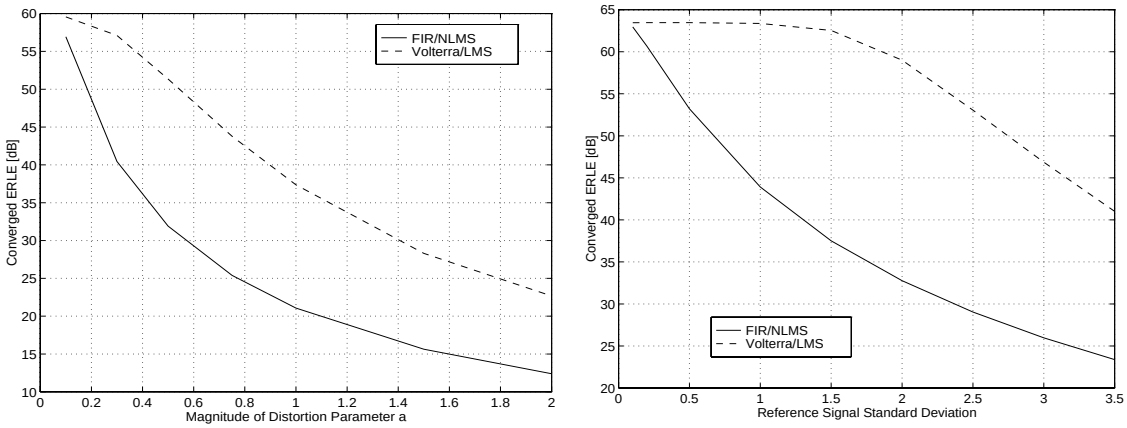

(a) (b)

FIGURE 5.2 Simulation results. Converged ERLE using a Volterra filter for the identification of a simulated nonlinear system generated using (a) distortion method #2 (b) distortion method #3.

In the simultions presented above, the Volterra filter consistently outperforms the linear FIR filter.

5.1.2 Experimental Results

A fully connected 3rd order adaptive Volterra filter with m_1=1000, m_2=100 and m_3=40 is constructed in an attempt to model *real-world* loudspeaker nonlinearity in a typical AEC configuration. Tap updates are based on the algorithm in Appendix D.8 with a normalized step size parameter α_1=0.5, μ_2=1e-1 and μ_3=1e-2. Three experiments are conducted, using data which was recorded in different venues using different HFT's. For all experiments, the sound source is fil-

tered noise, as per the test set-up described in Section 4.2.3, recorded at a volumes ranging from 55 to 100 dB SPL as measured at 0.5 m directly above the loudspeaker.

HFT #1, Anechoic Chamber, with and without enclosure. The loudspeaker and microphone from HFT #1 are removed and placed in an anechoic chamber for the first set of measurements. Subsequently, they are placed back inside the HFT enclosure for a second round of measurements. The results shown in Figure 5.3(a) illustrate that approximately 6 dB improvement in converged ERLE can be obtained using the LMS-Volterra filter compared to a1000 tap NLMS-FIR filter for identifying an LREM consisting of the audio transducers only. In Figure 5.3(b) the converged

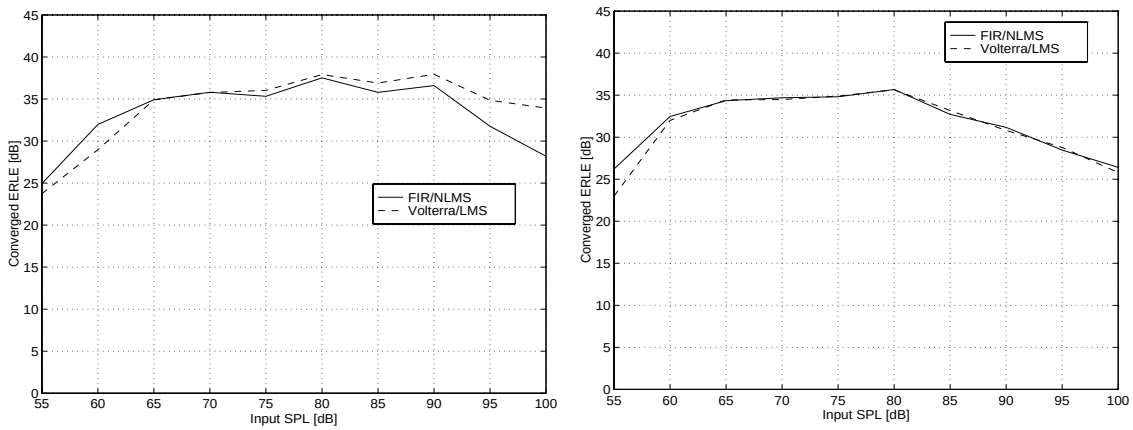

FIGURE 5.3 HFT #1 results, anechoic chamber. Converged ERLE vs. SPL for (a) separately mounted transducer components and (b) with components mounted inside the enclosure.

ERLE vs. volume is shown for HFT#1 with the components mounted inside the enclosure. Notice that the LMS-Volterra filter is no longer able to obtain any gains over the FIR filter. This is due to the vibration limits as discussed in Section 4.5. The converged weights of the Volterra filter are illustrated in Figure 5.4(a), (b) and (c) which show the weight values obtained for the linear, quadratic and cubic sections respectively. The *difference* between the linear weights obtained with the

NLMS algorithm is also shown in Figure 5.4(d).

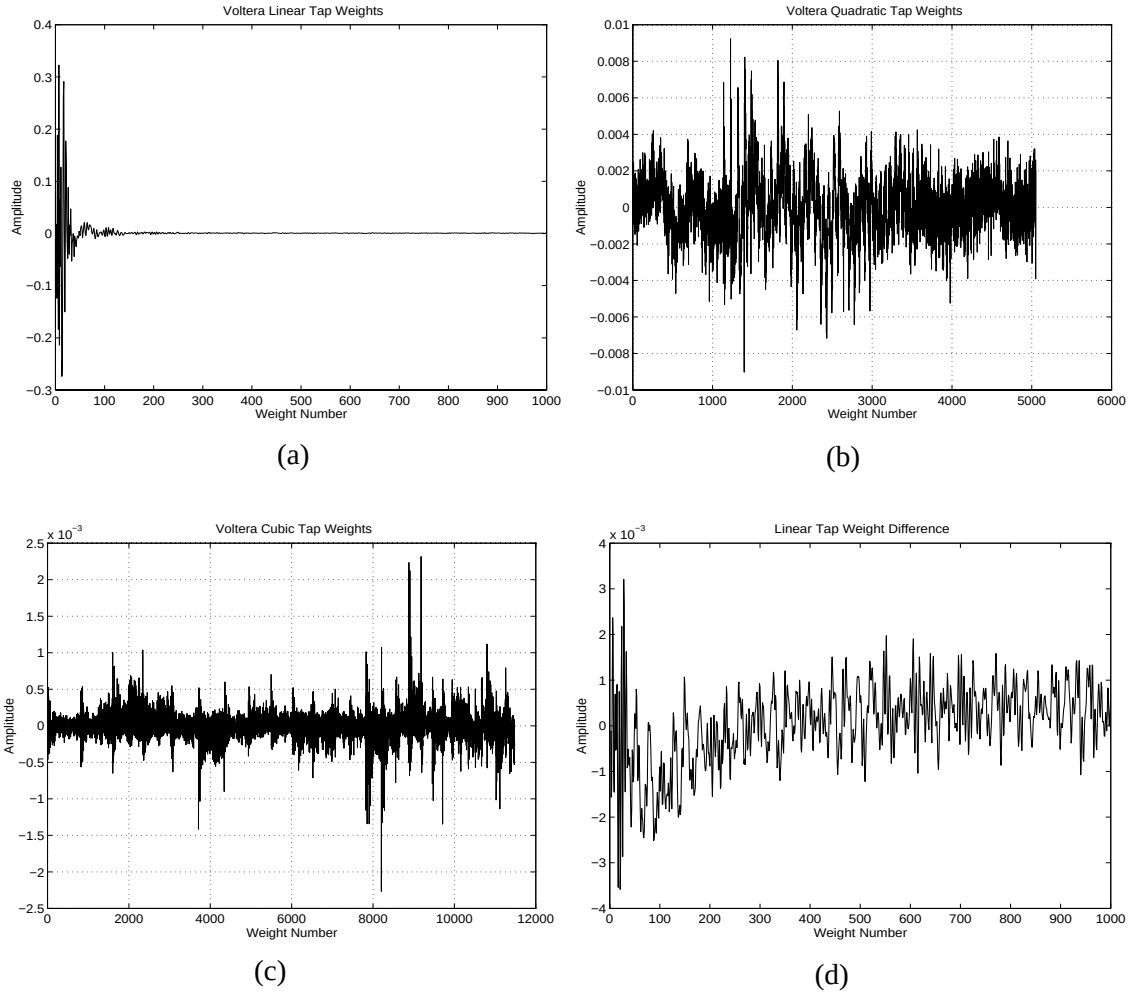

FIGURE 5.4 Volterra tap weights for HFT #1 at 100 dB SPL. (a) Linear tap weights, (b) quadratic tap weights. (c) Cubic tap weights. (d) difference between Volterra and FIR linear tap weights.

HFT #6 in Conference Room #2. HFT #6 is stiffened against vibration. The results shown in Figure 5.5 indicate that using this HFT a 7.1 dB performance improvement over the NLMS-FIR filter may be obtained.

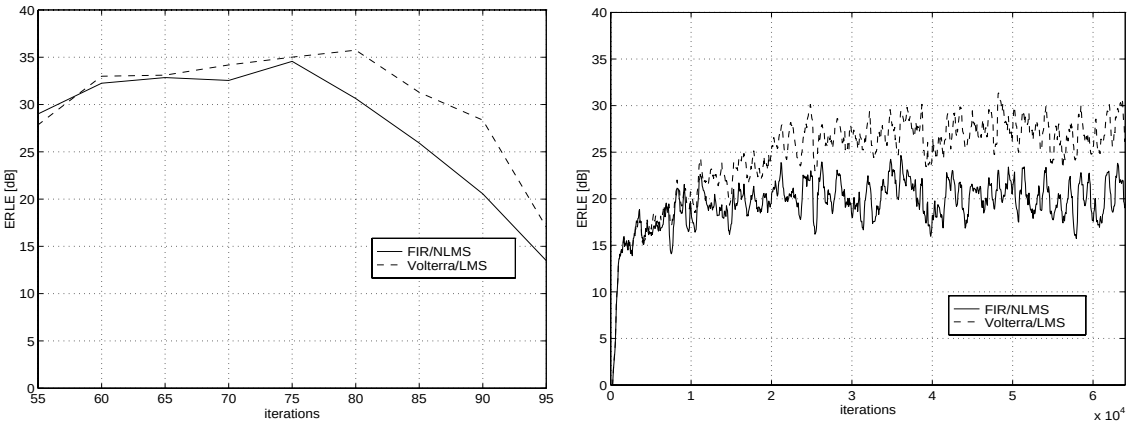

(a) (b)

FIGURE 5.5 HFT #6 results. (a) Converged ERLE vs. SPL. (b) Convergence curves for data at 90 dB SPL.

A summary of the experimental results showing the regions of greatest improvement over the FIR filter structure is shown in Table 5.1.

TABLE 5.2 Summary of experimental parameters and results for the Volterra filter.

Experiment Location	Figure	Components	SPL Volume	Converged ERLE		Improvement over FIR
			[dB]	FIR/ NLMS	Volterra /LMS	dB
Anechoic	Figure 5.3 (a)	HFT #1 Components	100	27.3dB	33.5 dB	6.2
Anechoic	Figure 5.3 (b)	HFT #1	95	28.6	28.8	0.2
Conference	Figure 5.5 (a)	HFT #6	90	21.2 dB	28.3 dB	7.1

5.1.3 Discussion

The LMS-Volterra filter is easily able to outperform the NLMS-FIR filter by several 10's of dB when presented with *simulated* data. However, the convergence rate may be severely limited by the increased eigenvalue spread of the input data, which becomes prohibitive as the number of filter parameters increases.

Assuming an LMS update, the Volterra filter will have a an approximate complexity of $2M_e$+2

where M_e is the dimension of the extended weight vector according to equation (3.59). Assuming a 1000 tap input from which 100 taps and 40 taps are used to obtain the quadratic and cubic sections respectively, the length of the extended vector will be will be 17530 weights, resulting in astaggering complexity of approximately 35062 multiplications per iteration.

For nonlinear AEC's using *experimental* data, it appears that the nonlinear Volterra filter can improve the ERLE significantly, for example by 7.1dB using HFT #6. However these results are highly dependent on the type of HFT being tested. An improvement could only be obtained when either (i) audio components were isolated (and vibration was not a limiting factor) or (ii) HFT #6 was used (HFT#6 is stiffened against vibration). The experimental results also show that the convergence is quite slow, and given the added complexity, this technique has a disadvantage for real-time applications. These results suggest that alternative models and structures should be investigated.

Experimental results also show that there is very little difference between the *linear* weights obtained using either the FIR or Volterra filter, and that only a small percentage of the nonlinear weights are significant. Although results are not presented here showing nonlinear tap weights for other volumes, analysis of experimental data at other volumes has determined that they do change significantly with a change in applied volume. *A set of nonlinear weights for one volume does not necessarily correspond to the weights obtained at a different volume*. This means that a significant number of higher order weights must be retained to obtain a good modelling accuracy, however, this results in an overwhelming number of weights and poor convergence. An "on-line" technique for selecting the significant weights and pruning nonsignificant weights would be advantageous for obtaining reduced complexity, however this is beyond the scope of this thesis.

5.2 Neural Network Adaptive Filter

As an alternative to Volterra filters, *artificial neural network* (ANN) filters can be used to perform nonlinear adaptive filtering. The "conventional" neural network filter structure uses a tapped delay line (TDL) at the input to a static MLP as illustrated in Figure 5.6. Waibel *et al*. first proposed this structure in [46] and referred to it as a *tapped delay line neural network* (TDNN). The structure is defined by the nomenclature (n_i,h_1,h_2,n_o) which refers to the number of input nodes (i.e. number of

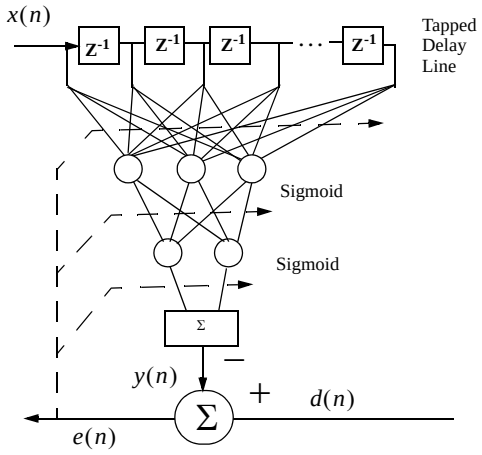

FIGURE 5.6 Tapped delay line neural network (TDNN) filter.

inputs from the TDL), the number of neurons in the first and second hidden layers, and the number of output nodes respectively. For all the results that follow, n_o is set equal to 1 and each node in the hidden layer has a *tanh*( ) sigmoid function defined by the equation (3.6). The output node is a linear summation and the activation potential to each sigmoid includes an adjustable bias.

5.2.1 Computer Simulation Examples

A two layer TDNN filter is applied to the three distortion models described in Section 4.6.1. Tap updates are based on the gradient BP method using a normalized step size (with respect to the power in the TDL) with α=0.5. For each of the simulation results, the algorithms are allowed to

train for 64,000 samples and the converged ERLE results are obtained from the average of the last 4000 points.

Simulation #1: Selection of number of hidden nodes for a two layer TDNN. In this test a comparison of the two layer TDNN and FIR filters is presented using a 10 tap input with a normalized step size of 0.2, and distortion model #1. The reference signal $r(n)$ in this test case is a uniformly distributed white noise source with unit variance, which is applied directly to the distortion generator (quadratic and cubic distortion) and dispersive LREM, similar to the method in Figure 4.16. The number of hidden nodes is first selected by trying a number of different architectures based on the models $(10,n_1,1)$ where n_1 represents the number of hidden nodes. The results showing converged ERLE are shown in Figure 5.7 for different n_1 with quadratic/cubic distortion generated according to method #1, for high level distortion (a=b=c=1) and low level distortion (a=1, b=c=0.2). Figure 5.7(a) shows the result when an unfiltered reference is used and Figure 5.7(b) show the results for a bandpass filtered reference.

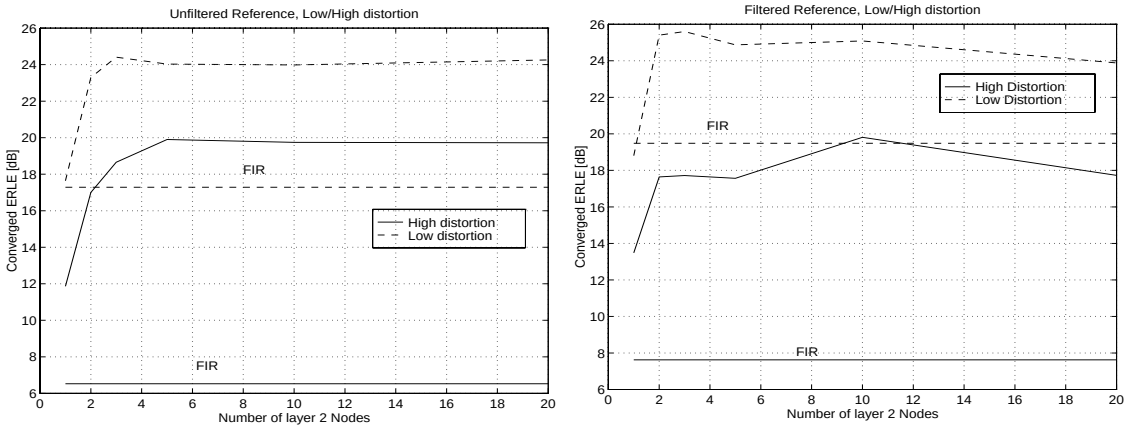

(a) (b)

FIGURE 5.7 Simulation #1 results showing converged ERLE vs. increasing number of hidden nodes for a $(10,h_1,1)$ TDNN. (a) Unfiltered reference (b) Filtered reference.

Based on these results, a (10,5,1) model was chosen for subsequent tests as a good compromise

between complexity and performance. The results of Figure 5.7 show that there is very little difference between the performance of the TDNN structure when the reference data is filtered or unfiltered. For “low level” distortion with b=c=0.2, the simulated TDNN performance in Figure 5.7 is between 6 and 7 dB higher than the equivalent FIR structure.

Simulation #2: Distortion models #1, #2 and #3. The simulation results shown in Figure 5.8 (a) (b) and (c) are obtained using the methods in Section 4.6 and distortion models #1, #2 and #3 respectively.Again, the TDNN structure obtains a higher ERLE value in the *high* distortion ranges, but is generally not as good as the FIR-NLMS structure as *low* distortion levels.

Simulation #3: Comparison of two and three layer TDNN. In this simulation, a comparison of the number of parameters for two and three layer TDNNs is done for the case where the artificial room impulse response is of length 500. In this simulation, distortion model #1 is used with a=1, b=c=0.2.Results shown in Table 5.3 summarize the results.

TABLE 5.3 Simulation results using TDNNs with one and two hidden layers.

LREM order	Type	Size	Step Size	Converged ERLE [dB]
500	FIR	(500 tap)	0.5	16.3
500	2 hidden layers	TDNN (500,5,5,1)	0.5	15.1
500	2 hidden layers	TDNN(500,5,2,1)	0.5	15.5
500	2 hidden layers	TDNN(500,2,2,1)	0.5	16.0
500	1 hidden layer	TDNN(500,5,1)	0.5	16.9
500	1 hidden layer	TDNN(500,2,1)	0.5	17.3
500	1 hidden layer	TDNN(500,1,1)	0.5	17.5

The three layer network consistently performs *worse* than the FIR linear counterpart and suggests that in the context of nonlinear AEC application, *networks with a single hidden layer are suitable to the task.*

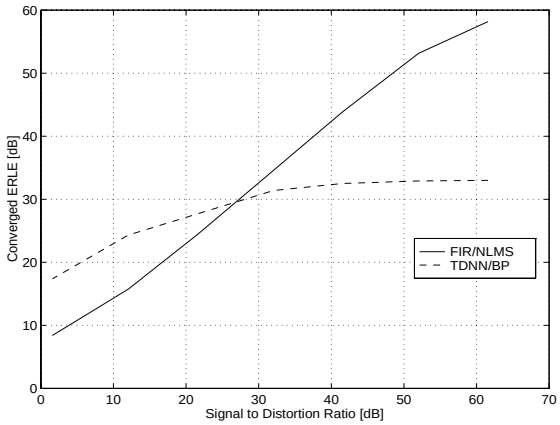

(a)

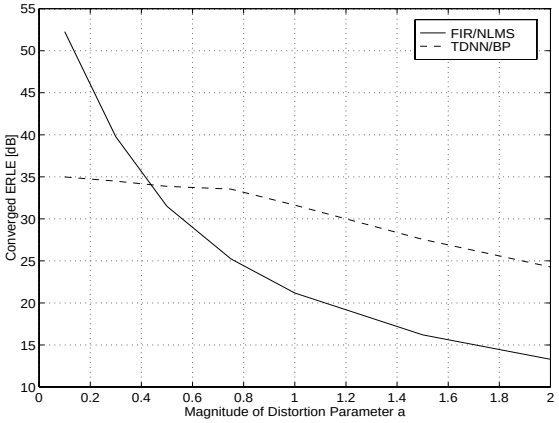

(b)

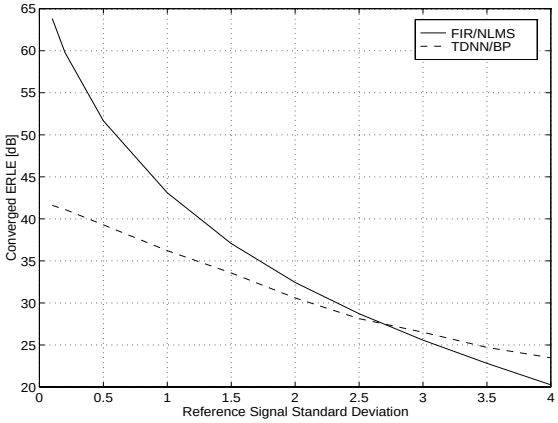

(c)

FIGURE 5.8 Simulation results for (a) distortion method #1, (b) distortion method #2 and (c) distortion method #3. A (10,5,1) TDNN is used for (a) and (b) and a (15,5,1) TDNN is used for (c) to cover the impulse response generated by method #3.

5.2.2 Development of a Mixed Linear-Sigmoid Activation Function

A neural network filter will generate a finite amount of distortion due to the nonlinear nature of the sigmoid. In some simulations, the TDNN performs worse or only slightly better than a conventional FIR adaptive filter, especially at low distortion values as demonstrated in Section 5.2.1. In order to mitigate this effect, a *mixed linear-sigmoid activation function* is proposed which has a linear portion in the middle The nonlinear node consists of a linearized hyperbolic tangent function

which is linear for inputs below a user definable amplitude p, where $0 \le p \le 1$. By setting the parameter p it is possible to reduce the modelling error by a few dB compared to a conventional (i.e. p=0) sigmoid[1]. The node activation function $\varphi(s,p)$ is defined by;

$$\varphi(s,p) = \begin{cases} s & ;|s| \le p \\ \text{sign}(s)\left[(1-p)\cdot\tanh\left(\dfrac{|s|-p}{1-p}\right)+p\right] & ;|s| > p \end{cases} \quad (5.1)$$

where s is the input. Differentiating (5.36) with respect to s, we obtain the slope of the activation function:

$$\varphi'_s(s,p) = \begin{cases} 1 & ;|s| \le p \\ \text{sign}(s)[1-\tanh(\theta)^2] & ;|s| > p \end{cases} \quad (5.2)$$

$$\text{where } \theta = \left(\frac{|s|-p}{1-p}\right)$$

Figure 5.9 shows the activation function of equation (5.36) with values of p equal to 0.0, 0.5, and 0.9, along with the associated $\varphi'_s(s,p)$ values.

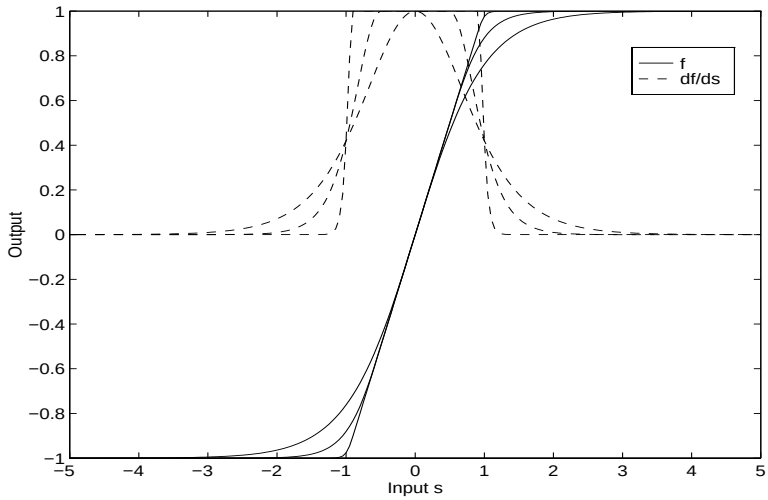

FIGURE 5.9 Adaptive activation function and derivative with respect to *s* for *p*=0.0, 0.5 and 0.9.

1. Improvements depend on the severity of the nonlinear distortion.

For data that is weakly nonlinear, the weights in the TDNN will adjust to provide an activation in the linear region of the sigmoid, and thus offer improved performance. Simulation results showing the effect of varying the linear region versus converged ERLE are shown in Figure 5.10 using distortion model #1 when a=1, b=c=0.01 (low distortion) and b=c=0.5 (high distortion). The optimum value of linear region is highly dependent on the severity of nonlinearity encountered, however, based on these results, the linear region p was set to either 0.0 or 0.5 in subsequent simulations, as a good compromise between the two extremes. A better solution is to implement an *adaptive* activation function, and this is discussed further in Section 5.5.

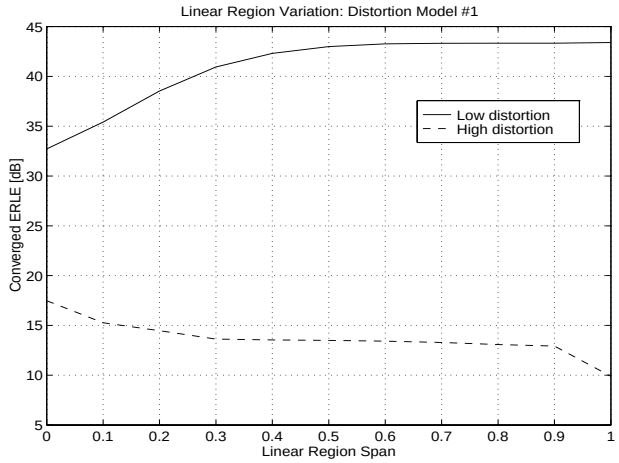

FIGURE 5.10 Effect of changing linear region in a mixed linear-sigmoidal activation function. (10,5,1) TDNN on distortion model #1 with a=1 and b=c=0.01 (low distortion) and b=c=0.5 (high distortion)

5.2.3 Experimental Results

A fully connected two-layer TDNN is used to model the loudspeaker nonlinearity in a typical AEC configuration. Tap updates are based on the BP algorithm with a normalized step size parameter α=0.5. For the experiments that follow, the sound source is filtered noise, as per the test set-up

described in Section 4.2.3, recorded at a various volumes ranging from 50 to 100 dB SPL as measured at 0.5 m directly above the loudspeaker.

HFT #3, Anechoic Chamber, no enclosure. The results in Figure 5.11 indicate that a significant difference in performance comes about as a result of changing the "linear" region of the sigmoid activation function, for the case where 300 taps are used in the input TDL. For example, by changing *p* from 0.5 to 0.0, an *improvement* of 4.8 dB ERLE is seen in the 100 dB SPL range, but a *degradation* of 1.9 dB is observed at 75 dB SPL. Another significant result is that a (1000,1,1) structure performs worse than a (300,1,1) TDNN structure, all other parameters being the same.

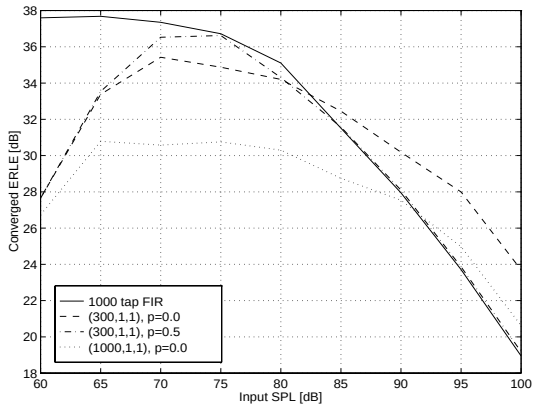

FIGURE 5.11 HFT #3 experimental results, anechoic chamber, components only.

HFT #1, Anechoic Chamber, with and without enclosure. The results shown in Figure 5.12 (a) are for the isolated components case and illustrate that a marginal improvement in converged ERLE can be seen using a (300,1,1) TDNN as compared to the standard 1000 tap NLMS-FIR filter. *However, at 75 dB SPL, an improvement of approximately 4 dB is obtained. Note that this level of improvement was not achieved using the Volterra filter structure* (refer to Figure 5.3 a). The results for the transducers mounted inside the HFT enclosure are shown in Figure 5.12 (b). The

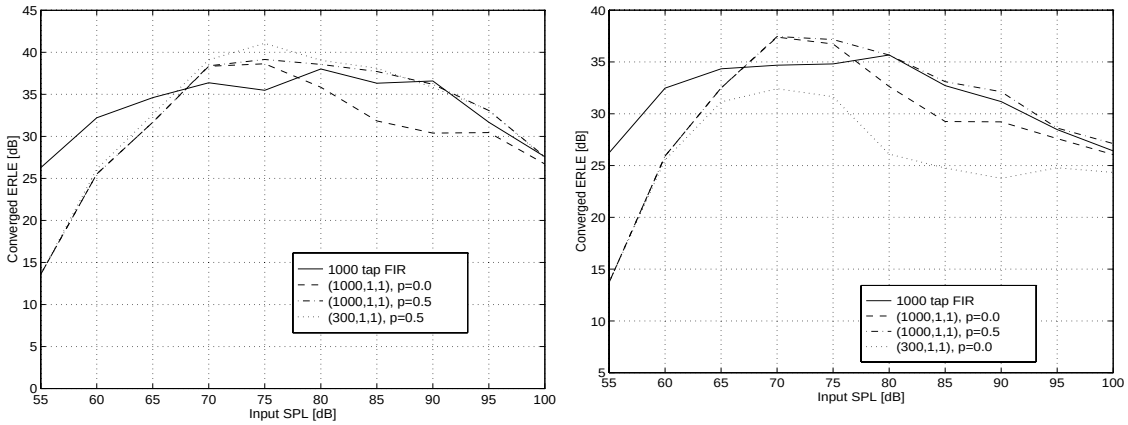

(a) (b)

FIGURE 5.12 HFT #1 results, anechoic chamber, TDNN. Converged ERLE vs. SPL for (a) separately mounted transducer components and (b) with components mounted inside the HFT enclosure.

TDNN structure has difficulty in identifying the HFT transfer function, but again, this can be attributed to the vibration limits as discussed in Section 4.5

HFT #6 in Conference Room #2. HFT #6 is stiffened against vibration. The results shown in Figure 5.13 indicate that performance is better than the NLMS-FIR filter for volumes greater than 57 dB SPL when using an HFT #6. Over 5 dB improvement is observed at 65 dB SPL.

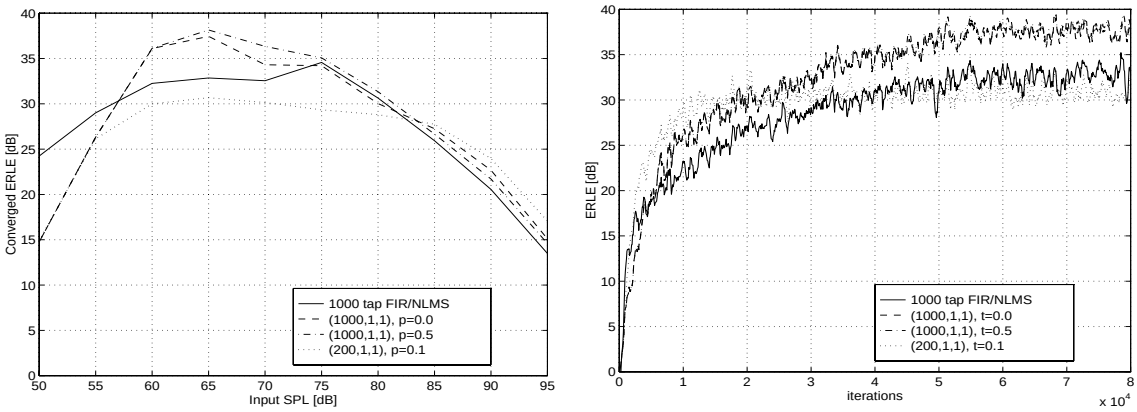

(a) (b)

FIGURE 5.13 HFT #6 results for a 2 layer TDNN. (a) Converged ERLE vs. SPL for the NLMS, (1000,1,1) and (200,1,1) structure. (b) Convergence curve for data at 65 dB SPL.

A summary of the experimental results showing the areas of greatest improvement is given in Table 5.1.

TABLE 5.4 Summary of experimental results showing regions of greatest improvement.

Figure	**Experiment /Location**	**HFT**	**TDNN parameters**		**SPL**	**Converged ERLE**		**Improvement over FIR**
			Model	***p***	**[dB]**	**1000 tap FIR/ NLMS**	**TDNN/ BP**	**[dB]**
Figure 5.12(a)	Anechoic	HFT #1 Components	(300,1,1)	0.5	75	35.5 dB	41.1 dB	5.6 dB
Figure 5.12(b)	Anechoic	HFT #1	(1000,1,1)	0.5	70	34.7 dB	37.5	2.8 dB
Figure 5.11	Anechoic	HFT #3 Components	(300,1,1)	0	100	18.9 dB	23.7	4.8 dB
Figure 5.13	Conference	HFT #6	(1000,1,1)	0.5	65	32.8dB	38.1 dB	5.3 dB
Figure 5.13	Conference	HFT #6	(200,1,1)	0.1	95	13.4	17.1	3.7 dB

5.2.4 TIP/TP Performance for the TDNN in the Undermodelled Case

Experimental data was applied to the TDNN structure to determine the optimum length for the TDNN section for the highest volume (100 dB SPL) case. The results shown in Figure 5.14 illustrate that for a system with undermodelling of the impulse length, a TDNN structure has improved ERLE performance compared to the NLMS-FIR filter. The experimental data was obtained from HFT #3 components in an anechoic chamber. The TDNN model is an (n_0,2,3,1) structure. The best performance occurs when the number of input taps n_0=150 taps. Here the difference between the TDNN and FIR ERLE value is approximately 5.5 dB.

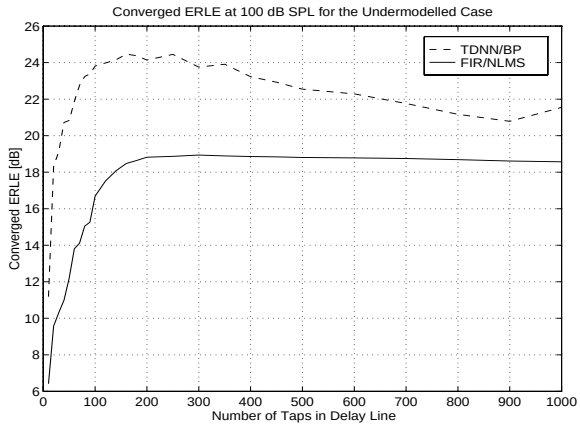

FIGURE 5.14 HFT #3 components (i.e no enclosure), anechoic chamber. In an undermodelled state a TDNN obtains a higher ERLE as compared with the FIR structure.

5.2.5 Discussion

The simulation results presented in Section 5.2.1 indicate that the TDNN structure is capable of obtaining improved steady state ERLE performance when the nonlinear distortion becomes significant. For low distortion, the TDNN is unable to model the nonlinearity as well as the linear FIR filter.

The complexity breakdown for a two layer TDNN is listed in Table 5.5.

TABLE 5.5 TDNN complexity assuming a single node output.

Equation Number	Description	Layer	Mults.
(3.60)	vector dot product	Input	n_0*n_1
(3.67)	weight update	Input	n_0*n_1+2
(3.67)	bias update	Hidden	n_1
(3.60)	vector dot product	Hidden	n_1
(3.67)	weight update	Hidden	n_1+2
(3.67)	bias update	Output	1
(3.68)	delta calculation	Output	1
(3.68)	delta calculation	Hidden	n_1+2
	TOTAL		$4*n_1+2*n_0*n_1+8$

Note: n_0 equals the number of input nodes (TDL length), and n_1 equals the number of hidden layer nodes.

If we assume a 1000 tap input, with a 2 node hidden layer (i.e. n_0=1000, n_1=2), the complexity is approximately 4015 multiplications per iteration.

Simulations using LREM's of length 500 show that a TDNN with a *single* hidden layer is preferable over one with two hidden layers, and that a single node in the hidden layer was sufficient to obtain ERLE improvements. From the perspective of nonlinear AEC application, this is beneficial since such structures have a complexity comparable to the NLMS-FIR filter.

The use of an activation function with a definable linear region is beneficial in low distortion environments. Simulation results have shown that for low distortion environments, a large linear region is preferable, whereas for high distortion environments, the converse is true, and suggests that some form of *adaptive control* of the activation function may be beneficial.

Experimental results in Section 5.2.3 show that a two layer TDNN can obtain improvements in converged ERLE between 2.8 and 5.6 dB at medium to high volumes where the distortion is greatest, but does not perform as well as the linear FIR filter at low volumes. This is also observed in the simulations.

When HFT's contain significant vibration due to poor enclosure design, the TDNN structure is unable to obtain any clear improvements in ERLE, similar to results presented for the Volterra case. However, where the HFT components are isolated, or where the HFT design mitigates the vibration problem, the TDNN can improve the ERLE by up to 5.6 dB compared to the NLMS-FIR filter.

TDNN performance also depends on the type of HFT being used. For example, at 65 dB SPL, a (1000,1,1) TDNN structure will yield a net ERLE *gain* of 5.3 dB for HFT #6 but can have a net *loss* of 3.8 dB for HFT #1.

A surprising new result demonstrated in Section 5.2.4 is that a simple multilayer TDNN structure is capable of obtaining improved ERLE convergence over that of a linear FIR structure for the *undermodelled* case and suggests an intelligent way of combining low order TDNNs with linear FIR structures for obtaining improved performance in both the low and high volume ranges.

5.3 Comparison of Results - Volterra vs. TDNN

Complexity. For low order systems, the Volterra network is an attractive option for dealing with weak nonlinearities. However, in AEC applications, the system orders make the complexity prohibitively large. The TDNN offers comparable performance at a fraction of the cost of a fully connected Volterra filter. For example, a 1000 tap NLMS-FIR filter will have a complexity of approximately 2004 multiplications per iteration. The TDNN structure has a computational requirement of 4015, approximately *twice* that of the LMS algorithm. By comparison, the Volterra complexity is *17 to 20 times* that of the LMS algorithm.

Convergence. The Volterra algorithm has an initial convergence comparable to the NLMS algorithm but slows down considerably as the MSE decreases. The TDNN structure has a slower initial convergence than the NLMS algorithm but can obtain a steady state MSE faster than the Volterra algorithm. This suggests that a method of improving the convergence, without sacrificing tracking ability would be advantageous.

Modelling Accuracy. The Volterra filter obtains slightly better error performance than the TDNN structure for most of the cases investigated. For low volumes, the Volterra filter obtains the same performance as the linear FIR structure. The TDNN structure on the other hand has difficulty in obtaining the same performance as the linear FIR structure at low to medium volumes as predicted by the computer simulations. However, the TDNN does offer significant improvements in the mid

and high volume ranges and suggests that a combination of linear and nonlinear architectures might be required for obtaining good performance both in low and high volumes. This is the topic of the next section.

5.4 Two Stage Neural Filter

In this section a new nonlinear adaptive filter for improving the echo cancellation performance at both low and high volumes for handsfree telephones is proposed. The proposed structure shown in Figure 5.15 consists of both nonlinear and linear sections and is constructed based on observations from the previous sections. The nonlinear section consist of a two layer neural network that cancels the first part of the AIR where most of the energy is contained. The linear section effectively ensures that residual signals not cancelled by the nonlinear section are accurately modelled. The weight update equations for the nonlinear portion are based on the gradient backpropagation algorithm with a normalized adaptive step size. The nonlinear node is defined by equation (5.1) and the linear region parameter p was set to 0.2 since it was found that this produced an ERLE approximately 1.5 dB higher[1] than with a conventional (i.e. p=0) sigmoid for the lower volumes.

5.4.1 Weight Update Equations

In Figure 5.15, the output $y(k)$ of the neural network portion at time k is defined by;

$$y(k) = w^{(2)}(k)x^{(2)}(k) + w_b^{(2)}(k) \quad (5.3)$$

$$x^{(2)}(k) = \varphi(s(k)) \quad (5.4)$$

1. Based on several tests varying the linear region using field data collected using HFT #6.

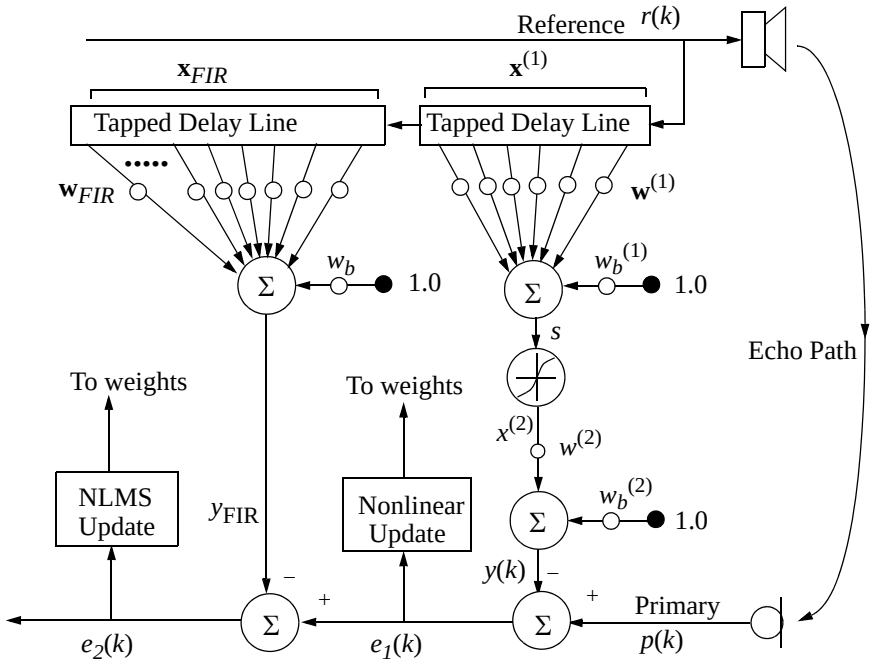

FIGURE 5.15 Proposed two stage nonlinear AEC structure consists of both nonlinear and linear sections.

$$s(k) = \mathbf{w}^{(1)}(k)^T \mathbf{x}^{(1)}(k) + w_b{}^{(1)}(k) \tag{5.5}$$

where $\mathbf{x}^{(l)}(k)$ represents the input vector to layer l, $\mathbf{w}^{(l)}(k)$ represents the weight vector in layer l, $w^{(l)}{}_b(k)$ represents the single bias weight for layer l, $s(k)$ represents the input to the nonlinear node and T is the transpose operator. The weight update equations are described by;

$$\mathbf{w}^{(l)}(k+1) = \mathbf{w}^{(l)}(k) - \mu_{TDNN}(k)\delta^{(l+1)}(\dot{k}) \cdot \mathbf{x}^{(l)}(k) \tag{5.6}$$

$$w_b^{(l)}(k+1) = w_b{}^{(l)}(k) - \mu_{TDNN}(k)\delta^{(l+1)}(\dot{k}) \tag{5.7}$$

$$\delta^{(l+1)}(k) = \begin{cases} -2e_1(k) & ;l=2, \text{output layer} \\ \varphi'(s(k))\delta^{(l+2)}(k)w^{(l+1)}(k) & ;l=1, \text{hidden layer} \end{cases} \quad (5.8)$$

where $e_1(k) = p(k) - y(k)$, $\varphi(\ )$ represents the derivative of the activation function at the input value $s(k)$, $\delta^{(l+1)}(k)$ represents the local gradient "delta" term in layer $l+1$, and $\mu_{TDNN}(k)$ is the normalized step size parameter defined by;

$$\mu_{TDNN}(k) = \frac{\alpha}{2 + \mathbf{x}^{(1)}(k)^T \mathbf{x}^{(1)}(k) + [x^{(2)}]^2} \quad (5.9)$$

The parameter α is a number between 0 and 2, and is set to 0.5. The weights in the linear portion of the proposed structure are updated using the NLMS algorithm;

$$\mathbf{w}_{FIR}(k+1) = \mathbf{w}_{FIR}(k) - \left[\frac{\alpha}{1 + \mathbf{x}_{FIR}(k)^T \mathbf{x}_{FIR}(k)}\right] e_2(\dot{k}) \cdot \mathbf{x}_{FIR}(k) \quad (5.10)$$

$$w_b(k+1) = w_b(k) - \left[\frac{\alpha}{1 + \mathbf{x}_{FIR}(k)^T \mathbf{x}_{FIR}(k)}\right] e_2(k) \quad (5.11)$$

Complexity. The complexity of this algorithm is obtained by summing up the number of calculations in the weight update equations according to Table 5.6. Here, the division needed to compute the normalized step size is counted as one operation, the sigmoid function and deltas are assumed to be obtained from a ROM lookup table in DSP hardware, and m_1 and m_2 refer to the lengths of the TDLs in the nonlinear and linear sections respectively.

TABLE 5.6 Complexity of the two stage neural filter.

Equation Number	Description	Layer	Multiplications or Divisions
(5.3)	output	2	1
(5.4)	sigmoid	2	3
(5.5)	vector dot product	1	n_1

TABLE 5.6 Complexity of the two stage neural filter.

Equation Number	Description	Layer	Multiplications or Divisions
(5.6)	weight update	Hidden	n_1+2
(5.7)	bias update	Hidden	1
(5.8)	delta calculation	Hidden	3
(5.6)	weight update	Output	2
(5.7)	bias update	Output	1
(5.8)	delta calculation	Output	1
(5.9)	normalized step size	TDNN	3
	FIR output	FIR	n_2
(5.9)	normalized step size	FIR	2
(5.10)	weight update	FIR	n_2+2
(5.11)	bias update	FIR	1
TOTAL			2*(n_1+n_2)+22

Note: n_1 equals the length of the TDNN portion TDL and n_2 equals the length of the FIR portion TDL.

By comparison, the NLMS algorithm requires 2M+1 operations, where M is the order of the filter.

5.4.2 Experimental Results

Measurement Setup. Measurements are performed in Conference Room #2 using HFT #6 which is placed on top of the conference table. The reference source signal consists of white noise which is bandlimited from 300 Hz to 3400 Hz. The filtered reference signal is then amplified such that the loudspeaker produces a sound pressure level (SPL) from 60dB to 95dB as measured 0.5m directly above the loudspeaker. Primary and reference DAT signals are subsequently downloaded to a computer via an ARIEL DSP96 board sampling at 16 kHz. These samples are then applied to both the proposed structure and a 600 tap linear adaptive FIR filter which has DC bias compensation and weights updated in the same fashion as equations (4.4) through (4.7). In the proposed structure, the number of taps in the nonlinear section delay line equals 200 to cover the bulk of the loudspeaker impulse response. The number of taps in the linear section is 400 for a total impulse

length of 600 taps which is sufficient to cover the bulk of the impulse response for Conference Room #2. For each SPL, both algorithms are tested with the same input data of length 80,000 to allow convergence to a steady state at which point the average ERLE is measured and plotted.

Results. In Figure 5.16 (a), experimental results are shown for the case where keys have been taped down to prevent rattling at high volumes. Over 11 dB of improvement can be seen at 95 dB SPL compared to the linear algorithm, and between 0-2 dB improvement is obtained over the rest of the volume range. Figure 5.16 (b) shows the corresponding power spectral density of the primary and reference signals, as well as the error signals for the linear and nonlinear algorithms.

Figure 5.16 (c) shows experimental results for the case where keys are not taped down. Finally, the convergence curves for case (c) are shown in Figure 5.16 (d). At low volumes in the vicinity of 60 dB SPL, the proposed structure improves the ERLE by 3 dB as compared to the NLMS-FIR filter even though there is little nonlinear distortion in this range. In the low volume ranges, room noise and two-point suspension nonlinearities are the dominant limitations and the proposed structure offers some improvement. In the medium volume range from 70-75 dB SPL, the proposed structure performs about 1 dB poorer than the linear filter due to an extra bias weight variance not included in the linear filter, and also because the sigmoid function will generate some small amount of distortion for any $|s| > p$ even when the inputs are linear. However, in the vicinity of 80 to 95 dB SPL where nonlinear effects dominate, the proposed structure clearly outperforms the linear filter in terms of converged ERLE and demonstrates over 8 dB improvement at 90 dB SPL.

5.4.3 Discussion

A new structure to mitigate nonlinear loudspeaker distortion effects in AEC's has been presented in this subsection. The architecture is simple and the update algorithms are based on stochastic

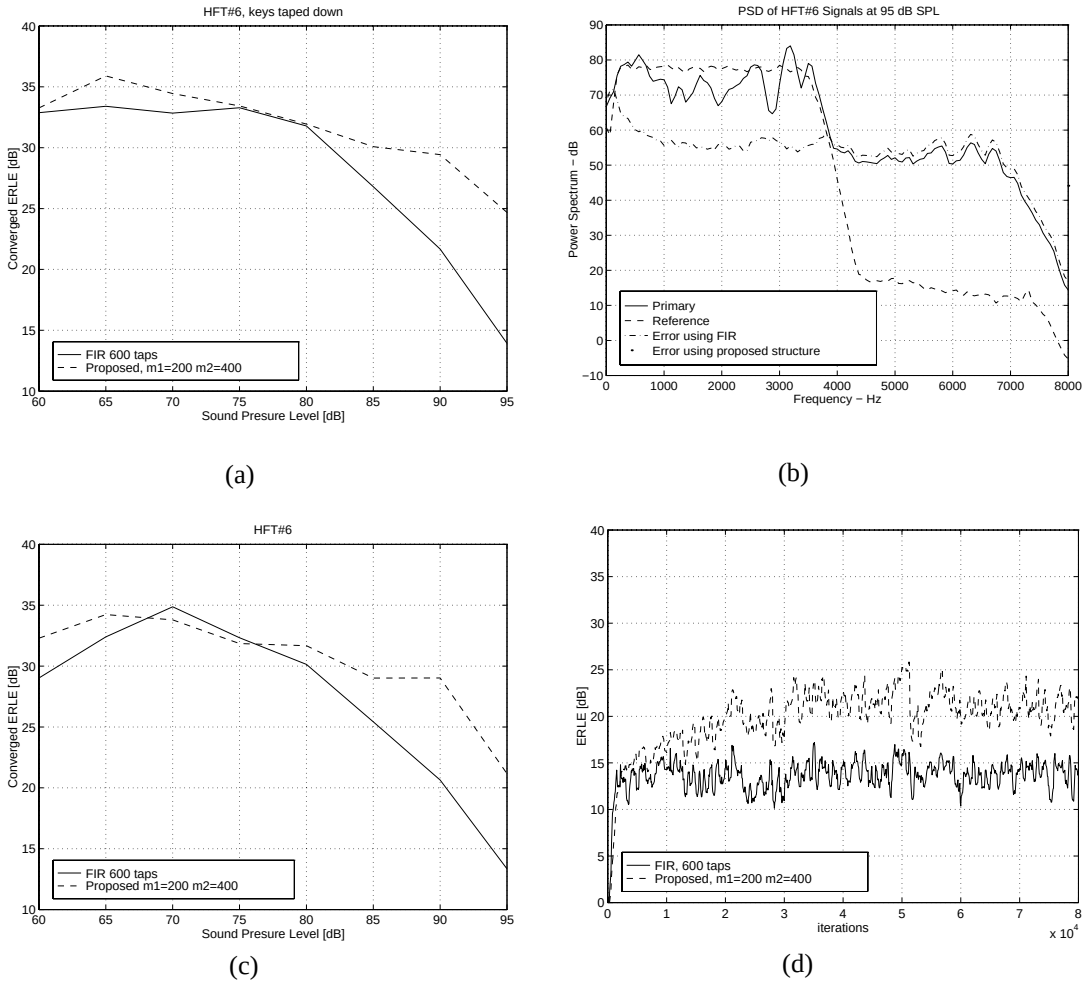

FIGURE 5.16 Experimental results showing performance of the proposed structure using HFT #6 in conference room #2. (a) Converged ERLE, keys taped down. (b) plot of PSD of signals for the taped keys case. (c) Converged ERLE, keys not taped. (d) convergence curve, keys not taped down.

gradient methods. Experimental measurements in a conference room indicate that this new structure is capable of improving the ERLE by over 8 dB at high volumes where nonlinear effects are significant and by over 3 dB at low volumes where room noise is significant. Most striking is the difference in performance between data sets that have been collected with and without the keys taped down (i.e. to prevent rattling). By taping the keys down, the proposed structure will achieve 1-2 dB improvement in converged ERLE in the low-medium volume ranges and a 4 dB improve-

ment in converged ERLE at 95 dB SPL compared to the case where the key movement is not restricted.

For the experimental results presented, the complexity of the two stage neural filter is only 2% greater than the NLM-FIR filter. This is a marginal increase in complexity for the improvements obtained.

Plots of the power spectral density of the signals (See Figure 5.16 (b)) also show that the error signal is reduced in amplitude *evenly* across the full bandwidth, as compared to the error obtained with the FIR/NLMS algorithm which closely follows the out-of-band primary signal PSD. For the proposed structure, the error spectral density near the nyquist sampling frequency does not follow the primary signal amplitude and this is due to the distortion “regeneration” phenomenon associated with passing a signal through a nonlinear sigmoid.

5.5 Variable Activation Function

In this section, the mixed linear-sigmoid activation function described previously in Section 5.2.2 is modified so that it is fully adaptive. The motivation for pursuing this idea is based on both simulation results (see Figure 5.10) and experimental results (see Section 5.2.3) which show that improvements can be made by changing the size of the linear region in the activation function.

The idea of using an adaptive activation function in the realm of adaptive filtering has been previously proposed by Zhan and Li [148] as a method for realizing arbitrary nonlinear filters. However, the adaptive neural filter algorithm that [148] proposes is limited in application since the activation function is placed at the output only and does not allow for placement in a hidden layer. As well, the method proposed in [148] requires that training of the activation function be performed with all other weights being held constant. In this section, these restrictions are removed by

developing a training algorithm that allows the activation function to assume a fully adaptive role regardless of its placement within the network, and without limitations on the training of the network weights.

5.5.1 Development of the Learning Algorithm

We define the sigmoid function as given previously in equation (5.1), repeated here for convenience.

$$\varphi(s,p) = \begin{cases} s & ;|s| \le p \\ \text{sign}(s)\left[(1-p)\cdot\tanh\left(\dfrac{|s|-p}{1-p}\right)+p\right] & ;|s| > p \end{cases} \tag{5.12}$$

where s is the input and p defines the linear region. The instantaneous cost function J_{inst} at time n is defined as;

$$J(n) = J_{inst}(n) = \frac{1}{2}\sum_{i=1}^{N_L} e_i^2(n) \tag{5.13}$$

where;

$$e_i(n) = d_i(n) - y_i(n) \tag{5.14}$$

The algorithm attempts to minimize the J by the delta rule [87] for the vectors **w** and **p** by incrementing at each step towards the optimum vector using the negative gradient at that point. The weight update equations for the weight vector **w** are shown in Section 3.7.1. For **p** we have;

$$\mathbf{p}(n+1) = \mathbf{p}(n) - \eta\frac{\partial J}{\partial \mathbf{p}} \tag{5.15}$$

p is a vector consisting of all the p parameters for the sigmoids

$$\mathbf{p}(n) = [p_1^{(1)}(n), p_2^{(1)}(n), \ldots, p_{n_1}^{(1)}(n), \ldots p_{n_L}^{(L)}(n)] \quad (5.16)$$

and η is a fixed step sizes.The output of node *j* in layer *l* is;

$$x_j^{(l)}(n) = \varphi(s_j^{(l)}(n), p_j^{(l)}(n)) \quad (5.17)$$

where φ represents the nonlinear activation function and $s_j^{(l)}(n)$ is the node activation input.

The derivation of the correction applied to vector **p** may be done by expanding the gradient as follows using the chain rule:

$$\frac{\partial J(n)}{\partial p_j(n)} = \frac{\partial J(n)}{\partial e_j(n)} \frac{\partial e_j(n)}{\partial x_j(n)} \frac{\partial x_j(n)}{\partial p_j(n)} \quad (5.18)$$

Differentiating (5.13) with respect to $e_j(n)$, we get

$$\frac{\partial J(n)}{\partial e_j(n)} = e_j(n) \quad (5.19)$$

Differentiating (5.14) with respect to $x_j(n)$, we get

$$\frac{\partial e_j(n)}{\partial x_j(n)} = -1 \quad (5.20)$$

Differentiating (5.17) with respect to $p_j(n)$, we get

$$\frac{\partial x_j(n)}{\partial p_j(n)} = \varphi'_p(s_j(n), p_j(n)) \quad (5.21)$$

where $\varphi'_p(s_j^{(l)}(n), p_j(n))$ signifies derivative of the activation function output with respect to the argument $p_j(n)$. Differentiating (5.12) with respect to *p,* and dropping reference to *n*, we get:

$$\varphi'_p(s,p) = \begin{cases} 0 & ;|s| \le p \\ \text{sign}(s)\left\{-\tanh(\theta) + (1-p)[1-\tanh(\theta)^2]\left[\dfrac{\theta-1}{1-p}\right] + 1\right\} & ;|s| > a \end{cases} \quad (5.22)$$

$$\text{where } \theta = \left(\frac{|s|-p}{1-p}\right)$$

Figure 5.17 shows the activation function of equation (5.12) with values of a equal to 0, 0.5 and 0.9, along with the associated $\varphi'_s(s,p)$ and $\varphi'_p(s,p)$ values.

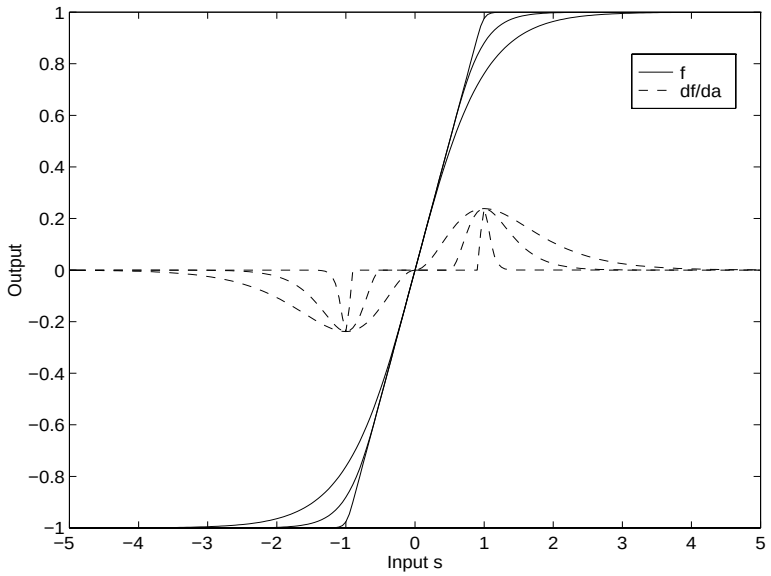

FIGURE 5.17 Adaptive activation function and derivative with respect to *p* as the input *s* varies for values of *p*=0.0, 0.5 and 0.9.

The correction $\Delta p_j(n)$ applied to $p_j(n)$ can now be redefined using the delta rule as:

$$\Delta p_j(n) = \eta \xi_j(n) \quad (5.23)$$

where the local gradient $\xi_j(n)$ for the parameter *p* is defined by

$$\xi_j(n) = \frac{\partial J(n)}{\partial e_j(n)} \frac{\partial e_j(n)}{\partial x_j(n)} \frac{\partial x_j(n)}{\partial p_j(n)} = -e_j(n)\varphi'_p(s_j(n), p_j(n)) \quad (5.24)$$

Equation (5.24) is derived based on the adaptive activation function being in the output layer. If the neuron is located in a hidden layer of the network, we must redefine the local gradient for neuron *j* in the same way as the BP algorithm as follows:

$$\xi_j(n) = -\frac{\partial J(n)}{\partial x_j(n)}\frac{\partial x_j(n)}{\partial p_j(n)} = -\frac{\partial J(n)}{\partial x_j(n)}\varphi'_p(s_j(n), p_j(n)) \tag{5.25}$$

where

$$\frac{\partial J(n)}{\partial x_j(n)} = -\sum_{k=1}^{N_l} e_k(n)\varphi_k(s_k(n))w_{jk}(n) = -\sum_{k=1}^{N_l} \delta_k(n)w_{jk}(n) \tag{5.26}$$

Using (5.26) in (5.25), we obtain the local gradient $\xi_j(n)$ for a hidden neuron *j* in layer *l*,

$$\xi_j^{(l)}(n) = \varphi'(p_j^{(l)}(n)) \sum_{k=1}^{N_l} \delta_k^{(l+1)}(n)w_{jk}^{(l)}(n) \tag{5.27}$$

Equation (5.27) shows that the local gradient $\xi_j(n)$ is dependent on both the derivative (with respect to *p*) of the associated activation function as well as the weighted sum of the δ's computed for the neurons in the next hidden or output layer which is connected to neuron *j*.

It should be noted that there is no restriction on the type of nonlinearity used. For example, we may define an alternate hyperbolic tangent function such as:

$$\begin{aligned} \varphi(s, p) &= \frac{1}{p}\tanh(sp) \\ \varphi'_s(s, p) &= 1 - (\tanh(sp))^2 \\ \varphi'_p(s, p) &= \frac{s}{p}[1 - (\tanh(sp))^2] - \frac{1}{p^2}\tanh(sp) \end{aligned} \tag{5.28}$$

Yamada *et al*. [149] have used a similar unit function to construct a direct neural network controller for robot manipulators, but with a different definition from that described above and without giving the learning algorithm of the parameter *p*. A plot of the function and slope of (5.28) with respect to the activation input *s* and the variable *p* is shown in Figure 5.18 for values of *p*= 0.5 and 2. It differs somewhat from that of (5.12) in that the function becomes linear as *p* approaches 0 and highly nonlinear as *p* approaches infinity.

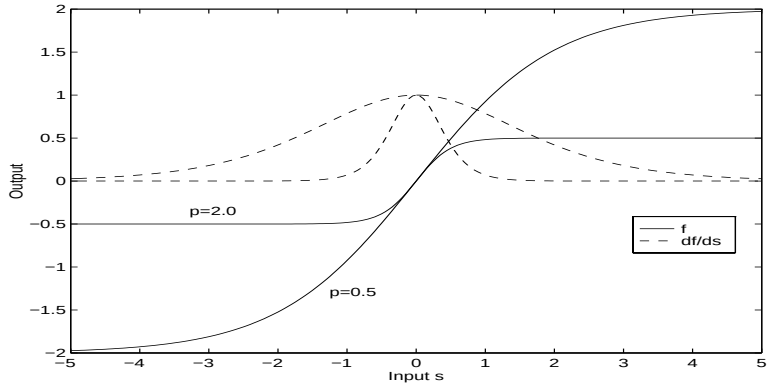

(a)

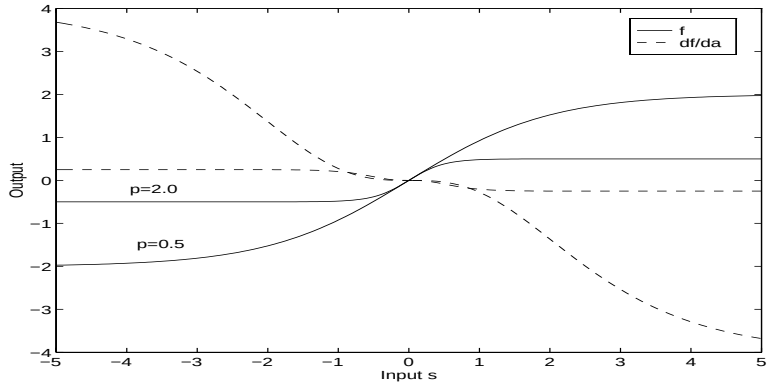

(b)

FIGURE 5.18 Alternate activation function and derivative with respect to *s* as the input *s* varies (b) derivative with respect to *p* as the input *s* varies.

The advantage of the sigmoid of equation (5.28) is that a two layer TDNN structure with fixed activation functions and a single weight on the output is similar to a *single layer* TDNN with a

variable activation function. The complete algorithm is summarized below:

BP Algorithm with Variable Activation (VA) Functions:

Step 1: Initialization. Set all synaptic weights in input layer to zeros, and all other weights and threshold levels to small random numbers that are uniformly distributed.

Step 2: Forward Computation. For all training samples, compute the activation potentials and outputs of the networks forward layer by layer using the following equations:

$$s_j^{(l+1)}(n) = \sum_{i=0}^{N_l} w_{ij}^{(l)}(n) x_i^{(l)}(n) \qquad (5.29)$$

where $x_i^{(l)}(n)$ represents both the output from the previous layer and the input to weight matrix elements $w_{ij}^{(l)}(n)$ at time *n*. The output of node *j* in layer *l* is;

$$x_j^{(l)}(n) = \varphi(s_j^{(l)}(n), p_j^{(l)}(n)) \qquad (5.30)$$

Compute the error signal $e(n)$ produced at the output layer (i.e. $l=L$) of the network;

$$e(n) = d(n) - x_1^{(L)}(n) \qquad (5.31)$$

Step 3: Backpropagation of Errors. Compute the local gradients δ's and ξ's of the network by proceeding backward, layer by layer:

$$\delta_j^{(l)}(n) = \begin{cases} -2e(n)\varphi_s'(s_j^{(L)}(n), p_j^{(L)}(n)) & \ldots l = L \\ \varphi_s'(s_j^{(l)}(n), p_j^{(l)}(n)) \cdot \sum_{k=1}^{N_{L+1}} \delta_k^{(l+1)}(n) \cdot w_{jk}^{(l)}(n) & \ldots 1 \le l \le L-1 \end{cases} \quad (5.32)$$

$$\xi_j^{(l)}(n) = \begin{cases} -2e(n)\varphi_p'(s_j^{(L)}(n), p_j^{(L)}(n)) & \ldots l = L \\ \varphi_p'(s_j^{(l)}(n), p_j^{(l)}(n)) \cdot \sum_{k=1}^{N_{L+1}} \delta_k^{(l+1)}(n) \cdot w_{jk}^{(l)}(n) & \ldots 1 \le l \le L-1 \end{cases} \quad (5.33)$$

Step 4: Update Parameters.

$$w_{ij}^{(l)}(n+1) = w_{ij}^{(l)}(n) - \mu\delta_j^{(l+1)}(n) \bullet x_i^{(l)}(n) \quad (5.34)$$

$$p_j^{(l)}(n+1) = p_j^{(l)}(n) - \eta\xi_j^{(l+1)}(n) \quad (5.35)$$

The value of $p_j^{(l)}(n+1)$ should be clamped above 0 for the sigmoid of equation (5.28) and between 0 and 1 for the sigmoid function of equation (5.12).

5.5.2 Simulation Examples

In this section, the proposed algorithm is applied to the identification of a nonlinear system constructed using simulation method #1. The model is a (10,5,1) two layer network with a variable activation function in the hidden layer, and a linear activation function in the output layer. A normalized step size of 0.1 is used for updating the layer weights and the step size for adapting the activation function is set to 0.001. Also shown for comparison is the NLMS-FIR filter using

α=0.1.

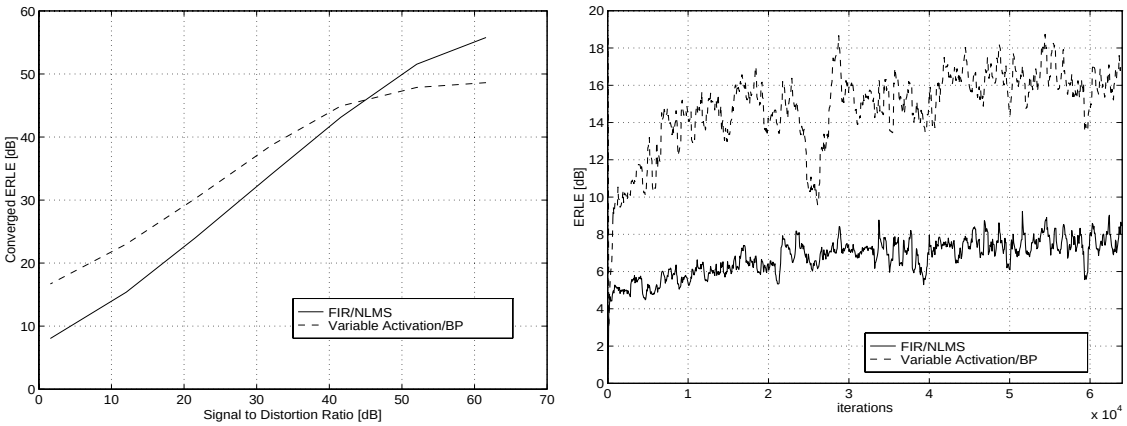

(a) (b)

FIGURE 5.19 Simulation results for distortion method #1, (10,5,1) variable activation TDNN, filtered reference signal. (a) converged ERLE vs. SDR (b) convergence curve for the highest distortion level.

Simulation results in Figure 5.19 show that the variable activation TDNN is capable of achieving a higher ERLE over the NLMS-FIR filter from 0-45 dB SDR and also achieves better steady state ERLE compared to the conventional (i.e fixed activation function) model of Section 5.2.

5.5.3 Experimental Results

HFT #6 in Conference Room #2. In this experiment, a single *hidden* layer TDNN with variable activation (VA) function is applied to the measured data. A normalized step size of α=0.5 is used for the weight updates, and a fixed step size of 0.001 is used for the update of the *p* parameter.

The results shown in Figure 5.20 (a) indicate that the single layer VA TDNN filter has similar performance to the regular TDNN structure results shown Figure 5.13. However, the VA TDNN filter steady state ERLE performance *is between 1 and 5 dB better than the fixed activation function TDNN* (See Figure 5.13) in the 57-95 dB SPL ranges. In the 50-55 dB range the performance is still poorer than the FIR structure. Figure 5.20 (b) shows the corresponding convergence for the 95

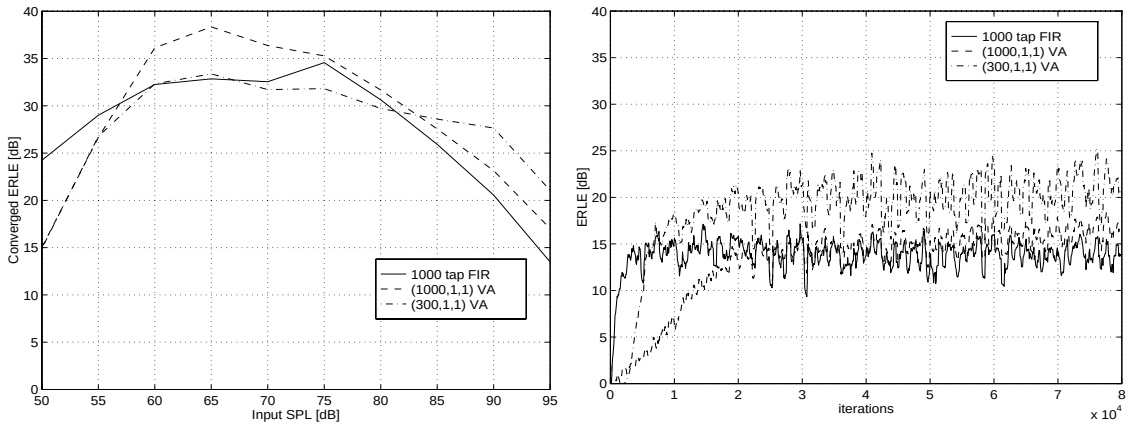

(a) (b)

FIGURE 5.20 Experimental results for the variable activation function TDNN. (a) Converged ERLE vs. SPL (b) convergence curve for an SPL of 95 dB.

dB SPL case.

5.5.4 Discussion

Both simulationand experimental results show that the VA-TDNN *is capable of achieving lower modelling error for the identification of a nonlinear system that has a widely varying range of nonlinearity* (for example a loudspeaker going into and out of the saturation range) compared to a network using a conventional fixed sigmoid activation function. However, the convergence rate is *slower* than the fixed activation TDNN especially for higher distortion values near 95 dB SPL. In terms of application to AEC, the slowing of convergence is an undesirable feature, however, methods exist to improve the convergence performance of neural networks, and this is discussed further in Chapter 6.

The results shown in Figure 5.20 (c) indicate that a single hidden layer TDNN can still achieve significant modelling accuracy improvements as compared to the FIR structure, although they are almost identical in architecture, save for the activation function. The important point to stress is

that this architecture has a complexity only slightly more than the NLMS algorithm since back-propagation through several layers is not longer necessary and suggests that for the nonlinear AEC problem, it is possible to obtain significant improvements in converged ERLE using simple non-linear mechanisms.

Similar to the conventional TDNN case, there is a significant improvement in converged ERLE in the 60-75 dB SPL volume range. *It suggests even in the so-called "linear" range of the loud-speaker, there is small level of nonlinear distortion in the LREM that can be compensated, result-ing in improved performance*.

The VA structures presented in this section still do not model the low volume ranges very well. The performance, for example at 55 dB SPL is still approximately 9 dB worse than the linear FIR structure. Various parameter changes were made to see if this would make a difference, however, no conclusive results were obtained to demonstrate a clear reason why this phenomenon occurs.

5.6 MLP with FIR Synapses and Variable Activation Function

Recent interest in deriving temporal neural network structures for modelling time-dependent signals has resulted in MLP structures with synapses described by FIR filters [49][47] and IIR filters [42][43]. The architecture can be considered an extension of the classical feedforward structure described previously in Section 3.7. In this section we examine the FIR MLP, which can be considered an ideal architecture for modelling cascaded linear-nonlinear-linear temporal structures of the type illustrated in Figure 5.21. The FIR MLP is *generalized* to include the variable activation (VA) functions developed in Section 5.5 and is then applied to simulated and experimental data.

The motivation for pursuing this line of attack is based on the encouraging results in [150] which document a number of techniques for application in Time Series Prediction. The two most success-

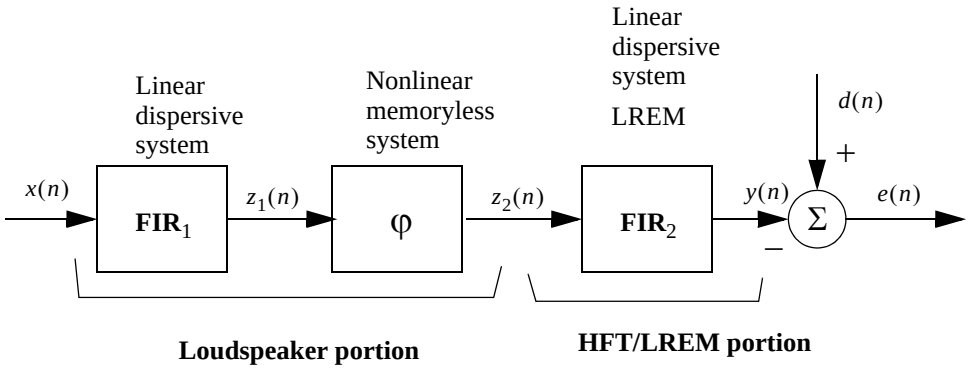

FIGURE 5.21 Using the FIR MLP to represent a cascaded linear-nonlinear-linear subsystem (i.e. nonlinear HFT).

ful techniques outlined in [150] are based on *function approximation* using FIR and IIR filters between synapses of a neural network and a state space modelling to develop a *representation* of the system without knowing the system equations.

State space modelling has already found success in nonlinear system identification and filtering (see for example [79] [81]), and encouraging results are presented for the application of FIR MLP architectures to time series prediction [49][47][151], however, no application of the FIR MLP method has been found in the literature in the realm of real-time nonlinear adaptive filtering. Consequently, the application of VA FIR MLPs to nonlinear AEC is examined here.

5.6.1 Network Architecture

The FIR MLP architecture is shown in Figure 5.22. Define the internal states of the network:

$$x_j^{(l)}(n),\ 1 \le j \le N_l \tag{5.36}$$

where

$x_j^{(l)}(n)$ represent the input to the *j-th* FIR synaptic filter in the l^{th} input layer

N_l represents the number of nodes in layer l.

For the input layer, l=0, and for the output layer, l=L. The output of the i^{th} FIR synapse is;

$$z_{ij}^{(l+1)}(n) = [\mathbf{w}_{ij}^{(l)}(n) \bullet \mathbf{x}_i^{(l)}(n)] \quad (5.37)$$

where $\bullet$ represents the dot product of vectors

$$\mathbf{w}_{ij}^{(l)} = [w_{ij}^{(l)}(0), w_{ij}^{(l)}(1), \ldots, w_{ij}^{(l)}(T^{(l)})]^T \quad (5.38)$$

represents the FIR weight vector connecting the output of neuron i in the l^{th} layer to the input of neuron j in the l+1$^{\text{th}}$ layer and

$$\mathbf{x}_i^{(l)} = [x_i^{(l)}(n), x_i^{(l)}(n-1), \ldots, x_i^{(l)}(n-T^{(l)})]^T \quad (5.39)$$

represents the vector formed from the output $x_i^{(l)}(n)$ from the previous layer and the TDL of the FIR connecting node i in the l^{th} layer to node j in the l+1$^{\text{th}}$ layer. The activation level at the input to the sigmoid nonlinearity of neuron j in layer l is

$$s_j^{(l)}(n) = \sum_{i=0}^{N_l} z_{ij}^{(l)}(n) - \theta_j^{(l)}(n) \quad (5.40)$$

where $\theta_j^{(l)}(n)$ is the bias added to the net input. The output at the l^{th} layer is obtained by putting $s_j^{(l)}(n)$ through the activation function.

$$x_j^{(l)}(n) = \varphi(s_j^{(l)}(n), p_j^{(l)}(n)) \quad (5.41)$$

5.6.2 Derivation of the Modified Temporal BP Learning Algorithm

An algorithm for training networks having FIR synapses was first published by Wan [47] which is based on the total squared error over the entire sequence of inputs as opposed to the “instantaneous

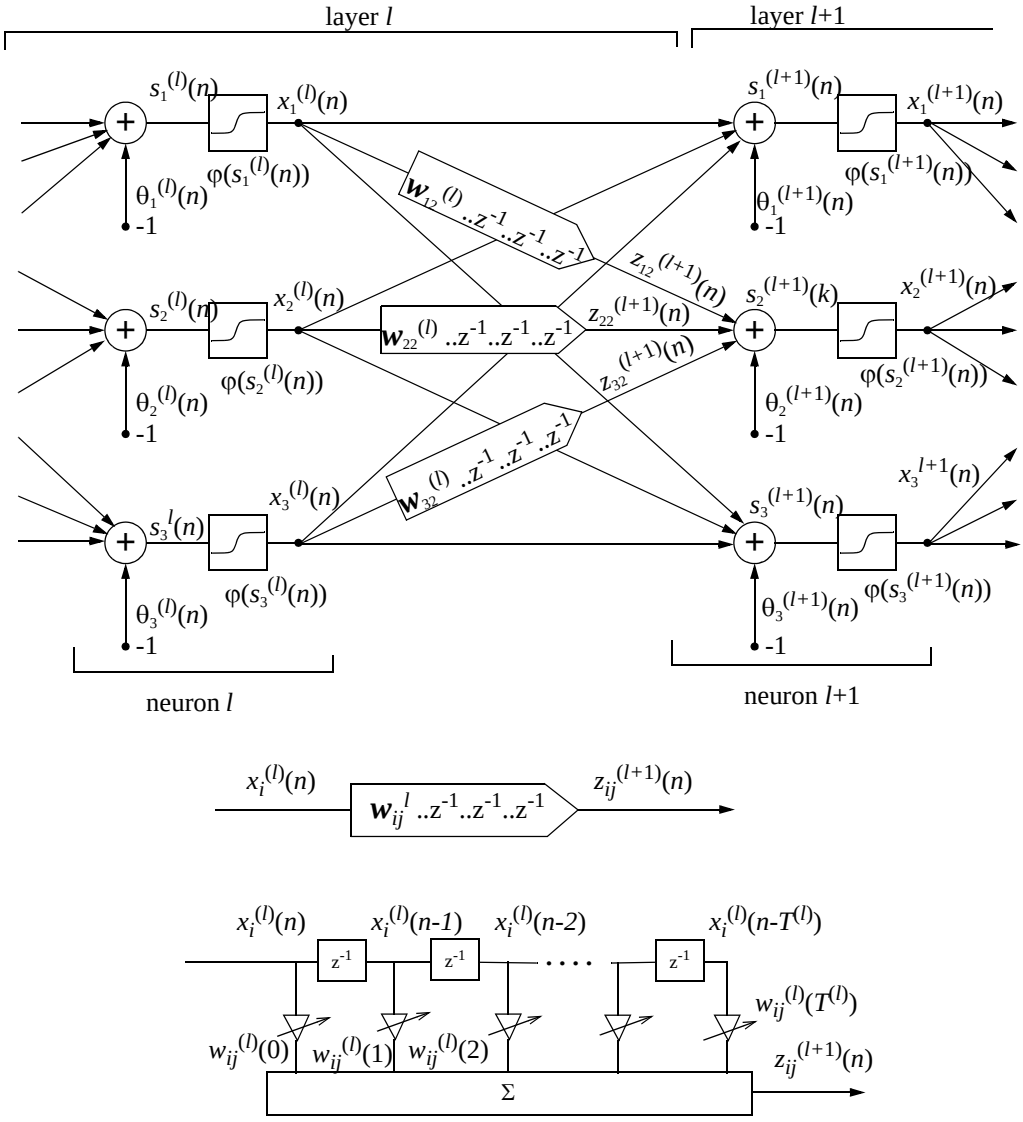

FIGURE 5.22 Forward signal propagation in the FIR MLP.

error". The calculations for the deltas $\delta_j^{(l)}(n)$ in [47] are in fact non-causal. Since it takes time for the output of any internal neuron to completely propagate through the network, the change in the total error due to a change in an internal state is a function of *future* values within the network. The solution is to add a finite number of delay operators into the network states $x_j^{(l)}(n)$ and propagate the deltas backwards *without* delay. The result is that the internal weights are updated at

time (*n*) based on the deltas and internal states at time (*n*-*D*) where *D* is some fixed delay. This is analogous to the delayed LMS algorithm (Kabal [152]) which exhibits a slower convergence (but similar misadjustment) as compared to the standard LMS algorithm.

In [153], several training algorithms are presented for the FIR MLP based on whether the performance criteria is obtained using an *instantaneous error*, or the *total error* by summing the instantaneous error over all time steps in a training sequence. The authors conclude that algorithms based on minimization of the total error are very inefficient for networks of more than two layers. Wan's original temporal algorithm in [47] uses a total cost function and has an update delay to maintain causality. Since the system we are trying to identify has a large order for FIR_2, which is representative of a typical room response (See Figure 5.21), the update algorithms based on the total cost function are not investigated since this would involve a large delay in the tap weight update, and consequently slower convergence.

The parameter update equations are derived in a way similar to Wan's method [47], but with modifications as follows:

- We use an instantaneous cost function (rather than total cost function over all time).
- The adaptive activation function derived in Section 5.5 is used.

We first consider the weight updates, and then the updates of the variable sigmoid parameter *p*.

Weight Update Derivation. The most straight forward way of updating the weight vectors is to minimize the instantaneous cost function *J* (See equation (5.13)) using the stochastic gradient descent algorithm at each increment of time *n* according to [47];

$$\begin{aligned}\mathbf{w}_{ij}^{(l)}(n+1) &= \mathbf{w}_{ij}^{(l)}(n) - \mu\frac{\partial J}{\partial \mathbf{w}_{ij}^{(l)}(n)} \\ &= \mathbf{w}_{ij}^{(l)}(n) - \mu\frac{\partial J}{\partial s_j^{(l+1)}(n)}\frac{\partial s_j^{(l+1)}(n)}{\partial \mathbf{w}_{ij}^{(l)}(n)}\end{aligned} \tag{5.42}$$

The partial derivative of $s_j^{(l+1)}(n)$ with respect to the weight vector $\mathbf{w}_{ij}^{(l)}(n)$ is given by

$$\frac{\partial s_j^{(l+1)}(n)}{\partial \mathbf{w}_{ij}^{(l)}(n)} = \mathbf{x}_i^{(l)}(n) \tag{5.43}$$

The local gradient for neuron *j* in layer *l* is defined as

$$\delta^{(l)}(n) = \frac{\partial J}{\partial s_j^{(l)}(n)} \tag{5.44}$$

Hence (5.42) may be written in the familiar form

$$\mathbf{w}_{ij}^{(l)}(n+1) = \mathbf{w}_{ij}^{(l)}(n) - \mu\delta_j^{(l+1)}(n)\mathbf{x}_i^{(l)}(n) \tag{5.45}$$

Case 1: Output Layer Weights.

$$\delta_j^{(L)}(n) = \frac{\partial e^2(n)}{\partial s_j^{(L)}(n)} = -e_j(n)\varphi'_s(s_j^{(L)}(n), p_j^{(L)}(n)) \tag{5.46}$$

Case 2: Hidden Layer Weights. For a hidden layer, we use the chain rule, expanding over all N_{l+1} inputs $s^{(l+1)}(n)$ in the next layer. However, instead of expanding over all time as is done in [47], the expansion is only done at time $k=n$ since we are only concerned with the instantaneous error.

$$\delta_j^{(l)}(n) = \frac{\partial e^2(n)}{\partial s_j^{(l)}(n)} = \sum_{k=1}^{N_{l+1}} \sum_{t=n}^{n} \frac{\partial J(n)}{\partial s_j^{(l+1)}(t)} \frac{\partial s_k^{(l+1)}(t)}{\partial s_j^{(l)}(n)}$$
$$= \sum_{k=1}^{N_{l+1}} \frac{\partial J(n)}{\partial s_j^{(l+1)}(n)} \frac{\partial s_k^{(l+1)}(n)}{\partial s_j^{(l)}(n)} = \sum_{k=1}^{N_{l+1}} \delta_j^{(l+1)} \frac{\partial s_k^{(l+1)}(n)}{\partial s_j^{(l)}(n)} \tag{5.47}$$
$$= \varphi'_s(s_j^{(l)}(n), p_j^{(l)}(n)) \sum_{k=1}^{N_{l+1}} \delta_j^{(l+1)} \frac{\partial z_{jk}^{(l+1)}(n)}{\partial x_j^{(l)}(n)}$$

Recall that

$$z_{jk}^{(l+1)}(n) = [\mathbf{w}_{jk}^{(l)}(n) \bullet \mathbf{x}_j^{(l)}(n)] = \sum_{t=0}^{T^{(l)}} w_{jk}^{(l)}(t) x_j^{(l)}(n-t) \tag{5.48}$$

where $T^{(l)}$ is the number of delays in the FIR sections in layer l. Thus for the instantaneous case we obtain

$$\frac{\partial z_{jk}^{(l+1)}(n)}{\partial x_j^{(l)}(n)} = w_{jk}^{(l)}(n) \tag{5.49}$$

Algorithm 1: Instantaneous Gradient. Substitution of (5.49) into (5.47), we get the delta update for the hidden layer,

$$\delta_j^{(l)}(n) = \varphi'_s(s_j^{(l)}(n), p_j^{(l)}(n)) \sum_{k=1}^{N_{l+1}} \delta_j^{(l+1)}(n) w_{jk}^{(l)}(n) \tag{5.50}$$

This can be considered an *approximate* instantaneous gradient. The δ terms are calculated using standard backpropagation through the first weight of each FIR synapse, and the rest of the coefficients are ignored.

Algorithm 2: Accumulated Gradient. A different form is achieved if the gradient is calculated over a short time window $1 \le n_w \le T^{(l)}$ by delaying the calculation of the gradient until all contributions from feedforward delay elements can be combined.

$$\delta_j^{(l)}(n) = \varphi'_s(s_j^{(l)}(n)) \sum_{k=1}^{N_{l+1}} v_{jk}^{(l)}(n) \tag{5.51}$$

$$v_{jk}^{(l)}(n) = [\bar{\Delta}_k^{(l+1)}(n) \bullet \bar{\mathbf{w}}_{jk}^{(l)}(n)] \tag{5.52}$$

where the quantities $\bar{\Delta}_k^{(l+1)}(n)$ and $\bar{\mathbf{w}}_{jk}^{(l)}(n)$ define the length of the accumulated gradients, defined by

$$\bar{\Delta}_k^{(l+1)}(n) = [\delta_k^l(n), \delta_k^l(n-1), \ldots, \delta_k^l(n-n_w)]^T \tag{5.53}$$

$$\bar{\mathbf{w}}_{jk}^{(l)}(n) = [w_{jk}^{(l)}(0), w_{jk}^{(l)}(1), \ldots, w_{jk}^{(l)}(n_w)]^T \tag{5.54}$$

In this case, the backpropagated error is obtained from a backward filter, and all the coefficients up to the $n_w{}^{th}$ coefficient will have an influence on the δ value. Figure 5.23 illustrates this process.

Algorithm 1 was first proposed by Back and Tsoi [49]. The tapped delay line in the FIR synapse allows a number of options in calculating the gradient. However, the gradient can be obtained from an instantaneous estimate, i.e. using only the first weight in the backward filter, or from $T^{(l)}$ delay sections, i.e. using the entire FIR synapse. It may be observed that *Algorithm 1* is just a special case of *Algorithm 2*, since it can be obtained by fixing the gradient window parameter n_w=1. However, rather than fixing n_w=1 as is done in [49], the value of n_w in the above derivation is allowed to assume any value between 1 and $T^{(l)}$ and thus offers an *additional* degree of flexibility not offered in the algorithm presented in [153].

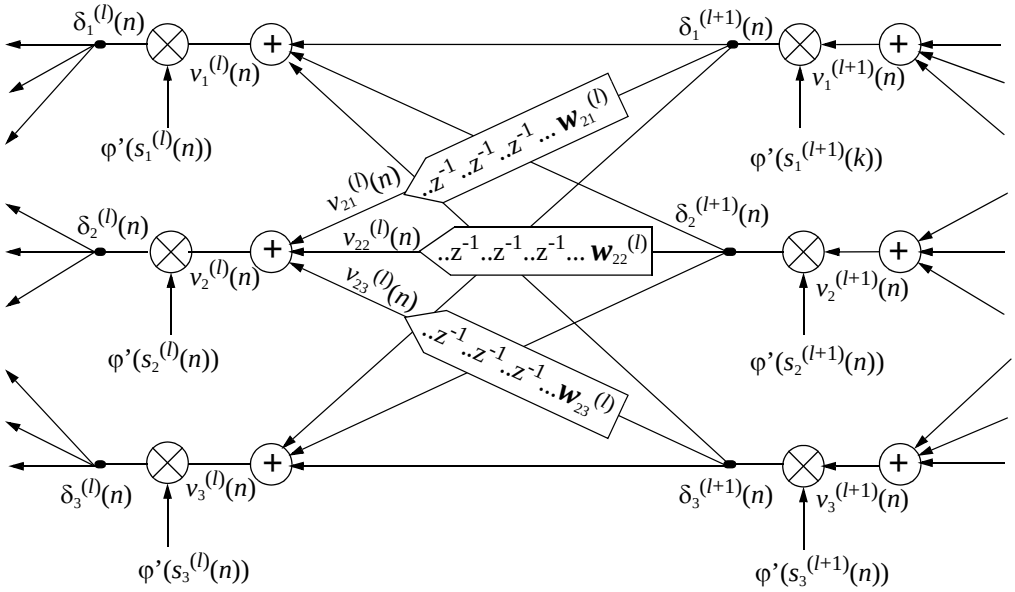

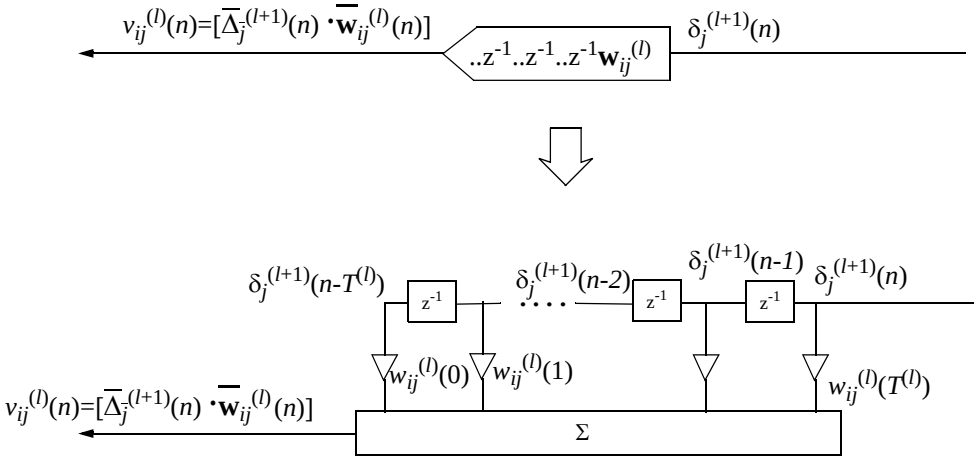

FIGURE 5.23 Backward filter propagation of "accumulated" gradient terms.

Modification for the Variable Activation Function. The inclusion of a variable activation function can be done in the same manner as outlined in Section 5.5. The adaptation of p is done according to the stochastic gradient update:

$$\mathbf{p}(n+1) = \mathbf{p}(n) - \eta \frac{\partial J}{\partial \mathbf{p}} \tag{5.55}$$

$$\begin{aligned} \frac{\partial J}{\partial p_j(n)} = \xi_j^{(l)}(n) &= \frac{\partial \varphi(s_j^l(n))}{\partial p_j(n)} \sum_{k=1}^{N_l} \left[\bar{\Delta}_k^{(l+1)}(n) \bullet \bar{\mathbf{w}}_{jk}^{(l)}(n) \right] \\ &= \varphi'_p(s_j^{(l)}(n), p_j^{(l)}(n)) \sum_{k=1}^{N_l} \left[\bar{\Delta}_k^{(l+1)}(n) \bullet \bar{\mathbf{w}}_{jk}^{(l)}(n) \right] \end{aligned} \tag{5.56}$$

Essentially, the derivative of the activation function is computed with respect to p and then it is multiplied by the *filtered* delta vector, which is the quantity in brackets. Equation (5.56) has the same format as (5.27) with the exception deltas and weights are now vector operator due to the FIR synapses.

Summarizing, the complete adaptation algorithm for the parameter updates can be expressed as follows;

FIR MLP Algorithm with Variable Activation Functions:

Step 1: Initialization. Set all synaptic weights in the input layer to zeros, and all other weights and threshold levels to small random numbers that are uniformly distributed.

Step 2: Forward Computation. For all training samples, compute the activation potentials and outputs of the networks forward layer by layer using the following equations:

$$s_j^{(l+1)}(n) = \sum_{i=0}^{N_l} [\mathbf{w}_{ij}^{(l)}(n) \bullet \mathbf{x}_i^{(l)}(n)] - \theta_j^{(l)}(n) \quad (5.57)$$

Compute the output of node j in layer l using;

$$x_j^{(l)}(n) = \varphi(s_j^{(l)}(n), p_j^{(l)}(n)) \quad (5.58)$$

Compute the error signal $e(n)$ produced at the output layer (i.e. $l=L$) of the network;

$$e(n) = d(n) - x_1^{(L)}(n) \quad (5.59)$$

Step 3: Backpropagation of Errors. Compute the local gradients δ's and ξ's of the network by proceeding backward, layer by layer:

$$\delta_j^{(l)}(n) = \begin{cases} -2e(n)\varphi_s'(s_j^{(L)}(n), p_j^{(L)}(n)) & \ldots l = L \\ \varphi_s'(s_j^{(l)}(n), p_j^{(l)}(n)) \cdot \sum_{k=1}^{N_{L+1}} \left[\bar{\Delta}_k^{(l+1)}(n) \bullet \bar{\mathbf{w}}_{jk}^{(l)}(n)\right] & \ldots 1 \le l \le L-1 \end{cases} \quad (5.60)$$

$$\xi_j^{(l)}(n) = \begin{cases} -2e(n)\varphi_p'(s_j^{(L)}(n), p_j^{(L)}(n)) & \ldots l = L \\ \varphi_p'(s_j^{(l)}(n), p_j^{(l)}(n)) \cdot \sum_{k=1}^{N_{L+1}} \left[\bar{\Delta}_k^{(l+1)}(n) \bullet \bar{\mathbf{w}}_{jk}^{(l)}(n)\right] & \ldots 1 \le l \le L-1 \end{cases} \quad (5.61)$$

where $\bar{\Delta}_k^{(l+1)}(n)$ and $\bar{\mathbf{w}}_{jk}^{(l)}(n)$ are vectors of length $1 \le n_w \le T^{(l)}$.

Step 4: Update Parameters.

$$\mathbf{w}_{ij}^{(l)}(n+1) = \mathbf{w}_{ij}^{(l)}(n) - \mu\delta_j^{(l+1)}(n)\mathbf{x}_i^{(l)}(n) \quad (5.62)$$

$$p_j^{(l)}(n+1) = p_j^{(l)}(n) - \eta \xi_j^{(l+1)}(n) \quad (5.63)$$

The value of $p_j^{(l)}(n+1)$ should be clamped above 0 for the sigmoid of equation (5.28) and between 0 and 1 for the sigmoid function of equation (5.12). If the values of $p_j^{(l)}$ are fixed (i.e. not updated) and n_w is set equal to $T^{(l)}$ for all sections, the above algorithm defaults to the *instantaneous cost accumulated gradient algorithm* proposed in [153].

5.6.3 Simulation Results

In this section we apply the proposed structure to the identification of a nonlinear system as shown in Figure 5.24 with the following parameters: Number of taps in first FIR section = 5, the activation function used was defined by equation (5.12) with parameter p =0.5, and the number of taps in the 2nd FIR section is 10. Both of the FIR sections have the weights and biases randomly assigned.

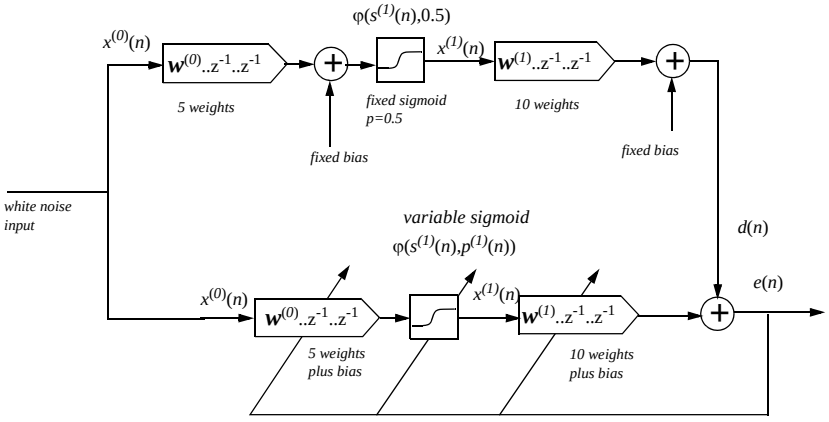

FIGURE 5.24 System identification using the proposed model.

Three structures were tested. The first structure (called 'FIR') is a conventional FIR structure consisting of 15 taps with the inclusion of a bias weight to compensate for output bias. Fifteen taps were chosen to accommodate the impulse length of the "unknown" system. The normalized step size alpha was set to 0.1 and it was trained with the NLMS algorithm.

The second structure tested (called 'IC') consists of two FIR sections with a *fixed* sigmoidal activation function between them, essentially equation (5.12) with p=0. The number of taps is the FIR sections is set to 5 and 10 respectively, and the gradient accumulation n_w is set to 1. This is equivalent to *IC-2* in [153].The normalized step size alpha was set to 0.1.

The third structure is the proposed architecture with variable activation function and gradient accumulation. It has a similar architecture to the second structure except we allow the activation function to adapt parameters p according to the proposed training algorithm, and set the gradient accumulation window n_w to 1 or 3. The normalized step size alpha was set to 0.1. This algorithm is called 'ICVA'.

The training sequence consists of 8000 randomly generated data points. For all the algorithms, the normalized mean square error (NMSE) is plotted according to the formula;

$$NMSE(n) = 10\log\left(\frac{\sum_{r=0}^{500}[e_r(k)]^2}{\sum_{r=0}^{500}[d_r(k)]^2}\right) dB \qquad (5.64)$$

where $e_r(k)$ and $d_r(k)$ represent the averaged error and desired signals and r represents the window values over which these averages are then smoothed, in this case equal to 500. The convergence results are shown in Figure 5.25 .The FIR structure trained with the NLMS algorithm is

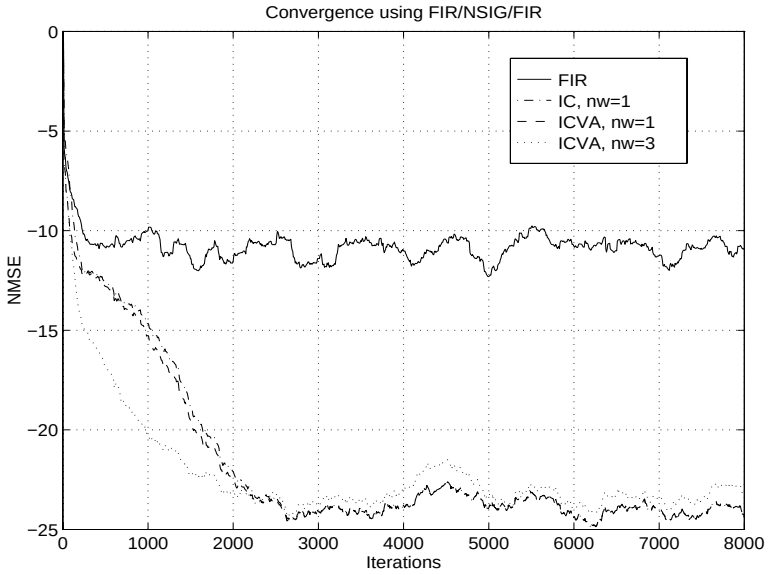

FIGURE 5.25 Comparison of convergence using the proposed algorithms.

clearly unable to identify the unknown system accurately, and obtains an average NMSE of only -- 11 dB. Both the IC structure and ICVA structure with n_w=1 perform considerably better than the FIR structure. The ICVA structure is able to achieve a slightly faster convergence in the 0-2000 iteration range, and both converge to approximately -24 dB NMSE. By increasing the gradient accumulation window, an increase in convergence speed is seen to occur. With n_w=1, ICVA achieves -20 dB NMSE after 1500 iterations. With n_w=3, the same NMSE is achieved after only 1000 iterations.

5.6.4 Experimental Results

HFT #6 in Conference Room #2. The ICVA architecture is applied to experimental data collected in this venue. Two different architectures are evaluated. The first architecture is similar to that shown in Figure 5.24 and has 150 taps in the first FIR section, followed by 850 taps in the second FIR section. The gradient accumulation window is equal to 100, the normalized step size = 0.5 and

the adaptive parameter step size is 0.01. The sigmoid of equation (5.28) is used. This architecture is called “150/850 ICVA”. The second architecture is simplified by using a single variable activation function in front of a 1000 tap FIR structure, i.e. the first FIR section is absent. This architecture is called “0/1000 ICVA” and has the same parameters as the first architecture. Note that this architecture is almost identical to a conventional FIR structure, however, it is still necessary to use the temporal backpropagation algorithm due to the TDL in the FIR portion.

The results shown in Figure 5.26 (a) indicate that the 150/850 ICVA obtains a lower converged ERLE with respect to the conventional two layer TDNN (see for comparison results in Figure 5.13) but obtains a converged ERLE approximately 1 dB better than the conventional TDNN at 95 dB SPL. The 0/1000 ICVA structure obtains 2 to 3 dB better performance than the FIR model at SPL levels between 60 and 70 dB, but is worse at other volumes.

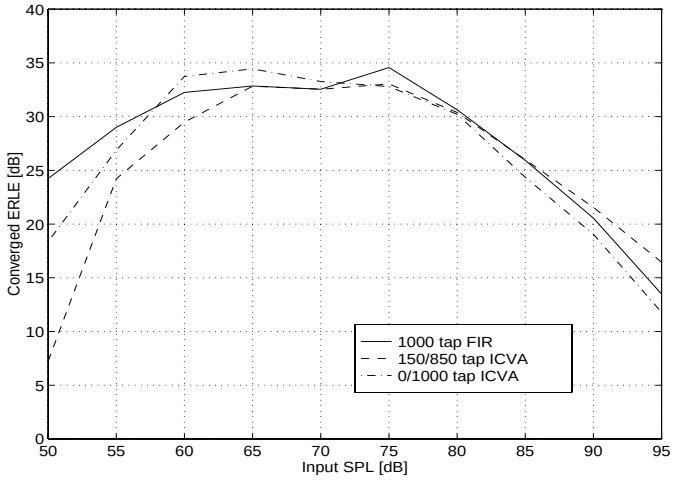

FIGURE 5.26 Experimental results. HFT #6 in conference room 2 showing a comparison of FIR, VA-FIR MLP using 150/800 taps in first/second FIR sections, and simplified VA-FIR MLP with only one FIR section following adaptive sigmoid.

5.6.5 Discussion

Simulation results presented in Section 5.6.3 illustrate the improved convergence can be obtained by utilizing an adaptive activation function with gradient accumulation window. The proposed structure can be considered as a new alternative architecture to conventional MLPs which utilize fixed sigmoidal activation functions only. By selecting the size of the gradient accumulation window, a trade-off between convergence performance and complexity can be achieved, and that for low order systems, the gain is impressive. Plots of the converged MSE also show that the excess MSE is higher when gradient accumulation is used, compared to when the accumulation is not used, i.e. n_w=1. The experimental results presented in Section 5.6.4 indicate that the proposed VA-FIR-MLP structure is not as good as the conventional TDNN utilizing an *adaptive* activation function (See Section 5.5.3). As well, the performance at low volumes does not equal that of the linear FIR, although at medium and high volumes it is 1-2 dB better.

5.7 Summary

This chapter has addressed methods to combat nonlinear loudspeaker distortion in AEC's, by the application of some known and newly proposed nonlinear structures. In Section 5.1 results using a 3rd order Volterra structure are presented. The following conclusions can be summarized:

- Although the Volterra filter can obtain a high degree of modelling accuracy in simulation examples (for example 10's of dB better than a linear model), the performance obtained using experimentally obtained data was typically only one or 2 dB better than the linear models.
- The convergence is slow since the number of taps required to accurately model a physical HFT is large (several tens of thousands).

The TDNN was proposed as an alternative nonlinear model in Section 5.2 since it has the ability to generalize a wide range of nonlinear functions, and does not suffer from the curse of dimensional-

ity. The following conclusion can be made:

- Several computer examples showed that the *simulated* performance gains of the TDNN structure would not be as significant as obtained with the Volterra filter.
- When applied to experimentally obtained data, the TDNN models attained up to 5.6 dB higher converged ERLE than the Volterra models (Refer to Table 5.1).
- Structures with a single hidden layer with a small number of hidden nodes (i.e. one or two) are adequate for modelling the AEC process. In terms of complexity, this is welcome news, since the number of weights is a multiplicative function of the number of nodes between layers.
- A mixed linear sigmoid activation function was subsequently developed and it was demonstrated that by varying the linear range, several dBs of improved ERLE could be obtained (Refer to Figure 5.10).
- A TDNN is capable of several dB's of improvement in converged ERLE in the undermodelled case[1] compared to an FIR structure with an equivalent number of taps in the TDL as measured using HFT #3 (Refer to Figure 5.14).

The conventional TDNN also has some detrimental effects, for example, poorer performance than the FIR structure at low and medium volumes. As a result, several new TDNN based architectures were developed to try to mitigate some of the problems associated with the conventional TDNN.

A new structure for nonlinear AEC, the *two stage neural filter*, was presented in Section 5.4.

- A simple gradient based learning algorithm was presented which has a complexity of $2(n_1 + n_2) + 22$ operations per iteration, where n_1 and n_2 refer to the lengths of the TDLs in the nonlinear and linear sections respectively.
- Experimental results on HFT #6 indicate that this new structure is capable of 3 dB improved ERLE at the low volumes, and up to 11 dB improvement at high volume ranges, compared to the equivalent length FIR structure

1. Typically the TIP/TP ratio (see Section 4.4.2) is the limiting factor for undermodelled linear systems, however, it appears that for nonlinear systems, this may not be the case.

- The performance of proposed structure matches the linear FIR structure in the medium volume range.

It was demonstrated in Section 5.2 that by varying the linear region of the mixed linear-sigmoid activation functions, improved performance could be obtained. This was the motivation for developing a the VA-TDNN structure using a fully *adaptive activation function*, as discussed in Section 5.5. The VA-TDNN structure *obtains the best overall performance* of all the models tested on the experimental data (See Figure 5.20).

Finally, in Section 5.6, the VA-FIR-MLP was presented as a method for identification of cascaded nonlinear/linear/nonlinear systems. Computer simulations showed the efficacy of this model for the identification of low-order nonlinear cascaded systems, however the experimental results show that it is not as effective as the methods presented in the previous sections, although some gains could be obtained in the high volume ranges.

All of the structures developed in this chapter were tested using filtered *noise* as the input, even though the final application is for nonlinear acoustic echo cancellation, where the input signal is speech. It is well known that instantaneous gradient based learning algorithms suffer from slow convergence when coloured signals like speech are applied. In this chapter, the main performance criterion is the the *steady-state* ERLE value, so given sufficient training time, filtered noise was an appropriate input. However, for applications using speech as the input signal, it is necessary to invoke nonlinear training algorithms that are less sensitive to the characteristics of the input signals. This is the focus of Chapter 6.

Chapter 6
Conjugate Gradient Methods for Improved Performance

In previous chapters it was shown that several TDNN based structures can be applied to improve the overall steady-state MSE. However, the convergence rate in general was not as fast as the FIR structure trained with the NLMS algorithm. In this chapter, a new training algorithm is developed to improve the convergence rate without affecting the tracking ability. The algorithm is based on the fast conjugate gradient (FCG) algorithm which is modified for application to MLPs using the gradient backpropagation algorithm. In Section 6.1 the linear FCG algorithm is presented and then extended to neural networks. It is then used on the two stage neural filter developed in Section 5.4 and applied to both simulated and experimental data, including speech, to illustrate the performance advantages that can be obtained.

In Section 6.2, a variation on the FCG algorithm employing *gradient reuse* and a variable step-size line search algorithm is presented. This variation is for linear structures only. Section 6.2.9 presents a summary and discussion of the results.

6.1 Fast Conjugate Gradient Backpropagation

The conventional backpropagation (BP) algorithm presented in Section 3.7.1 is probably the most widely used supervised learning algorithm in neural network applications. However, with a large number of weights, the BP learning time is excessively long and its use become impractical. The conjugate gradient algorithm is well suited for the neural network learning problem since it is fast, simple and requires little additional storage space (only the current and previous gradient and search vectors and weights must be stored). The CG method speeds up the BP learning time significantly and does not suffer from the inefficiencies and possible instabilities that arise using the BP with a fixed step size. In fact, the CG algorithm has been found in some studies [71] to be an order of magnitude faster than the conventional BP using momentum.

Partial CG methods introduced in Section 3.4 allow further simplification of the CG algorithm by restricting the weight updates for a number of iterations $k<m$, where m is the filter order. Partial CG algorithms provide a stepping point for the formulation of *fast* (i.e. numerically less intensive) versions of the CG algorithm.

6.1.1 Fast Conjugate Gradient Algorithm for Linear Adaptive Filters

Boray and Srinath [73] recently developed a *fast conjugate gradient algorithm* (FCG) for linear adaptive filtering using an averaged instantaneous gradient over a *window* of past sample values. They showed that the advantages of this windowed approach are (i) better tracking and convergence is achieved in nonstationary environments with correlated data compared to the RLS algorithm, and (ii) there are no stability problems associated with an exponential forgetting factor as in the RLS algorithm. The CG algorithm achieves convergence speed comparable to the RLS algorithm even when the input signal autocorrelation matrix is ill conditioned [73]. However, the CG

computational burden is still high compared to variations based on the LMS algorithm [154] hence the FCG algorithm is a welcome method to simplify the CG further.

In the conventional CG algorithm the gradients are normally calculated as *true* gradients meaning that at least *m* conjugate directions can be calculated, and that all the training data is available for calculation of the gradient. However, in real time filtering and system identification an *on-line* method of approximating the gradient is required. If we use an *instantaneous* gradient estimate, as is done in the LMS algorithm, the CG algorithm will terminate in one step and essentially defaults to the LMS algorithm. This is because there will not be any more directions conjugate to the initial direction vector. However, a better approximation to the gradient can be obtained by calculating the *estimate* based on a *window* n_w of past values of inputs [73]. The algorithm tries to minimize a *partial* cost function constructed by summing n_w instantaneous cost functions using the *current* weight vector $\mathbf{w}(n)$;

$$J_{partial}(n) = \sum_{i=0}^{n_w-1} J_{inst}(n-i)\Big|_{\mathbf{w}(n)} \tag{5.65}$$

It can be shown [73] that there will be at least $\min(m,n_w)$ linearly independent direction vectors in the gradient estimate, where *m* is the filter order. Specifically the *instantaneous* gradient estimate at time *n* is replaced by a *windowed* estimate as follows;

$$\mathbf{g}_k(n) = [\overline{\nabla f(\mathbf{w}_k(n))}] \approx \left(\frac{2}{n_w}\right)\left[\sum_{i=0}^{n_w-1}\left\{[\mathbf{w}_k{}^T(n)\mathbf{x}(n-i) - d(n-i)]\mathbf{x}(n-i)\right\}\right] \tag{5.66}$$

The *linear* FCG algorithm the same as that listed in Section 3.4.4 except that the computation of $\mathbf{g}_k(n)$ is done according to (5.66) and the iteration count is terminated when $k=n_w$.

Simplification of the FCG algorithm. The computation of the optimum step size α_k in (3.44) still requires $2mn_w$ multiplies and one division. By removing the calculation of α_k and replacing it with a *constant* value, the calculation of **p** and **y** are also no longer required, thus simplifying the algorithm further. However, instead of using a fixed step size as proposed in [73], a normalized step size is used in all subsequent simulations, defined by

$$\tilde{\alpha}(n) = \frac{\alpha}{\mathbf{x}^T(n)\mathbf{x}(n) + \varepsilon} \qquad (5.67)$$

where $0 < \alpha < 2$ and ε is some small value. This slight variation of the algorithm is used in all the simulations. It should be pointed out that by avoiding the calculation of α_k at each iteration, there is no guarantee that the successive direction vectors will be truly conjugate. This will result in reduced convergence rates over that of the CG algorithm. The FCG algorithm for linear FIR filters is summarized below:

Fast Conjugate Gradient Algorithm for Linear FIR Filters:

Initialization: $\mathbf{w}_0(0)=\mathbf{0}$

For each iteration *n*, do steps 1,2 and 3.

Step 1:

a) Starting with an initial weight vector $\mathbf{w}_0(n)$ compute the following;

$$\mathbf{g}_0(n) = [\overline{\nabla f(\mathbf{w}_0(n))}] \qquad (5.68)$$

b) set $\mathbf{d}_0(n) = \mathbf{g}_0(n)$

c) compute the normalized step size $\tilde{\alpha}(n)$ according to (5.67)

Step 2:

Repeat for k=0,1,. . . ,n_w-1

a) set $\mathbf{w}_{k+1}(n) = \mathbf{w}_k(n) + \tilde{\alpha}\mathbf{d}_k(n)$

b) Compute the gradient estimate at the new weight vector $\mathbf{w}_{k+1}(n)$

$$\mathbf{g}_{k+1}(n) = [\overline{\nabla f(\mathbf{w}_{k+1}(n))}] \tag{5.69}$$

(*c*) Unless k=n_w-1, obtain the new direction vector

$$\mathbf{d}_{k+1}(n) = -\mathbf{g}_{k+1}(n) + \beta_k \mathbf{d}_k(n) \tag{5.70}$$

$$\text{where} \quad \beta_k = \frac{\mathbf{g}_{k+1}^T(n)\mathbf{g}_{k+1}(n)}{\mathbf{g}_k^T(n)\mathbf{g}_k(n)} \tag{5.71}$$

and repeat *Step 2 (a)*.

***Step 3*:**

Replace $\mathbf{w}_0(n)$ by $\mathbf{w}_m(n)$ and go back to *Step 1*.

6.1.2 Extension of the FCG Algorithm to Neural Networks

We can extend the FCG algorithm to the nonlinear case, for neural networks. The *nonlinear FCG* (NFCG) algorithm is similar to the algorithm presented in the previous section. The differences are (1) the network is nonlinear (2) the errors must be computed for hidden layers and not just the output layer (3) the previous values of the *hidden layer* outputs must be retained as well as the output layers in order to compute the windowed gradient. The cost function to be minimized takes the form of equation (5.65) however, the vector $\mathbf{w}(n)$ is now an M^{th} order supervector defined by

$$[\mathbf{w}(n)]^T = [[\mathbf{w}^{(0)}(n)]^T, [\mathbf{w}^{(1)}(n)]^T, [\mathbf{w}^{(2)}(n)]^T, \ldots [\mathbf{w}^{(L)}(n)]^T] \tag{5.72}$$

where

$$\mathbf{w}^{(l)}(n) = [w_{11}^{(l)}(n), w_{12}^{(l)}(n), \ldots, w_{N_l N_{l+1}}^{(l)}(n)]^T \quad (5.73)$$

is the weight vector connecting layer l to layer $l+1$ at time (n), M equals the total number of weights in the network and L is the total number of layers in the network. The windowed gradient vector $\mathbf{g}(n) = [\overline{\nabla f(\mathbf{w}(n))}]$ is also now of length M, with individual elements corresponding to the weights listed in equation (5.73).

The gradient is computed using the average squared error of a *window* of training input/output pairs. Similar expressions for the CG and BP algorithms have been developed by several authors, including Charlambous [72], Johansson *et. al.* [71], as well as Adeli and Hung [155]. However, these expressions are based on the *batch* training mode using the *full* set of input/output pairs, and not the windowed method proposed here.

Errors are backpropagated to *previous* layers in the same way as the conventional BP algorithm. The important point is that the window is moved for each new sample of the input that comes in i.e. it is a *sliding* window of past input/output pairs. The NFCG is summarized below;

Nonlinear FCG (NFCG) Algorithm

Initialization: Set weights and biases to random values between -1 and +1..

For each iteration n, do Steps 1,2, and 3.

Step 1. a) Starting with an initial weight vector $\mathbf{w}_0(n)$, compute the following;

$$\mathbf{g}_0(n) = [\overline{\nabla f(\mathbf{w}_0(n))}] = \left(\frac{2}{n_w}\right)\left[\sum_{i=0}^{n_w-1} \mathbf{g}_{inst}(n-i)\Big|_{\mathbf{w}_0(n),\, \mathbf{u}^{(0)}(n-i),\, d(n-i)}\right] \quad (5.74)$$

b) set $\mathbf{d}_0(n) = -\mathbf{g}_0(n)$

c) compute the normalized step size parameter α according to;

$$\tilde{\alpha} = \frac{\gamma}{\varepsilon + \left\|\mathbf{u}^{(0)}(n)\right\|^2} = \frac{\gamma}{\varepsilon + \mathbf{u}^{(0)T}(n)\mathbf{u}^{(0)}(n)} \tag{5.75}$$

Note that $\tilde{\alpha}$ could be replaced by a fixed step size here if desired;

Step 2. Repeat for k=0,1,. n_w-1 where $n_w \le m$

a) set $\mathbf{w}_{k+1}(n) = \mathbf{w}_k(n) + \alpha\mathbf{d}_k(n)$

b) compute an estimate of the gradient at $\mathbf{w}_{k+1}(n)$;

$$\mathbf{g}_{k+1}(n) = [\overline{\nabla f(\mathbf{w}_{k+1}(n))}] = \left(\frac{2}{n_w}\right)\left[\sum_{i=0}^{n_w-1} \mathbf{g}_{inst}(n-i)\Big|_{\mathbf{w}_{k+1}(n),\, \mathbf{u}^{(0)}(n-i),\, d(n-i)}\right] \tag{5.76}$$

c) Unless $k=n_w$-1, set $\mathbf{d}_{k+1}(n) = -\mathbf{g}_{k+1}(n) + \beta_k\mathbf{d}_k(n)$,where;

$$\beta_k = \frac{\mathbf{g}_{k+1}^T(n)\mathbf{g}_{k+1}(n)}{\mathbf{g}_k^T(n)\mathbf{g}_k(n)} \tag{5.77}$$

Note that if $\beta_k > 1$, *go directly to Step three.*

Repeat *Step 2 a).*

Step 3. Replace $\mathbf{w}_0(n)$ by $\mathbf{w}_k(n)$ and go back to *Step 1*.

$\mathbf{g}_{inst}(n\text{-}i)$ is the *instantaneous* gradient calculated with the current network weight vector $\mathbf{w}_0(n)$ and past inputs $\mathbf{u}^{(o)}(n\text{-}i)$ and $d(n\text{-}i)$. Both $\mathbf{g}_{inst}(n\text{-}i)$ and $\mathbf{w}_0(n)$ are vectors of length M, where M is the total number of weights in the network. The calculation of individual elements of the instantaneous gradient vector $\mathbf{g}_{inst}(n-i)$ is done by performing the following steps;

$$g_{ij}^{(l)}(n-i) = \delta_j^{(l+1)}(n-i) \cdot u_i^{(l)}(n-i) \quad (5.78)$$

where $g_{ij}^{(l)}(n-i)$ is the instantaneous gradient from the data *i* time steps in the past for weight $w_{ij}^{(l)}(n)$ in the *l-th* layer, and;

$$\delta_j^{(l)}(n-i) = \begin{cases} -2e(n-i)\varphi'(s_j^{(L)}(n-i)) & \dots l = L \\ \varphi'(s_j^{(l)}(n-i)) \cdot \sum_{k=1}^{N_{L+1}} \delta_k^{(l+1)}(n-i) \cdot w_{jk}^{(l)}(n) & \dots 1 \le l \le L-1 \end{cases} \quad (5.79)$$

$$e(n-i) = d(n-i) - N[\mathbf{w}_{k+1}(n), \mathbf{u}^{(0)}(n-i)] \quad (5.80)$$

Note that $\varphi[\mathbf{w}_{k+1}(n), \mathbf{u}^{(0)}(n-i)]$ represent the nonlinear output of the neural network at time *n* using the current weight vector $\mathbf{w}_{k+1}(n)$ with past input vectors $\mathbf{u}^{(0)}(n-i)$. An illustration of the terms is shown in Figure 3.7 and Figure 3.8.

Complexity. The choice of n_w =1 implies no averaging in the gradient estimate and the NFCG algorithm reverts to the BP algorithm. For higher values of n_w the complexity approaches that of algorithms that use the second derivative for obtaining the optimum step size and direction which have complexity $O(m^3)$[74]. The complexity of the NCG algorithm is $O(mn_w^2)$ since in *Step 2*, the weights are updated n_w times per iteration and the calculation of the averaged gradient is $O(mn_w)$.

6.1.3 Computer Simulation

In this section, we apply the NFCG algorithm to the identification of a nonlinear system constructed by generating a signal which is hard limited and convolved with an exponentially decaying 50 tap impulse. The system is illustrated in Figure 6.1. The input signal $x(n)$ is obtained by a first order autoregressive (AR) process according to;

$$y(n) = 0.9y(n-1) + v(n) \tag{5.81}$$

where $v(n)$ is a unit variance white noise sequence. The hard limiter has a linear region up to 0.5, beyond which the output is clipped with a slope of 0.2. Two hundred independent trials are used in the averaging of the normalized MSE.

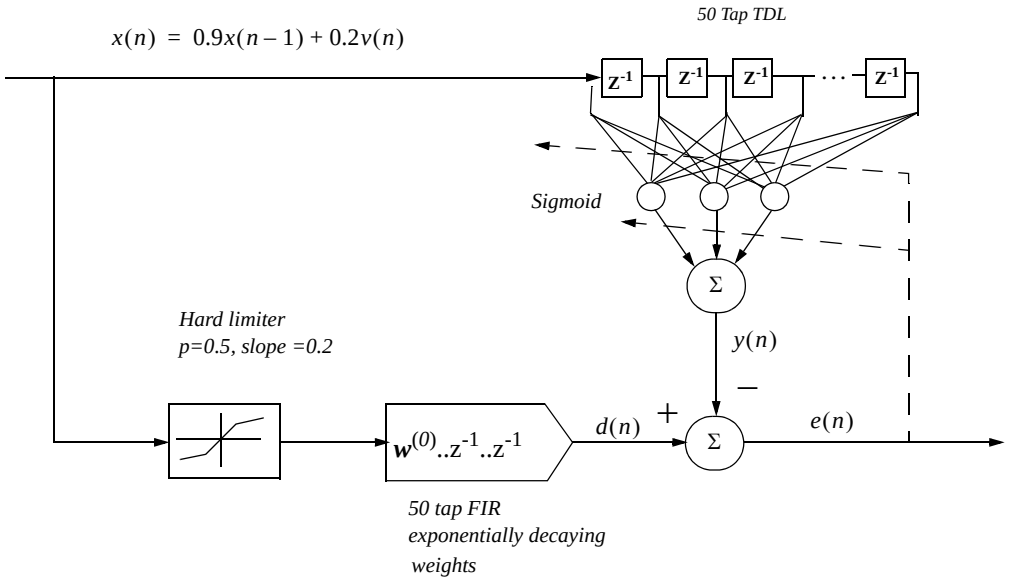

FIGURE 6.1 System identification model.

The results in Figure 6.2 show that for the AR input, the NFCG algorithm converges at a rate much faster than the conventional BP algorithm, depending on the size of the gradient averaging window

n_w. The larger the choice of n_w, the higher the convergence rate. The final misadjustment is approximately -18 dB for all cases.

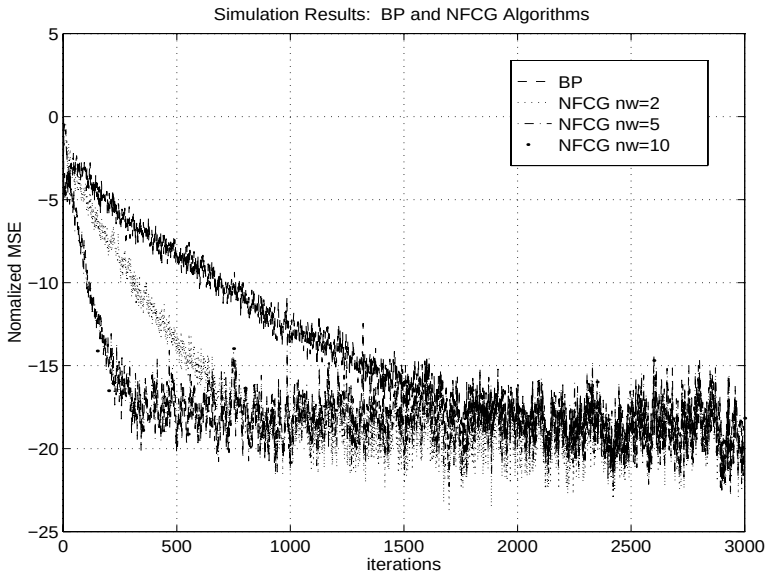

FIGURE 6.2 Simulation results showing the averaged NMSE performance of the BP and NFCG algorithms with n_w=2, 5, and 10 for the system identification model of Figure 6.1. Two hundred independent trials are used in the averaging process

Convergence Rate Improvement. The convergence rate improvement is not a linear function of the window size. For example, the BP algorithm, which is equivalent to the NFCG with n_w=1, takes approximately 1400 iterations to reach -15 dB NMSE. For window sizes n_w=2, 5, and 10, the number of iterations required to reach the same NMSE are approximately 600,200 and 150 respectively. As a result, it can be seen that the convergence rate improvement becomes progressively smaller for large window sizes, and that for n_w>5, the convergence rate improvements are small.

6.1.4 Experimental Results

In this section two experiments are performed using data collected from actual LREM and HFT components. In the first experiment, a filtered noise signal is applied to loudspeaker SPK#2 (refer to Appendix B) which is mounted in a standard baffle and placed inside an anechoic chamber. This is the reference signal. The primary signal is picked up by MIC#1. The primary and reference signals are then applied to a conventional TDNN structure which is trained with the BP and NFCG algorithms.

In experiment #2, data is collected inside Conference Room #2 using HFT#6. Real speech signals are applied as the reference signal. The primary and reference signals are then applied to the two stage neural filter (See Section 5.4) which is trained with the BP and NFCG algorithms. For comparison purposes, the performance of an FIR filter trained with the accelerated SFTF algorithm (see Appendix D.5) is also shown. The accelerated SFTF algorithm is used to remove the long training time associated with LMS based training algorithms when using speech inputs, which may be as long as 10 seconds [156].

Experiment #1, Noise Input. The volume is 100 dB SPL as measured at 0.5 meters from the loudspeaker. The microphone is placed 15 cm. from the loudspeaker output. The signals are sampled at 16 kHz and are later transferred to a computer for off-line analysis. Two adaptive filter structures were tested to identify the system (i) a 150 tap linear transversal filter trained using the NLMS algorithm (ii) a 3 layer TDNN with 150 input taps trained with both the BP and NFCG algorithms. The experimental results shown in Figure 6.3 show the results for all cases. The NLMS has fast convergence but is incapable of obtaining an ERLE of greater than 19 dB due to the nonlinear loudspeaker. The TDNN trained with the BP algorithm is capable of identifying the system more effectively and achieves 25 dB ERLE but the initial convergence is much slower than the NLMS

algorithm. Training the TDNN using the NFCG with a window size n_w=5 results in convergence speed equivalent to the NLMS structure as well as obtaining 24 dB ERLE.

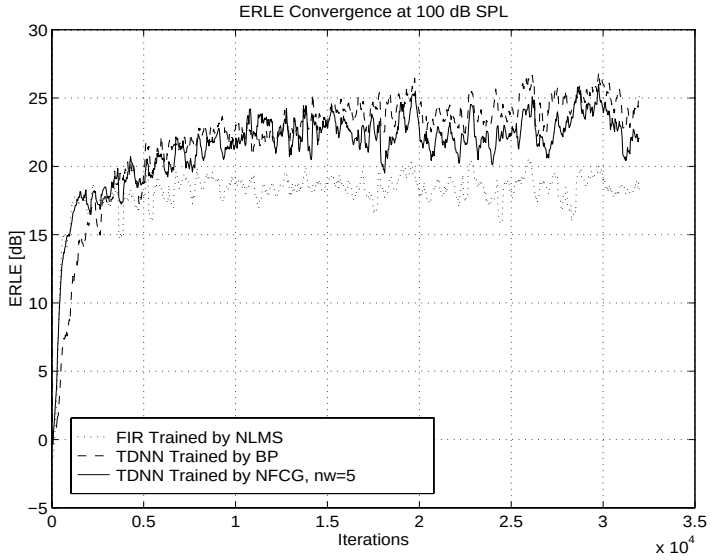

FIGURE 6.3 Experiment #1 results comparing converged ERLE curves of a 150 tap FIR structure trained using the NLMS algorithm with that of a TDNN trained with the BP and NFCG algorithm.

Experiment #2, Speech Input. The average volume of the speech signal as measured 0.5 m from the loudspeaker is 95 dB SPL, which is a comfortable listening level 6-10 ft. from the HFT. The HFT is placed in the middle of the conference table. The parameters are listed in Table 6.1.

TABLE 6.1 Experiment #2 parameters.

Item	Parameters
Data	160,000 samples @16 kHz sampling. 95 dB SPL average volume at 0.5 m.
FIR Trained with Accelerated SFTF	N=600, λ=0.9998, acceleration factor=0.95, soft initialization constant=200.
Two stage neural filter trained with NFCG algorithm	N_1=150, N_2=450, number of hidden nodes=1, neural network normalized step size α=0.5, nlms step size α=0.5,window size n_w=5 for TDNN section

Figure 6.4 shows the speech signal amplitude as a function of time. The converged ERLE results shown in Figure 6.5 and Figure 6.6 indicate that the proposed structure/algorithm outperforms the FIR structure trained with the accelerated SFTF algorithm by approximately 5 dB.

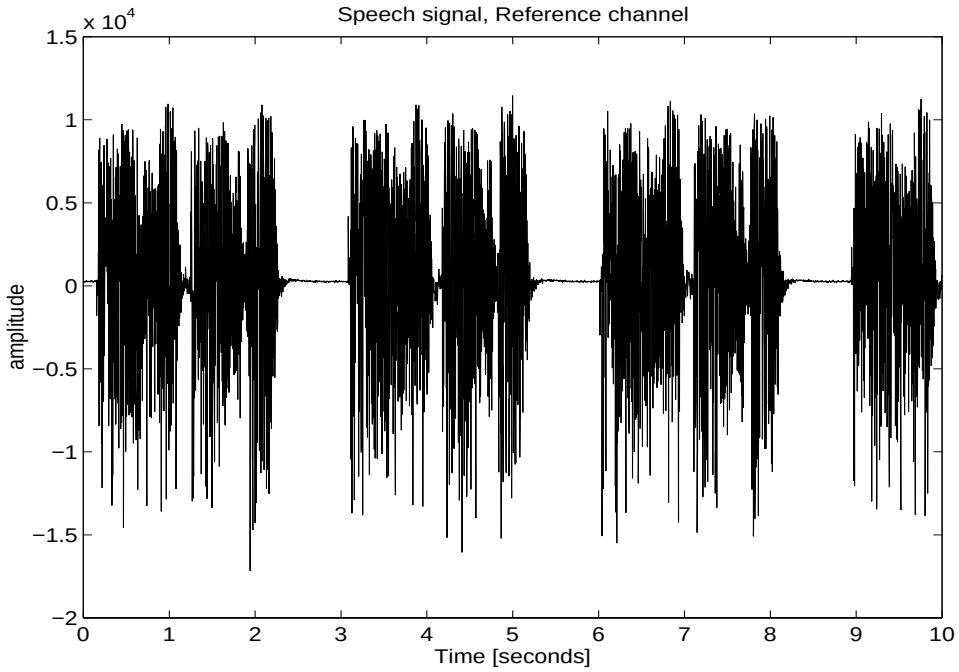

FIGURE 6.4 Reference signal speech signal.

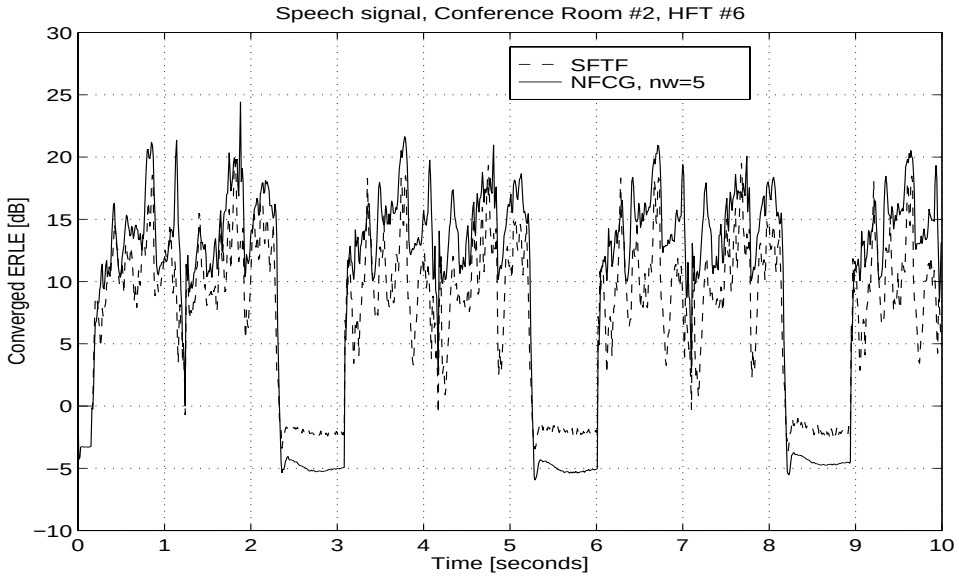

FIGURE 6.5 Experiment #2 results. Converged ERLE results with speech input. Gaps show where pauses in speech are located.

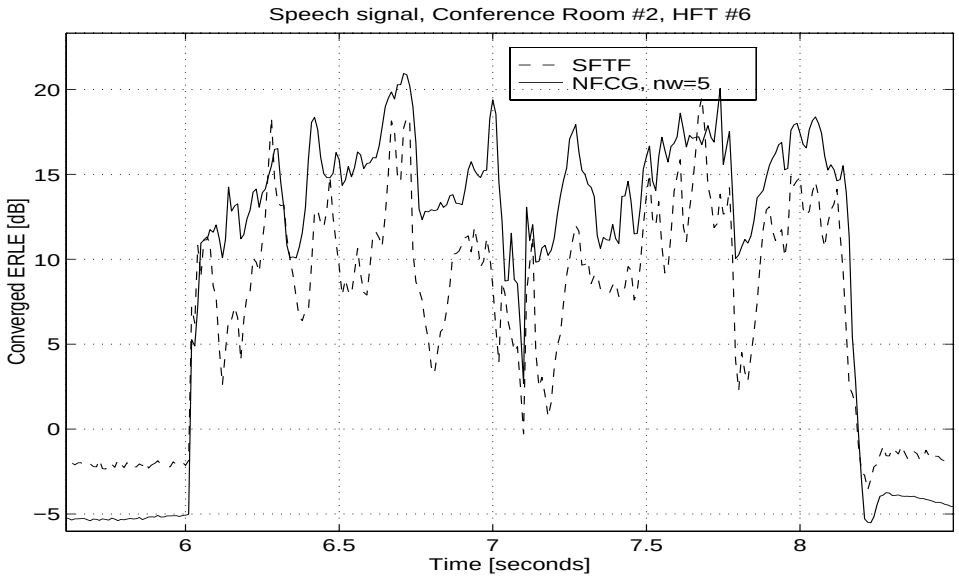

FIGURE 6.6 Experiment #2 results. Close up of speech period between 6 and 8 seconds. The two stage neural filter trained with proposed algorithm achieves approximately 5 dB higher ERLE that the FIR filter trained with stabilized SFTF algorithm.

6.1.5 Discussion

The results presented in this section have shown that the NFCG algorithm is capable of improving the convergence rate of neural network based adaptive filters. When applied to the two stage neural filter from Section 5.4, the NFCG algorithm achieves a 5 dB improvement in ERLE compared to the accelerated SFTF algorithm when trained with real speech signals at loud volumes where loudspeaker nonlinearities become significant. Simulation results in Section 6.1.3 also indicate that by varying the size of the gradient window n_w, we can obtain improved convergence speed with a corresponding increase in complexity. A window size of n_w=5 was found sufficient to speed the initial convergence rate of the two stage neural filter to be no worse than the linear FIR trained with the NLMS algorithm, when applied to data collected from a loudspeaker/microphone placed in an anechoic chamber.

One of the important features of the NFCG algorithm is that the gradient window can be made arbitrarily small to “tailor” the algorithm to a particular application. Thus, where a modest increase in convergence is desired without compromising tracking ability, a small n_w can be chosen. Low values of n_w will result in slower convergence, however, the advantages are reduced complexity and faster tracking capability. This is important for AEC applications where reduced complexity is of utmost importance. It has been shown that linear algorithms based on instantaneous gradient LMS type updates have superior tracking ability compared to faster algorithms based on least squares minimization [95]. The performance of partial CG algorithms falls between algorithms based on instantaneous and full gradient (i.e. least squares) methods [70]. Hence, as the window size becomes large and the convergence improves, the dynamic tracking performance will suffer. It is therefore reasonable to assume that a similar performance trade-off will be noticed in extensions of CG methods to the nonlinear domain, like the NFCG.

6.2 Conjugate Gradient Reuse Algorithm with Dynamic Line Search

The fast CG algorithm presented in Section 6.1.1 was obtained by substituting the optimum step size α_k with a fixed step size, thus avoiding the computation of the difference vector $\mathbf{y}_k(n)$ and its gradient $\mathbf{p}_k(n)$. It is possible however, to estimate a *reasonable* value of α_k using an *inaccurate* line search technique.

In this section a new *linear* algorithm which is presented which combines the FCG algorithm and the Modified Variable Step Size (MVSS) algorithm [55] to provide a convergence/tracking performance/complexity trade-off. The MVSS algorithm is used to perform an inaccurate one dimensional line search along the conjugate direction vector $\mathbf{d}_k(n)$ at each iteration *k*. By selecting an appropriate number of steps performed during the line search, it is possible to achieve the same performance as the FCG algorithm but using a *smaller* window size, and therefore reduced complexity. This algorithm is called the Variable step size CG (VCG) algorithm.

A simplified version of the VCG algorithm is also presented that *reuses* weight updates (i.e *gradient reuse*) to avoid calculating gradients and conjugate directions at every sample *n*. This simplified algorithm only invokes the conjugate gradient update every *P*th sample resulting in an overall complexity reduction by a factor of *P* as compared to the FCG algorithm. This new algorithm is called the *conjugate gradient reuse* (CGR) algorithm.

Simulation results show that improved convergence and tracking is obtained compared to the NLMS, RLS, FCG and MVSS algorithms when the input data is correlated and the environment is nonstationary.

6.2.1 Inaccurate Line Search

There are two kinds of line searches, accurate line searches and inaccurate line searches. Accurate line searches are very attractive theoretically, however, they are very expensive to carry out and the algorithm may spend a considerable amount of computing effort locating the exact minimum point on a descent direction.

Typically, an accurate line search involves bracketing or straddling the minimum and then using a cubic interpolation algorithm to determine the exact minimum [71]. A stochastic line search algorithm has been presented in [157] which recursively minimizes the sum of squared errors on a linear manifold. It is similar to fast RLS algorithms since it iteratively calculates the optimum step size parameter. Other line search techniques such as the scaled conjugate gradient (SCG) algorithm [158] have been proposed in the literature, however, all the aforementioned accurate line searches are formulated for full gradients and do not work for partial CG methods.

Inaccurate line searches typically terminate a search before it has converged. Several popular techniques are Armijo's Rule [159] and the Goldstein Test [70]. The basic idea is to guarantee a proper, namely not to large and not too small, step size is selected. The FCG algorithm is the extreme case of an inaccurate line search, where only a single fixed step is taken toward the minimum. The MVSS algorithm may also be applied as an inaccurate line search algorithm and this is described next.

6.2.2 The MVSS Line Search Algorithm

The MVSS algorithm [55] is a variable step size (VSS) LMS type algorithm that dynamically adjusts the step size during the search for the minimum of a performance surface. The MVSS calculates at each iteration a step size based on the autocorrelation of adjacent *error* samples. When

the error correlation is large, dynamic step size control adjusts the step size to be large thus speeding up the convergence. Thus, when the filter is far from the optimum and the autocorrelation of the error signal is large, the step size is large. This has the effect of reducing the number of iterations needed to find the minimum of a particular conjugate direction by increasing the line search step size where appropriate and in this respect is similar to the line search algorithm in the SCG algorithm and Armijo's rule. Specifically, the step size is updated by the following formulas;

$$\mu(k+1) = \begin{cases} \mu_{max} & ;\mu(k+1) \geq \mu_{max} \\ \mu_{min} & ;\mu(k+1) \leq \mu_{min} \\ \zeta\mu(k) + \gamma\rho^2(k) & ;\mu_{min} < \mu(k+1) < \mu_{max} \end{cases} \quad (5.82)$$

$$\text{where} \quad \rho(k) = \Gamma\rho(k-1) + (1-\Gamma)e(k)e(k-1) \quad (5.83)$$

$$\text{and} \quad \begin{cases} 0 < \zeta < 1 \\ \Gamma < 1 \\ \gamma > 0 \end{cases} \quad (5.84)$$

The parameter γ controls the convergence time. The parameter ζ controls the averaging of the step size update and Γ controls the averaging time constant of the filtered error update. The parameter ρ gives a short time estimate of the error signal autocorrelation. Typical parameter values are ζ=0.97, Γ=0.99, γ=1e-5 [55]. The advantage of the MVSS algorithm over the standard VSS algorithm is its relative *insensitivity* to noisy signals due to the time average autocorrelation process. This technique is adopted in the FCG algorithm to dynamically control the step size update during the line search. A measure of the "minimum" of the line search can be obtained by examining $e(j)$ and $e(j\text{-}1)$ where j is the line search iteration count. If $e(j) < e(j-1)$ then the algorithm is still searching for the minimum of the performance surface along this particular direction. If

$e(j) \geq e(j-1)$ then the minimum has been reached, at which point we exit the search and replace the initial weight vector $\mathbf{w}_o$ with the one used to generate $e(j\text{-}1)$.

6.2.3 Maximum and Minimum Step Sizes

Due to the inaccuracy of the line search, the step size α_k will not be exact and the direction vectors $\mathbf{d}_k$ will not be **Q**-conjugate. For general nonlinear problems, an indication that the algorithm is getting stuck, or near the minimum, is that very small steps are being taken. Subsequently orthogonality between successive gradients is lost, $\mathbf{g}_{k+1} \approx \mathbf{g}_k$ [71] and it is possible that the calculation of β_k will be close to or larger than 1 and cause instability.

Proakis [160] demonstrated that the conventional CG algorithm resembles the operation of a first-order recursive filter whose output $\mathbf{d}_k$ is given by equation (5.70). An *m*-dimensional filter is in effect a set of *m* identical single-pole (low pass) filters operating in parallel which corresponds to filtering the gradients with a time-variant filter. This can provide faster convergence than the conventional LMS algorithm, however, if β_k is close to or larger than 1, as may happen with partial CG methods using inaccurate line searches, successive iterations will only serve to move the weight vector away from the optimum value and make the algorithm unstable. Proakis found it necessary to limit the value of $\beta_k < 1$ in a channel equalization experiment and obtained the conditions for stability which can be expressed as follows [160];

$$0 < \mu_k < \frac{2(1+\beta_k)}{\lambda_{max}} \tag{5.85}$$

where $0 < \beta_k < 1$ and λ_{max} is the maximum eigenvalue of the input data. Specifically, the gradient averaging *extends* the upper limit of the region of stability of μ_k from $2/\lambda_{max}$ to $2(1+\beta_k)/\lambda_{max}$ but β_k must be kept below 1.

In [161] Shanno shows that the use of inaccurate line searches using the Polak-Ribiere or Fletcher-Reeves method may yield conjugate directions $\mathbf{d}_k$ which are not descent directions, resulting in numerical instability. A method for calculating $\mathbf{d}_k$ is derived which guarantees a descent direction. Since Shanno's method is not used here for computing successive $\mathbf{d}_k$, the maximum step size boundary in (5.85) is checked each iteration and then a limit $\mu_{max}/10$ is imposed on the minimum step size.

6.2.4 Variable Step Size CG Algorithm using MVSS Line Search

The complete algorithm is summarized below and uses triply indexed parameters. The parameter *n* refers to the main iteration number, where the data is shifted in on a sample by sample basis, *k* represents the conjugate direction iteration count and *j* represents the line search iteration count.

Conjugate Gradient Algorithm with MVSS Line Search (VCG)

Initialization: $\mathbf{w}_0(0)=\mathbf{0}$, $\beta_k(0)=0$.

For each iteration n, do steps 1,2 and 3.

Step 1:

1a) Shift in new data into vector $\mathbf{x}(n)$

1b) Starting with an initial weight vector $\mathbf{w}_0(n)$, compute the initial error;

$$e(n) = \mathbf{w}_0^T(n)\mathbf{x}(n) - d(n) \tag{5.86}$$

1c) Compute the maximum step size according to

$$\mu_{max}(n) = \frac{1 + \beta_k(n)}{\mathbf{x}^T(n)\mathbf{x}(n)} \tag{5.87}$$

1d) Compute the *initial* windowed gradient estimate;

$$\mathbf{g}_0(n) = [\overline{\nabla f(\mathbf{w}_0(n))}] = \left(\frac{2}{n_w}\right)\left[\sum_{i=0}^{n_w-1}\left\{[\mathbf{w}_0{}^T(n)\mathbf{x}(n-i) - d(n-i)]\mathbf{x}(n-i)\right\}\right] \quad (5.88)$$

1e) set $\mathbf{d}_0(n) = -\mathbf{g}_0(n)$

Step 2: Repeat for k=0,1,. n_w-1 where $n_w \le m$

2*a)* set $\mu_{k,0}(n) = \mu_{max}(n)$ and $\mathbf{w}_{k,0}(n) = \mathbf{w}_k(n)$

Repeat Steps *2b-1)* through *2b-4)* for j=1,. n_w where $n_w \le m$

2b-1) Set $\mathbf{w}_{k,j}(n) = \mathbf{w}_{k,j-1}(n) + \mu_{k,j}(n)\mathbf{d}_k(n)$

2b-2) Compute the new error output using

$$e_{k,j}(n) = \mathbf{w}_{k,j}{}^T(n)\mathbf{x}(n) - d(n) \quad (5.89)$$

2b-3) Adjust the step size

$$\mu_{k,j}(n) = \begin{cases} \mu_{max}(n) & ;\mu_{k,j}(n) \ge \mu_{max}(n) \\ \mu_{min}(n) & ;\mu_{k,j}(n) \le \mu_{min}(n) \\ \zeta\mu_{k,j-1}(n) + \gamma\rho_j^2(n) & ;\mu_{min}(n) < \mu_{k,j}(n) < \mu_{max}(n) \end{cases} \quad (5.90)$$

$$\text{where} \quad \rho_j(n) = \Gamma\rho_{j-1}(n) + (1-\Gamma)e_j(n)e_{j-1}(n) \quad (5.91)$$

2b-4) if $e_{k,j}(n) > e_{k,j-1}(n)$ then proceed to *Step 2c)*, else goto *Step 2b-1)*.

2c) restore the "optimum" weight vector $\mathbf{w}_{k+1}(n) = \mathbf{w}_{k,j}(n)$ for this direction.

2*d)* Unless k=m_w-1, set $\mathbf{d}_{k+1}(n) = -\mathbf{g}_{k+1}(n) + \beta_k(n)\mathbf{d}_k(n)$,where;

$$\beta_k(n) = \frac{\mathbf{g}_{k+1}^T(n)\mathbf{g}_{k+1}(n)}{\mathbf{g}_k^T(n)\mathbf{g}_k(n)} \quad \text{and} \tag{5.92}$$

$$\mathbf{g}_{k+1}(n) = [\overline{\nabla f(\mathbf{w}_{k+1}(n))}]$$
$$= \left(\frac{2}{n_w}\right)\left[\sum_{i=n-n_w+1}^{n}\left\{[\mathbf{w}_{k+1}{}^T(n)\mathbf{x}(i) - d(i)]\mathbf{x}(i)\right\}\right] \tag{5.93}$$

I f $\beta_k(n) > 1$, *go directly to Step 3), otherwise go to Step 2)*

Step 3. Replace $\mathbf{w}_0(n+1)$ by $\mathbf{w}_k(n)$, and go back to *Step 1*.

The MVSS line search is performed in *Step 2b-1)* where the newly computed direction vector $\mathbf{d}_k$ is used to successively update $\mathbf{w}_k$.

Note that $\mathbf{d}_k(n) = -\mathbf{g}_k(n) = -[\overline{\nabla f(\mathbf{w}_k(n))}]$ only during the *first* iteration of the line search when k=0 and that during successive iterations, $\mathbf{d}_k$ will change. We have imposed an allowed limit of nw steps of loop *2b)* to reach the minimum of a particular conjugate direction during the line search. This factor was chosen to place a limit on the number of steps taken should the direction estimate be in the wrong direction. If the minimum of a particular conjugate direction has not been reached before the next conjugate direction is calculated, or if the gradient estimate is poor, there is no guarantee that the new directions will be conjugate with respect to one another. This will slow convergence, however, it is still superior to the NLMS algorithm.

6.2.5 Gradient Reuse

The VCG provides an *averaged* gradient which also points in the optimum direction towards the minimum of the performance surface based on the available information in the gradient window. If we assume that the performance surface does not change too rapidly, then it is safe to assume that by *reusing* the conjugate *gradient* updates (as opposed to conjugate *direction* updates), we can still step in the right direction and at the same time avoid the calculation of the true gradient. If we only allow a gradient calculation every P input samples, we obtain a reduction in the complexity by a factor of P over the VCG. This is the basis of the VCG algorithm with gradient reuse (VCGR). A variation of this idea was proposed by Hush and Salas [162] for reducing the computational complexity of backpropagation weight updates in neural networks where they showed that the convergence rate speed-up or slow-down is a related to the reuse rate. It is also possible to reuse the weight updates several times per *sample* iteration n, i.e. $P<1$, however for the application described here, we only update the weights once per sample with a gradient calculation every P samples. The trade-off is that the convergence rate will become *poorer* in correlated environments as P increases. However, it provides a basis for trading computationally complexity for performance in the same way as the gradient window size n_w. The algorithm is the same as the VCG except for the following changes which are indicated with an asterisk in bold type;

VCG with Gradient Reuse (VCGR)

Initialization: $\mathbf{w}_0(0)=\mathbf{0}$, $\beta_k(0)=0$.

******count=0;***

For each iteration *n*, do steps 1,2 and 3.

Step 1:

1a) Shift in new data into vector $\mathbf{x}(n)$

1b) Starting with an initial weight vector $\mathbf{w}_0(n)$, compute the initial error;

$$e(n) = \mathbf{w}_0^T(n)\mathbf{x}(n) - d(n) \quad (5.94)$$

******count=count+1***

******if count=P, continue, else goto Step 3)***

Perform rest of *Step 1)* and *Step 2) here*

Step 3.

****** If count=1,***

$$\Delta\mathbf{w}_k(n) = \mathbf{w}_k(n) - \mathbf{w}_o(n) \quad (5.95)$$

$$\mathbf{w}_o(n+1) = \mathbf{w}_k(n) \quad (5.96)$$

****** else***

$$\mathbf{w}_o(n+1) = \mathbf{w}_o(n) + \Delta\mathbf{w}_k(n) \quad (5.97)$$

Replace $\mathbf{w}_0(n+1)$ by $\mathbf{w}_k(n)$, and go back to *Step 1*.

6.2.6 Complexity

In the regular CG algorithm, the number of multiplications required in *Step 1)* is $3m^2$ per gradient calculation or $6m^2$ total. In step 2), the number of multiplications per sample is $m(6m^2 + 6m)$ per sample for an overall total of $6m^3 + 12m^2$. In the VCG, the number of multiplications per sample in *Step 1*) is $2mn_w + 1$. *Step 2b* is done R times resulting in a complexity of $n_w R(2m + 6)$ multiplications per sample where $R \le n_w$. *Step 2d)* is done n_w-1 times for a complexity of $(n_w - 1)(2mn_w + 3m)$ multiplications per sample. Summing all of these contributions, the overall complexity of the VCG is equal to;

$$(2mn_w + 1) + n_w R(2m + 6) + (n_w - 1)(2mn_w + 3m) \qquad (5.98)$$

multiplications per sample. For R =1 the VCG will default to the FCG algorithm and for n_w=1, it reverts to the NLMS algorithm. The standard RLS algorithm has complexity of ($2m^2$+4m). The VCG has a slight increase in computational complexity over the FCG algorithm due to the conjugate direction reuse rate R. However, if fewer than R successive steps of *2b)* are needed before the minimum is reached, this estimate of complexity would represent an upper bound. It is possible to limit the value of R to some value smaller than n_w to provide a limited complexity increase. Simulation results will show that by using a restricted R, *it is possible to obtain the same performance with the VCG as with the FCG algorithm, even though the latter requires a larger window size to obtain this performance and is therefore more complex*.

The VCGR algorithm only performs gradient calculations every P samples, and this reduces the complexity to;

$$(m + 1) + \frac{2mn_w + n_w R(2m + 6) + (n_w - 1)(2mn_w + 3m)}{P} \qquad (5.99)$$

multiplications per sample for $R \geq 2$. For P=1, the simplified algorithm reverts to the VCG. Table 6.2 gives comparative complexities of the CG, FCG, VCG, VCGR and RLS algorithms for m=50, n_w=5, R=2 and P=3.

TABLE 6.2 Comparison of algorithm complexity.

Algorithm	**Mult./sample**	**Mult./sample for m=50, n_w=5**
CG	$6m^3 + 12m^2$	780,000
FCG	$(2mn_w + 1) + n_w(2m + 6) + (n_w - 1)(2mn_w + 3m)$	3631
VCG	$(2mn_w + 1) + n_wR(2m + 6) + (n_w - 1)(2mn_w + 3m)$	4161
VCGR	$(m + 1) + \frac{2mn_w + n_wR(2m + 6) + (n_w - 1)(2mn_w + 3m)}{P}$	1438
RLS	$2m^2 + 4m$	5200

6.2.7 Computer Simulations

In this section, we apply the VCG algorithm to the problem of system identification as illustrated in Figure 6.7.

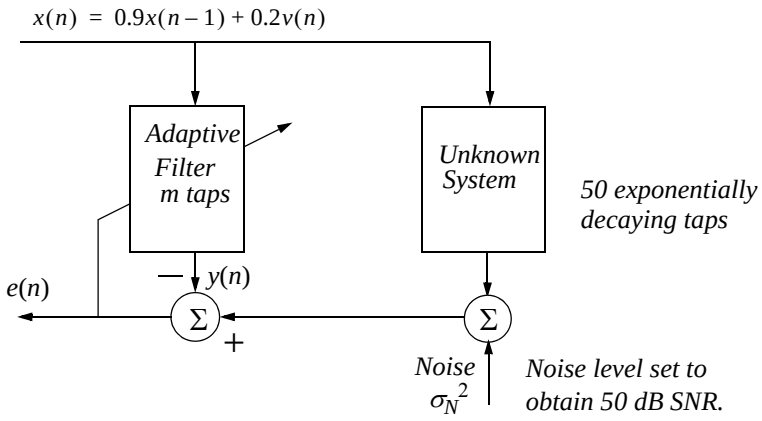

FIGURE 6.7 System identification model. An uncorrelated noise source with variance σ_N^2 is added to the adaptive filter output y(n) to produce an SNR of 50 dB.

The unknown system is modelled by an impulse 50 taps long which is obtained from an exponentially decaying set of random values between ±1. This is representative of an LREM obtained in a highly damped conference room or in automobiles where both fast convergence and tracking are required. The input to the system is a coloured noise sequence obtained from a single pole autoregressive process described by equation (5.81). This signal is then filtered by the unknown system and finally, a small amplitude uncorrelated white gaussian noise signal is then added to the system output to produce a desired signal to noise ratio of 50 dB. In order to demonstrate the tracking capabilities of the VCG, the unknown system impulse response is changed halfway through the data sequence by multiplying all coefficients by -1.0. This change in the transfer function will cause a temporary increase in the mean square error as the algorithms try to readjust the weights to the new optimum weight vector and gives some measure of the tracking performance of a training algorithm. Subsequently, the NMSE convergence curves for the RLS, NLMS, FCG, MVSS and VCG are plotted for comparison. The NMSE curves are obtained by averaging the error and desired signals over 100 independent runs and then smoothing according to the following formula,

$$NMSE(n) = 10\log\left(\frac{\sum_{r=0}^{50}[\overline{e}_r(k)]^2}{\sum_{r=0}^{50}[\overline{d}_r(k)]^2}\right) dB \qquad (5.100)$$

where $\overline{e}_r(k)$ and $\overline{d}_r(k)$ represent the *averaged* error and desired signals averaged over 100 independent trials and r represents the window values over which these averages are then smoothed, in this case equal to 50. A summary of the parameters used in the simulations is listed in Table 6.3.

TABLE 6.3 List of parameters used for simulations #1, #2 and #3.

Algorithm	#Taps m	$\overline{\alpha}$	λ	μ_{max}	μ_{min}	ξ	Γ	γ	n_w	SNR
NLMS	50	0.5	0.5							50 dB
RLS	50		0.997							50 dB
MVSS	50			1.0	1e-5	0.97	0.99	1e9		50 dB
FCG	50	0.5							5	50 dB
VCG	50			see eqn. (5.87)	$\frac{\mu_{max}}{10}$	0.4	0.4	1e2	5	50 dB

The ξ parameter for the MVSS is large since the data sequences used are 16 bit integer which have been normalized with respect to 32768. The window sizes for the FCG and VCG algorithm are both set to 5 which provides a good performance/complexity trade-off. The minimum step size for the line search portion of the VCG algorithm was chosen as $\mu_{min} = \frac{\mu_{max}}{10}$. The signal to noise ratio of the desired signal *d* is set to 50 dB.

Simulation #1, Correlated Input: Figure 6.8 shows the results when the input is coloured by the first order autoregressive process described by equation (5.81). During the first part of the training, the RLS converges quickly owing to its insensitivity to eigenvalue spread. The FCG and VCG algorithms also converge quickly but the VCG is faster than the FCG algorithm. Both the MVSS and NLMS have poor convergence characteristics due to the correlated input data. At iteration 1000, the unknown system is changed and the RLS algorithm has problems tracking due to the forgetting factor λ being close to 1 and only manages to obtain a lower error than the NLMS and MVSS algorithms by iteration 1500. The VCG and FCG algorithms convergence rates after iteration 1000 are almost identical to the initial convergence rate. *The VCG obtains the best convergence rate of all the above algorithms.*

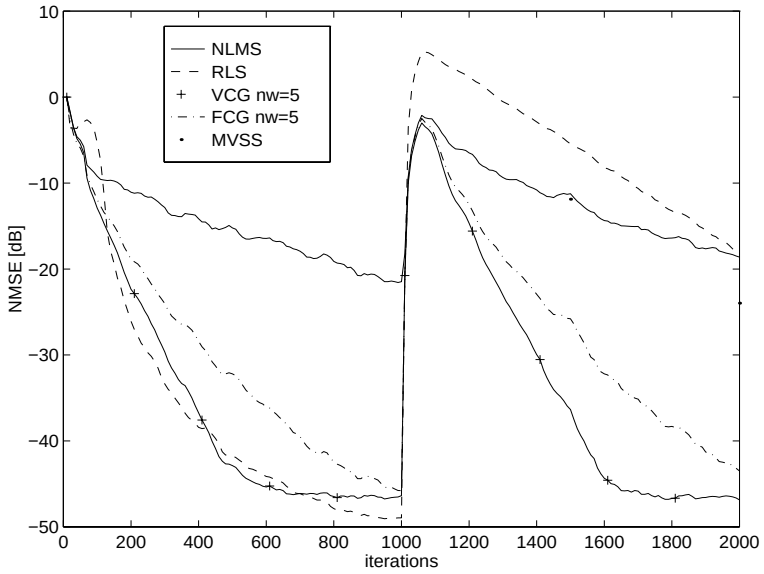

FIGURE 6.8 Simulation #1 results. Correlated noise input with a sudden change in the unknown system transfer function at iteration 1000.

Simulation #2, Comparison of FCG and VCG Algorithms Using Diferent n_w: The conditions for this simulation are the same as in simulation #1 (correlated input) with parameters as listed in Table 6.3. The results in Figure 6.9 show the performance of the VCG with a *limited* conjugate direction reuse rate *R*, as compared to the FCG algorithm using n_w=5 and n_w=8. In this experiment, the NMSE curves were obtained using the parameters listed in Table 6.3 which also indicates the relative complexity.

TABLE 6.4 Parameter and complexity comparison for FCG (n_w=5 and 8) and VCGR algorithm (n_w=5, *R*=2).

Algorithm	#Taps *m*	α	ξ	Γ	γ	n_w	R	SNR	Complexity (mults/iter)
VCG	50		0.4	0.4	1e2	5	2	50 dB	4161
FCG	50	0.5				5		50 dB	3631
FCG	50	0.5				8		50 dB	8299

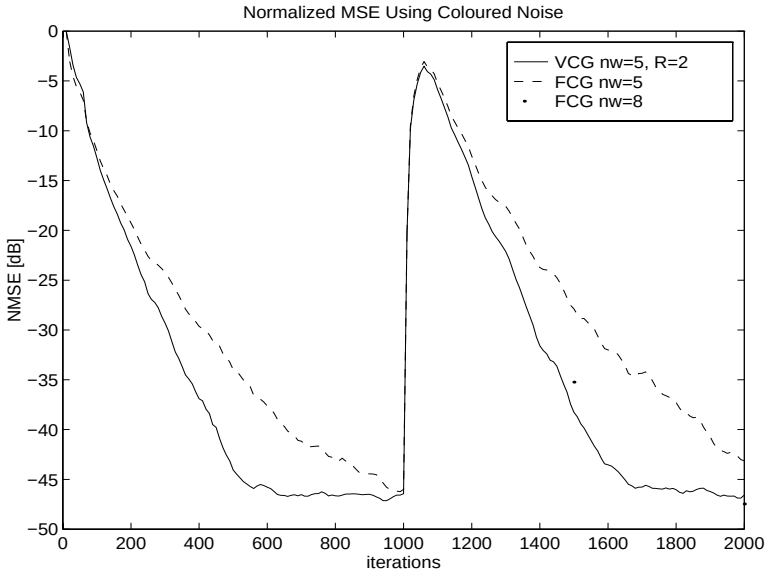

FIGURE 6.9 Simulation #2 results. Comparison of FCG and VCGR using a limited gradient reuse rate. Correlated noise input with a sudden change in the unknown system transfer function at iteration 1000.

The gradient averaging window n_w in the FCG algorithm had to be increased to 8 in order to obtain the same tracking convergence performance as the VCG algorithm with R=2 and n_w=5. *As a result, the complexity of the FCG (n_w=8) is approximately 100% greater than the VCG (n_w=5, R=2) for similar performance results using correlated input signals.*

Simulation #3, VCGR (Simplified VCG) performance: The conditions for this simulation are the same as in Simulation #1 with parameters as listed in Table 6.3. The results in Figure 6.10 show the performance of VCG and VCGR, as compared to the NLMS and FCG algorithms. The convergence curves illustrate that the VCG outperforms all other algorithms. The convergence of the VCGR algorithm (n_w=5, R=P=5) outperform the NLMS algorithm 300 samples after the transfer function change even with a reduced gradient update rate.

A comparison of the relative complexities is shown in Table 6.3.

TABLE 6.5 Comparative complexity using NLMS, FCG, VCG and VCGR (n_W=*R*=*P*=5).

Algorithm	**#Taps *m***	α	ξ	Γ	γ	n_w	***R***	***P***	**SNR**	**Complexity (mults/iter)**
NLMS	50	0.5							50 dB	102
FCG	50	0.5				5			50 dB	3631
VCG	50		0.4	0.4	1e2	5	5	1	50 dB	5751
VCGR	50		0.4	0.4	1e2	5	5	3	50 dB	1968
VCGR	50		0.4	0.4	1e2	5	5	5	50 dB	1201

The complexity of the VCGR (n_w=5, *P=5*) for this case is approximately 20% of th FCG. There are some transients during the first few iterations since the initial weight change estimates (which are reused *P* times) will be inaccurate during this period. The transients are higher for increased *P* both during initial convergence and when the transfer function is changed at iteration 1000 but will die out as the algorithm converges. The results indicate that depending on the value of *P*, the convergence rate can be tailored to be fast or slow. Increasing the value of *P* reduces the convergence rate (and complexity) such that it falls somewhere between the FCG and NLMS algorithms.

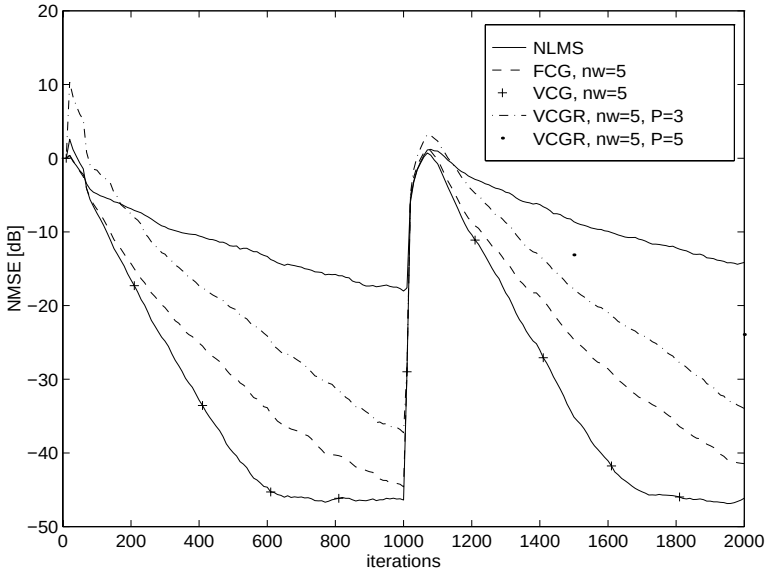

FIGURE 6.10 Simulation #3 results. Simplified VCG performance results (VCGR). Correlated noise input with a sudden change in the unknown system transfer function at iteration 1000.

6.2.8 Application to Acoustic Echo Cancellation

In this section, the VCG algorithm is applied to a real speech signal as recorded in Conference room #1 using HFT #1 at an average volume of 70 dB SPL. A 20 second speech excitation signal[1] was created by concatenating seven repeated speech segments illustrated in Figure 6.11 to generate the complete 20 second segment shown in Figure 6.12. *Room nonstationarities are introduced during the fifth burst (11-14 seconds) by waving a hand quickly approximately 1 foot above the HFT.* It is possible therefore to observe the characteristics of the algorithm with speech and room nonstationarity. A comparison of the NLMS, MVSS, accelerated SFTF, FCG and VCG algorithms

1. The speech signal is obtained from Nortel as a result of analysis of “typical” conversations on telecommunication networks. The speech signal is recorded at 8kHz.

is shown in Figure 6.13. The number of taps used is 1000, which is sufficient to ensure that the TIP/TP ratio is not a limiting factor. The parameters used are listed in Table 6.6.

TABLE 6.6 Algorithm parameters

Algorithm	Parameters
NLMS	N=1000, α=1.0, halting parameter=0.2
MVSS	N=1000, ξ=0.97, Γ=0.99, $\gamma=10^9$, μ_{max}=1.0, $\mu_{min}=10^{-5}$
Accelerated SFTF	N=1000, λ=0.9998, acceleration factor=0.90, soft initialization constant=50, halting parameter=0.2
VCG	N=1000, ξ=0.4, Γ=0.4, $\gamma=10^2$, n_w=3, halting parameter=0.2
FCG	N=1000, α=1.0, n_w=3

A close-in view of the *initial convergence* of the algorithms is shown in Figure 6.14. The VCG algorithm attains the fastest convergence and achieves 20 dB of ERLE at 0.5 seconds. The FCG algorithm closely follows the VCG convergence but has approximately 1-2 dB poorer ERLE performance.

The results in Figure 6.15 show a close-in view of the *tracking performance* of the algorithms during the speech burst where a nonstationarity in the room response occurs. The average ERLE values calculated between 11.75 and 13.5 seconds are listed in Table 6.7.

TABLE 6.7 Average ERLE calculated between 11.75-13.5 seconds.

Algorithm	Average ERLE
NLMS	14.14 dB
SFTF	16.13 dB
VCG	15.33 dB
FCG	16.56 dB
MVSS	15.28 dB

On average, the FCG algorithm obtains the best tracking performance, however it is only 2.4 dB better than the NLMS algorithm. The VCG algorithm obtains a 1.19 dB improvement over the NLMS algorithm.

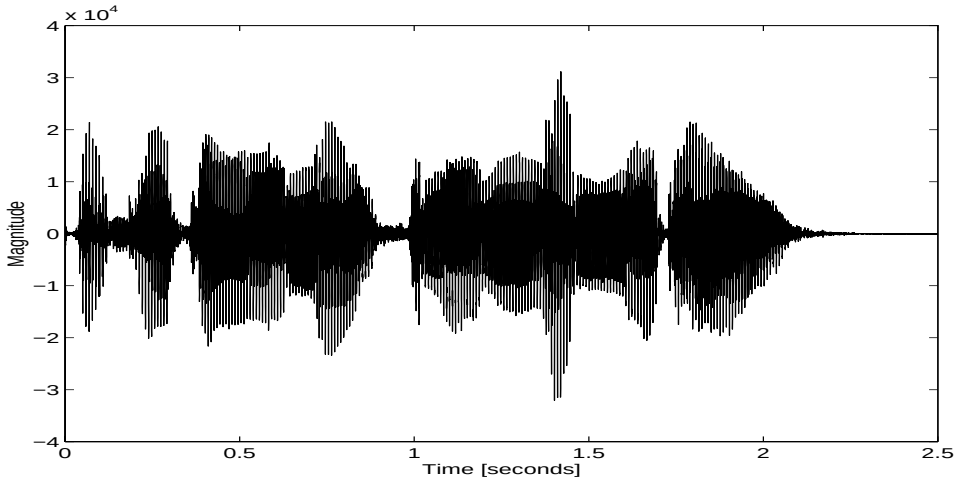

FIGURE 6.11 Time series plot of the speech excitation signal.

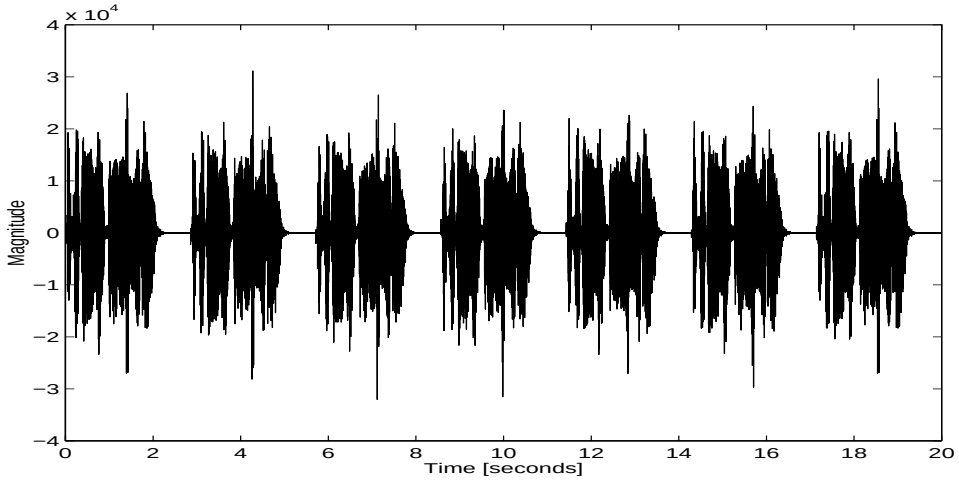

FIGURE 6.12 Time series plot of the complete excitation signal.

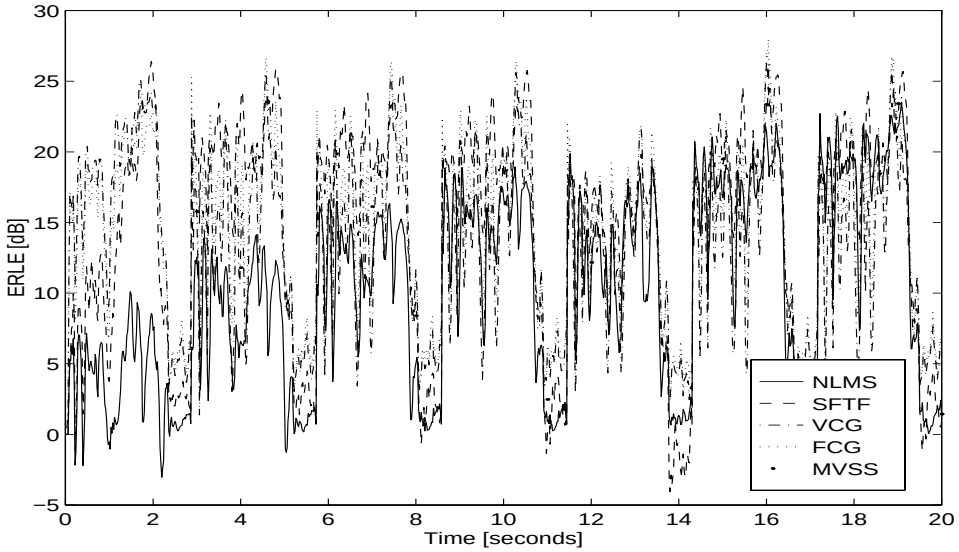

FIGURE 6.13 Results for different algorithms using speech excitation. A nonstationarity occurs between 11.5 and 14 seconds.

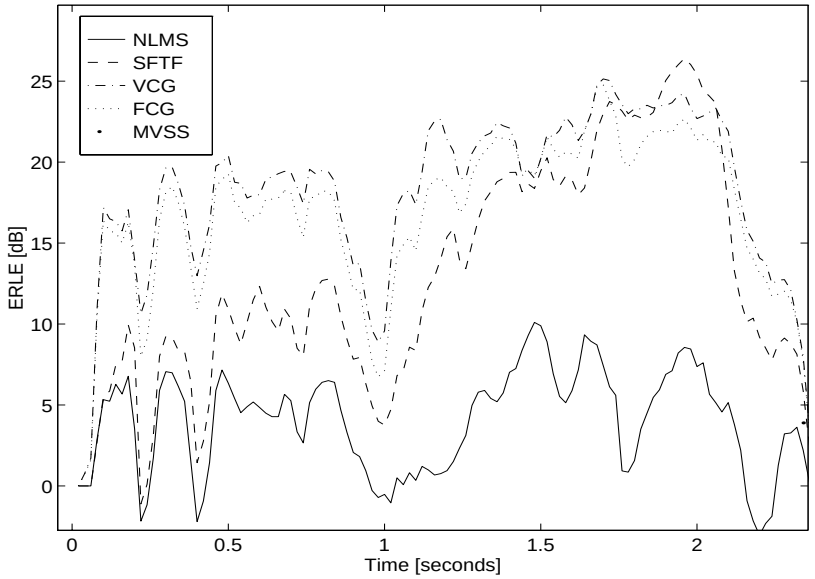

FIGURE 6.14 Close up view illustrating initial convergence performance of algorithms.

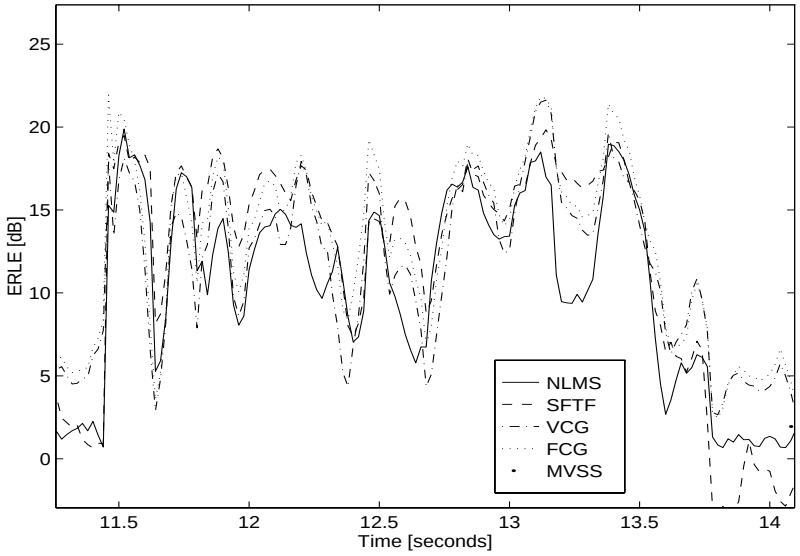

FIGURE 6.15 Close up view illustrating tracking performance of algorithms.

6.2.9 Discussion

The VCG algorithm has reduced complexity as compared to the regular CG and is slightly more complex than the FCG algorithm depending on the number of iterations performed during the one dimensional line search. In computer simulations, the VCG algorithm has been shown to have better convergence and tracking properties than the FCG in correlated nonstationary environments and can achieve the same performance as the FCG with reduced complexity. When applied to real speech signals, the VCG algorithm is found to have superior convergence compared to the accelerated SFTF algorithm, however, it exhibits poorer tracking ability than the FCG algorithm but is still better than the NLMS algorithm by approximately 1.2 dB. In terms of AEC application, it is found that the VCG and FCG algorithms can offer improvements in initial convergence and tracking ability with real speech inputs compared to standard algorithms like NLMS and SFTF.

6.3 Summary

This chapter has presented two new methods to enhance the convergence rate of adaptive filters. The first training method, presented in Section 6.1, is based on extending the linear fast conjugate gradient method to the nonlinear domain, specifically neural based adaptive filters. This new training method enhances the convergence rate as compared to the conventional backpropagation algorithm by using a gradient averaging window and simplified conjugate gradient computations. Computer simulations show that the convergence rate can be 'tailored' depending on the size of the gradient window. The proposed algorithm was then applied to the nonlinear TDNN-FIR structure and trained with experimentally obtained data, consisting of both noise and speech signals which were recorded at high volumes. The experimental results show that the proposed algorithm, when applied to TDNN based adaptive filters, can obtain better ERLE performance than the linear FIR counterpart trained using the accelerated SFTF algorithm with real speech signals. Up to 5 dB improvement in ERLE is obtained at 95 dB SPL. Also, the initial convergence is comparable to that obtained by the accelerated SFTF algorithm.

The second training method, presented in Section 6.2, is intended for, but by no means restricted to linear adaptive filters. The method combines the FCG algorithm with a one dimensional line search, based on the MVSS algorithm. The MVSS algorithm is used to provide a dynamic step size to replace the optimum step size as calculated in the conventional CG algorithm, and hence can be considered as an alternate to other line search methods like Armijo's rule. A simplified version of the proposed algorithm is also presented which utilizes the concept of gradient reuse to reduce the computational complexity, depending on the reuse rate. Experimental results using real speech signals show that the VCG algorithm is capable of improved initial convergence rate as compared to the SFTF algorithm and has improved tracking ability as compared to the NLMS algorithm.

Chapter 7
Conclusions

7.1 Summary of this Research

The objective of this thesis was the investigation of nonlinear adaptive filter structures and algorithms for identifying cascaded linear and nonlinear systems with specific application to compensating for nonlinear loudspeaker effects in acoustic echo cancellers (AEC's) placed inside handsfree telephones (HFT's) . We concentrated our investigations on neural based filters as a computationally attractive alternatives to third order Volterra filters and developed several architectures to identify cascaded linear and nonlinear systems such as those encountered in the handsfree telephone domain. We determined that HFT enclosure resonances and vibrations can be a more serious limitation than loudspeaker nonlinearity to the achievement of a high steady-state Echo Return Loss Enhancement (ERLE). By controlling mechanical vibrations and resonances through appropriate design, neural based filters can provide substantial improvements in ERLE. Finally, we concentrated on developing a nonlinear training algorithm that was efficient, in that a performance/complexity trade-off could be selected. When applied to real world HFT's using

noise and speech training signals, significant improvements in converged ERLE could be obtained.

We asked ourselves four questions in the Chapter 1:

1. *What sort of limitations do typical nonlinear loudspeakers present to achieving high ERLE values in typical HFT's ?*
2. *What kind of filters are best suited for nonlinear AEC applications and how can we arrive at that conclusion?*
3. *How can an efficient nonlinear structure and training algorithm be designed that is not overly complicated yet provide reasonable improvements in performance?*
4. *Can the new structures/algorithms be successfully applied in real-world applications?*

A review of nonlinear loudspeaker dynamics and performance in Chapter 2 indicates the following:

- The major cause of distortion in loudspeakers is due to nonuniform flux density and two point suspension nonlinearity which become predominant at low frequencies and high volumes. Two point suspension nonlinearity is present also at extremely low volumes.
- The Volterra filter has found some success in modelling *low frequency* (woofer) loudspeakers for high quality studio applications. A 3rd order filter is usually necessary to reduce nonlinear distortion to target values of -30 dB.
- No applications in the literature could be found dealing with mid-frequency, low quality loudspeakers that are typically used in HFT's.

In Chapter 4, we looked at the the acoustic echo cancellation problem and determined the following:

- Although high values of ERLE are often stipulated in specifications[1], there is little information on how nonlinear loudspeaker performance impacts on the practical achievement of these values.
- Transducer nonlinearities limit the achievable ERLE at high and extremely low volumes. Transducer *quality* also plays a role in determining the achievable ERLE value.
- Vibration and key rattling is a limitation. It is shown in Chapter 5 that this limitation can prevent nonlinear algorithms from achieving their full potential if not controlled adequately.

Our first question is now answered. However, achieving 40 dB of echo cancellation even in the linear range of the loudspeaker appears to be possible only when *separated* loudspeaker and microphone components are used in anechoic conditions. When placed inside a typical HFT enclosure, vibrations, rattling and other effects will serve to limit the achievable ERLE to below 35 dB.

In Chapter 4 a subsection on the application of infinite impulse response (IIR) structures for AEC's arrived at the following conclusions:

- Experimental results performed on both separate transducers in an anechoic chamber and HFT's in furnished conference rooms suggest that IIR structures are not well suited to modelling a typical loudspeaker-room-enclosure-microphone (LREM) even though *some* literature suggests otherwise.
- A Hankel norm approximation error bound for IIR filters is shown to have similar characteris-

1. Typical specifications are at least 30 dB of cancellation in 0.1 seconds.

tics to the Total Impulse Power to Tail Power (TIP/TP) ratio at low filter orders.

This partially answers our second question, namely, feedforward structures should be considered as more promising candidates for AEC applications than recursive structures.

In Chapter 5, Volterra and neural filters were examined as possible candidates for a nonlinear AEC. The following conclusions can be summarized:

- Simulation results show that the Volterra filter can obtain a higher modelling accuracy than a neural based filter. However, experimental results show that when presented with real-world signals, neural filters can achieve equal or better results compared to the Volterra filter.
- For AEC applications where the model order is quite large Volterra filters have a much higher complexity than neural based filters for equivalent performance results.
- A tapped delay line neural network (TDNN) filter can achieve better performance than a linear finite impulse response (FIR) filter only when the nonlinear distortion is greater than several percent of the primary signal power. Given that some improvement can be made with a neural filter, a low number of hidden nodes is sufficient to provide several dB of ERLE improvement.
- In the undermodelled case, the TDNN provides a significant improvement in ERLE compared to the linear FIR which in the linear region is fundamentally limited by the TIP/TP ratio.
- The TDNN was found to have poorer performance at low distortion levels compared to the linear FIR filter. A *linear* region in the activation function was found to improve the modelling accuracy at both low and high distortion levels compared to networks using hyperbolic tangent function activation functions.

We are now in a position to completely answer the second question, namely that simple, feedforward neural based filters can achieve the best performance complexity trade-off compared to Volterra algorithms and recursive IIR structures.

Since simplicity of design is of utmost importance in AEC design, several new neural filters were subsequently proposed, the most successful being the two stage neural filter. The two stage neural filter has the following features:

- The neural filter is composed of a TDNN in parallel with an FIR filter. The TDNN portion models the first part of the LREM where most of the signal energy is contained. The FIR portion models the remaining echo tail.
- A low order TDNN with a single hidden layer and one or two hidden nodes is sufficient to model nonlinearities typically encountered in the AEC domain. Experimental results show that the converged steady-state ERLE of a real world HFT can be improved by up to 11 dB when trained with a filtered noise signal.

The variable activation function was proposed which adapts to be highly linear when trained with signals which have little nonlinear distortion. A training algorithm was developed.

As an alternative to weakened nonlinear systems which consist of fixed nonlinearities sandwiched between linear adaptive filters, the synaptic FIR multilayer perceptron (MLP) with variable activation function was proposed (VA-FIR MLP), along with an appropriate backpropagation (BP) based training method.

- Computer simulations show that the VA-FIR MLP is well suited to identifying low order nonlinear systems of the sandwiched linear-nonlinear-linear type. For application to nonlinear AEC, experimental results show that it is not as effective as the two stage neural filter described

earlier.

We can now answer the first part of Question 3). By mixing neural networks and linear FIR structures, a two stage neural filter has been constructed which maintains the benefits of both filter types keeps the overall architectural complexity low.

In order to study the performance of the structures proposed in Chapter 5, a nonlinear fast conjugate gradient (NFCG) backpropagation algorithm is developed in Chapter 6. The NFCG algorithm has the following features:

- The NFCG is based on the standard conjugate gradient (CG) algorithm. It is developed by extending the fast conjugate gradient (FCG) algorithm to the nonlinear case, specifically neural networks.
- There is a complexity/performance trade-off which is determined by the size of the gradient averaging window.

We can now answer the last part of Question 3). A simple algorithm based on the CG method can be used to train the nonlinear network and provide a complexity/performance trade-off.

When applied to the two stage neural filter of Chapter 5 using real speech inputs at an average volume of 95 dB SPL, the NFCG is capable of improving the ERLE by approximately 5 dB as compared to an FIR trained with the accelerated Stabilized Fast Transversal Filter (SFTF) algorithm.

A linear variation on the FCG algorithm is also developed which uses a dynamic step size calculation using the modified variable step size (MVSS) algorithm. Experimental results using speech signals in a conference room environment show that the variable step size CG (VCG) algorithm

achieves the fastest convergence rate of several algorithms tested, including the FCG and accelerated SFTF algorithm.

Finally, Question 4) is answered. The proposed architectures and algorithms have been successfully applied to real world signal processing applications.

7.2 Summary of Contributions

The investigation, development and subsequent simulation and experimental performance results presented in this thesis provide several important contributions to the field of neural networks, acoustic echo cancellation, and nonlinear system identification. These contributions are briefly summarized here:

1. Vibration and rattling within the HFT handset can present a physical limitation to achievable ERLE which may or may not be more severe than nonlinear loudspeaker distortion. It must be controlled in order to allow nonlinear speech and echo cancellation algorithms/structures to work effectively.

2. A two stage neural filter has been developed. It has a simple architecture that requires only a small number of nonlinear nodes. It is capable of providing up to 11 dB ERLE improvement at high volumes using training signals consisting of noise and up to 5 dB improvement when using real speech signals.

3. The development of a variable activation function and update equations for incorporation into a a standard TDNN or synaptic FIR MLP has been presented. The update equations are based on the temporal backpropagation algorithm with modifications to allow for a window of accumulated gradients.

4. A fast conjugate gradient algorithm for neural networks has been developed and applied to the TDNN and two stage neural filter. The update equations are based on the fast conjugate gradient algorithm which has been modified for application to neural networks. A linear FCG algorithm that incorporates MVSS line search and gradient reuse to obtain complexity reductions is also presented which obtains substantial convergence rate improvements with real speech signals.

5. Publication of several refereed conference and journal papers which report on the research results. See [51],[126],[127],[163],[164],[165],[166],[167].

7.3 Suggestions for Future Research

During the course of this research, several issues arose which merit further research. These are summarized below:

- Combining frequency domain and nonlinear methods. The GMDF [137] algorithm is a successful AEC algorithm that might benefit from the addition of nonlinear signal processing of the form described in this thesis. The GMDF algorithm is capable of achieving high levels of converged ERLE with speech inputs[1], however it would appear that further improvements may not be possible without the inclusion of some sort of nonlinear signal processing.

- Investigation of methods to model and reduce vibrations and resonances within a handsfree terminal, including proper selection, orientation and mounting of both the loudspeaker and microphone elements. This would improve the achievable steady state ERLE and perceived speech quality.

1. Recent measurements performed by J.P. Lariviere [168] have produced real-world ERLE values of 35-40 dB using speech inputs recorded at mid volumes in the 70 dB SPL range.

- Experimental determination of the typical parameters of small inexpensive loudspeakers typically used in HFT's using a laser displacement system and determination of how closely these fit the theoretical models. The nonlinear modelling presented in Chapter 2 assumed that the inductance $L(x) = L_0$ and the higher order terms $L_1 x + L_2 x^2$ were negligible. This may be an invalid assumption for these types of loudspeakers.

- Application of the conjugate gradient training algorithms in Chapter 6 to the structures which contain variable activation functions.

7.4 Conclusion

In conclusion, this thesis has presented the key highlights in our study on the use of nonlinear signal processing techniques to the field of acoustic echo control. The research results have given positive, definitive answers to the four questions posed previously.

In an ideal world, all problems would be isolated from one another, and the solution procedures would involve direct methods, based on the principle of divide and conquer. However, in the real world, every piece of matter is immutably connected with every other piece of matter in some way, either directly or vicariously, and what may appear to be an obvious solution to a problem at first glance is often cursory. We are then presented with the opportunity to solve a small part of a much larger puzzle. Indeed, the puzzle is limitless.

References

[1] M.E. Knappe, R.A. Goubran,"Steady State Performance Limitations of Full-Band Acoustic Echo Cancellers", Presented at *ICASSP* 1994, Australia.

[2] H. F. Olson, *Acoustical Engineering*, Toronto: D. Van Nostrand Company Inc., 1964.

[3] K. B. Benson (eds.), *Audio Engineering Handbook*, Toronto: McGraw-Hill Book Company, 1988

[4] A. M. Kaizer, "Modeling of the Nonlinear Response of an Electrodynamic Loudspeaker by a Volterra Series Expansion", *J. Audio Eng. Soc.*, Vol. 35, No. 6, June 1987, pp. 421-433.

[5] M.H. Knudsen, J.G. Jensen, V.Julskaer, P. Rubak, "Determination of Loudspeaker Driver Parameters Using a System Identificatin Technique", *J. Audio Eng. Soc.*, Vol. 37, No. 9, Sept. 1989, pp. 700-708

[6] X. Y. Gao, W. M. Snelgrove, "Adaptive Linearization of a Loudspeaker", *ICASSP* 1991 Vol. 3, pp 3589-3592.

[7] Ljung, L., *System Identification: Theory for the User.* Prentice-Hall, Englewood Cliffs, NJ, 1987.

[8] Wolfgang Klippel, "Dynamic Measurement and Interpretation of the Nonlinear Parameters of Electrodynamic Loudspeakers", *J. Audio Eng. Soc.*, Vol. 38, No. 12, Dec. 1990, pp. 944-956.

[9] H. Jang, K. Kim, "Identification of Loudspeaker Nonlinearities Using the NARMAX Modeling Technique", *Journal of the Audio Engineering Society*, Vol. 42, No. 1/2, Jan./Feb. 1994, pp. 50-59.

[10] S. Boyd, Y. S. Tang, L. O. Chua, "Measuring Volterra Kernels", *IEEE Transactions on Circuits and Systems*, Vol. CAS-30, No. 8, Aug. 1983, pp. 571-577.

[11] George Niedrist, "Echo suppression for Loudspeaker-Microphone System Measurements" *J. Audio Eng. Soc*., Vol. 41, No. 3, March 1993, pp 143-153.

[12] A.J.M. Kaizer, *On the Design of Broadband Electrodynamic Loudspeakers and Multiway Loudspeaker Systems*, Ph.D. Thesis, Eindhoven University of Technology, The Netherlands, 1986, Chapter 6.

[13] H. Schurer, C. H. Slump, O.E. Herrmann, "Second Order Volterra Inverses for Compensation of Loudspeaker Nonlinearity", *1995 IEEE Workshop on Applications of Signal Processing to Audio and Acoustics*, New Paltz, N.Y., 1995.

[14] R. de Vries, A. Perkhoff, C. Slump, O. Herrmann, "Digital Compensation of Nonlinear Distortion in Loudspeakers", in *Proc. 1993 ICASSP*, Vol. 1, pp. 165-168.

[15] Wolfgang Klippel, "The Mirror Filter- A New Basis for Reducing Nonlinear Distortion and Equalizing Response in Woofer Systems", *J. Audio Eng. Soc.*, Vol. 40, No. 9, Sept. 1992, pp. 675-691.

[16] Teixeira, V., J. Ribeiro, F. Restivo, D. Freitas, "Study of Loudspeaker electromechanical nonlinearities and their compensation" *Proceedings ICSPAT'96*, pp. 321-325.

[17] P. Chang, C. Lin, B. Yeh, "Inverse Filtering of a Loudspeaker and Room Acoustics Using Time-delay Neural Networks", *Journal of the Acoustic Society of America*, Vol 95, No. 6, June 1994, pp. 3400-3408.

[18] D.R. Birt, "Nonlinearities in Moving -Coil Loudspeakers with Overhung Voice Coils", *J. Audio Eng. Soc*., Vol. 39, pp. 219-231, April, 1991.

[19] Egbert de Boer, "Theory of Motional Feedback, "*IRE Transactions on Audio*, Jan.-Feb. 1961, pp15-21.

[20] R. A. Greiner, T.M. Sims, "Loudspeaker Distortion Reduction", *J. Audio Eng. Soc.*, Vol. 32, No. 12, Dec. 1984, pp. 956-963.

[21] D.De Greef, J. Vandewege, " Acceleration Feedback Loudspeaker", *Wireless World*, Sept. 1981, pp. 32-36.

[22] L. Li, "Nonlinear adaptive prediction of nonstationary signals and its application to speech communications", Ph.D. dissertation, Dept. of Elect. and Comput. Eng., McMaster Univ., 1994.

[23] V. J. Mathews, "Adaptive Polynomial Filters", *IEEE Signal Processing Magazine*, July 1991, pp. 10-26.

[24] A.S. Weigund, N. A. Gershenfeld, *Time Series Prediction, Forecasting the Future and Understanding the Past*, Proceeding of the NATO Advanced Research Workshop on Comparative Time Series Analysis, Santa Fe, New Mexico, May, 1992.

[25] M. Schetzen, *The Volterra and Wiener Theories of Nonlinear Systems*, John Wiley & Sons, 1980.

[26] C. E. Davila, A. J. Welch, H. G. Rylander, "A Second Order Adaptive Volterra Filter with Rapid Convergence", *I.E.E.E. Transactions on Acoustics Speech and Signal Processing*, Vol. ASSP-35, No. 9, Sept. 1987, pp. 1259-1263.

[27] T. Koh, E. J. Powers, "Second-Order Volterra Filtering and Its Application to Nonlinear System Identification", *I.E.E.E. Transactions on Acoustics Speech and Signal Processing*, Vol. ASSP-33, No. 6, Dec. 1985, pp. 1445-1455.

[28] T. Koh, E. J. Powers, "An Adaptive Nonlinear Digital Filter With Lattice Orthogonalization", *Proc. of IEEE International Conference on Acoustics, Speech, and Signal Processing*, 1983, pp. 37-40.

[29] G. L. Sicuranza, G. Ramponi, "Adaptive Nonlinear Digital Filters Using Distributed Arithmetic", *I.E.E.E. Transactions on Acoustics Speech and Signal Processing*, Vol. ASSP-34, No. 3, June 1986, pp. 518-526.

[30] O. Agazzi, D. G. Messerschmitt, D. A. Hodges, "Nonlinear Echo Cancellation of Data Signals", *IEEE Transactions on Communications*, Vol. COM-30, No. 11, Nov. 1982, pp. 2421-2433

[31] G. L. Sicuranza, A. Bucconi, P. Mitri, "Adaptive Echo Cancellation with Nonlinear Digital Filters", *Proc. of IEEE International Conference on Acoustics, Speech, and Signal Processing*, 1984, pp. 3.10.1-3.10.4.

[32] M. J. Smith, C. F. N. Cowan, P. F. Adams. "Nonlinear Echo Cancellers Based on Transpose Distributed Arithmetic", *IEEE Transactions on Circuits and Systems*, Vol. 35, No. 1, Jan. 1988, pp. 6-18.

[33] M. J. Coker, D. N. Simkins, "A Nonlinear Adaptive Noise Canceller", *Proc. of IEEE International Conference on Acoustics, Speech, and Signal Processing*, Vol. 2, 1980, pp. 470-473.

[34] J. C. Stapleton, S. C. Bass, "Adaptive Noise Cancellation for a Class of Nonlinear Dynamic Reference Channels", *Proc. of IEEE International Symposium on Circuits and Systems*, 1984, pp. 268-271.

[35] Y.S. Cho, E. J. Powers, "Estimation of Nonlinear Distortion Using Digital Higher Order Spectra and Volterra Series", ISCS 1992, pp. 2781-22784.

[36] Y.S. Cho, E. J. Powers, "Two-tone vs. Random Process Inputs for Nonlinear Distortion Estimation", *ICASSP 1992*, Vol. II, pp. 209-212.

[37] C. F. N. Cowan, P. F. Adams, "Nonlinear System Modelling: Concept and Application", *Proc. of IEEE International Conference on Acoustics, Speech, and Signal Processing*, 1984, pp. 45.6.1-45.6.4.

[38] J. Namiki, , "An automatically controlled predistorter for multilevel quadrature amplitude modulation",*IEEE Trans. Comm.*, Vol. 5, May 1983, pp. 707-711.

[39] S.Chen, S. A. Billings, P.M. Grant, "Nonlinear System Identification Using Neural Networks", *Int. J. Control*, Vol. 51, No. 6, pp. 1191-1214, 1990.

[40] S. Chen, S.A. Billings, “Neural networks for nonlinear dynamic system modelling and identification”, Int. J. Control, 1992, Vol. 56, No. 2, pp. 319-346.

[41] S. Haykin, L. Li, “Nonlinear adaptive prediction of nonstationary signals”, *IEEE Trans. Sig. Proc.* , Vol 43, No. 2, Feb. 1995, pp. 526-535.

[42] P. Campolucci, A. Uncini, F. Piazza, “Fast adaptive IIR-MLP neural networks for signal processing applications”, *ICASSP* 1996, Vol 6, pp 3530-3533.

[43] P. Campolucci, A. Uncini, F. Piazza, “On-line learning algorithms for neural networks with IIR synapses”, *ICNN* 1995.

[44] W. G. Knecht, “Nonlinear Noise Filtering and Beamforming Using the Perceptron and Its Volterra Aproximation”, *IEEE Trans. Audio and Acoustics*, Vol. 2, No. 1, Jan. 1994, pp. 55-62.

[45] W. G. Knecht, M.E. Schenkel, G.S. Moschytz, “Neural Networks for Speech Enhancement”, *IEEE Trans. Audio and Acoustics*, Vol. 3, No. 11, Nov. 1995, pp. 433-438.

[46] Waibel, A., Hanazawa, T. Hinton, G. Shikano, K. and Lang, K., “Phoneme recognition using time-delay neural networks”, *IEEE Trans. Speech, Sig. Proc*., vol ASSP-37, March 1989, pp.328-339.

[47] E. Wan, “Temporal Backpropagation for FIR neural Networks”, *Proc. IJCNN*, Vol. I, June 1990, pp. 575-580.

[48] A.C. Tsoi, A. Back, “Locally Recurrent Globally Feedforward Networks, A Critical Review of Architectures”, *IEEE Trans. Neural Networks*, Vol. 5, No. 2, March 1994, pp. 229-239.

[49] A. D. Back, A. C. Tsoi, “FIR and IIR Synapses, a New Neural Network Architecture for Time Series Modeling”, *Neural Computation*, No. 3, 1991, pp. 375-385.

[50] J. Shan, F. Li, “A New Algorithm for Realizing Nonlinear Filters--Adaptive Neural Filters”, *Proceedings, ICASSP 1994*, Vol.3, pp. 89-92.

[51] A. N. Birkett, R. A. Goubran**, “**Acoustic Echo Cancellation Using NLMS-Neural Network Structures”, *Proceedings of ICASSP 1995*, Detroit, MI., Vol. 5, pp. 3035-3038.

[52] D. A. Johms, W. M. Snelgrove, A. S. Sedra, “Adaptive Recursive State-Space Filters Using a Gradient-Based Algorithm”, *IEEE Transaction on Circuits and Systems*, Vol. 37, No. 6, June, 1990, pp. 673-684.

[53] J. Treichler, C. R. Johnson, M. G. Larimore, *Topics in Digital Signal Processing: Theory and Design of Adaptive Filters*, John Wiley and Sons, 1987.

[54] B. Widrow, S. D. Stearns, *Adaptive Signal Processing*, Englewood Cliffs, N.J.: Prentice-Hall, 1985.

[55] K. Mayyas, T. Aboulnasr, “A Robust Variable Step Size LMS-Type Algorithm: Analysis and Simulations”, *ICASSP’95*, pp. 1408-1411.

[56] Kwong, R.H. and E.W. Johnston, “A variable step size LMS algorithm” IEEE Trans. Signal Processing, Vol. 40, No. 7, pp. 1633-1642, July 1992.

[57] C. R. Johnson, “Adaptive IIR Filtering:Current Results and Open Issues”, *I.E.E.E. Transactions on Information Theory*, Vol. IT-30, No. 2, March 1984, pp. 237-250.

[58] H. Fan, W.K. Jenkins, “An Investiation of an Adaptive IIR Echo Canceller: Advantages and Problems”, *IEEE Transaction on Acoustics Speech and Signal Processing*, Vol. 36, No. 12, Dec. 1988, pp. 1819-1834.

[59] P. A. Regalia, “Stable and Efficient Lattice Algorithms for Adaptive IIR Filtering”, *IEEE Transactions on Signal Processing*, Vol. 40, No. 2, Feb. 1992, pp. 375-388.

[60] J. J. Shynk, “Adaptive IIR Filtering Using Parallel-Form Realizations”, *IEEE Transactions on Acoustics, Speech, and Signal Processing*, Vol. ASSP-37, No. 4, pp. 519-533.

[61] K.X. Miao, H. Fan, M. Doroslovacki, “Cascade Lattice IIR Adaptive Filters”, *IEEE Transactions on Signal Processing*, Vol. 42, No. 4, April 1994, pp. 721-742.

[62] J. J. Shynk, “ Adaptive IIR Filtering”, *IEEE ASSP Magazine*, Vol. 6, April 1989, pp. 4-21.

[63] K. Steiglitz, L.E. McBride, “A technique for the identification of linear systems”, *IEEE Trans. Automat. Contr.*, Vol. AC-10, pp. 461-464, Oct. 1965.

[64] J.B. Kennedy, C.E. Rohrs, “The composite regressor algorithm for IIR adaptive systems”, *IEEE Trans. Sig. Proc.*, Vol. 41, pp. 617-628, Feb. 1993.

[65] G. Simon, G. Peceli, “A new composite gradient algorithm to achieve global convergence”, *IEEE Trans. Circ. Systems II: Analog and Dig. Sig. Proc.*, Vol. 42, No. 10, pp. 681-684, Oct. 1995.

[66] J. Lin, R. Unbehauen, “Bias Remedy Least mean Square Equation Error Algorithm for IIR Parameter Recursive Estimation”, *IEEE Transactions on Signal Processing*, Vol. 40, No. 1, Jan. 1992, pp. 62-69.

[67] A Benallal and A Gilloire, "Improvement of the Tracking Capability of the Numerically Stable Fast RLS Algorithms for Adaptive Filtering", Proc. ICASSP 1989, pp. 1031-1034.

[68] A. Gilloire, T. Petillon, “A Comparison of NLMS and Fast RLS Algorithms for the Identification of Time-varying Systems with noisy outputs”, *Signal Processing V: Theories and Applications,* L. Torres, E. Masgrau and M.A. Lagunas (eds.), Elsevier Science Publishers B.V., 1990, pp.417-420.

[69] M. R. Hestenes, *Conjugate Direction Methods in Optimization*, Springer-Verlag,1980.

[70] D. Luenberger, *Introduction to Linear and Nonlinear Programming*, Addison-Wesley Publishing Company, 1973.

[71] Johansson, E.M., F. U. Dowla and D.M. Goodman, “Backpropagation learning for multilayer feed-forward neural networks using the conjugate gradient method”, *International Journal of Neural Systems*, Vol. 2, No. 4, 1992, pp. 291-301

[72] C. Charlambous, “Conjugate Gradient Algorithms for Efficient Training of Artificial Neural Networks”, *Proc. IEEE*, Vol. 139, No. 3, pp. 301-310, 1992

[73] G. K. Boray, M. D. Srinath, “Conjugate Gradient Techniques for Adaptive Filtering”, *IEEE Trans. on Circuits ans Systems-I: Fundamental Theory and Applications*, Vol. 39, No. 1, Jan. 1992, pp.1-10.

[74] W. Buntine, A. A. Weigend,” Computing Second Derivative in Feed-Forward Networks: A review”; *IEEE Trans. Neural Networks*, Vol. 5, No. 3, pp. 481-488, May 1994.

[75] J. Sjoberg, Q. Zhang, L. Ljung, A. Benveniste, B. Deylon, P. Glorennec, H. Hjalmarsson, A. Juditsky, “ Nonlinear Black-box Modelling in System Identification: A Unified Overview”, unpublished manuscript, June 16, 1995.

[76] K. S. Narendra, K. Parthasarathy, “ Identification and Control of Dynamical Systems Using Neural Networks”, *IEEE Tansactions on Neural Networks*, Vol. 1, No. 1, March 1990, pp. 4-27.

[77] D. Urbani, P. Roussel-Ragot, L. Personnaz, G. Dreyfus, “The Selection of Neural Models of Nonlinear Dynamical Systems by Statistical Tests”, *Neural Networks for Signal Processing IV: Proceedings of the 1994 IEEE Workshop*, pp. 229-237.

[78] S. Chen, S. A. Billings, “Representations of Nonlinear Systems: The NARMAX Model”, *International Journal of Control*, Vol. 49, No. 3, 1989, pp. 1013-1032.

[79] F. X. Y. Gao, W. M. Snelgrove, “Adaptive Nonlinear State-Space Filters”, *Proc. of IEEE International Symposium on Circuits and Systems*, 1990, pp. 3122-3125.

[80] F. X. Y. Gao, W. M. Snelgrove, “Adaptive Nonlinear Recursive State-Space Filters”, *IEEE Trans. Circ. and Sys. II: Analog and Dig. Sig. Proc.*, Vol. 41, No. 11, pp. 760-764, Nov. 1994.

[81] F. X. Y. Gao, W. M. Snelgrove, D. A. Johns, “Nonlinear IIR Adaptive Filtering Using a Bilinear Structure”, *Proc. of IEEE International Symposium on Circuits and Systems*, 1989, pp. 1740-1743.

[82] Mohler, R.R., and W.J. Kolodziej, “An overview of bilinear system theory and applications”, IEEE Trans. Systems, Man, and Cybernetics, Vol. SMC-10, pp. 683-688, October, 1980.

[83] Panicker, T.M, V. J. Mathews and G.L. Sicuranza, “Adaptive parallel cascade truncated volterra filters”, Submitted to *IEEE Trans. on Sig. Processing* (in review process), May, 1996.

[84] Roy, E., R.W. Stewart and T.S. Durrani, “Theory and applications of adaptive second order IIR Volterra filters”, Proceedings ICASSP 96, Vol. 3, pp. 1598-1601.

[85] G. L. Sicuranza, G. Ramponi, “A Variable-Step Adaptation Algorithm for Memory Oriented Volterra Filters”, *I.E.E.E. Transactions on Acoustics Speech and Signal Processing*, Vol. ASSP-35, No. 10, Oct. 1987, pp. 1492-1494.

[86] D.E. Rumelhart, G.E. McClelland, eds., *Parallel Distributed Processing: Explorations in the Microstructure of Cognition*, Vol. 1. Cambridge, MA:MIT Press, 1986.

[87] S. Haykin, *Neural Networks: A comprehensive foundation*, Macmillan Publishing Co., Englewood Cliffs, NJ: , 1994.

[88] Y Pao, *Adaptive Pattern Recognition and Neural Networks*, Addison-Wesley Publishing Company, Inc

[89] R. A. Jacobs, “Increased Rates of Convergence Through Learning Rate Adaptation”, *Neural Networks*, Vol.1, No. 4, 1988, pp. 295-307.

[90] R. Scalero, N. Tepedelenlioglu, “A Fast New Algorithm for Training Feedforward Neural Networks”, *IEEE Trans. Sig. Proc.*, Vol. 40, No. 1, pp. 202-210,Jan. 1992.

[91] S. Shah, F. Palmieri, “MEKA- a Fast Local Algorithm for Training Feedforward Neural Networks”, *Inernational Joint Conference on Neural Netorks*, Vol. 3, pp. 41-46, San Diego, CA, 1990.

[92] S. Singhal, L. Wu. “Training feedforward Networks with the Extended Kalman Algorithm” in *Proc. ICASSP*, 1989, pp. 1187-1190.

[93] G. Chen, H. Ogmen, “Modified Extended Kalman Filtering for Suprevised Learning”, *Int. J. Systems Sci.*, Vol. 24, No. 6, pp. 1207-1214, 1993.

[94] D. Ruck, S. Rogers, M. Kabrisky, P. Maybeck, M. Oxley, “Comparative Analysis of Backpropagation and the Extended Kalman Filter for Training Multilayer Perceptrons”, *IEEE Trans. on Pattern Analysis and Machine Intelligence*, Vol. 14, No. 6, June 1992, pp. 686-691.

[95] H. Yuan, *Dynamic Behavior of Acoustic Echo Cancellation*, M. Eng. Thesis, Carleton University, Ottawa, Canada, 1994.

[96] G. W. Davidson, D. D. Falconer, “Reduced Complexity Echo Cancellation Using Orthonormal Functions”, *I.E.E.E. Transactions on Circuits and Systems*, Vol. 38 No. 1, Jan. 1991, pp. 20-28.

[97] M. E. Knappe, *Acoustic Echo Cancellation: Performance and Structures*, M. Eng. Thesis, Carleton University, Ottawa, Canada, 1992.

[98] B. Basnett, “An Overview of Audio Technologies in Teleconferencing: From Source to Receiver and Back”, in *Proceedings of the Canadian Acoustics Symposium*, Vol. 22, No. 2, Sept. 1994, Ottawa, Canada, pp. 65-66.

[99] E. Hansler, “The Hands-Free Telephone Problem”, 1992 *I.E.E.E. International Symposium on Circuits and Systems* , pp. 1914-1917.

[100] E. Hansler, “The Hands-Free Telephone Problem: An Annotated Bibliogray ”, *Signal Processing*, Vol. 27,1992, pp. 259-271

[101] E. Hansler, “The Hands-Free Telephone Problem: An Annotated Bibliogray Update”, *Ann. Telecommun.* Vol. 49, No. 7-8, 1994, pp. 360-367.

[102] R. Wehrmann, J.V.D. List, P. Meissner, “A Noise Insensitive Compromise Gradient Method for the Adjustment of Adaptive Echo Cancellers”, *IEEE Trans. Comm*. COM-28, No. 5, 1980, pp. 753-759.

[103] *** "General Characteristics of International Telephone Connections and International Telephone Circuits: Acoustic Echo Controllers" Recommendation G.167, *ITU-TSS* (03/1993)

[104] *** "General Characteristics of International Telephone Connections and International Telephone Circuits: Echo Ccancellers" Recommendation G.165, *ITU-TSS* (03/1993)

[105] *** "Transmission Performance of Group Audio Terminals (GATS)", Recommendation P.30 *CCITT Blue Book* (1988) Vol. 5.

[106] ***, "Transmission Characteristics of Hands-free Telephones", Recommendation P.34, *CCITT Blue Book* (1988), Vol. 5.

[107] *CCITT Blue Book* (1988) P.34, P.50, P.51,P.76,P.79,and supplement No. 2 of the P recommendations.

[108] *** "Technical Characteristics of Telephony Terminals- Part 3: PCM A-law, loudspeaking and hands-free function", *ETSI draft I-ETS* 300 245-3: ISDN (April, 1993).

[109] A. Gilloire, “Performance Evaluation of Acoustic Echo Control: required Values and Measurement Procedures”, *Annales des Telecommunications*, Vol. 49, No. 7-8, Jul.-Aug. 1994, pp. 368-372.

[110] H. Yasukawa, M. Ogawa, M. Nishino, “Echo Return Loss Required for Acoustic Echo Controller based on subjective assessment”, *IEICE Trans. E* ., Vol. 74, 1991, pp 629-705.

[111] J. C. Cox, “The Minimum Detectable Delay of Speech and Music”, *ICASSP* 1984, pp. 213-216.

[112] S. McCaslin, N. Van Bavel, “Effects of Quasi-periodic Training Signals on Acoustic Echo Canceller Performance”, in *Annales des Telecommunications*, Vol. 49, No. 7-8, Jul.-Aug. 1994, pp. 380-385.

[113] H. Kuttruff, *Room Acoustics*, London, U.K.: Elsevier, 1991, 3rd. Ed.

[114] M. Mboup, M. Bonnet, “IIR Filtering for Acoustic Echo Cancellation”, *Asilomar Conference on Signals, Systems and Computers*, Vol. 1, pp. 203-206, November 1991.

[115] M. R. Schroeder, H.K. Kuttruff, *J. Acoust. Soc. America*, Vol 34, 1962, 76.

[116] M. Tahernezhadi, L. Liu, “Real Time Implementation of an IIR Acoustic Echo Canceller on ADSP21020”, ICASSP 1995, pp. 2723-2726.

[117] Chao, J. and Tsujii, S., “A stable and distortion-free IIR echo and howling canceller”, *IEEE Trans. Sig. Proc*., Vol. 39, No. 8, pp. 1812-1821, Aug. 1991.

[118] Chao, J. and Tsujii, S., “ A new configuration for echo canceller adaptable during double talk periods”, *IEEE Trans. Comm*., Vol. 37, No. 9, pp. 947-969, Sept., 1989.

[119] H. Fan, W.K. Jenkins, “An Investiation of an Adaptive IIR Echo Canceller: Advantages and Problems”, *IEEE Transaction on Acoustics Speech and Signal Processing*, Vol. 36, No. 12, Dec. 1988, pp. 1819-1834.

[120] K. Glover, “All optimal Hankel-norm approximations of linear multivariable systems and their L∞-error bounds”, *Int. Journal of Control*, Vol. 39, No. 6, pp. 1115-1193, 1984.

[121] S. Holford and P. Agathoklis, “The Use of Model Reduction Techniques for Designing IIR Filters with Linear Phase in the Passband”, IEEE Trans. Sig. Proc., Vol. 44, No. 10, Oct.1996, pp.2396-2404.

[122] S. Gudvangen, S. J. Flockton, “Comparison of Pole-Zero and All-Zero Modelling of Acoustic Transfer Functions”, Electronic Letters, Vol. 28, No. 21, Oct. 1992, pp. 1976-1978.

[123] S. Gudvangen, S.J. Flockton, “Modelling of Acoustic Transfer-Functions for Echo Cancellers”, in *IEE Proceedings on Vision , Image and Signal Processing*, 1995, Feb. Vol. 142, No.1, PP. 47-51.

[124] H. Yasukawa, “An acoustic echo canceller with sub-band noise cancelling” Electronics Letters, Vol. 28, No. 15, pp. 1403-1404, July, 1992.

[125] C. Caraiscos, B.Liu, “A Roundoff Error Analysis of the LMS Adaptive Algorithm”, *I.E.E.E. Trans. on Acoustics, Speech and Sig. Proc*. Vol. ASSP-32, No. 1, Feb. 1984, pp. 34-41.

[126] A.N. Birkett, R. A. Goubran, “Limitations of Handsfree Acoustic Echo Cancellers due to Nonlinear Loudspeaker Distortion and Enclosure Vibration Effects”, in *1995 IEEE ASSP Workshop on Appl. of Sig. Proc. to Aud. and Acoustics*, New Paltz, New York, Oct. 1995.

[127] A. N. Birkett, R. A. Goubran, “Nonlinear loudspeaker compensation for handsfree acoustic echo cancellation”, *IEE Electronics Letters*, Vol. 32, No. 12, pp. 1063-1064, June 1996.

[128] S. M. Kuo, Z. Pan, “Distributed Acoustic Echo Cancellation System with Double-talk Detector”, *J. Acoust. Soc. Am*. No. 6, Dec.1993, pp. 3057-3060.

[129] S.M. Kuo, J. Chen, “Analysis of finite length acoustic echo cancellation system”, Speech Communication, Vol. 16, 1995, pp. 255-260.

[130] R. D. Poltmann, “Stochastic Gradient Algorithm for System Identification Using Adaptive FIR-Filters with too Low Number of Coefficients”, *IEEE Trans. on Circ. and Syst.*, Vol. 35, No. 2, Feb. 1988, pp. 247-250.

[131] E. Eleftheriou, D.D. Falconer, “Tracking Properties and Steady State Performance of RLS Adaptive Filter Algorithms”, *IEEE Trans. on Acoust., Speech and Sig. Proc*., Vol ASSP-34, No. 3, June, 1986, pp. 499-510.

[132] R. B. Wallace, R. A. Goubran, “ Parallel Adaptive Filter Structures for Acoustic Noise Cancellation”, 1992 *I.E.E.E. International Symposium on Circuits and Systems* , pp. 525-528.

[133] A. Gilloire, M. Vetterli, “Adaptive Filtering in Subbands with Critical Sampling: Analysis, Experiments, and Application to Acoustic Echo Cancellation”, *I.E.E.E. Transactions on Signal Processing*, Vol. 40, No. 8 Aug. 1992, pp. 1862-1875.

[134] A. Gilloire, T. Petillon, S. Theodoridis, “Acoustic Echo Cancellation Using Fast RLS Adaptive Filters with Reduced Complexity”, *1992, IEEE Int. Symp. on Circ. and Sys*., pp. 2065-2068.

[135] Sommen, Piet C.W., P.J. Van Gerwen, H, J. Kotmans, A.J.E.M. Jansen, “Convergence analysis of a frequency domain adaptive filter with exponential power averaging and generalized window function”, IEEE Trans. Circ. Syst., Vol. CAS-34, No.7, 1987, July, pp. 788-798.

[136] P. Naylor, J. Alcazar, J. Boudy, Y. Grenier, “Enhancement of Hands-free Telecommunications”, in *Annales des Telecommunications*, Vol. 49, No. 7-8, Jul.-Aug. 1994, pp.373-379.

[137] J. Prado, E. Moulines, “Frequency Domain Adaptive Filtering with Applications to Acoustic Echo Cancellation”, in *Annales des Telecommunications*, Vol. 49, No. 7-8, Jul.-Aug. 1994, pp. 414-428.

[138] J. Soo, K. Pang, “Multidelay Block Frequency Domain adaptive Filter”, *IEEE Trans. on Acoustics, Speech and Sig. Proc*., Vol. 38, No. 2, Feb. 1990, pp. 373-376.

[139] D. Mansour, A. Gray, “Unconstained frequency domain adaptive filter”, *IEEE Trans. ASSP*, Vol. 30, No. 5, pp. 726-734, 1982.

[140] O. Rioul, M. Vetterli, “Wavelets and Signal Processing”, *IEEE Signal Processing Magazine*, Oct. 1991, pp.14-38.

[141] T. Petillon, A. Gilloire, S. Theodoridis, “A Fast Newton Transversal Filter: An Efficient Scheme for Acoustic Echo Cancellation in Mobile Radio”, *IEEE Trans. on Sig. Proc.* Vol. 42, No. 3, March 1994, pp. 509-518.

[142] E. Martine, A. Gilloire, P. Le Scan, “CAD of Signal processing Architectures: An Application to Acoustic Echo Cancellation”, in *Annales des Telecommunications*, Vol. 49, No. 7-8, Jul.-Aug. 1994, pp. 447-459.

[143] Gay, S.L. and S. Tavathia, “The fast affine projection algorithm”, *Proceedings, ICASSP 1995*, Vol 3, pp. 3023-3026.

[144] Liu, Q.G. , B. Champagne and K.C. Ho, “On the use of a modified fast affine projection algorithm in subbands for acoustic echo control”, *Proceedings IEEE DSP Workshop*, Sept. 1995.

[145] H. P. Meana, et. al., “A Time Varying Step Size Normalized LMS Echo Canceler Algorithm”, *Proceedings ICASSP 1994*, Vol 2, pp. 249-252.

[146] S. Makino, Y. Keneda, N. Koizumi, “Exponentially Weighted Stepsize NLMS Adaptive Filter Based on the Statistics of Room Impulse Response”,*IEEE Trans. on Speech and Audio Proc.*, Vol. 1, No. 1, Jan 1993, pp. 101-108.

[147] Dr. A. Van Shyndel, Nortel, Personal Communication.

[148] J. Zhan, F. Li, “A new algorithm for realizing arbitrary nonlinear filters- Adaptive neural filters”, Proceedings, ICASSP 1994, Vol. 3, pp. 89-92.

[149] Yamada, T. Yabuta, T. and Takahashi, K., “Remarks on an adaptive type self tuning controller using neural networks”, *Proceedings of IECON*, 1991, pp. 1389-1394.

[150] A.S. Weigund, N. A. Gershenfeld, *Time Series Prediction, Forecasting the Future and Understanding the Past*, Proceeding of the NATO Advanced Research Workshop on Comparative Time Series Analysis, Santa Fe, New Mexico, May, 1992.

[151] A. D. Back, A. C. Tsoi, “An Adaptive Lattice Architecture for Dynamic Multilayer Perceptrons”, *Neural Computation*, No. 4, 1992, pp. 922-931.

[152] P. Kabal, “The Stability of Adaptive Minimum Mean Square Error Equalizers Using Delayed Adjustment”, *IEEE Trans. Comm.*, Vol COM-31, No. 3, March 1983, pp. 430-432.

[153] A. Back, E. Wan, S. Lawrence, Ah Chung Tsoi, “Algorithms for Multilayer Perceptrons with FIR Filter synapses”, *Neural Networks for Signal Processing IV: Proceeding s of the1994 IEEE Workshop*, John Vlontzos, Jenq-Neng Hwang, E. Wilson Editors, IEEE Press, New York, pp. 146-154.

[154] J. S. Lim, C. K. Un, “Conjugate Gradient Algorithm for Block FIR Adaptive Filtering”, *Electronic Letters*, 4th March, 1993, Vol. 29, No. 5, pp.428-429.

[155] Adeli, H., and S.L. Hung, “An adaptive conjugate gradient learning algorithm for efficient training of neural networks”, *Applied Mathematics and Computation*, Vol. 62, 1994, pp. 81-102.

[156] Webster, T., “Tracking Performance of Acoustic Echo Cancellers”, M. Eng. Thesis, Carleton University, June., 1995.

[157] C. E. Davila, “Line Search Algorithms for Adaptive Filtering”, *IEEE Trans. Sig. Proc.*, Vol 41, No. 7, pp. 2490-2494, July 1993.

[158] M. S. Moller, “A scaled conjugate gradient algorithm for fast supervised learning” *Neural Networks*, Vol. 6, No. 4, pp. 525-534, 1993.

[159] W.X. Zheng, “Application of Simplified Line Searches in the Design of Adaptive Envelope-Constrained Filters”, IEEE Trans. Circ. and Syst., vol. 43, no. 10, Oct. 1996, pp. 854-858.

[160] J. Proakis, “Channel Identification for High Speed Digital Communications”, *IEEE Trans. Automat. Control*, Vol. AC-19, pp. 916-922, Dec. 1974.

[161] D. F. Shanno, “Conjugate gradient methods with inexact line searches”, *Mathematics of Operations Research*, Vol. 3, pp. 244-256, 1978.

[162] D. R. Hush, J. M. Salas, “Improving the Learning Rate of Back-Propagation with the Gradient Reuse Algorithm”, *Proceedings IEEE Int. Conf. on Neural Nets*, Vol.1, 1988,pp. 441-448.

[163] A.N. Birkett, R.A. Goubran, “Conjugate Gradient Reuse Algorithm Using a Variable Step-Size Line Search”, Accepted for publication in *1997 International Symposium on Circuits and Systems*, Hong Kong, June 1997.

[164] A.N. Birkett, R.A. Goubran, “Nonlinear adaptive filtering with FIR synapses and adaptive activation functions”, Accepted for publication in *Proceedings ICASSP’97*, Munich, April 1997.

[165] A.N. Birkett, R.A. Goubran, “Fast nonlinear adaptive filtering using a partial conjugate gradient algorithm”, *Proceedings ICASSP’96*, Atlanta Georgia, Vol 6, pp. 3542-3545, May 1996.

[166] A.N. Birkett, R.A. Goubran, “Nonlinear echo cancellation using a partial adaptive time delay neural network” *Neural Networks for Signal Processing V: Proceedings of the 1995 IEEE Workshop*, pp. 249-258, Aug. 1995.

[167] A.N. Birkett, R.A. Goubran, “Acoustic echo cancellation for handsfree telephony using neural networks” *Neural Networks for Signal Processing IV: Proceedings of the 1994 IEEE Workshop*, pp. 249-258, Aug. 1994.

[168] Lariviere, Jeff P., “Tutorial on the Generalized multidelay frequency domain adaptive filtering with applications to acoustic echo cancellation”, Interim research report, Carleton University, September, 1996.

[169] J. J. Shynk, “Adaptive IIR Filtering Using Parallel-Form Realizations”, *IEEE Transactions on Acoustics, Speech, and Signal Processing*, Vol. ASSP-37, No. 4, pp. 519-533.

[170] P. A. Regalia, “Stable and Efficient Lattice Algorithms for Adaptive IIR Filtering”, *IEEE Transactions on Signal Processing*, Vol. 40, No. 2, Feb. 1992, pp. 375-388.

[171] L. Ljung and T Soderstrom, Theory and Practice of Recursive Identification, MIT Press, 1983.

Appendix A Recording Venues

Conference Room #1

Minto 3033

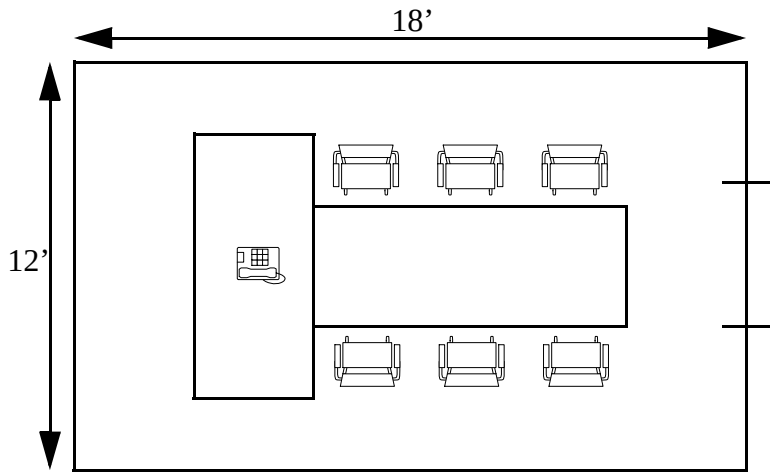

FIGURE A.1 Conference room #1 (Minto 3033).

Characteristics:

- rectangular : 12’W x 18’L x 10’H
- reflective walls and floor.
- two tables, 6 padded chairs arranged around one table.
- ventilation fan on

Conference Room #2

Minto 2014

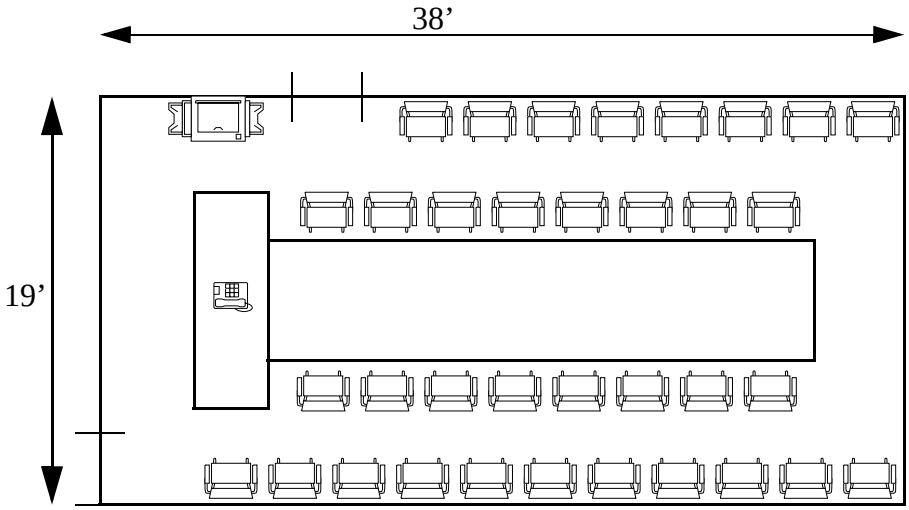

FIGURE A.2 Conference room #2 (Minto 2014)

Characteristics:

- rectangular conference room: 19’W x 38’ L x 10’H
- furnished. padded chairs, paintings, one small sound absorbing tile.
- floor is carpeted.
- ventilation fan on.

Standard Audio Baffle
(Anechoic Recordings)

.

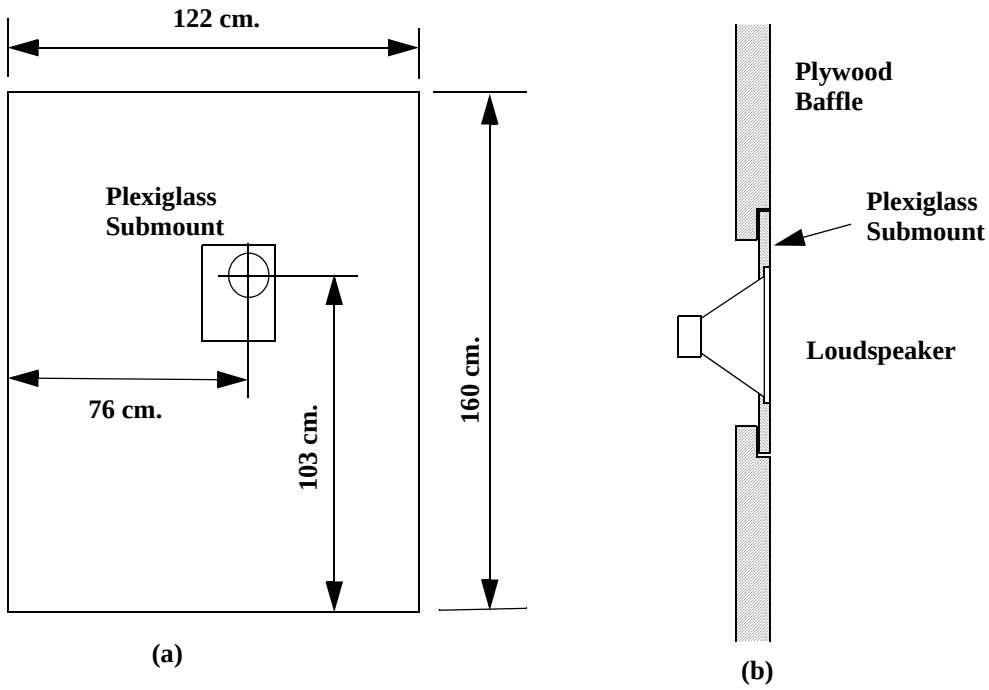

FIGURE A.3 Standard baffle used to test stand-alone loudspeakers. (a) Dimensions of plywood section (b) Detail of plexiglass submount.

Notes:

- The loudspeaker is placed in standard baffle to remove effects of vibrations and resonances within the HFT enclosure.
- Used during anechoic recordings.
- The large size approximates an “infinite baffle” characteristic.
- Dimensions are offset to prevent vibrational modes within the baffle.

Appendix B Equipment Parameters

TABLE B.1Parameters of HFT and transducer equipment.

Parameter	Model	Rating	Notes
SPK#1	CF050-A00604	50Ω, 2W	2” dia. round, large magnet.
SPK#2	LS06C050	50Ω, 0.5W	2.25” x 3” oval. Medium size magnet.
SPK#3	AD4061/W8	8Ω, 10W	4” dia. round. Large magnet, high quality.
MIC#1	Archer 270-090	4.5VDC thru ext. 1kΩ. S/N >40 dB , Sens.=-6.5 dB	Electret Microphone (low quality).
MIC#2	Audio Technica AT831b and power module	Cardiod sens. -44 dBm 200Ω.	“High quality” microphone element.
HFT#1	Northern Telecom / NT8B04AA	SPK#2	$75 price range
HFT#2	Mitel/Superset 430	60Ω, 0.5W, 2.5”round spkr.	Office set functions
HFT #3	Mitel/Superset 410	60Ω, 0.5W, 2.5”round spkr.	Office set functions
HFT#4	Telemax/ CP268A	8Ω, 0.25W, 2”round spkr.	$30 price range
HFT#5	Panasonic / KX-T2315	32Ω, 0.4W, 2.5”round spkr.	$120 price range
HFT#6	Norther Telecomm / Vista 350	50Ω, 0.5W, 2”round spkr.	Electret mic. inside a rubber grommet. Loudspeaker not screwed to enclosure.
SPL Meter	Realistic 33-2050	50-125 dB SPL	0dB=0.0002 μbar.
DAT #1	TEAC DA-P20		Portable
DAT #2	Sony TC-D7		Portable
Noise Generator	General Radio Company 1390-B	0.0005-5 Vrms range and 20 kHz/500kHz/ 5Mhz selectable BW.	Noise diode, amplified.
Audio Ampliofier	Samson Servo-150	75W rms/channel. 2 channels.	Studio quality.

Appendix C Circuit Schematics

A number of circuits were required in order to make the appropriate measurements. The schematics are shown in Sections C.1 through C.7.

C.1 Primary Conditioning Amplifier

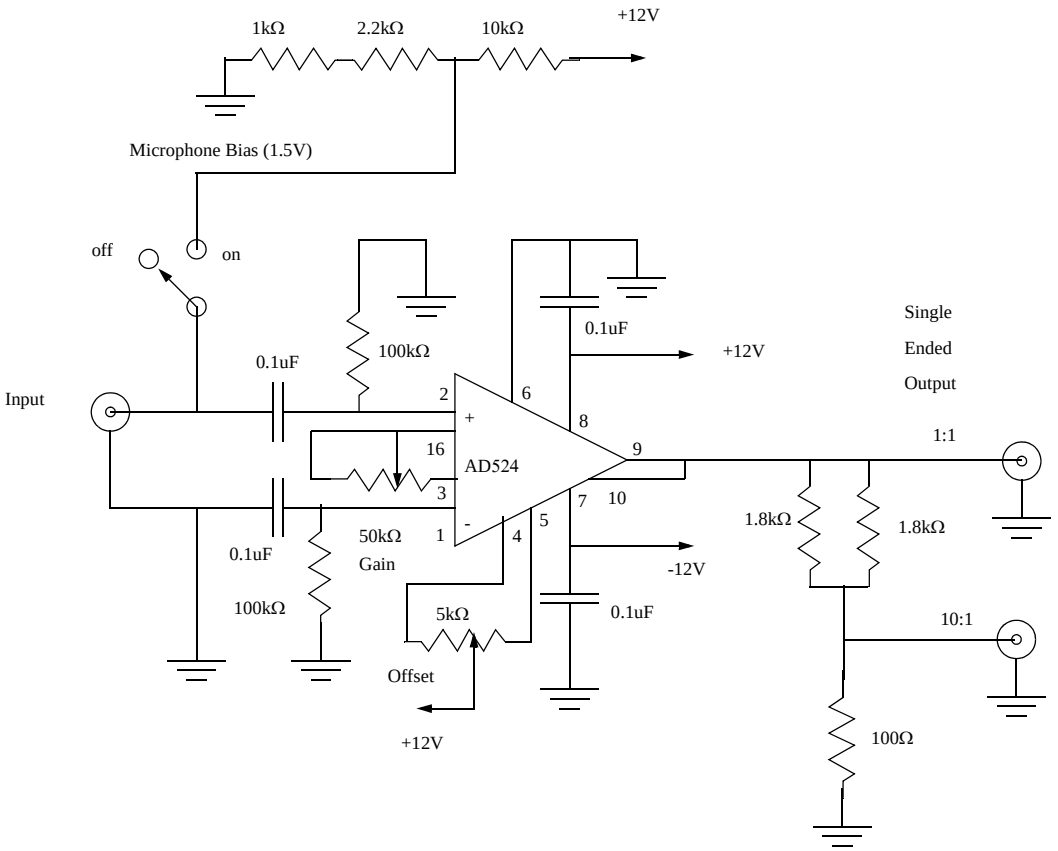

AD524: Instrumentation Amplifier.

C.2 Reference Conditioning Amplifier

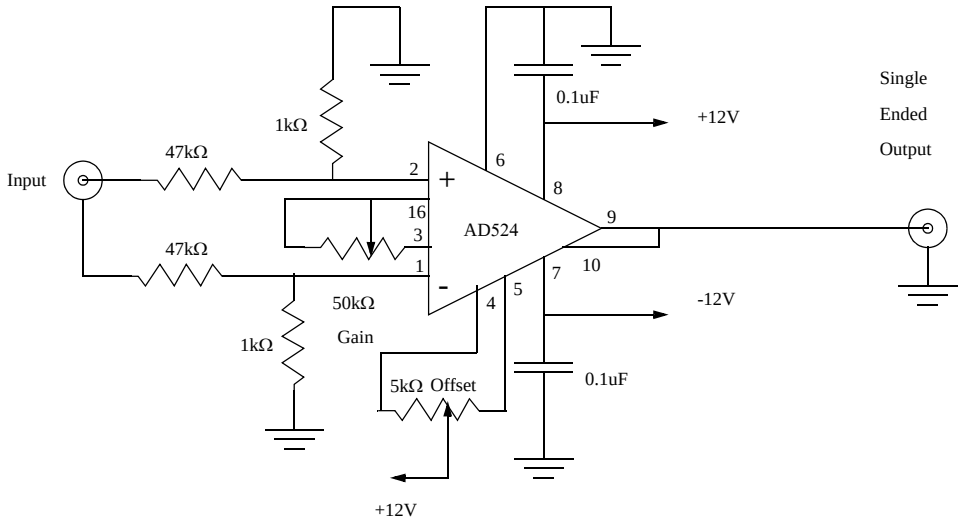

AD524: Instrumentation Amplifier.

C.3 Switched Capacitor Filter

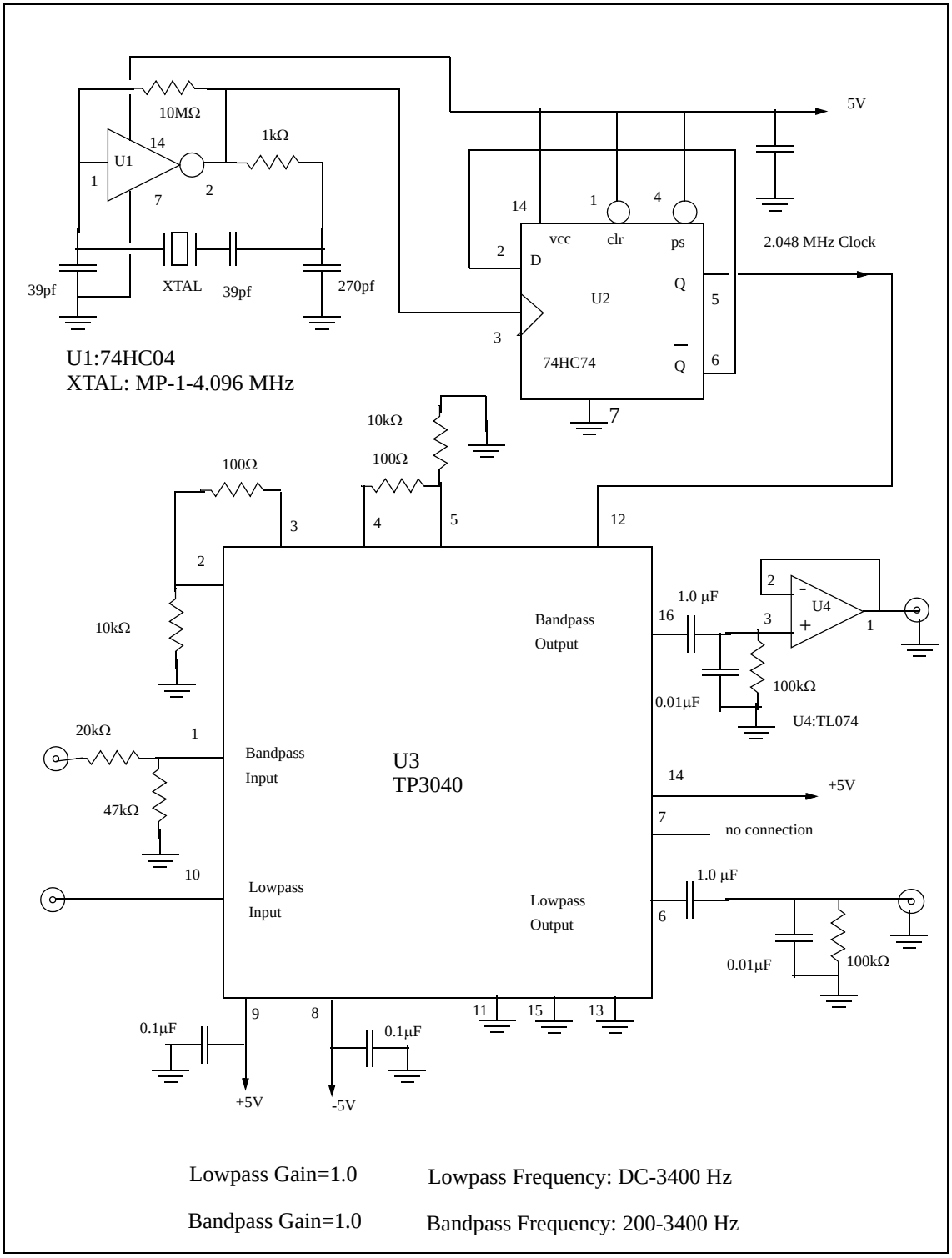

C.4 Resistive Attenuator Circuits

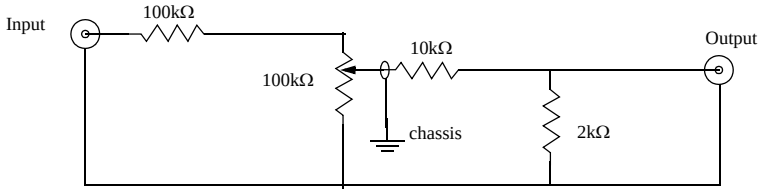

Output impedance approximates microphone loading.

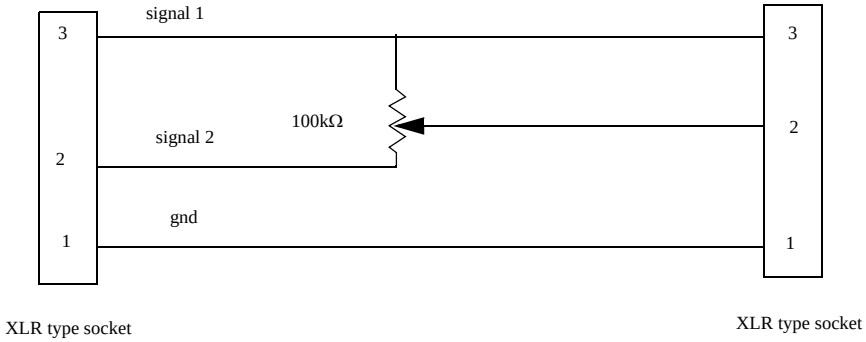

C.5 General Purpose Amplifiers

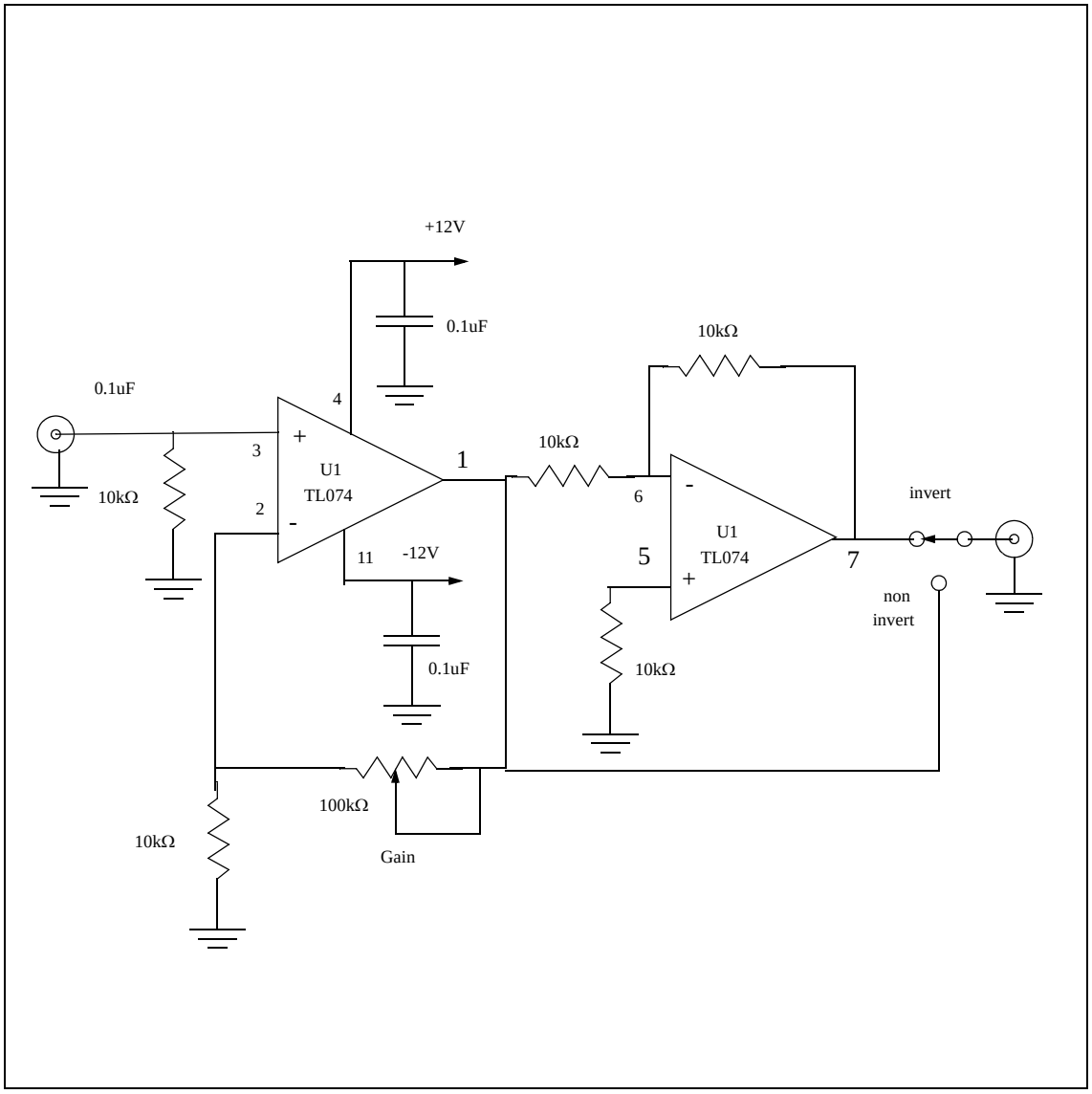

Appendix D Algorithms

D.1 The LMS Algorithm

Initialization.
$$\mathbf{w}(n) = \mathbf{0} \tag{D.1}$$

Algorithm.
$$e(n) = y(n) - \mathbf{w}(n)^T \cdot \mathbf{x}(n) \tag{D.2}$$

$$\mathbf{w}(n+1) = \mathbf{w}(n) + \mu \cdot e(n) \cdot \mathbf{x}(n) \tag{D.3}$$

Stability. μ is the step size which must be chosen to ensure stability:

$$0 < \mu < \frac{2}{\sum_{i=0}^{M-1} \lambda_i} \tag{D.4}$$

where λ_i are the eigenvalues of the input correlation matrix.

D.2 The Normalized LMS Algorithm

Initialization.
$$\mathbf{w}(n) = \mathbf{0} \tag{D.5}$$

Algorithm.
$$e(n) = y(n) - \mathbf{w}(n)^T \cdot \mathbf{x}(n) \tag{D.6}$$

$$\mathbf{w}(n+1) = \mathbf{w}(n) + \frac{\alpha \cdot e(n) \cdot \mathbf{x}(n)}{\varepsilon + \|\mathbf{x}(n)\|^2} \tag{D.7}$$

where

- α is the normalized step size constant.
- ε is a small positive constant used to place a lower bound on the input signal power.

Stability. $0<\alpha<2$.

D.3 The Modified Variable Step Size Algorithm

The MVSS is a robust variable step size algorithm for LMS type filters that estimates the autocorrelation of the error signal to determine when the minimum of the performance surface is reached. When the error correlation is large, dynamic step size control adjusts the step size to be large thus speeding up the convergence. When the error correlation is small, as is the case in high noise environments, or when the minimum is reached, the step size is reduced correspondingly.

Initialization.

$$\mathbf{w}(n) = \mathbf{0} \tag{D.8}$$

Algorithm.

$$e(n) = y(n) - \mathbf{w}(n)^T \cdot \mathbf{x}(n) \tag{D.9}$$

$$\mathbf{w}(n+1) = \mathbf{w}(n) + \mu(n) \cdot e(n) \cdot \mathbf{x}(n) \tag{D.10}$$

$$\mu(n+1) = \begin{cases} \mu_{max} & ;\mu(n+1) \geq \mu_{max} \\ \mu_{min} & ;\mu(n+1) \leq \mu_{min} \\ \zeta\mu(n) + \gamma\rho^2(n) & ;\mu_{min} < \mu(n+1) < \mu_{max} \end{cases} \tag{D.11}$$

where,

$$\rho(n) = \Gamma\rho(n-1) + (1-\Gamma)e(n)e(n-1) \tag{D.12}$$

$$\text{and} \quad \begin{cases} 0 < \zeta < 1 \\ \Gamma < 1 \\ \gamma > 0 \end{cases} \tag{D.13}$$

The parameter γ controls the convergence time as well as the final misadjustment. The parameter ζ controls the averaging of the step size update and Γ controls the averaging time constant of the filtered error update. The parameter ρ gives a short time estimate of the error signal autocorrelation. Typical parameter values are ζ=0.97, Γ=0.99, γ=1e-5 [55].

D.4 The Exponentially Weighted RLS Algorithm

The exponentially weighted RLS algorithm can be constructed from the *accelerated steepest descent algorithm*.

$$\begin{aligned} \varepsilon(n) &= y(n) - \mathbf{w}^T(n-1)\mathbf{x}(n) \\ \mathbf{w}(n) &= \mathbf{w}(n-1) + \mu(n)\varepsilon(n)\mathbf{P}(n-1)\mathbf{x}(n) \end{aligned} \qquad (D.14)$$

by setting the variables $\mathbf{P}(n-1)$ and $\mu(n)$ as follows;

$$\begin{aligned} \mathbf{P}(n-1) &\approx \mathbf{R}^{-1}(n-1) \\ \mu(n) &= \frac{1}{1+q(n)} \end{aligned} \qquad (D.15)$$

where;

$$q(n) = \lambda^{-1}\mathbf{x}^T(n)\mathbf{P}(n-1)\mathbf{x}(n) \qquad (D.16)$$

$\mathbf{P}(n-1)$ is the estimated inverse of the M by M autocorrelation matrix $\mathbf{R}$ at time n-1.

λ is a forgetting factor between 0 and 1.

ε is the a priori estimation error based on the weight vector at time n-1.

The term q is a measure of the input signal power just as $\mathbf{x}^T(n)\mathbf{x}(n)$ would be, but with a normalization introduced by $\mathbf{P}(n-1)$. The *matrix inversion lemma* [171] is employed to recursively compute $\mathbf{P}(n)$. It reduces the complexity from $O(M^3)$ to $O(M^2)$ by using the previous value $\mathbf{P}(n-1)$ as follows;

$$\mathbf{P}(n) = \lambda^{-1}\mathbf{P}(n-1) - \lambda^{-1}\mathbf{k}(n)\mathbf{x}^T(n)\mathbf{P}(n-1) \qquad (D.17)$$

where the gain vector $\mathbf{k}(n)$ is described by;

$$\mathbf{k}(n) = \frac{\lambda^{-1}\mathbf{P}(n-1)\mathbf{x}(n)}{1+q(n)} \qquad (D.18)$$

D.5 The Accelerated 8N-SFTF Algorithm

Initialization.

$$\alpha(0) = \zeta \cdot \lambda^{N}$$

$$\beta(0) = \zeta$$

ζ is the initial input variance and should be set large enough to prevent start-up divergence. A value between 1 and 200 appears reasonable for filter orders up to 1200 taps.

$$\gamma_N(0) = 1$$

$$\mathbf{x}_N = \mathbf{a}_N = \mathbf{b}_N = \mathbf{k}_N = \mathbf{w}_N = \mathbf{0}$$

$$\mathbf{k}_{N+1} = \mathbf{0} \qquad (D.19)$$

Phase 1: Prediction Part.

- Compute the forward prediction error $e_f(n)$.

$$e_f(n) = x(n) - \mathbf{a}_N(n-1)^T \cdot \mathbf{x}_N(n-1) \qquad (D.20)$$

- Compute the variance α of the forward prediction error.

$$\alpha(n) = \lambda \cdot \alpha(n-1) + \gamma_N(n-1) \cdot e_f(n)^2 \qquad (D.21)$$

- Compute the likelihood variable γ of order N+1.

$$\gamma_{N+1}(n) = \frac{\lambda \cdot \alpha(n-1)}{\alpha(n)} \cdot \gamma_N(n-1) \qquad (D.22)$$

- Compute the first auxiliary variable **s** and the dual Kalman gain **k** of order N+1.

$$\mathbf{s}_{N+1}(n) = \frac{e_f(n)}{\lambda \cdot \alpha(n-1)} \cdot \begin{bmatrix} 1 \\ -\mathbf{a}_N(n-1) \end{bmatrix} \quad (D.23)$$

$$\mathbf{k}_{N+1}(n) = \begin{bmatrix} 0 \\ \tilde{\mathbf{k}}_N(n-1) \end{bmatrix} - \mathbf{s}_{N+1}(n) \quad (D.24)$$

- Update the coefficients of the forward predictor $\mathbf{a}_N$.

$$\mathbf{a}_N(n) = \mathbf{a}_N(n-1) - e_f(n) \cdot \gamma_N(n-1) \cdot \mathbf{k}_N(n-1) \quad (D.25)$$

- Compute the backward prediction error $e_b(n)$.

$$e_b(n) = x(n-N) - \mathbf{b}_N(n-1)^T \cdot \mathbf{x}_N(n) \quad (D.26)$$

- Stabilize the backward prediction error.

$$\tilde{e}_b(n) = 2 \cdot e_b(n) + \lambda \cdot \beta(n-1) \cdot \mathbf{k}_{N+1}^{N+1}(n) \quad (D.27)$$

- Compute the likelihood variable of order N.

$$\gamma_N(n) = \frac{\gamma_{N+1}(n)}{1 + \gamma_{N+1}(n) \cdot \tilde{e}_b(n) \cdot \mathbf{k}_{N+1}^{N+1}(n)} \quad (D.28)$$

- Compute the second auxiliary variable **u** and the dual Kalman gain **k** of order *N*.

$$\mathbf{u}_{M+1}(n) = -\mathbf{k}_{N+1}^{N+1}(n) \cdot \begin{bmatrix} -\mathbf{b}_N(n-1) \\ 1 \end{bmatrix} \quad (D.29)$$

$$\begin{bmatrix} \mathbf{k}_N(n) \\ 0 \end{bmatrix} = \mathbf{k}_{N+1}(n) + \mathbf{u}_{M+1}(n) \quad (D.30)$$

- Update the coefficients of the backward predictor **b**.

$$\mathbf{b}_N(n) = \mathbf{b}_N(n-1) - \tilde{e}_b(n) \cdot \gamma_N(n) \cdot \mathbf{k}_N(n) \quad (D.31)$$

- Compute the variance β of the backward prediction error.

$$\beta(n) = \lambda \cdot \beta(n-1) + \gamma_N(n) \cdot \tilde{e_b}(n)^2 \qquad (D.32)$$

Phase 2: Filtering Part.

$$e(n) = y(n) - \mathbf{w}_N(n-1)^T \cdot \mathbf{x}_N(n) \qquad (D.33)$$

$$\mathbf{w}_N(n) = \mathbf{w}_N(n-1) - \eta(n) \cdot e(n) \cdot \gamma_N(n) \cdot \mathbf{k}_N(n) \qquad (D.34)$$

where

$$\eta(n) = \frac{1}{1 - \rho \cdot \gamma_N(n)} \qquad (D.35)$$

and ρ is the acceleration factor which varies the effective accelerated forgetting factor λ_{acc} between λ (ρ=0) and 0 (ρ=1), according to;

$$\lambda_{acc} = \frac{(1-\rho)\lambda}{1 - \rho\lambda} \qquad (D.36)$$

Stability. $\left(1 - \frac{1}{2N}\right) < \lambda < 1$ (Note: the lower bound should be avoided)

Conditional Re-initialization. The prediction part of the algorithm must be re-initialized following periods of poor excitation, which is typical with speech. This is accomplished by resetting *all* prediction variables whenever $\gamma_N(n)$ approaches zero without clearing $\mathbf{w}_N(n)$, i.e,.

$$\mathbf{a}_N = \mathbf{b}_N = \mathbf{k}_N = \mathbf{0} \qquad (D.37)$$

$$\alpha(n) = \zeta \cdot \lambda^N \qquad \beta(0) = \zeta \qquad (D.38)$$

D.6 Equation Error LMS-IIR Algorithm

Initialization.

$$\mathbf{w}(n) = \mathbf{0} \tag{D.39}$$

Algorithm.

$$y(n) = \mathbf{w}^T(n)\mathbf{u}(n) \tag{D.40}$$

$$e(n) = d(n) - y(n) \tag{D.41}$$

$$\mathbf{w}(n+1) = \mathbf{w}(n) + \mu e(n)\mathbf{u}(n) \tag{D.42}$$

where;

$$\mathbf{w}(n) = [a_1(n), a_2(n) \ldots a_{n_a}(n), b_0(n), b_1(n) \ldots b_{n_b}(n)]^T \tag{D.43}$$

$$\mathbf{u}(n) = [d(n-1), \ldots, d(n-n_a), x(n), x(n-1), \ldots, x(n-n_b)]^T \tag{D.44}$$

$$\mu = [\mu^a{}_1, \ldots, \mu^a{}_{n_a}, \mu^b{}_0, \ldots, \mu^b{}_{n_b}] \tag{D.45}$$

The step sizes μ^a and μ^b can be fixed or normalized with respect to the input power in the same way as the NLMS algorithm.

D.7 Output Error LMS-IIR Algorithm with Simplified Gradient

The output of an OE-IIR filter is defined by;

$$y(n) = \sum_{i=1}^{n_a} a_i(n)y(n-i) + \sum_{i=0}^{n_b} b_i(n)x(n-i) \tag{D.46}$$

The parameter update is obtained by minimizing J respect to the weight vector $\mathbf{w}$;

$$\begin{aligned}\nabla_{\mathbf{w}}(J) &= \frac{\partial}{\partial \mathbf{w}}(e^2(n)) = 2e(n)\frac{\partial}{\partial \mathbf{w}}[d(n)-y(n)] \\ &= -2e(n)\frac{\partial}{\partial \mathbf{w}}[y(n)] = -2e(n)\nabla_{\mathbf{w}}(y(n))\end{aligned} \tag{D.47}$$

where the gradient $\nabla_{\mathbf{w}}(y(n))$ is the following column vector;

$$\nabla_{\mathbf{w}}(y(n)) = \left[\frac{\partial y(n)}{\partial a_1(n)}, \ldots, \frac{\partial y(n)}{\partial a_{n_a}(n)}, \frac{\partial y(n)}{\partial b_0(n)}, \ldots, \frac{\partial y(n)}{\partial b_{n_b}(n)}\right]^T \tag{D.48}$$

Each component $\nabla_{\mathbf{w}}(y(n))$ of may be obtained by differentiating (D.46) to obtain;

$$\frac{\partial y(n)}{\partial a_i(n)} = y(n-i) + \sum_{m=1}^{n_a} a_m(n)\frac{\partial y(n-m)}{\partial a_i(n)} \approx y(n-i) + \sum_{m=1}^{n_a} a_m(n)\frac{\partial y(n-m)}{\partial a_i(n-m)} \tag{D.49}$$

$$\frac{\partial y(n)}{\partial b_i(n)} = x(n-i) + \sum_{m=1}^{n_a} a_m(n)\frac{\partial y(n-m)}{\partial b_i(n)} \approx x(n-i) + \sum_{m=1}^{n_a} a_m(n)\frac{\partial y(n-m)}{\partial b_i(n-m)} \tag{D.50}$$

The approximation is valid if the step size is chosen sufficiently small [62]. We may now rewrite (D.48) using the approximations of (D.49) and (D.50) as a purely “autoregressively” filtered regressor;

$$\mathbf{u}_f(n) = \mathbf{u}(n) + \sum_{m=1}^{n_a} a_m(n)\mathbf{u}_f(n-i) \tag{D.51}$$

$\mathbf{u}_f(n)$ can be viewed as an *approximate* gradient estimate of the current output $y(n)$ with respect to the weight vector **w**. The calculation of $\mathbf{u}_f(n)$ is numerically intensive due to the AR filtering by the a_i coefficients for *each* component. A simplified gradient calculation can be made by assuming that the filtered regressor vector can be approximated by taking delayed outputs of the

first filtered component only. As a result, the filtered regressor becomes;

$$\mathbf{u}_f(n) = [y_f(n-1), y_f(n-2)\ldots y_f(n-n_a), x_f(n), x_f(n-1), \ldots x_f(n-n_b)]^T \qquad (D.52)$$

Figure D.1 shows how the simplified gradient vector is obtained by filtering the $x(n)$ and $y(n)$ by the all pole section $1 - A(z)$, and then selecting delayed versions of $x(n)$ and $y(n)$..

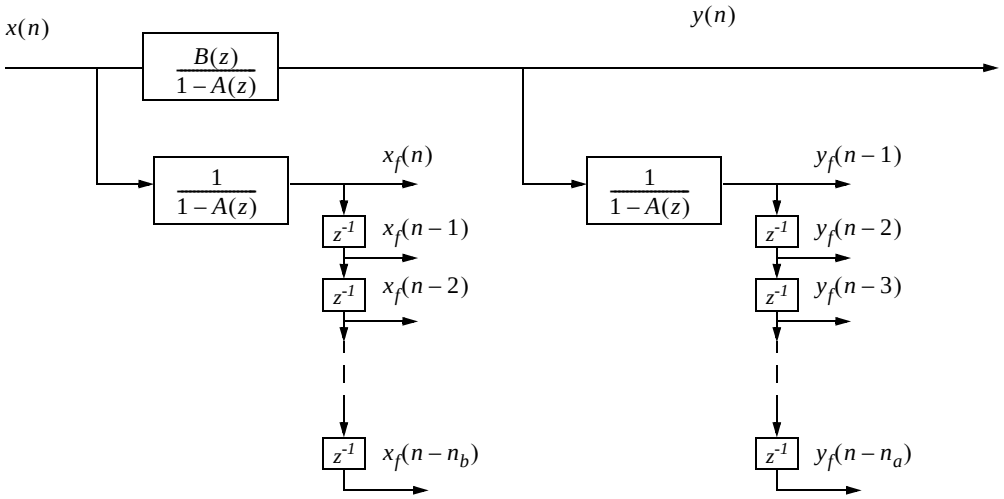

FIGURE D.1 The OE simplified gradient evaluation.

Stability Monitoring. One of the drawbacks with IIR algorithms is that the poles may update outside of the unit circle and cause instability. Various tests may be performed to ensure that the updates are stable, but this tends to either add complexity or compromise the performance of the algorithm. If the sum of the magnitude of all the pole coefficients is less than zero, then stability is guaranteed [62] however, it severely limits the values of $a_i(n)$ especially for large n_a.

$$\sum_{i=1}^{n_a} |a_i(n)| < 1, \qquad \textit{for all } n \qquad (4.53)$$

Stability monitoring may be simplified by using parallel or cascaded structures which consist of

1st or 2nd order IIR sections [169] which have a simpler stability check, referred to as the stability triangle [62]. Lattice structures also have simple stability checks (see [170])

Combining (D.46) through (D.52) yields the adaptive IIR-LMS filter algorithm with the same form as the accelerated steepest descent algorithm of equation (D.14).

OE_IIR Algorithm with Simplified Gradient

Initialization.

$$\mathbf{w}(n) = \mathbf{0} \tag{D.54}$$

Vector Definitions.

$$\mathbf{w}(n) = [a_1(n), a_2(n)\ldots a_{n_a}(n), b_0(n), b_1(n)\ldots b_{n_b}(n)]^T \tag{D.55}$$

$$\mathbf{u}(n) = [y(n-1), \ldots, y(n-n_a), x(n), x(n-1), \ldots, x(n-n_b)]^T \tag{D.56}$$

$$y_f(n) = y(n) + \sum_{m=1}^{n_a} a_m(n) y_f(n-m) \tag{D.57}$$

$$x_f(n) = x(n) + \sum_{m=1}^{n_a} a_m(n) x_f(n-m) \tag{D.58}$$

$$\mathbf{u}_f(n) = [y_f(n-1), y_f(n-2)\ldots y_f(n-n_a), x_f(n), x_f(n-1), \ldots x_f(n-n_b)]^T \tag{D.59}$$

Algorithm.

$$e(n) = d(n) - \mathbf{w}^T(n)\mathbf{u}(n) \tag{D.60}$$

$$\mathbf{w}(n+1) = w(n) + \mathbf{MP}(n)\mathbf{u}_f(n)e(n) \tag{D.61}$$

The matrix $\mathbf{P}(n)$ is replaced with the identity matrix **I** in the same manner as $\mathbf{P}(n)$ is replaced with the identity matrix in the LMS algorithm, and;

$$\mathbf{M} = diag[\mu_1, \ldots \mu_{n_a}, \rho_0, \ldots \rho_{n_b}] \; . \tag{D.62}$$

represents the fixed step sizes. Alternately, if we wish to solve for the coefficients in a least-squares sense, we may replace $\mathbf{P}(n)$ with an estimate of the inverse Hessian matrix, updated according to;

$$\mathbf{P}^{-1}(n) = \lambda \mathbf{P}^{-1}(n-1) + (1-\lambda)\mathbf{u}_f(n-1)\mathbf{u}_f^T(n-1) \tag{D.63}$$

and **M** with a fixed step size μ. Alternately, **P** may be update using the *matrix inversion lemma* [171];

$$\mathbf{P}(n) = \frac{1}{\lambda}\left[\mathbf{P}(n-1) - \frac{\mathbf{P}(n-1)\mathbf{u}_f(n)\mathbf{u}_f^T(n)\mathbf{P}(n-1)}{\frac{\lambda}{\mu} + \mathbf{u}_f^T(n)\mathbf{P}(n-1)\mathbf{u}_f(n)}\right] \tag{D.64}$$

D.8 The LMS Volterra Algorithm

Mapping and Regressor Construction. For a p^{th} order polynomial system, construct the p^{th} order weight and input vectors.

$$\mathbf{h}_p(n) = [h_p(m_1, m_1, \ldots, m_1), h_p(m_1, m_1, \ldots, m_2), \ldots, h_p(m_p, m_p, \ldots, m_p)]^T \tag{D.65}$$

$$\mathbf{x}_p(n) = \mathbf{x}_1(n) \otimes \mathbf{x}_{p-1}(n) \tag{D.66}$$

where ⊗ is the Kronecker product of vectors and it is assumed that the duplicate terms have been removed. Next construct the extended weight and input vectors.

$$\mathbf{h}_e{}^T(n) = [h_0, \mathbf{h}^T{}_1(n), \ldots, \mathbf{h}_p^T] \quad \text{(D.67)}$$

$$\mathbf{x}_e{}^T(n) = [1, \mathbf{x}^T{}_1(n), \ldots, \mathbf{x}_p^T] \quad \text{(D.68)}$$

Initialization. $$\mathbf{h}_e(n) = \mathbf{0} \quad \text{(D.69)}$$

Algorithm. $$e(n) = d(n) - \mathbf{h}_e^T(n) \cdot \mathbf{x}_e(n) \quad \text{(D.70)}$$

For each p^{th} order polynomial section update the weights.

$$\mathbf{h}_p(n+1) = \mathbf{h}_p(n) + \mu_p e(n)\mathbf{x}_p(n) \quad \text{(D.71)}$$

where μ_p is the step size for the p^{th} power term. Alternately, a normalized step size may be computed for each p^{th} order power term as;

$$\tilde{\mu_p} = \frac{\alpha}{\varepsilon + \left\|\mathbf{x}_p(n)\right\|^2} \quad \text{(D.72)}$$

Stability. Each μ_p is chosen to ensure stability according to:

$$0 < \mu_p < \frac{2}{\sum_{i=0}^{M-1} \lambda_i} \quad \text{(D.73)}$$

where λ_i are the eigenvalues of the p^{th} extended input correlation matrix.

Appendix E Statistics of a Nonlinear Function

E.1 Mean and Variance

Expected Value: The expected value or *mean* of a continuous random variable *X* having a probability density function *f*(*x*) is given by;

$$E(X) = m = \int_{-\infty}^{\infty} xf(x)dx \tag{E.1}$$

If *X* is a continuous random variable with probability distribution *f*(*x*) and *g*(*x*) is any real valued function of X, then;

$$E(g(X)) = \int_{-\infty}^{\infty} g(x)f(x)dx \tag{E.2}$$

Variance: if *X* is a random variable with mean *m*, then the *variance* equals;

$$V(X) = E(X^2) - m^2 \tag{E.3}$$

For any random variable *X* and constants *a* and *b*;

$$E(aX + b) = aE(X) + b \tag{E.4}$$

$$V(aX + b) = a^2V(X) \tag{E.5}$$

E.2 The Normal and Uniform Distribution

Normal Distribution: The normal distribution probability density function is given by;

$$f(x) = \frac{1}{\sigma\sqrt{2\pi}} e^{-x^2/2\sigma^2} \tag{E.6}$$

where σ is the standard deviation of the signal, usually set to one.

Higher Order Moments: The higher order moments may be obtained from the following equation.

$$E(X^n) = \begin{cases} 0 & n = 2k+1 \\ 1 \cdot 3 \ldots (n-1)\sigma^n & n = 2k \end{cases} \tag{E.7}$$

Variance of The Normal Distribution: The variance of the normal distribution is obtained by substituting (E.7) into (E.3) to obtain;

$$V(X) = \sigma^2 \tag{E.8}$$

The Uniform Distribution: The uniform probability density function is given by;

$$\begin{aligned} f(x) &= \frac{1}{(b-a)} \qquad a \le x \le b \\ f(x) &= 0 \qquad elsewhere \end{aligned} \tag{E.9}$$

Mean of the Uniform Distribution: Using the above probability function and equation (E.2) we can find $E(X)$ as;

$$E(X) = \frac{b+a}{2} \tag{E.10}$$

Higher Order Moments: Similarly, substituting X^2, X^3, X^4, X^5, X^6 into (E.2), we can get;

$$E(X^2) = \frac{b^2 + ab + a^2}{3} \tag{E.11}$$

$$E(X^3) = \frac{b^3 + b^2a + ba^2 + a^3}{4} \tag{E.12}$$

$$E(X^4) = \frac{b^4 + b^3a + b^2a^2 + ba^3 + a^4}{5} \tag{E.13}$$

$$E(X^5) = \frac{b^5 + b^4a + b^3a^2 + b^2a^3 + ba^4 + a^5}{6} \tag{E.14}$$

$$E(X^6) = \frac{b^6 + ab^5 + a^2b^4 + a^3b^3 + a^4b^2 + a^5b + a^6}{7} \quad \text{(E.15)}$$

Variance of The Uniform Distribution: The variance of a zero mean variable X with a uniform distribution between *a* and *b* can be computed by substituting (E.10) and (E.11) into (E.3) to obtain;

$$V(X) = \frac{(b-a)^2}{12} \quad \text{(E.16)}$$

E.3 Mean and Variance of a Nonlinear Function

If *y* is a function of a random variable *X*, i.e.;

$$y = uX + vX^2 + wX^3 \quad \text{(E.17)}$$

then the *mean* of the function *y* is given by;

$$E(y) = uE(X) + vE(X^2) + wE(X^3) \quad \text{(E.18)}$$

and the *variance* of the function *y* is given by the relationship;

$$V(y) = E(y^2) - [E(y)]^2 \quad \text{(E.19)}$$

where $E(y^2)$ is given by the following equation;

$$E(y^2) = u^2E(X^2) + 2uvE(X^3) + (v^2 + 2uw)E(X^4) + 2vwE(X^5) + w^2E(X^6) \quad \text{(E.20)}$$

E.4 Nonlinear Examples

Example 1: Signal-to-Distortion Ratio (SDR) Assuming a Uniform Distribution for *X*

Assume *X* has a range between -1 and +1. Calculate the signal to distortion of a variable *y* where *y* is a function of *X*, represented by the following equation;

$$y = \frac{\alpha X + \beta X^2 + \delta X^3}{|\alpha| + |\beta| + |\delta|} \tag{E.21}$$

This may be expressed as;

$$\begin{aligned} y &= s + d \\ &= uX + vX^2 + wX^3 \end{aligned} \tag{E.22}$$

where we have divided y into *signal* (*s*) and *distortion* (*d*) components,

$$\begin{aligned} s &= uX \\ d &= vX^2 + wX^3 \end{aligned} \tag{E.23}$$

$$\text{and} \begin{cases} u = \dfrac{\alpha}{|\alpha| + |\beta| + |\delta|} \\ v = \dfrac{\beta}{|\alpha| + |\beta| + |\delta|} \\ w = \dfrac{\delta}{|\alpha| + |\beta| + |\delta|} \end{cases} \tag{E.24}$$

The higher order moments of X are calculated using equations (E.11) through (E.15).

$E(X)=0$
$E(X^2)=1/3$
$E(X^3)=0$
$E(X^4)=1/5$
$E(X^5)=0$
$E(X^6)=1/7$

The variance of the undistorted signal $s=uX$ is obtained by setting v and w equal to zero in equation (E.17) and applying (E.19);

$$V(s) = E(s^2) - [E(s)]^2 = u^2 E(X^2) - 0 = \frac{u^2}{3} \tag{E.25}$$

The variance of the distortion signal $d=vX^2+wX^3$ is obtained by first computing the moments;

$$E(d) = vE(X^2) + uE(X^3) = v/3 \tag{E.26}$$

$$\begin{aligned} E(d^2) &= v^2E(X^4) + 2vwE(X^5) + w^2E(X^6) \\ &= v^2/5 + w^2/7 \end{aligned} \tag{E.27}$$

hence,

$$V(d) = v^2/5 + w^2/7 - [v/3]^2 = 4v^2/45 + w^2/7 \tag{E.28}$$

The *signal to distortion ratio* (SDR) is determined as $10 \log_{10} (V(s)/V(d))$.

Example 2: Signal-to-Distortion Ratio (SDR) Assuming a Normal Distribution for *X*

Assume X has a unit standard deviation. The higher order moments are calculated using equation (E.7).

$E(X)=0$
$E(X^2)=1$
$E(X^3)=0$
$E(X^4)=3$
$E(X^5)=0$
$E(X^6)=5$

since $\sigma=1$.

The variance of the undistorted signal $s=uX$ is obtained by applying (E.19);

$$V(s) = E(s^2) - [E(s)]^2 = u^2E(X^2) - 0 = u^2 \tag{E.29}$$

The variance of the distortion signal $d=vX^2+wX^3$ is obtained by first computing the moments;

$$E(d) = vE(X^2) + uE(X^3) = v \tag{E.30}$$

$$\begin{aligned} E(d^2) &= v^2E(X^4) + 2vwE(X^5) + w^2E(X^6) \\ &= 3v^2 + 5w^2 \end{aligned} \tag{E.31}$$

hence,

$$V(d) = 3v^2 + 5w^2 - v^2 = 2v^2 + 5w^2 \tag{E.32}$$

(E.33)

The SDR is determined as $10 \log_{10} (V(s)/V(d))$.

E.5 Implications for Adaptive Systems

From the above analysis, the SDR is a nonlinear function of *both* the input standard deviation (if noise) and the characteristics of the signal. This is illustrated in Figure E.1, which shows the calculated SDR for a cubic system similar to (E.21) where α=1, β=δ=0.2 are fixed as the standard deviation of the input noise signal is changed. The range of the SDR's is significantly different

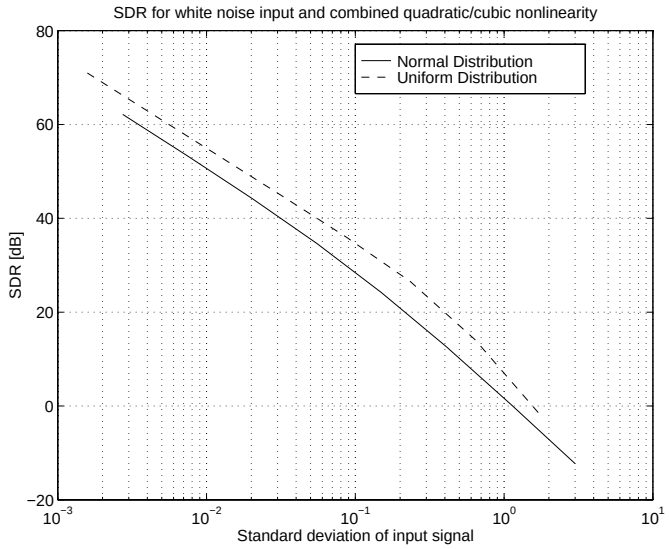

FIGURE E.1 Computed SDR for a cubic order system where the standard deviation of the input signal changes.

between the two signals due to the *outliers* in the normal distribution. This has important implica-

tions for adaptive systems that deal with inputs that have high *peak-to-RMS* ratios, for example speech. Essentially, the higher the peak-to RMS ratio encountered in the nonlinear domain, the lower the SDR and the worse the linear algorithms will perform in identifying the unknown system.